

DOCTORAL THESIS



Studies in Low Temperature
Self-Reduction of By-Products
from Integrated Iron and Steelmaking

Ryan Robinson

Luleå University of Technology
Department of Chemical Engineering and Geosciences
Division of Process Metallurgy

Studies in Low Temperature Self-Reduction of By-Products from Integrated Iron and Steelmaking

Ryan Robinson

Luleå University of Technology
Department of Chemical Engineering and Geosciences
Division of Process Metallurgy
SE-971 87 Luleå
Sweden

2008

PREFACE

The recycling and/or refining of iron-bearing by-products from integrated iron and steelmaking production is a vital technological endeavour for today's steel industry. Considerable amounts of fine-grained dust, sludge and mill scale are generated from iron and steel production annually. These by-products require some form of pre-treatment before recycling. Traditionally, a large part of these by-products were fed to the sinter plant but in Sweden, as a result of increased environmental accountability, the last sinter plants were closed during the mid 1990s. Increasing environmental regulation and increasing economical incentive to recycle by-products on-site have led the industry to consider recycling techniques that are economically viable and environmentally sound. Cold bond agglomeration is a low energy, environmentally suitable alternative to sintering of these by-products.

The aim of this thesis is to study the feasibility for effective recycling of cold bonded by-product agglomerates in the integrated iron and steelmaking process. On a fundamental level, this thesis investigates the properties of cold bonded pellets at room temperature and when subjected to high temperatures. The research topics include:

- Characterization of various cold bonded agglomerate blends
- Pellet cold strength and production capacity
- Self-reducing behavior of cold bonded pellets
- Large scale testing in an experimental blast furnace and a basic oxygen furnace

The work completed for this doctoral thesis was conducted in part at the Division of Process Metallurgy and in part as collaboration with industry in a research project within MiMeR (Minerals and Metals Recycling Research Center) at Luleå University of Technology as well as a research exchange with the Laboratory of Material and Metallurgical Engineering at the University of Nancy, France.

LIST OF PAPERS

This thesis is based on the following papers:

- 1) **Recycling of Sludge and Dust to the BOF Converter by Cold Bonded Pelletizing**, F. Su, H.-O. Lampinen, R. Robinson, ISIJ International, Vol. 44, 2004, No. 4, p. 770-776. *R. Robinson's contributions to this publication were as a participant in the design and execution of lab scale pelletizing tests, testing and evaluation of pellet cold strength and capacity, performing and evaluating thermal analysis experiments on pellet samples, and as an observer during full scale testing of pellets in the BOF converter.*
- 2) **Recycling of By-Product Pellets as Burden in the Blast Furnace Process: A Lab and Pilot Scale Investigation**, R. Robinson and L. Sundqvist Ökvist, Steel Research International 75, 2004, No. 2, p. 99-105. *R. Robinson's contributions to this publication were as a participant in probe material and gas sampling from the EBF, performing and evaluating thermal analysis experiments on pellet samples, and evaluating probe (gas, material and temperature) measurements.*
- 3) **High Temperature Properties of By-Product Cold Bonded Pellets Containing Blast Furnace Flue Dust**, R. Robinson, Thermochemical Acta, 2005, vol. 432, nr. 1, July 1, p. 112-123.
- 4) **A Mechanistic Study of Ca(OH)₂ Dehydration in the Presence of Graphite or Hematite in Relevance to Reactions in Agglomerates of Iron and Steelmaking By-Products**, R. Robinson, F. Patisson, B. Björkman, Manuscript. *F. Patisson has contributed knowledge of gas-solid kinetic analysis and B. Björkman as a supervisor.*
- 5) **Optimization in the Ca(OH)₂-C-Fe₂O₃ System with Regard to Internal Recycling in Integrated Steelmaking: Practical and Kinetic Studies**, R. Robinson, F. Patisson, B. Björkman, Manuscript. *F. Patisson has contributed knowledge of gas-solid kinetic analysis and B. Björkman as a supervisor.*

Related publications not included in this thesis:

- 6) **Recycling of Sludge and Dust through the BF and BOF By Cold Bonded Pelletizing at SSAB Tunnplat**, F. Su, H-O Lampinen, R. Robinson, L-E Eriksson, TMS fall 2002 Extraction and Processing Division Meeting on Recycling and Waste Treatment in Mineral and Metal Processing : technical and economic aspects. Luleå : Luleå Univ. of Technology : Stift. för metallurgisk forskning, 2002. s. 139-148
- 7) **Industrial Tests on Charging Cold Bonded Pellets as Part of Burden Materials in the BOF Converter**, F. Su, H.-O. Lampinen, R. Robinson, Proc. REWAS '2004: Global Symposium on Recycling, Waste Treatment and Clean Technology, Madrid, Spain, Sept. 26-29, 2004, Vol. 2, p. 1943-1952.
- 8) **High Temperature Properties of Iron and Steelmaking By-Product Cold Bonded Pellets**, R. Robinson, L. Sundqvist Ökvist, Proceedings, 5th European Coke and Ironmaking Congress. Stockholm: Jernkontoret, 2005. s. Tu3:2 1-15.
- 9) **Low Temperature Behavior of the Ca(OH)₂-C System and it's Significance on the Self-Reduction of Cold Bonded By-Product Agglomerates**, R. Robinson, N. Menad, B. Björkman, The Fourth International Congress on the Science and Technology of Ironmaking : Proceedings, ICSTI 06. The Iron and Steel Institute of Japan, 2006.

- 10) **Assessment of Ladle Slag as Binder Alternative for Cold Bonded Briquettes**, D. Adolfsson, R. Robinson, J. Blagojevic, F. Su, Proceedings of the 2008 Global Symposium on Recycling, Waste Treatment and Clean Technology (REWAS 2008), October 12-15, 2008, Cancun, Mexico.

ABSTRACT

Within the last decade, the landfill tax in Sweden has increased over 70% with comparable rates in the UK and elsewhere in EU. This development, among others, highlights the incentive for increased recycling efforts of fine particulate solid by-products in the iron and steel making industry in order to avoid depositing costs and to recover valuable metal fractions. As pre-treatment is necessary for recycling fine particulate material, cold bonded agglomeration is considered to be a well-suited alternative for recycling of steel industry by-product dust and sludge.

The major objective of this work has been to provide insight to help further the development of cold bonded agglomeration technology in order to increase the recycling of iron and steelmaking by-products. Laboratory pelletizing tests were conducted based on a factorial design test plan to help identify those variables that most influence the cold strength and capacity of product cold bonded pellets (CBPs). The design variables were the individual components of the by-product pellet mix; i.e. blast furnace (BF) flue dust, oily mill scale sludge, both fine and coarse basic oxygen furnace (BOF) dust and Portland cement as binder. A similar statistical procedure was used to plan reduction experiments in inert gas over a temperature range of 20-1200°C. The results from cold strength and reduction tests have been evaluated using multivariate statistical analysis to model the experimental variables with chosen responses in order to help identify those variables that have most significance. For agglomerate sizes used in this study, pellet blends with large fractions of particles in the size range of 10-40 µm promote good self-reduction while maintaining good cold strength.

The fundamental reactions occurring during the heat treatment of CBPs have also been studied. BF flue dust, which contains fractions of coal and coke particles, has been included in the CBP blend as a source of solid reductant. Thermal analysis was performed on samples in inert atmosphere at a heating rate of 10°C/min in order to observe their high temperature properties, specifically, the mechanism(s) of self-reduction. The gases generated during thermal analysis were analyzed with a mass spectrometer. Furthermore, raw and heat treated pellet samples were analyzed using X-ray diffraction and scanning electron microscopy. Results demonstrate that the decomposition of hydrates and carbonates in CBP samples contribute, as gaseous intermediates, to the prereduction of contained iron oxides. The gaseous intermediates are responsible for an initial gasification of carbon contained in BF flue dust leading to low temperature iron oxide reduction. The step-wise reduction of iron oxides in the pellets at the given conditions begins at roughly 500°C and is nearly complete at 1200°C.

Detailed studies of the system $\text{Ca}(\text{OH})_2\text{-C-Fe}_2\text{O}_3$ have also been conducted because of the inherent importance of this system in the self-reduction of by-product agglomerates. Experiments have confirmed that carbon gasification does occur during the dehydration of lime and kinetic results correlate well with behavior observed in CBPs. Hematite reduction in the simplified chemical system is controlled by either carbon gasification or availability of direct contact with graphite depending on hematite grain size. The latter results show less correlation with CBP behavior. After dehydration of $\text{Ca}(\text{OH})_2$, calcium ferrite formation begins at temperatures below 600°C. Furthermore, the effect of varying composition in the $\text{Ca}(\text{OH})_2\text{-C-Fe}_2\text{O}_3$ system has been studied in order to optimize self-reduction and low temperature bonding characteristics.

The metallurgical characteristics of CBPs have been tested in additional laboratory tests; i.e. isothermal reduction, BF simulation, and softening and melting tests. The results indicate that CBPs show a marked decrease in tumbler strength during reduction between 700 and 900°C when $\text{CO}/\text{CO}_2 > 1$ but as a fraction of the normal ferrous burden, ~10%, show good softening and melting properties.

Large-scale trials with CBPs have been conducted in a commercial BOF and a pilot scale BF. Results from BOF testing show that charging of CBPs is feasible at levels of at least 2.2 wt% of the total charge. At these levels, CBP addition resulted in no adverse disturbances to steel and slag chemistry and to the process in general. Results from pilot scale BF tests show that operation was very stable during testing with 150 kg CBPs/tHM but that the burden descent rate and burden gas distribution were disturbed during periods with more CBP burden. The rate of reducing agents was significantly decreased and slag amount was increased when CBPs were charged.

ACKNOWLEDGEMENTS

I would like to thank first and foremost my supervisors, Professor Bo Björkman, Dr. Noureddine Menad and Dr. Caisa Samuelsson, for all their support and supervision during the course of this work.

I would also like to thank my friends and colleagues at the Division of Process Metallurgy. The relaxed and genuine atmosphere there has helped my studies and research tremendously. I would especially like to thank Birgitta Nyberg for her never-tiring help with logistics in laboratory.

My thanks go to all colleagues at member companies involved in MiMeR (Minerals and Metals Recycling Research Center) working group 1 for all their suggestions and support during project work. I am especially grateful to Dr. Lena Sundqvist-Ökvist now at MEFOS, Dr. Fenwei Su and Hans-Olof Lampinen from SSAB and Håkan Johansson from BDX Industrier AB for their integral role in the earlier parts of this work. I am also thankful to LKAB for giving me the opportunity to participate during EBF trials as well as all the assistance I have received from LKAB personnel during the course of my work.

Financial support from MiMeR member companies, VINNOVA (Swedish Agency for Innovation Systems), Stiftelsen för Konung Carl XVI Gustafs 50-årsfond and Luleå University of Technology is also gratefully acknowledged.

Finally, I would like to thank my Swedish in-laws for all their support and especially my wonderful wife Johanna for her show of unequalled patience, understanding and love during the ‘surprisingly’ long wait for the conclusion of this thesis. And of course, to my parents and relatives across the Atlantic who are still contemplating “why Sweden?” but to whom I am deeply indebted for the person I have become.

Ryan Robinson
October 2008, Luleå, Sweden

CONTENTS

1. INTRODUCTION	9
1.1. BACKGROUND.....	9
1.2. COLD BONDED PELLETIZING.....	9
1.2.1. Agglomeration theory	10
1.2.2. Portland cement as binder	10
1.2.3. Raw material benefaction.....	10
1.2.4. Pelletizing	11
1.2.5. Curing	11
1.3. COLD BONDED AGGLOMERATES IN THE BOF.....	11
1.3.1. Effect on BOF process	12
1.4. COLD BONDED AGGLOMERATES IN THE BF.....	12
1.4.1. Effect on BF process	13
1.5. SELF REDUCTION AND BONDING PHASE FORMATION IN CBPs.....	13
1.5.1. Reduction of iron oxide with C _(s)	13
1.5.2. Calcium ferrite formation and stability	14
1.6. AIM AND SCOPE OF THIS WORK	14
1.6.1. Characterization of CBPs	15
1.6.2. Pelletizing tests including cold strength and capacity	15
1.6.3. Large scale tests in the BF and BOF	15
1.6.4. Reactivity of CBP during heat treatment.....	15
1.6.5. Low temperature behavior of the Ca(OH) ₂ -C-Fe ₂ O ₃ system	15
2. EXPERIMENTAL.....	18
2.1. MATERIALS	18
2.1.1. Raw materials for BOF recycling	18
2.1.2. Raw materials for BF recycling	18
2.1.3. Particle size distribution of by-products.....	18
2.1.4. Particle size distribution of chemical reagents	19
2.1.5. Chemical analysis of raw materials.....	20
2.1.6. XRD analysis of raw materials	20
2.2. EXPERIMENTAL DESIGN.....	21
2.2.1. Factorial design for BOF pellet.....	21
2.2.2. Factorial design for BF pellet.....	22
2.3. EXPERIMENTAL PROCEDURE	22
2.3.1. Laboratory pelletizing tests.....	22
2.3.2. TTH tests	22
2.3.3. Thermal analysis	22
2.3.4. Simulated BF tests	23
2.3.5. Isothermal reduction tests	24
2.3.6. Softening and melting tests	24
2.3.7. Chemical analysis	24
2.3.8. Particle sized analysis	25
2.3.9. X-ray diffraction analysis	25
2.3.10. Scanning electron microscope examination	25
2.3.11. Industrial tests in the BOF	25
2.3.12. Pilot scale tests in the experimental BF (EBF).....	25
2.4. KINETIC ANALYSIS.....	26
2.4.1. Friedman and regression analysis	26
2.4.2. Master plot, Z(a), analysis	27
3. RESULTS AND DISCUSSION.....	29

3.1. CBP OPTIMIZATION AND LARGE SCALE TESTING	29
3.1.1. TTH and capacity results.....	29
3.1.2. Thermal analysis results.....	31
3.1.3. Multivariate analysis of pellet blends L1-L11	34
3.1.4. Large scale testing of CBPs.....	38
3.2. SELF-REDUCTION STUDIES.....	44
3.2.1. Reactivity of CBP during heat treatment in inert atmosphere	44
3.2.2. Low temperature self-reduction study of $\text{Ca}(\text{OH})_2\text{-C-Fe}_2\text{O}_3$ system....	48
4. CONCLUSIONS	62
5. FUTURE WORK.....	64
REFERENCES	
PAPERS 1-5	

CHAPTER 1

INTRODUCTION

1.1 BACKGROUND

In the global steel industry, more than 400 kg of solid by-product is generated per ton of steel produced. Most of this by-product (70-80%) is in the form of slag, which after due diligence, is now widely used in the cement industry and for road and civil construction. The remaining solid by-products can be classified as dusts, sludge, and oily/non-oily mill scale.^[1] Traditionally, a large majority of these by-products have been recycled back to the BF through the balling and sintering process. In Sweden, the sintering process has met considerable opposition due to its adverse environmental impacts, specifically dioxin emissions, resulting in the closure of all sinter plants. Barring the sintering process, the fraction of by-products classified as fine particulate, 60% of dusts and sludge, is very difficult to recycle without extensive pre-treatment. These dusts are problematic to recycle not only because of their small particle size but also for their high content of tramp impurities of which the saleable impurities content is not high enough to make further processing economical.^[2] In recent years as costs for dumping solid by-products from the steel industry in landfills have increased due to lack of land availability and increasing environmental restrictions, the recycling of these solid by-products, not only to avoid landfill costs but also to recover valuable metal fractions, has become a near necessity.

In Sweden, the recycling of iron-bearing dust and sludge generated in integrated steel plants can currently be realized by using one or two of four methods that include; cold bonded agglomeration, injection, direct reduction and smelting reduction. Of these, cold bonded agglomeration is considered to be the process best suited for recycling of the fine fraction of steel industry by-product dust and sludge from the comprehensive viewpoint of technical, economic and environmental aspects.^{[3]-[8]}

The method of cold bonded agglomeration is generally achieved by one of two means; briquetting or pelletizing. Cold bonded briquetting is superior to pelletizing when the raw material blend has a broad particle size distribution with significant amounts of both fine and coarse particles. When the raw material blend has a particle size distribution approximately $80\% < 200-250 \mu\text{m}$, cold bonded pelletizing is considered to be the optimal method of agglomeration.^[9] It is this method that is of interest in the current work.

1.2 COLD BONDED PELLETIZING

Cold bonded pelletizing of fine iron ores originated in Sweden, where a patent was applied for by Svensson.^[10] Cold bonded pelletizing has some particular features that differ from the earlier traditional pelletizing techniques used for fine iron ores. These features consist of (i) material blending with binder (cement) at lower temperatures; (ii) balling of fines under normal atmospheric conditions and (iii) pellet self-hardening at room temperature or at $70-100^\circ\text{C}$ with a relative humidity of 70%.

The first cold bonded pelletizing plant, the Grangcold plant, started operation at Grängesberg, Sweden in 1971.^[11] Subsequently, the cold bonded pelletizing method has triggered great interest in the world not only for treatment of iron ores but of other minerals as well. The cold bonded pelletizing related patents and know-how in the industry were developed further in some countries, Japan in

particular.^{[12],[13]} In the 1980's it became evident that cold bonded pelletization was an economically feasible method for agglomerating iron-bearing dust and sludge.

1.2.1 AGGLOMERATION THEORY

Cold strength is one of the most important factors to control when dealing with CBP quality. Theoretical considerations of agglomerate cold strength have focused on the binding mechanisms and cohesive forces involved in the process.^{[8],[14]} The tensile strength of an agglomerate held together by binding mechanisms at the particle contact points can be defined as follows:^[15]

$$P = \varphi \frac{1 - \varepsilon}{\varepsilon} \frac{1}{d} f(\delta) f(d) \quad (1)$$

where P is the tensile strength, d is the particle size, δ is the wetting angle, φ is the fraction of pores filled with water and ε is the porosity, calculated using apparent density, ρ_a , and true density, ρ_t :

$$\varepsilon = (1 - \rho_a / \rho_t) \times 100 \text{ (%)} \quad (2)$$

As seen in Eq. (1), the tensile strength increases with increasing surface tension and decreasing porosity and particle size values. Therefore, the cold strength of a CBP is optimized by selecting a suitable binder featuring high adhesion or binding forces, using a raw material with a small representative particle size and applying suitable curing techniques that produce permanent bonds with high strength.^[16]

1.2.2 PORTLAND CEMENT AS BINDER

Portland cement has long been used as a binder for cold bonded agglomeration of iron-bearing fines. Among the advantages for using Portland cement as a binder are: it is readily available, has comparably low cost, has good cold strength properties and has little or no effect on blast furnace chemistry.^[17] The relative high sulphur content of Portland cement can be a disadvantage for its use in sulphur sensitive metallurgical processes.

Portland cement is comprised of largely tricalcium silicate, $3\text{CaO} \cdot \text{SiO}_2$, and dicalcium silicate, $2\text{CaO} \cdot \text{SiO}_2$, also having minor contents of calcium aluminates, calcium ferrites and other phases. During hydration of Portland cement a $\text{CaO} \cdot \text{SiO}_2 \cdot \text{H}_2\text{O}$ (CSH) gel, consisting of calcium silicate based hydrates of various composition and structure, is formed along with portlandite, $\text{Ca}(\text{OH})_2$. The CSH gel is responsible for bonding discrete particles together in cold bonded agglomerates where the strength of these bonds depend on factors such as particle shape and size and content of binder.^[18]

1.2.3 RAW MATERIAL BENEFICIATION

A variety of techniques have been used to improve the properties of by-products making them more fitted for agglomeration and subsequent recycling in process operations. The goal of pretreating by-products before agglomeration is to reduce oil, water and tramp impurity content and to decrease the chemical variability while increasing the iron content of the by-products. Deoiling is accomplished by either thermal incineration or aqueous/organic washing techniques. Dewatering by standard techniques usually helps to remove a bulk of the oil content as well. Tramp impurities, particularly zinc and lead, can be removed by utilizing techniques such as hydrometallurgical leaching, size classification with the help of a hydrocyclone, flotation, sulfation roasting and other methods. But the previously mentioned methods have not found as wide an acceptance as the high temperature ($>1000^\circ\text{C}$) reduction techniques used for removal of tramp impurities from iron-bearing fines. The

chemistry of BF flue dust can vary considerably, but by using flotation techniques the dust can be concentrated into iron-rich and carbon-rich fractions thereby reducing variability.^[19] Optimal grinding of by-products in order to obtain a continuous particle size distribution satisfying the conditions of a “Fuller Curve” will help to homogenize the by-product blend as well.^[20]

1.2.4 PELLETIZING

Before pelletizing, the raw material (by-product blend) should be mixed with the preferred amount of cement, based on strength requirements, in order to further homogenize the raw material and ensure a maximum number of bond points.^[21] The raw material is then blended with an optimal amount of water to produce viscous homogenous slurry. This slurry is then fed to a standard disk or drum pelletizer and left to rotate under predetermined time and pelletizing parameters. After pelletizing, the green pellets are screened for optimal size and the undersize pellet fraction is returned to the pelletizer.^{[9],[12],[21],[22]}

1.2.5 CURING

Curing of green pellets is inherently dependent on the type of binder used. For example, strength development in calcium silicate based binders relies on hydration to form the CSH gel whilst a molasses based binder relies on the removal of moisture for strengthening.^[23] When using a calcium silicate based binder such as cement the strength development occurs quickly in the beginning and then tapers off slowly until the final strength is reached. For this reason, the curing process is divided into two steps, primary and secondary curing. Primary curing requires 1 to 3 days depending on the strength requirements and the curing conditions (normal atmospheric conditions or elevated temperature and relative humidity). Secondary curing requires a longer period of time under ambient conditions, limited only by the duration required to meet target strength values.^{[9]-[12],[21],[24]}

1.3 COLD BONDED AGGLOMERATES IN THE BOF

Preferably, by-product recycling is normally carried out in the ironmaking process stage to avoid unnecessary impurity flows into the steelmaking processes. In cases where by-product agglomerates contain critical levels of elements that are detrimental to the BF process due to accumulation/recirculation problems, i.e. zinc and alkali, or sub-par strength characteristics, i.e. high carbon content, these materials can be successfully recycled to the BOF process because it is not sensitive to the effects incurred by high vapor pressure elements and low agglomerate strength. Cold bonded by-product agglomerates can be used in several ways in the BOF. The most common uses are as a scrap substitute, a primary coolant and a dynamic coolant. If used as a scrap substitute (i.e. with scrap charge before hot metal addition in the BOF), the agglomerates will replace a portion of the scrap with regards to iron units; therefore it is imperative that they have relatively high iron content. Agglomerates are typically charged to the BOF by two different means, in the scrap box or through a material bin along with flux.^[25] A pair of studies has been conducted to see how effective the iron units from charged agglomerates report to the steel. During tests at plants using between 8,000 and 20,000 kg of agglomerates per heat, a recovery of greater than 90% of iron units to the molten steel has been observed when the agglomerates are used as scrap substitute.^[26] When charged at the beginning of the blowing period, cold bonded agglomerates containing blast furnace flue dust resulted in a recovery of 75% of iron units to molten steel.^[30]

When used as a primary coolant, by-product agglomerates will require an increase in the level of hot metal charge in order to thermally balance the agglomerate addition because of the increased cooling capacity incurred by their use. Cold bonded by-product agglomerates have a cooling capacity calculated between 2.1 and 2.6 times that of iron scrap depending on the chemical composition of agglomerates.^[17]

Dynamic coolants are used to change endpoint temperature and carbon content of steel during the final minutes of the blowing period. Here, the cooling effect of by-product agglomerates is not as effective as when used as primary coolants due to deficiency of carbon in the system to reduce iron oxides late in the blow.^[25]

1.3.1 EFFECTS ON BOF PROCESS

There are process parameters that can be greatly affected by the use of by-product oxide agglomerates in the BOF. These parameters include chemical composition of molten steel and slag, molten yield, endpoint performance and dust generation. During full-scale tests with agglomerate additions up to 10,000 kg/heat, both the molten yield and the iron content of slag show negligible changes when compared to heats without agglomerate addition.^[17] A main factor affecting molten yield is slopping. Slopping is influenced by many factors, which include lance height, oxygen flow rate, hot metal silicon content, additive moisture content and the foam ability of the slag.^{[12],[28]} It is reported that when agglomerates are charged as scrap substitute, slopping is increased with increasing silicon content of the hot metal. Likewise, some research states that slopping will increase with increasing FeO content in the slag before ignition (when the lance is lowered and decarburization accelerates).^[29] The endpoint performance, especially sulphur and phosphorous levels, is negligibly affected by agglomerate addition as well.^[27]

As mentioned earlier, addition of iron oxide bearing agglomerates require excess hot metal and if this is not possible due to vessel constraints then additional energy must be added in some other form to achieve the desired tap temperature. Supplemental energy can be incorporated into the by-product agglomerates as carbon or silicon addition. The effects of adding 20% coke breeze to a by-product agglomerate charge was studied and results indicate that roughly 85% of the carbon was utilized in reduction (assuming a CO/CO₂ ratio of 9:1).^[26] Further benefits of charging agglomerates with high carbon content to the BOF is the ensuing decrease in oxygen content in the metal bath alleviating both refractory lining damage and consumption of aluminium at the stirring station.^[30] On the other hand, iron oxide bearing agglomerates without carbon addition can be used as dynamic coolants in place of iron ore to help control hot metal temperature and/or as a partial scrap substitute to reduce cost.

Dust formation in the BOF can be explained collectively by four mechanisms: ejection of metal, ejection of slag, escape of charged material, and vaporization. The escape of charged material during blowing includes the use of cold bonded agglomerate charge. Inevitably, some part of all charged material will end up in the process dust but the extent of dust generation can be damped with the use of optimal material handling and charging techniques. As an example, most of the material charged to the BOF is sieved to avoid the entraining of small particles in the gas evolved during blowing.^[31]

1.4 COLD BONDED AGGLOMERATES IN THE BF

By-products deemed suitable for the BF process have been recycled via the sinter plant for decades. As environmental regulation and other factors have led to the closure of some sinter plants, the agglomeration and eventual recycling of these by-products in the BF has become a standard practice at a number of plants worldwide.^{[32]-[35]}

The BF process has a low tolerance for certain compounds; therefore, these compounds must be controlled to maintain acceptable levels for smooth BF operation. Zinc and lead containing materials should be avoided as charge to the BF due to their detrimental effect on furnace refractory lining, tuyere performance and their significance in skull formation. The alkali content of charge to the BF should also be controlled to avoid excessive alkali loading leading to accretion formation. Sulphur and

phosphorus contents in materials charged to the BF should be monitored as well to maintain acceptable limits in hot metal quality.^{[19],[36]}

Conditions in the BF process put more constraints on the binder system, used in agglomerate charge, than in the BOF. Charged agglomerates are required to maintain structural integrity from the top of the BF shaft into the cohesive zone. Premature breakdown or significant swelling of agglomerates could have detrimental affects to conditions in the BF.^[25] Testing at various plants has shown that when charged at levels up to 5% of the iron-bearing burden, by-product agglomerates have little or no detrimental effect on BF operation and actually decrease the rate of reducing agents required in the furnace when carbon is incorporated in the agglomerates.^{[32],[35],[37]}

1.4.2 EFFECT ON BF PROCESS

Accounts reported from those facilities having experience with by-product agglomerate charge as burden, have one major observation in common; increasing the cold bonded agglomerate charge above 5% of the iron-bearing burden will give increased furnace instability and eventual furnace failure. Effects on the BF stability include; erratic burden descent, furnace temperature profile changes, increased pressure drop and increased slag yield.^{[13],[32],[33]}

An upper limit for by-product agglomerate charge rate lies between 10 and 15% due to the observed drastic increase of burden hanging and slipping in the BF at these rates. Increased degradation of agglomerates in the furnace is the probable cause for irregular burden movement.^{[32],[35],[37]}

Due to water content, cold bonded agglomerates can retard temperature increase in the BF upper shaft. The gas temperature tends to fall due to heat requirements of water vaporization and the low temperature zone, 500-700°C, has a tendency to elongate. A result of decreased temperature is a delay in reduction of iron oxides but measures can be taken to avoid this, such as increasing the rate of reducing agents and controlling the burden distribution in the furnace.^{[13],[33]}

The pressure drop has been observed to increase with increasing cold bonded agglomerate addition to the BF. The cause of this can most likely be attributed to a reduction in bed permeability due to an increased fines generation from degradation of agglomerates. At higher rates of cold bonded agglomerate addition an increase in BF flue dust is observed as well.^{[32],[38]} In order to compensate for high temperature degradation, cement content in cold bonded agglomerates can be increased to give almost linear improvements in compression strength.^[9] One downfall of cold bonded agglomerate charge may be that cement binder and the high content of oxides in agglomerated materials will cause an increase in slag yield leading to additional energy requirements.^[38]

1.5 SELF REDUCTION AND BONDING PHASE FORMATION IN CBPs

1.5.1 REDUCTION OF IRON OXIDE WITH C_(s)

A good understanding of the self-reduction characteristics in agglomerates of iron oxide containing solid carbon is essential for the further development of cold bonded agglomerates containing by-products for use as recycle in the steelmaking industry. The literature contains a vast body of work related to the reduction behavior of composites containing various assemblages of iron oxide and carbon. Two comprehensive reviews on the reduction of iron oxide by carbon have been compiled by Szekely et al.^[39] and Prakash^[40]. A common conclusion among the majority of studies is that the rate of reduction of iron oxide by solid carbon is controlled by the gasification of carbon. Mantovani and Takano among others^{[41][42]} have reported that the reduction of self-reducing pellets containing a mixture of EAF dust and coal can be described by the following reactions: (1) direct reduction (solid/solid) between iron oxides and carbon; and (2) gas/solid reactions. As the speed of solid/solid

reaction is much slower than the gas/solid reaction, the global process occurs via gaseous intermediates such as $\text{CO}_{(\text{g})}$, $\text{CO}_{2(\text{g})}$, $\text{H}_{2(\text{g})}$ and $\text{H}_2\text{O}_{(\text{g})}$. Likewise, Kashiwaya et al.^[43] showed that the basic reaction mechanism of a composite pellet containing hematite and graphite starts at ~923 K as a reaction caused by the direct contact between iron oxide and carbon and then, after subsequent separation of the iron oxide/carbon interface, the reaction continues as a coupling phenomenon between reduction and carbon gasification.

Reduction can start at even lower temperatures in the event of gas generation inside the solid due to decomposition and/or volatilization. Mookherjee et al^[44] observed that the volatile matter in non-coking coal contributed to the reduction of iron ore at temperatures over 773 K. Furthermore, Lu et al.^{[45][46]} showed that volatile matter in coal contributed to the reduction of iron oxide and was effectively consumed in the process and direct contact of iron ore fines and coal fines increased the reduction rate in the *prereduction* stage before smelting reduction in a multi-stage reactor.

Various studies have been found in the literature concerning gasification of carbonaceous material in the presence of different metal-based sorbents/catalysts, mostly at elevated pressure ~20 MPa.^{[47][49]} Results from Sato et al.^[50] have shown that water contained in $\text{Ca}(\text{OH})_2$ molecules is sufficient to produce $\text{H}_{2(\text{g})}$ from reaction with carbon content in samples of a vacuum residue of Arabian light crude oil at temperatures above 600°C and pressures 4-5 MPa.

1.5.2 CALCIUM FERRITE FORMATION AND STABILITY

Concerning calcium ferrite (CF) or silico-ferrites of calcium and aluminium (SFCA) formation, the common view is that they typically form from hematite because iron in the ferrites is ferric. CF formation starts at ~750°C in pure air.^[51] Yang and Matthews^[52] found that calcium ferrites can form from magnetite at low oxygen partial pressures. In this case, the mechanism for calcium ferrite formation is likely to be that magnetite is oxidised to a meta-stable hematite, which quickly reacts with calcium oxide to form calcium ferrites. Orewczyk and Jasienska^[53] have found that calcium ferrites come from the reaction of magnetite and calcium oxide in an argon atmosphere at CaO levels above 3 wt%. However, calcium ferrite formation in this system can not develop well in the presence of silica.

CF phases are commonly referred to as the matrix or bonding phase in fluxed sinter or fluxed iron ore pellets.^[51] The morphology of calcium ferrite formation depends mainly on the temperature of reaction where four different types of ferrite can be observed depending on temperature and gas composition; fine acicular, long acicular, columnar, and dendritic. Acicular morphology is common in materials with intermediate and higher basicities heated at low temperatures. According to Pimenta and Seshadri,^[54] disintegration of the matrix phase in sinter is connected to the reduction of hematite content in ferrites to magnetite. Although, additions of Al_2O_3 have shown to increase the thermal stability of matrix ferrite phases to higher temperatures.

1.6 AIM AND SCOPE OF THIS WORK

A sizeable amount of work has been completed towards the study of cold bonded agglomerates as possible revert in metallurgical processes. The work reported in literature covers a broad base of subjects ranging from; the strength of agglomerates at room temperature, their high temperature strength, reaction thermodynamics and kinetics during heating as well as the performance of cold bonded agglomerates as charge in iron and steelmaking processes. While there have been earlier studies of the strength and high temperature behavior of self-reducing metallurgical by-product agglomerates,^[24] work is lacking on the cause-effect relationships for concurrent optimization of the room temperature strength and the self-reduction properties of cold bonded agglomerates based on varying by-product compositions. Furthermore, a better understanding of the low temperature

bonded pellets (CBPs). Specifically, the purpose is to identify the factors that most influence the concurrent optimization of room temperature strength and low temperature reduction through gaseous intermediates. Generally, the aim of this thesis is to study the feasibility for effective recycling of CBPs in the integrated iron and steelmaking process. Figure 1 shows a general layout of the thesis topics.

1.6.1 CHARACTERIZATION OF CBPs (Papers 1, 2, & 3)

A material characterization was performed on a preliminary laboratory pellet blend including particle size distribution of pellet ingredients, chemical analysis, x-ray diffraction and scanning electron microscopy. Some supplementary characterization was conducted on two pellet types used in pilot and full-scale tests.

1.6.2 PELLETIZING TESTS INCLUDING COLD STRENGTH AND CAPACITY (Paper 1)

Both laboratory and pilot scale pelletizing tests were conducted to find an optimal pellet blend for recycling to the BOF. Lab scale tests were conducted according to a 2-level, 3-factor experimental design of which the aim was to find the optimal blend of 3 factors (BOF fine sludge, BF flue dust and oily mill scale sludge) between 2 levels (high and low) with BOF coarse sludge as filler and Portland cement as binder. The test evaluation criteria applied on product pellets were the tumbler handling strength (TTH) of CBPs, the abrasion handling strength (ATH), and the production capacity of pellets within the size fraction 9-12.5 mm. The strength of CBPs is the main quality index controlled in the iron and steel-making processes. The method of TTH/ATH determination is an international standard in metallurgical production and production capacity is a standard quality criteria used at SSAB Luleå, Sweden.

1.6.3 LARGE-SCALE TESTS IN THE BF AND BOF (Papers 1 & 2)

In order to study the effect of CBP recycling in iron and steel production, large-scale tests have been conducted. A test campaign with CBP feed has been completed in an experimental BF in order to investigate the limits for CBP use in the BF process. Furthermore, full-scale industrial tests have been completed with CBP addition to the BOF; primarily to determine suitable by-product mixes for recycle in the BOF process and, to a lesser extent, trigger new thinking concerning the specifications for use, or non-use, of certain materials as charge during BOF steelmaking.

1.6.4 REACTIVITY OF CBP DURING HEAT TREATMENT (Paper 3)

Dynamic solid-state high temperature tests of different pellet blends have been carried out to study possible reactions and mechanisms occurring upon heating. A furnace equipped for simultaneous thermo-gravimetric, differential thermal and quadropole mass spectrometric analysis was used to heat pellet samples to temperatures between 20 and 1200°C in inert atmosphere. The heat-treated samples were investigated using x-ray diffraction and scanning electron microscopic analysis.

1.6.5 LOW TEMPERATURE BEHAVIOR OF THE $\text{Ca}(\text{OH})_2\text{-C-Fe}_2\text{O}_3$ SYSTEM (Papers 4 & 5)

Dynamic solid-state low temperature tests of different compositions of reagent grade $\text{Ca}(\text{OH})_2$, C, and Fe_2O_3 have been carried out to study in more detail the reaction mechanisms and kinetics of self-reduction. A furnace equipped for simultaneous thermo-gravimetric, differential thermal and quadropole mass spectrometric analysis was used to heat pellet samples to temperatures between 20 and 800°C in inert atmosphere. The heat-treated samples were investigated using x-ray diffraction and scanning electron microscopic analysis. Furthermore, TG results from experiments run at different

heating rates between 2 and 32°C/min have been analyzed using a kinetic evaluation software package to study the reaction mechanisms occurring during the dehydration of Ca(OH)₂ in the presence of solid carbon and Fe₂O₃, in order to clarify their role as eventual precursors to high temperature reduction and strength characteristics in feedstock agglomerates of iron and steelmaking by-products.

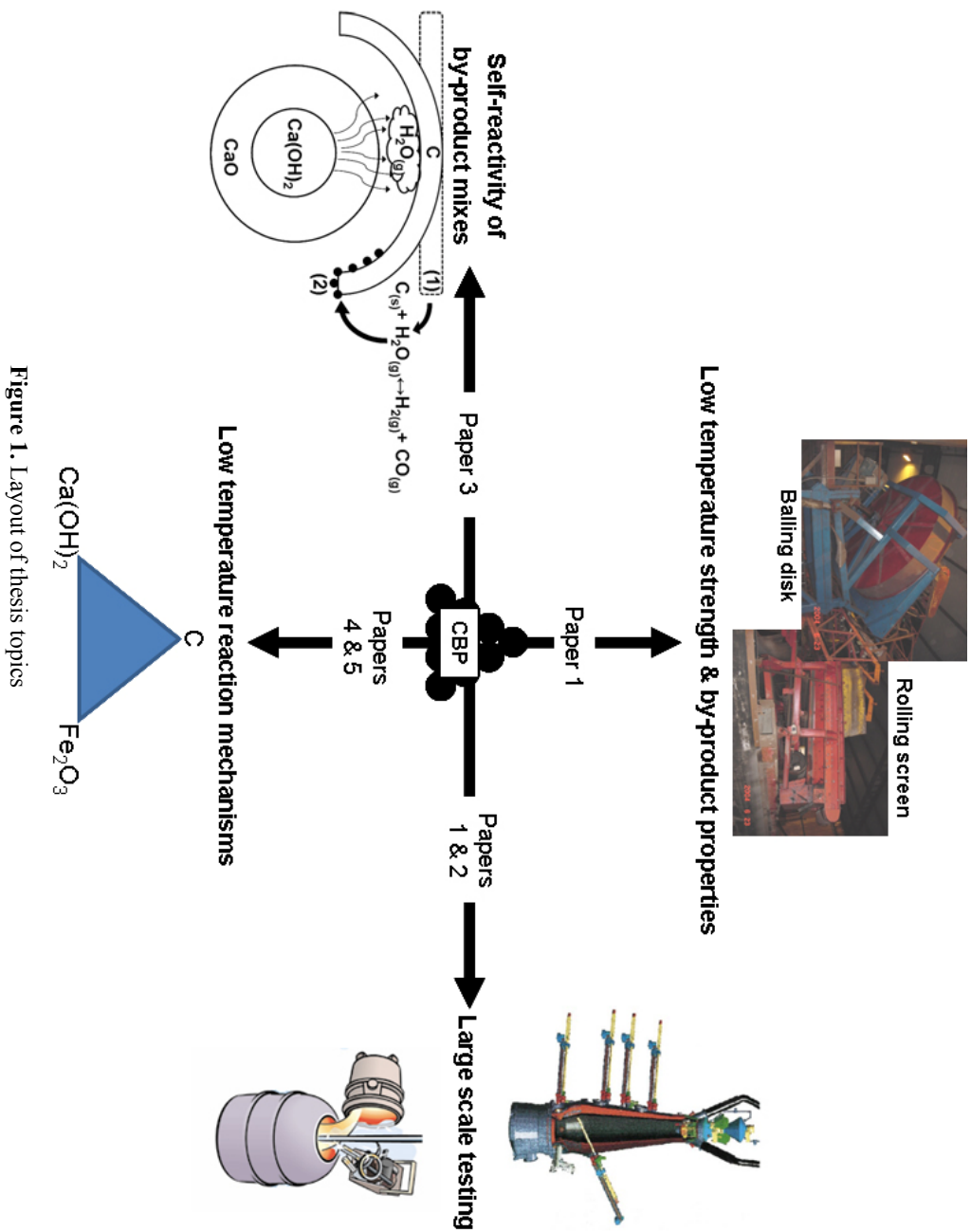


Figure 1. Layout of thesis topics

CHAPTER 2

EXPERIMENTAL

2.1 MATERIALS

2.1.1 RAW MATERIALS FOR BOF RECYCLING

The raw materials investigated in this thesis that are considered for BOF recycling are process by-products from iron and steelmaking. Samples of BOF fine and coarse sludge, BF flue dust and oily mill scale sludge were received from SSAB Luleå. LuleFrakt AB supplied Portland cement, used as binder in pelletizing. All metallurgical by-products were received in large drums and were therefore sub-sampled, using a rotating splitter, into samples of approximately 2 kg to maintain homogeneous integrity of the initial samples. The 2 kg samples were later used in laboratory cold bonded pelletizing experiments, excluding those samples which were sub-sampled into smaller samples for particle size, chemical and phase analysis.

2.1.2 RAW MATERIALS FOR BF RECYCLING

Prefabricated CBPs having a composition similar to that of cold bonded briquettes currently recycled in the BF at SSAB Luleå were also investigated. This pellet blend contains BOF fine and coarse sludge, BF flue dust, steelworks environment filter dust and cold bonded briquette fines. Contents of scrap fines, present in briquettes, were excluded from the pellet blend due to particle size specifications. A 5 kg sample of prefabricated pellets was received from SSAB Luleå for phase and thermal analysis.

2.1.3 PARTICLE SIZE DISTRIBUTION OF BY-PRODUCTS

As seen in Figure 2, the results of particle size measurements show that the raw materials have a broad range of particle size distributions. The raw materials are coarser with ascending order as follows: Cement < BF flue dust < filter dust* < BOF fine sludge < BOF coarse sludge < briquette fines* < oily mill scale sludge. However, particle size distribution results can be confusing when considering materials for agglomeration purposes. In order to optimize agglomeration properties, the goal is not only to attain a high packing density of particles but also to maintain an open inner structure for better gas transfer within the agglomerate.

As introduced by Forsmo et.al, the PaRMAC method for classifying particle size fractions can give more insightful information.^[61] Empirically chosen size fractions, “sand”<”stone”<”block”, can be considered as the building units in an optimal agglomerate. The “sand” particles fill the holes between the “stone” particles, which form the basic framework in the agglomerate, and the “block” particles are included to initiate balling during pellet production. This method, when used on the by-product raw materials given in Figure 2, show that; BOF fine sludge has the largest “sand” fraction (1-10 µm) at 5.15 wt.%, BF flue dust has the largest “stone” fraction (10-40 µm) at 12.57 wt.% and oily mill

* Not shown in Figure 2, briquette fines $d_{80} = 360 \mu\text{m}$, filter dust $d_{80} = 60 \mu\text{m}$

scale sludge has the largest “block” fraction (40-425 μm) at 81.66 wt.%. By designating the particle size distributions into ternary particle fractions, one can avoid oversimplifying the effect of particle size on agglomerate quality when using only a single descriptive particle size value such as d or d_{50} .

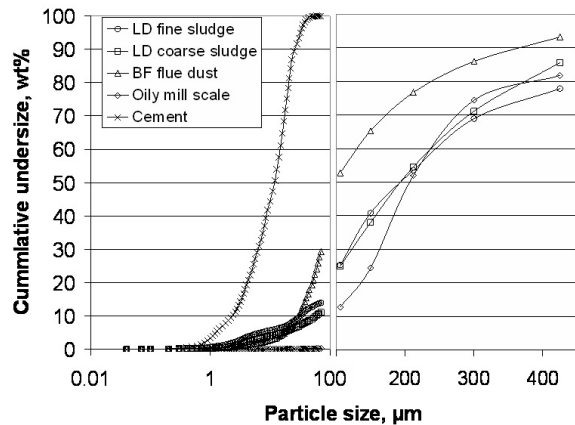


Figure 2. Particle size distribution of by-products

2.1.4 PARTICLE SIZE DISTRIBUTION OF CHEMICAL REAGENTS

Figure 3 shows the particle size distribution of the reagents used in low temperature self-reduction studies. Two different reagent hematite powders have been used; first a reagent hematite shown in Figure 3 which has been designated as “micro-sized” and a second designated as “nano-sized” hematite. The nano-sized reagent has an average particle diameter of 30 nm which was verified with microscopic observation.

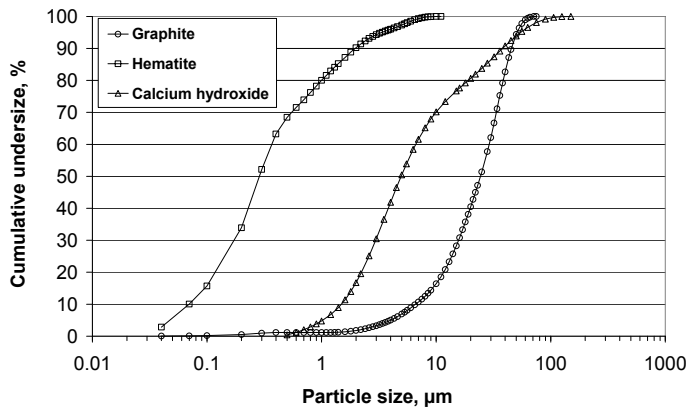


Figure 3. Particle size distribution of reagents

2.1.5 CHEMICAL ANALYSIS OF RAW PELLET MATERIALS

The chemical analysis for raw materials considered for BOF recycling is given in Table 1. These analyses differ for certain raw materials, specifically BF flue dust and BOF coarse sludge compositions, to those considered for BF recycling given in Table 2. The reason for this is that the CBPs produced for testing in the BF process were produced before BF #1 and #2 were decommissioned and replaced by BF #3 in the summer of 2000. With the new BF, hot metal production increased and an improved gas cleaning system increased dry dust recovery thereby changing the composition of BF flue dust. The composition of the coarse fraction of BOF sludge normally varies substantially over time due to changes in BOF operation.

The large difference in BOF coarse compositions given in Tables 2 and 3 do occur but the assay in Table 1 reflects the composition that is more common. As shown in Table 1 and Table 2, the sludge and dusts are primarily composed of iron oxide (20-75 wt%) with smaller fractions of major components CaO, MgO, SiO₂, Al₂O₃ and C. The chemical compositions of the by-products do not vary substantially between sampling periods, except for BF dust and LD coarse sludge.

Table 1. Chemical compositions of raw materials for recycle in BOF in wt%

	BOF fine	BOF coarse	BF-3 flue	Oily mill	Cement
Fe _{tot}	57.44	46.74	20.55	58.19	2.4
CaO	13.37	17.41	5.16	4.67	62
SiO ₂	0.91	1.38	4.98	6.47	20
MnO	0.93	0.67	0.62	0.84	-
P ₂ O ₅	0.13	0.14	0.07	0.13	-
Al ₂ O ₃	0.1	0.2	1.93	1.15	4.4
MgO	3.1	3.71	1.06	0.21	3.5
Na ₂ O	0.03	-	0.05	0.81	-
K ₂ O	0.04	0.04	0.06	0.18	1.4
V ₂ O ₅	0.31	0.62	0.17	0.07	-
TiO ₂	0.07	0.22	0.21	0.06	-
Cr ₂ O ₃	0.07	0.06	0.03	-	-
C	1.47	1.33	54.3	4.59	-
S	0.07	0.07	0.38	0.11	1
Zn	0.11	0.05	0.23	0.03	-

Table 2. Chemical compositions of raw materials for recycle in BF in wt%

	BOF fine	BOF coarse	Filter dust	BF-1 flue	BF-2 flue	Briq. fines
Fe _{tot}	53.7	74.4	65.8	30.8	35.6	39.3
CaO	13.9	9.62	0.56	6.54	6.52	16.6
SiO ₂	1.04	1.97	1.65	4.12	4.39	6.44
MnO	0.97	0.94	0.26	0.74	0.59	0.97
P ₂ O ₅	0.07	0.14	0.05	0.04	0.05	0.11
Al ₂ O ₃	0.10	0.15	0.39	1.54	1.55	1.96
MgO	3.35	3.19	1.16	1.34	1.72	3.27
K ₂ O	0.05	0.04	0.31	0.03	0.04	0.10
TiO ₂	0.09	0.31	0.23	0.20	0.29	0.49
Cr ₂ O ₃	0.06	0.08	0.19	0.03	0.05	0.11
C	1.64	1.01	0.55	35.3	30.6	11.7

2.1.6 XRD ANALYSIS OF RAW PELLET MATERIALS

XRD analysis was performed on the by-product raw materials used in the BOF cold bonded pellet blend. The major and minor phases present in the different by-products are listed in Table 3. The mineralogy between the different by-products varies mainly in the contents of metallic iron, iron oxide, carbonates and hydrates.

Table 3. XRD results for raw material by-products

By-products	Major phases	Minor phases
BOF fine sludge	Fe _{met} > FeO > CaCO ₃	Fe ₃ O ₄ > Ca(OH) ₂
BOF coarse sludge	Ca(OH) ₂ > CaCO ₃ > Fe _{met}	Fe ₃ O ₄ > FeO > Mg(OH) ₂
BF flue dust	Fe ₂ O ₃ > Fe ₃ O ₄ > CaCO ₃	C > SiO ₂
Oily millscale sludge	Fe ₃ O ₄ > FeO > Fe ₂ O ₃	Ca(OH) ₂ > CaSiO ₃

2.2 EXPERIMENTAL DESIGN

2.2.1 FACTORIAL DESIGN FOR BOF PELLET

A statistical design was used for BOF cold bonded pelletizing experiments. Figure 4 shows the design region for an experiment aimed at studying the effect of pellet blend on TTH and capacity responses. A full factorial design with two levels was used consisting of tests, L1 to L11. The three factors used in the design are: **A**) BOF fine sludge with levels, high (40 wt%) and low (20 wt%); **B**) BF flue dust with levels, high (30 wt%) and low (20 wt%); and **C**) oily mill scale sludge with levels, high (20 wt%) and low (10 wt%). These factors as well as a filler material (BOF coarse sludge) and a constant binder additive (10 wt% cement) comprise the 20 kg batches for each test. One central point test with two replicates is also included.

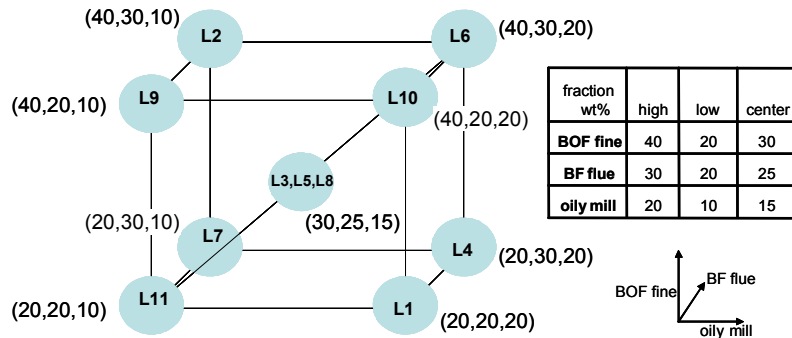


Figure 4. Design region BOF pellet

2.2.2 FACTORIAL DESIGN FOR BF PELLET

Design planning for BF cold bonded pelletizing experiments was conducted at SSAB Luleå. Figure 5 shows the design region for an experiment aimed at studying the effect of pellet blend on TTH and capacity responses. A full factorial design with two levels was used consisting of tests, B1 to B9. The three factors used in the design are: **A**) BOF fine sludge with levels, high (20 wt%) and low (0 wt%); **B**) BF flue dust with levels, high (30 wt%) and low (20 wt%); and **C**) Briquette fines with levels, high (10 wt%) and low (0 wt%). These factors as well as a filler material (BOF coarse sludge and steelworks environment filter dust) and a constant binder addition (10 wt% cement) comprise the 20 kg batches for each test. One central point test is also included.

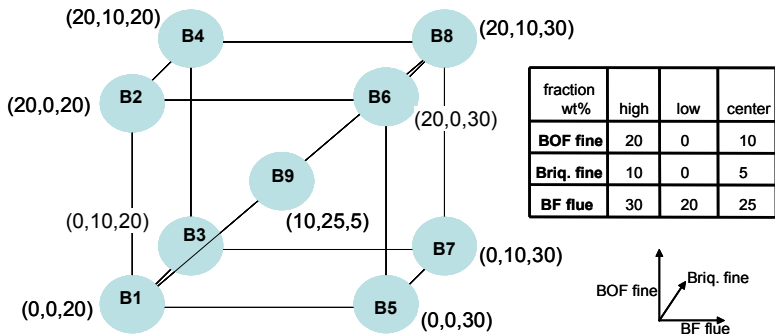


Figure 5. Design region BF pellet

2.3 EXPERIMENTAL PROCEDURE

2.3.1 LABORATORY PELLETIZING TESTS

A 20-kg sample that consisted of the by-products of interest and cement binder was mixed in a drum mixer for 4 minutes and then the blend was emptied into a container and was mixed further with 12.5-13.5% water for another 2 minutes. Next, the sample was left to hydrate for 20 minutes. After hydrating, the sample was fed into a disc pelletizer run with a rotating speed of 18 rpm at an angle of 45°. The sample was left to rotate in the pelletizer for 20 minutes, initially spraying small amounts of water on to the sample to stimulate ball formation. Different pelletizing time intervals and other pelletizing parameters were optimized and the results are reported in Paper 1. The newly balled pellets were spread out onto the floor and left to attain green strength for 1 hour and then were loaded into bins and cured for an additional 24 hours before sieving. The weight percent of total pellets mass within the size fraction of 9-12.5 mm was recorded as the capacity of the batch and that size fraction was subsequently used in the TTH test evaluation.

2.3.2 TTH TESTS

The test evaluation criteria, for cold strength, applied to the different pellet batches were the tumbler handling strength of CBPs (TTH) and the abrasion handling strength (ATH). The TTH determination is an international standard method in metallurgical production, ISO 3271, and these tests were carried out at LKAB. The TTH apparatus is a 100 cm wide cylindrical drum that, loaded with 3 kg of pellets sample, is rotated at a standardized speed and time. The pellets and fines are captured after tumbling and then sieved to fractions of +6 mm and -0.5 mm. The wt% of the +6 mm fraction is recorded as the TTH value and the -0.5 mm fraction as the ATH value. TTH tests conducted on pellet samples L1-L11 had a precision (defined as 2σ) of ± 3.2 wt%.

2.3.3 THERMAL ANALYSIS

A Netzsch STA 409 instrument equipped with simultaneous thermo-gravimetric (TG), differential thermal analysis (DTA) and a supplemental quadropole mass spectrometer (QMS) was used to study the high temperature properties of lab pellets; L1-L11, made for use in the BOF, and B4, made for use in the BF. The test conditions used in all tests were identical. Between 80-100 mg of sample were placed into an alumina crucible and heated from 20°C to 1200°C at a temperature rate of 10°C/min in Ar_(g) with a constant flow rate of 200 ml/min. Additional independent TG tests were conducted on samples of lab pellet B4 using between 2 and 2.5 g for each test heated to different temperatures and then held isothermally for 1 hour. The precision of TG data for tests L1-L11 was ± 2.03 wt% and for test B4 was ± 1.95 wt%. A schematic diagram of the thermal analysis instrument is given in Figure 6.

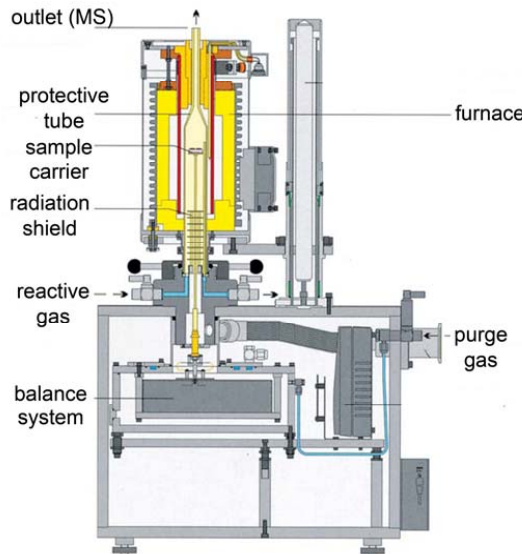


Figure 6. Schematic of the Netzsch STA 409 instrument used in experiments

A Setaram Setsys Evolution instrument equipped with simultaneous TG/DTA/QMS analysis was used in thermal analysis studies of reagent materials. The sensitivity of the TG balance is $\pm 0.3 \mu\text{g}$. Two types of tests were performed on the samples. First, in order to find an optimal composition, dynamic TG/DTA/QMS tests were conducted on samples heated from 20°C to 800°C at 10°C/min in helium with a constant flow rate of 60 ml/min. Second, in order to investigate the kinetic effect of heating rate, three different heating rates have been used; 2, 10, and 32°C/min. Cylindrical α -Al₂O₃ crucibles with a diameter of 4 mm and a capacity of 100 μl were used in these tests.

2.3.4 SIMULATED BF TESTS

Lab scale BF simulation tests were conducted on the CBP blend B4 at LKAB. A BF simulation experiment called TRTMAS that LKAB normally uses on its olivine pellets was used to test a sample of CBPs.

The test is divided into three temperature zones where the gas composition, a mixture of CO, CO₂, H₂, and N₂, and applied force to the sample are varied from zone to zone in an effort to simulate BF conditions. Figure 7 shows an example of the test conditions and Figure 8 shows a schematic of the BF simulation furnace.

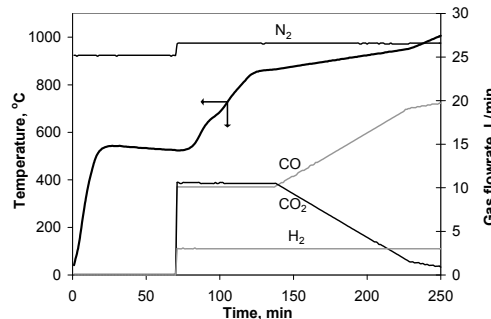


Figure 7. Temperature and gas profile for TRTMAS experiments

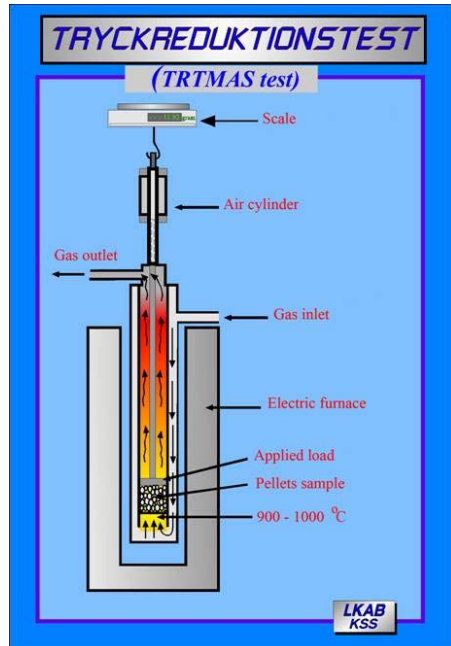


Figure 8. Schematic of the TRTMAS instrument at LKAB

2.3.5 ISOTHERMAL REDUCTION TESTS

Three different isothermal reduction lab scale tests were conducted on the cold bonded pellet blend B4 at LKAB. A low temperature isothermal reduction test, LTB test ISO 13930, was run at 500°C for 60 minutes with a gas flow of 20 NL/min (20% CO, 20% CO₂, 2% H₂, 58% N₂). Two high temperature isothermal reduction tests were also conducted on the pellets: ISO 4695 was run at 950°C for 109 minutes with a gas flow of 50 NL/min (40% CO, 60% N₂) and ISO 7992 was run at 1050°C for 65 minutes with a gas flow of 83 NL/min (40% CO, 2% H₂, 58% N₂).

2.3.6 SOFTENING AND MELTING TESTS

Experiments for evaluating softening and melting properties were conducted on mixed samples of LKAB's olivine iron ore pellets, MPBO, and CBPs, blend B4, using another BF simulation type test developed at MEFOS.^[62] The pellets samples, pre-reduced to 30% reduction degree, were placed between coke layers inside a graphite crucible with applied load and heated in a reducing environment until the height of the sample had stopped decreasing. During the test several types of data were logged including; temperature, shrinkage of the sample bed and the pressure drop over the sample bed.

2.3.7 CHEMICAL ANALYSIS

SSAB Luleå provided the chemical analysis of all the by-product sample materials. The techniques that were used are X-ray fluorescence and LECO combustion analysis. The raw materials used in the low temperature self-reduction study are all laboratory grade reagents. Calcium hydroxide, 99.8% pure powder, was supplied from Riedel-deHaen; Graphite, 99% pure and -300 mesh, was supplied from Alfa Aesar; micro-sized Hematite, 99.8% (metals basis) pure and -325 mesh powder, was supplied from Alfa Aesar and a nano-sized Hematite, 99.999% pure powder, was supplied from Aldrich.

2.3.8 PARTICLE SIZE ANALYSIS

Samples of roughly 100 mg each of the raw materials used in the production of CBPs batches L1-L11 were dry-sieved to various size fractions using a set of U.S. Standard Sieves conforming to ASTM standards with a precision of ± 2.61 wt%. The $-75\text{ }\mu\text{m}$ size fractions remaining after dry sieving were further analyzed using a CILAS particle size analyzer with a precision of ± 0.21 vol%. The values d' ($d_{63.2\%}$) and d_{50} have been used as quantitative measures of particle size distribution in multivariate analysis of results. The particle size of reagent grade samples of graphite, hematite, and calcium hydroxide (in alcohol) were analyzed using CILAS as well. Micro briquettes were prepared from the reagent powder mixtures in a hand press, 1.5N/mm^2 , resulting in cylinders having average dimensions of $3\text{mm } \phi \times 3\text{mm H}$ and sample weights of 15.7 ± 2.3 mg (micro-sized hematite) and 18 ± 1 mg (nano-sized hematite).

2.3.9 X-RAY DIFFRACTION ANALYSIS

Samples have been analyzed using a Siemens D5000 X-ray powder diffractometer using Ni filtered $\text{Cu K}\alpha$ radiation at 40 kV and 50 mA.

2.3.10 SCANNING ELECTRON MICROSCOPIC (SEM) EXAMINATION

Unpolished and polished samples were fixed on aluminium mounts and coated with a thin layer of gold-palladium alloy using a Bal-tec MCS 010 sputter coater. The coated specimens were then examined with a Philips XL 30 scanning electron microscope equipped with energy dispersive spectra (EDS) analysis.

2.3.11 INDUSTRIAL TESTS IN THE BOF

Industrial tests on charging CBPs in the BOF were carried out at the No. 2 BOF (114 tons) at SSAB Luleå, November 2001. Two reference tests, without CBPs, and eight sample tests, with CBPs, were conducted. The charging weight of CBPs varied from 0.5 to 2.5 tons. Scrap, desulphurized hot metal and CBPs were added to the BOF respectively. During blowing, slurry samples of generated dust were taken from a rake classifier with a sampling time of roughly 15 minutes. Steel product and slag samples were taken during each tapping.

2.3.12 PILOT SCALE TEST IN THE EXPERIMENTAL BLAST FURNACE (EBF)

Pilot scale tests with CBPs as part of the burden material in the BF process were carried out at the EBF owned by LKAB and located at MEFOS in Luleå. The test campaign included 2 reference periods, without CBPs, and 3 testing periods, with increasing CBP burden content: test period 1 (150 kg pellets/THM), test period 2 (300 kg pellets/THM), test period 3 (350 kg pellets/THM). A simplified layout of the EBF is shown in Figure 9. It has a working volume of 8.2 m^3 and a hearth diameter of 1.2 m. There are three tuyeres placed at 120° intervals. The blast is normally preheated to 1200°C in a new type of pebble heater. The EBF is equipped with a bell-type top. A moveable armor is used for the burden distribution control. Probes for temperature measurements, gas analysis and solid sampling over the blast furnace diameter are installed at three different levels. Process data are logged continuously and stored in a database where reports and trend charts are generated as well as process calculations are carried out. The EBF is a very sensitive tool for detecting differences in properties of different ferrous burdens. The response time is much shorter for the EBF compared to a commercial furnace.

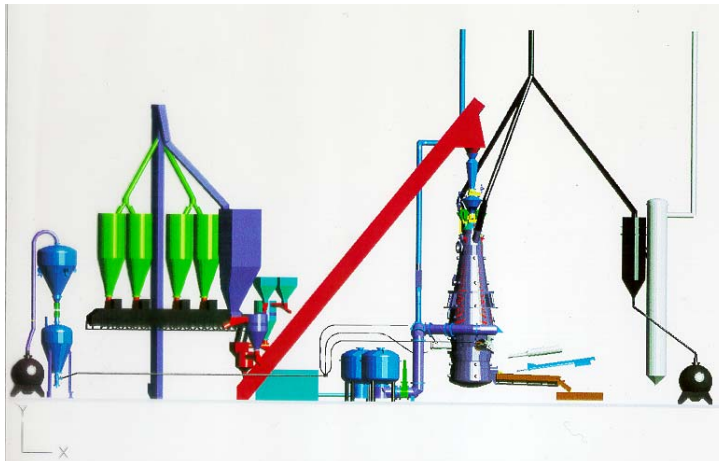


Figure 9. Schematic of LKAB's EBF and periphery equipment

2.4 KINETIC ANALYSIS

2.4.1 FRIEDMAN & REGRESSION ANALYSIS

TG results from experiments with reagent mixes have been analyzed using the Netzsch Thermokinetic software package^[55]. In the kinetic analysis, experimental TG results have been expressed as reaction extent α ,

$$\alpha = (W_i - W) / (W_i - W_f) \quad (3)$$

where W is the weight or wt% of the sample at a given time, and W_i and W_f are the initial and final values for the transformation.

A multi-curve method has been applied to the non-isothermal measurements of each sample, specifically the Friedman iso-conversion method. Friedman analysis is based on the Arrhenius equation in a form shown here in Eq. (4):

$$\ln(d\alpha/dt) = \ln(A/f(\alpha)) - E/RT \quad (4)$$

The software provides values for the activation energy, E , and the logarithm of the pre-exponential factor, $\log A$. This analysis has been used as a precursor to linear and non-linear regression parts of the kinetic analysis software in order to estimate the magnitude of activation energy in correlation to conversion degree and temperature. In the multiple linear regression section, a series of experimental data was fit to a variety of different kinetic models for a one-step process. Based on results from Friedman analysis and multiple linear regression, multivariate non-linear regression was used to fit TG data to multi-step consecutive processes with the goal of outlining reaction mechanisms of the systems; $\text{Ca}(\text{OH})_2$, $\text{Ca}(\text{OH})_2\text{-C}$, $\text{Ca}(\text{OH})_2\text{-Fe}_2\text{O}_3$, and $\text{Ca}(\text{OH})_2\text{-C-Fe}_2\text{O}_3$ within the temperature range of 300-800°C. The kinetic models appearing in this study are summarized in Table 4.

Table 4. Kinetic models used in the rate equation, $d\alpha/dt = -A \exp(-E_a/RT) f(\alpha)$

Code	$g(\alpha)^*$	$f(\alpha)^*$	Kinetic model type
Fn	$(1/(1-\alpha)^{n-1})-1$	$(1-\alpha)^n$	n^{th} -order
R2	$1-(1-\alpha)^{1/2}$	$2(1-\alpha)^{1/2}$	Two-dimensional phase boundary
R3	$1-(1-\alpha)^{1/3}$	$3(1-\alpha)^{2/3}$	Three-dimensional phase boundary
B1	$\ln(\alpha/(1-\alpha))+c$	$(1-\alpha)\alpha$	Prout-Tompkins autocatalysis
An	$(-\ln(1-\alpha))^{1/n}$	$n(1-\alpha)[-ln(1-\alpha)]^{(n-1)/n}$	Avrami-Erofeev n -dimensional nucleation/growth
D1	α^2	$1/2\alpha$	1D-diffusion
D2	$\alpha+(1-\alpha)\ln(1-\alpha)$	$-1/\ln(1-\alpha)$	2D-diffusion
D3	$[1-(1-\alpha)^{1/3}]^2$	$[3(1-\alpha)^{2/3}]/[2[1-(1-\alpha)^{1/3}]]$	3D-diffusion

* $g(\alpha)$ is the *integral* form of the reaction mechanism function, $f(\alpha)$ is the *derivative* form

A short summary of the physical meaning of each model in Table 4 is given below:^[56]

Order based (Fn) models

These are the simplest type of models because of their similarity to homogenous kinetic models. Accordingly, in these models the reaction rate is proportional to the amount or fraction remaining of reactant(s) raised to a particular power which is the reaction order.

Shrinking geometry (R2&R3) models

These models make the assumption that product nucleation occurs rapidly on the surface of the reactant crystal. The rate of reaction is then controlled by the resulting reaction interface progress toward the center of the crystal. If a solid particle is assumed to have cylindrical or spherical/cubical shapes the shrinking area (R2) or shrinking core (R3) models, can be derived.

Autocatalysis (B1) models

Autocatalysis is said to occur in solid-state kinetics if the growth of product nuclei promotes continued reaction because of the formation of imperfections such as dislocations or cracks at the reaction interface (i.e., branching).

Nucleation/growth (An) models

Because crystals have fluctuating local energies from imperfections due to impurities, surfaces, edges, dislocations, cracks, and point defects, nucleation can occur at these points of minimized energy. Nucleation is the formation of a new product phase at these extra reactive points in the lattice of the reactant. These nuclei then grow, or are ingested back into the reactant, at a rate dependent on the radius needed (critical radius) for continued nucleus growth.

Diffusion (D1, D2, D3) models

In diffusion-controlled reactions, the rate of product formation decreases proportionally with the thickness of the product barrier layer. The simplest model is for an infinite flat plane (D1). If reactant particles are assumed to be cylindrical, and diffusion occurs radially through a cylindrical shell with an increasing reaction zone, a two-dimensional diffusion (D2) model can be derived. A three-dimensional diffusion (D3) model is based on the assumption of spherical solid particles.

2.4.2 MASTER PLOT, $Z(\alpha)$, ANALYSIS

In order to more closely evaluate the possible kinetic models that best describe the transformations occurring in thermal analysis samples, a “master plot” can be constructed to compare theoretical curves with the current experimental curves. This method allows the user to discern the predominant kinetic model or family of models that best match the experimental results using a relationship that is

generally independent of the measured kinetic parameters. The specific master plot used in this thesis is based on the following function:^{[57]-[59]}

$$Z(\alpha) = \frac{d\alpha / dt}{\beta} \mu(x) T \quad (5)$$

by substituting the derivative and integral form of the Arrhenius rate equation into Eq. (5),

$$\frac{d\alpha}{dt} = Af(\alpha) \exp(-E / RT) \quad (6)$$

$$g(\alpha) = \frac{AE}{R\beta} \exp(-x) \frac{\mu(x)}{x} \quad (7)$$

where $x = E/RT$, $\beta = dT/dt$ and the fourth-degree rational approximation of the temperature integral taken from Senum and Yang:^[60]

$$\mu(x) = \frac{x^3 + 18x^2 + 88x + 96}{x^4 + 20x^3 + 120x^2 + 240x + 120} \quad (8)$$

we arrive at the expression,

$$Z(\alpha) = f(\alpha)g(\alpha) \quad (9)$$

As seen in Figure 10, the theoretical values of $Z(\alpha)$ for the most common kinetic models have been plotted against α using Eq. (9) and expressions for $f(\alpha)$ and $g(\alpha)$ from Table 4. Experimental values of $Z(\alpha)$ can be plotted using Eq. (5) and Eq. (8).

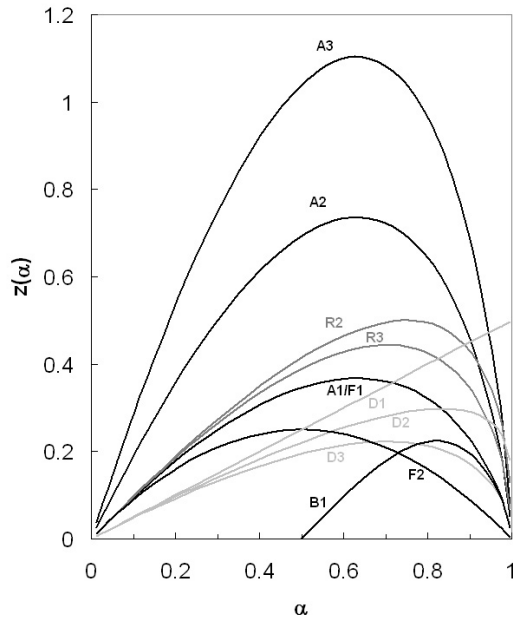


Figure 10. $Z(\alpha)$ master curves for theoretical kinetic models

CHAPTER 3

RESULTS AND DISCUSSION

3.1 CBP OPTIMIZATION AND LARGE SCALE TESTING

3.1.1 TTH AND CAPACITY RESULTS

Cold strength of agglomerates is an important aspect of agglomerate quality. When recycling agglomerates at various unit processes within an integrated iron and steelmaking plant they must have sufficient cold strength to withstand the physical stresses of transportation, loading, unloading and charging. In order to insure sufficient cold strength, the CBPs in this study were tested using the standardized TTH method. TTH tests were conducted on the 9-12mm size fraction of produced pellets, which is the typical fraction used for iron ore pellet testing. In this study, the wt. fraction of product pellets with sizes between 9 and 12mm is reported as the capacity for each specific pellet composition.

CBPs FOR THE BOF

Table 5 shows the sieving results from pelletizing tests, L1 to L11. Tests L1 and L6 had the lowest capacity while tests L8 and L4 had the highest capacity values. Test L1 has a large +16 mm pellet fraction indicating an excess addition of water to the pelletizing mix causing premature grain formation. Test L6 has a large -9 mm pellet fraction indicating a lack of sufficient grain formation. Tests L8 and L4 have pellet sizes that are more evenly distributed in the high and low sizes with a peak fraction between 9 and 12.5 mm.

Table 5. Pellet size distribution for tests L1-L11 wt%

Test No.	+16mm	+12.5 -16mm	+9 -12.5mm	+5 -9mm	+2 -5mm	-2mm
L1	79.35	7.82	5.89	3.69	1.32	1.93
L2	20.55	8.87	22.49	40.76	3.12	4.22
L3	8.53	5.06	16.62	53.68	12.09	4.02
L4	13.32	14.36	44.84	23.40	1.89	2.19
L5	11.39	6.77	33.72	43.69	1.92	2.50
L6	7.59	4.33	15.05	41.92	26.61	4.50
L7	38.98	19.14	31.53	6.11	2.13	2.11
L8	15.21	11.18	50.76	18.56	2.15	2.14
L9	21.45	13.09	41.81	19.41	2.38	1.86
L10	9.41	4.22	18.94	53.03	11.80	2.61
L11	12.78	11.28	41.22	31.98	1.56	1.18

The differences in pellet size distribution from test to test arise from raw material and pelletizing process characteristics and largely, water addition. Water was added to the pellet mixes in two stages; a primary addition that was identical for tests L1-L11 and a secondary addition that was sprayed onto the pellet mix while rotating in the pelletizing disc. The secondary water addition was used to help initiate ball formation and was not measured in amount and therefore could have lead to excess water addition. Table 6 gives TTH and capacity results from the factorial designed tests conducted to find an optimal pellet recipe for recycling in the BOF. Pellet test L9 gave the best TTH value at 97.6% and

L6 had the lowest at 88.3%. Generally, those pellet tests which contained a high level of oily mill scale sludge had lower TTH and capacity values. Pellet blend L9 had the largest TTH value and a good capacity value compared to the other blends. Therefore, pellet blend L9 was chosen as the optimal blend to use for further pelletizing tests in pilot scale. TTH and capacity results from tests L1-L11 are examined more closely in section 3.3.

Table 6. TTH and capacity results for BOF pellet tests

Test No.	Level	wt%	
		Cap	TTH
L1	A1B1C2	5.9	88.9
L2	A2B2C1	22.5	96.3
L3	ABC(1.5)	16.6	93.1
L4	A1B2C2	44.8	96.3
L5	ABC(1.5)	33.7	95.4
L6	A2B2C2	15.1	88.3
L7	A1B2C1	31.5	97.2
L8	ABC(1.5)	50.7	97.1
L9	A2B1C1	41.8	97.6
L10	A2B1C2	18.9	90.1
L11	A1B1C1	41.2	92.2
\bar{x}		29.3	93.9
σ		14.4	3.5
			2.9

CBPs FOR THE BF

The BF pellet design and testing was conducted at SSAB Luleå. Table 7 shows TTH and capacity results from the factorial designed tests conducted to find an optimal pellet recipe for recycling in the BF. Test B4 had the highest TTH value, 94.4%, and capacity, 55.7%, of the nine tests. Therefore, pellet blend B4 was chosen as the optimal blend for further pelletizing tests in pilot scale.

Table 7. TTH and capacity results for BF pellet tests

Test No.	Level	wt%	
		Cap	TTH
B1	A1B1C1	51.7	66.9
B2	A2B1C1	28.0	60.3
B3	A1B2C1	18.6	53.3
B4	A2B2C1	55.7	94.4
B5	A1B1C2	23.2	75.2
B6	A2B1C2	40.7	44.8
B7	A1B2C2	26.8	41.2
B8	A2B2C2	20.8	41.0
B9	ABC(1.5)	48.0	55.0
\bar{x}		34.8	59.1
σ		14.3	17.6

PILOT SCALE PELLETIZING

Pilot scale pelletizing tests were conducted using optimized pellets blends intended for use in the BF and BOF. These tests were carried out in 2000 and 2001 at LuleFrakt Brikett AB. After material mixing, the pellet mass was fed by transport band to a disc pelletizer, and then the produced pellets were sent to a rolling screen. The pellets with particle size greater than 10 mm were sent to a container by tractor. The pellets with particle size less than 10 mm were sent back to the disc pelletizer by transport band.

A BF pellet blend based on lab test B4 was used in pilot scale pelletizing tests, BF803 to BF822. The TTH value of BF pellets was more than 95% after 24 hrs, and the capacity was 9.7 tons/hr. A total amount of 43 tons of BF pellets were produced, however, only a portion of these were used in pilot scale tests of CBPs as burden material in the EBF.

BOF pellet blends based on lab test L9, BOF-R1 (with BF flue dust) and BOF-R2 (no BF flue dust), were used in pilot scale pelletizing tests. The TTH values for both tests were more than 94% after 24 hours, while the capacity of pellets was 13 tons/hr. Table 8 shows the chemical analysis from pilot scale tests for BF and BOF pellets. During these pilot scale tests, an amount of 74 tons of BOF pellets were produced.

Table 8. Chemical analysis from pilot scale pellets in wt%

Test blend	Fe _{tot}	CaO	SiO ₂	MnO	P ₂ O ₅	Al ₂ O ₃	MgO	Zn	S
BF mean	41.4	17.6	5.56	0.88	0.08	1.30	3.34	0.10	0.33
BOF-R1	41.3	17.5	5.52	0.73	0.11	1.47	3.45	0.10	0.12
BOF-R2	49.2	19.1	4.44	0.73	0.12	0.98	3.57	0.07	0.06

3.1.2 THERMAL ANALYSIS RESULTS

The behavior of cold bonded agglomerates during heating is an important aspect of agglomerate quality as well. Merits such as self-reducing and/or self-fluxing behavior can be critical for process application of cold bonded agglomerates. For example, a decrease in fuel consumption when using agglomerate burden in the BF and a decrease in cooling effect of agglomerate charge in the BOF. To help characterize the behavior that CBPs display during heating, TG/DTA/QMS experiments have been completed on pellet blends L1-L11 and B4.

BOF PELLET BLENDS L1-L11

Micro pellet samples from the -5 mm pellets size fraction produced from experimental pelletizing tests, L1-L11, were tested. Figure 11 shows the thermal analysis result from tests with pellet blend L9 and is representative of the results for the other 10 tests.

Absorbed moisture evaporation occurs in the range of roughly 40-140°C with 6.8% wt. loss indicated by the TG curves, accompanied by H₂O generation detected with QMS and a broad endothermic peak in the DTA curve. At temperatures between 230 and 480°C, chemically bound water is released slightly from the metallurgical by-products and largely from hydrated lime in cement with 4.9% wt. loss accompanied by endothermic peaks in the DTA curve. H₂ gas is detected in the range of roughly 320-600°C indicating possible cracking of H₂O generated from dehydroxylation or the steam-carbon reaction of H₂O with solid carbon in the sample.

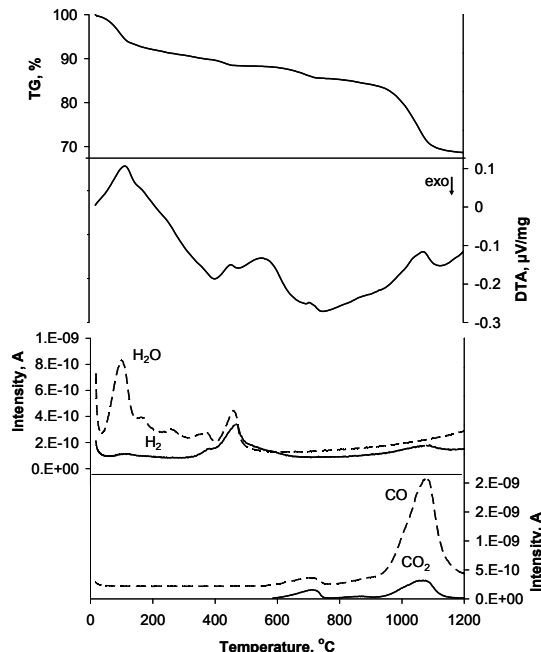


Figure 11. STA results for pellet L9

In the temperature range of 500-730°C there occur three thermal effects in the sample totalling 2.8% wt. loss. CO gas evolves during this temperature range coinciding with an endothermic effect at 500°C in DDTA results, indicating possible local carbon gasification via the steam-carbon reaction. Following CO generation, possible low temperature reduction of iron oxides occurs coinciding with an exothermic peak at roughly 565°C and CO₂ generation. Next, a premature decomposition of carbonates in the sample possibly occurs coinciding with an endothermic peak in the DTA curve at roughly 700°C and CO₂ evolution. Above 740°C, a transition occurs with 16.9% total wt. loss. In the range of approximately 740-900°C, CO is generated from possible direct reduction of iron oxides by solid carbon in the sample accompanied by a minor endothermic trend in the DTA curve. In the temperature range of 900-1200°C, possible direct reduction becomes more spontaneous signified by a small endothermic effect at 930°C in DDTA results. CO generated from direct reduction can take part in further reduction reactions coupled with carbon gasification indicated by a large endothermic peak at 1070°C in the DTA curve and a large CO:CO₂ ratio. The weight losses resulting from each transition in STA experiments L1-L11 are given in Table 9.

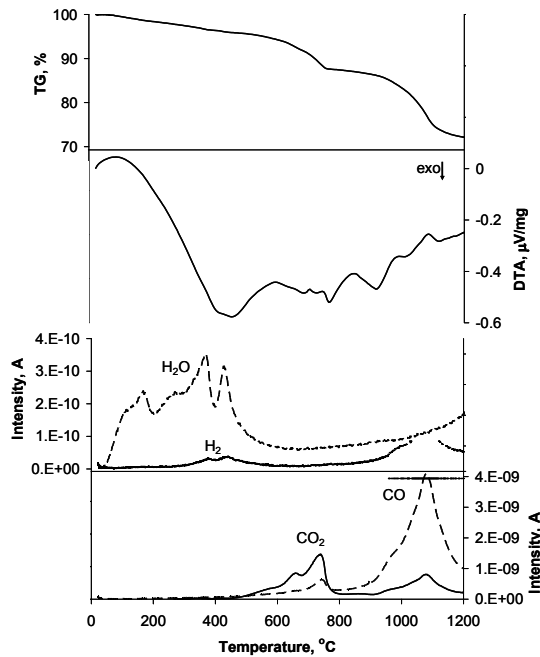
The first temperature transition (40-140°C) and the fourth temperature transition (740-1200°C) in the thermal analysis of pellet blends L1-L11 show the largest variation of weight loss according to standard deviation values in Table 9. During the first transition, the content of free moisture can be partly dependent on BOF fine sludge content due to its larger “sand” fraction than the other by-products in the pellet blend. Particles in the “sand” fraction show near colloidal behavior having a relatively large surface to volume ratio thereby promoting water adsorption. But more likely, it is the fact that moisture content is a difficult parameter to control in pellet production because considerable experience is required to optimize the moisture content for even a single raw material. During the fourth transition, the contents of iron oxides and carbon vary considerably between the pellet blends thereby varying the weight loss due to reduction and carbon gasification between blends.

Table 9. Weight loss in % from STA experiments L1-L11

Temperature transition	L1	L2	L3	L4	L5	L6	L7	L8	L9	L10	L11	χ	σ
40-140°C	3.23	5.66	5.5	5.87	5.79	2.36	3.74	5.09	6.79	6.11	1.68	4.71	1.68
230-480°C.	4.05	3.62	3.95	3.19	3.22	4.18	4.39	4.10	4.90	4.33	3.27	3.93	0.55
500-730°C	2.70	2.93	2.88	2.68	2.70	3.52	3.23	2.61	2.84	2.76	2.69	2.87	0.28
740-1200°C	16.72	17.86	18.18	17.54	16.76	22.33	21.13	17.39	16.95	19.54	15.35	18.16	2.06
total	26.70	30.07	30.51	29.28	28.47	32.39	32.49	29.19	31.48	32.74	22.99	29.66	2.90

BF PELLET BLEND B4

Samples of B4 pellets ground to -75 µm and weighing roughly 70 mg were tested using STA. Figure 12 shows the thermal analysis results from a sample of B4 which are similar to pellet sample L9 and correspond with the literature when compared to results from Mikhail and Turcotte^[63].

**Figure 12.** STA results for pellet B4

Absorbed moisture is detected in the temperature range 40-200°C with 1.6% wt. loss and a broad endothermic peak in the DTA curve. At temperatures between 200 and 460°C, chemically bonded water is released with 2.5% wt. loss accompanied by small endothermic effects in DDTA results and H₂O generation. H₂ is detected in the temperature range of 300-600°C indicating possible cracking of H₂O or the steam-carbon reaction of H₂O with solid carbon in the sample. The observation of CO₂ evolution and 1.7% wt. loss between 450 and 600°C, leads to the possible assumption that some carbon gasification, has occurred resulting in the low temperature reduction of some iron oxides in this temperature range. Here, CO₂ generation occurs at a lower temperature when compared to results from pellet sample L9 in Figure 10. This result can be attributed to better reaction kinetics during tests

with pellet sample B4 because the sample has been ground to $-75\text{ }\mu\text{m}$ having more surface area than the micro pellet L9. A premature decomposition of carbonates can occur in the temperature range of $615\text{-}685^\circ\text{C}$ with 2.3% wt. loss coinciding with a small endothermic peak in the DTA curve and CO_2 evolution. In the temperature range of $700\text{-}800^\circ\text{C}$, the CO_2 released from carbonate decomposition can possibly react further with solid carbon in the sample producing CO accompanied by an endothermic peak in the DTA curve and ca 4% wt. loss.

Above 800°C , a transition occurs with 16% total wt. loss. In the range of approximately $900\text{-}1000^\circ\text{C}$, CO is produced coinciding with an endothermic peak in the DTA curve. This can possibly be attributed to solid carbon taking part in direct reduction of iron oxides within the sample. In the temperature range of $1000\text{-}1200^\circ\text{C}$, the CO generated from reduction can take part in further iron oxide reduction coupled with carbon gasification signified by a large endothermic peak in the DTA curve and a large CO: CO_2 ratio.

3.1.3 MULTIVARIATE ANALYSIS OF PELLET BLENDS L1-L11

The benefit of a designed experiment lies in the option to evaluate experimental variables and responses and even to add new variables and responses with good statistical confidence. Preliminary results from the 2^3 factorial pellet design tests, L1-L11, are given in Paper 1. A more extensive treatment of experimental data from pellet tests L1-L11 has been done here to investigate how variations in raw material properties and production parameters affect both the cold strength and self-reduction degree of the different pellet blends. Calculations of reduction degree and carbon utilization for pellet tests L1-L11 were completed using results from chemical analysis, TG/DTA analysis and gas analysis (intensities I_{CO} and I_{CO_2} given in Table 10) in equations 10-14:

$$\Delta m_{O,\text{red}} = \Delta m_{\text{total,red}} \left[\frac{M_O I_{\text{CO}}}{M_{\text{CO}}(I_{\text{CO}} + I_{\text{CO}_2})} + \frac{M_{O_2} I_{\text{CO}_2}}{M_{\text{CO}_2}(I_{\text{CO}} + I_{\text{CO}_2})} \right] \quad (10)$$

Where $\Delta m_{\text{total,red}}$ is the total change in mass from TG data in the temperature transition $740\text{-}1200^\circ\text{C}$, M_x is the molecular weight of x , I_y is the maximum intensity of gas y from QMS data in the temperature transition $740\text{-}1200^\circ\text{C}$.

$$m_{O,\text{initial}} = 100 - m_{Fe_{\text{tot}}} - m_{\text{Oxides}} - m_{CO_2,\text{carbonates}} - m_{H_2O} \quad (11)$$

Where $m_{Fe_{\text{tot}}}$ is the initial wt% of total Fe from chemical analysis, m_{Oxides} is the initial wt% of oxides other than iron oxide from chemical analysis, $m_{CO_2,\text{carbonates}}$ is the initial wt% of CO_2 from TG data in the temperature transition $500\text{-}730^\circ\text{C}$, m_{H_2O} is the initial wt% of H_2O from TG data in the temperature transition $40\text{-}480^\circ\text{C}$.

$$\text{reduction \%} = \frac{\Delta m_{O,\text{red}}}{m_{O,\text{initial}}} \times 100 \quad (12)$$

Where reduction \% is the reduction degree, $\Delta m_{O,\text{red}}$ is the change in mass due to oxygen removal from iron oxide, $m_{O,\text{initial}}$ is the initial mass of oxygen bound to iron.

$$\Delta m_{C,\text{red}} = \Delta m_{\text{total,red}} \left[\frac{M_C I_{\text{CO}}}{M_{\text{CO}}(I_{\text{CO}} + I_{\text{CO}_2})} + \frac{M_C I_{\text{CO}_2}}{M_{\text{CO}_2}(I_{\text{CO}} + I_{\text{CO}_2})} \right] \quad (13)$$

$$carbon\ utilization\ \% = \frac{\Delta m_{C,red}}{m_{C,initial}} \times 100 \quad (14)$$

Where $\Delta m_{C,red}$ is the change in mass due to solid carbon removal and $m_{C,initial}$ is the initial wt% of solid carbon from chemical analysis.

Table 10. CO and CO₂ maximum intensities (A) during the temperature interval 740-1200°C

Test No.	$I_{CO} * 10^{-9}$	$I_{CO_2} * 10^{-9}$	$I_{CO}/(I_{CO}+I_{CO_2})$	$I_{CO_2}/(I_{CO}+I_{CO_2})$
L1	6.41	1.48	0.81	0.19
L2	9.35	2.99	0.76	0.24
L3	7.87	1.57	0.83	0.17
L4	8.90	1.81	0.83	0.17
L5	8.54	1.70	0.83	0.17
L6	4.30	0.89	0.83	0.17
L7	9.08	2.49	0.79	0.21
L8	8.99	1.87	0.83	0.17
L9	1.90	0.31	0.86	0.14
L10	8.21	1.76	0.82	0.18
L11	7.02	1.35	0.84	0.16
χ	7.32	1.66	0.82	0.18
σ	2.33	0.71	0.03	0.03

Some assumptions were made in order to simplify the calculation of reduction degree and carbon utilization. The vaporization and dehydration of H₂O is considered the only cause for weight loss during the temperature transition 40-480°C; CO₂ generation from the decomposition of carbonates is the single cause for weight loss during the temperature transition 500-730°C; and CO/CO₂ generation is exclusive to iron oxide reduction and carbon gasification during the temperature transition 740-1200°C.

Several model configurations have been analyzed, some with a single response; i.e. Reduction Degree, TTH, ATH, Capacity and Carbon Utilization, and some with multiple response combinations, i.e. Reduction Degree + TTH, have been analyzed. The Reduction Degree model, discussed in detail here, shows good fit to observed responses and has a relatively normal distribution of errors. A brief comparison to other models is made here as well.

REDUCTION DEGREE MODEL

The Reduction Degree model variables and statistics are given in Table 11. This model shows good fit to the observed variance, R²Y of 0.95, and predicted variance, Q² of 0.85. Figure 13 shows the cumulative model overview and consists of two significant principal components of which the first component creates the majority of fit in the model.

Table 11. Variable statistics for the Reduction Grade model

#) Variable (%) Y) Response	Min	Max	Min/Max	Mean	Median	StdDev	Skewness
1) LD-fine	0.20	0.40	0.50	0.30	0.30	0.09	-3.05E-07
2) MillScale	0.10	0.20	0.50	0.15	0.15	0.04	-3.05E-07
3) BF-dust	0.20	0.30	0.67	0.25	0.25	0.04	6.11E-07
4) LD-coarse	0.00	0.40	0.00	0.20	0.20	0.11	4.16E-08
5) Moisture	1.68	6.79	0.25	4.71	5.50	1.68	-0.75
6) Hydrates	3.19	4.90	0.65	3.93	4.05	0.55	0.03
Y) Red. Degree	52.41	100.20	0.52	70.40	68.66	13.09	1.14
28) d50 (μm)	149.90	160.50	0.93	155.20	155.20	4.20	3.33E-06
29) sand	6.69	7.48	0.90	7.09	7.09	0.22	-1.26E-06
30) stone	10.41	12.03	0.87	11.22	11.22	0.45	-3.26E-06
31) block	65.83	68.54	0.96	67.18	67.18	1.02	0.00
32) d' (μm)	195.40	225.10	0.87	209.10	208.80	8.32	0.32

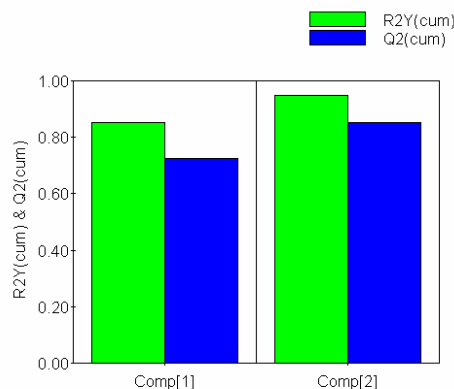


Figure 13. R2Y and Q2 for Reduction Degree model

The left side of Figure 14 shows the loadings plot with expanded variables, cross terms and square terms (i.e. C1x32, S6x6), included with normal design variable and responses. The number corresponding to each variable is shown in Table 11.

Loading plots describe the influence of X-variables on Y-variables and partly the correlation between all variables. Considering the significance of the two principal components in Figure 13, values projected on the first component (x-axis) have the greatest significance. Therefore, design variable *LD coarse* % has the greatest negative influence and design variable *BF dust* % has the greatest positive influence on Reduction Degree. Furthermore, the cross term *Moisture* % X *Stone* (C5x30) has the greatest negative influence and the cross term *LD coarse* % X *Moisture* % (C4x5) has the greatest positive influence on Reduction Degree

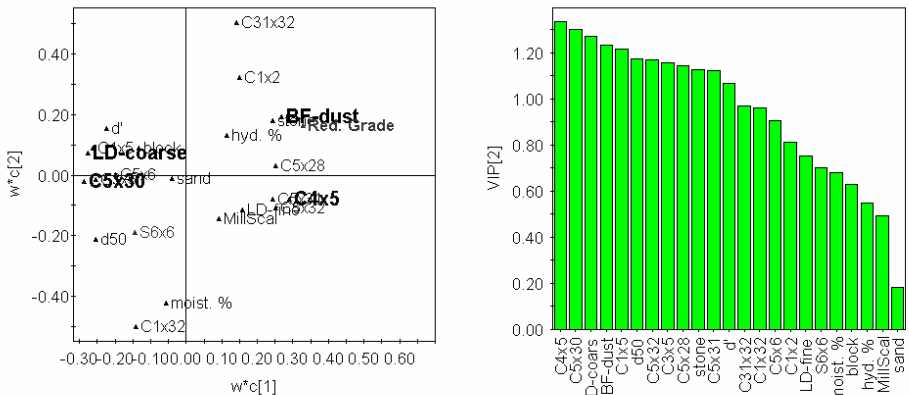


Figure 14. Left, loadings plot; Right, VIP plot

The significance of these variables can be seen more clearly in the right side of Figure 14, where all variables are ranked in descending order from left to right according to their importance to the response of Reduction Degree. VIP is defined as the sum over all the dimensions of the contributions of each variable of influence.

MODEL COMPARISON

Table 12 shows a comparison of model size and fit and lists the two largest variables of importance having either a negative (-) or a positive (+) influence for the given response(s). The TTH model explains roughly 90 % of the variance in TTH values and predicts roughly 73 % of the variance. Here it is evident that the prediction capacity of the TTH model is mediocre when compared to the Reduction Degree and Carbon Utilization models at roughly 85 %. Oily millscale content in the different pellet mixes has the largest effect, in this case a detrimental effect, on the TTH response. Conversely, the interaction between BOF fine and coarse sludge (*LD fine and coarse %*) has the 2nd largest effect, in this case a beneficial effect, on the TTH response.

From these results we see that the particle size distribution of the pellet blend plays a large role in the subsequent cold strength (TTH) of the produced pellet. Oily millscale sludge contains the largest particles among the raw materials in the pellet blend and when contents of oily millscale sludge are large enough a lack of structure could occur in the agglomerate due to a deficiency of bonding points for the cement during hydration. Oil content in the millscale sludge is another possible cause of decreased TTH values^[38], but this parameter was not considered in the current study. The interaction between BOF fine and coarse sludge shows a beneficial effect on the TTH value. The synergy between these two materials having relatively large fine-particle fractions possibly contributes to a more optimal particle size distribution in the pellet blend. Another reason for the positive effect on TTH can be contents of CaO and/or Ca(OH)₂ in BOF sludge contributing to better bonding within the pellet during hydration and curing.

Considering the model with a dual response, the Reduction Degree + TTH model, particle size distribution is the most critical factor when optimizing the performance of CBPs regarding both self-reduction degree and cold strength. It seems that pellet blends with larger stone fractions (10-40 µm) promote good self-reduction while maintaining good cold strength. The negative correlation of the responses with d_{50} indicates that raw pellet blends containing the by-products in this study should be milled to decrease the average particle size if the Reduction Degree + TTH response is to be fully

optimized. Conversely, any supplementary carbon added to the pellet blend should not be milled in reference to d_{50} having a positive correlation with the Carbon Utilization response.

Table 12. Comparison of model parameters based on response(s)

Model Response(s)	Significant Components	R2Y	Q2	VIP
TTH	2	0.902	0.732	<i>Oily millscale % (-) LD fine % X LD coarse % (+)</i>
Capacity	1	0.571	0.320	<i>d_{50} X Stone (+) BF flue % X Stone (-)</i>
Reduction Degree	2	0.949	0.852	<i>LD coarse % X Moisture % (+) Moisture % X Stone (-)</i>
Carbon Utilization	3	0.986	0.855	<i>d_{50} (+) BF flue % (-)</i>
Reduction Degree + TTH	4	0.947	0.713	<i>Stone (+) d_{50} (-)</i>

3.1.4 LARGE SCALE TESTING OF CBPs (Papers 1&2)

INDUSTRIAL TEST IN THE BOF (Paper 1)

As mentioned in section 2.3.4, industrial scale testing was completed using CBPs as charge in the BOF at SSAB Luleå, Sweden. Initially, pellet blend BOF-R1 (see Table 8) was chosen for industrial trials but this blend was eventually replaced by pellet blend BOF-R2, in order to avoid high sulphur contents in burden material. By removing BF flue dust from the final pellet blend, a change in the self-reduction behavior was inevitable.

Figure 15 shows a comparison of DTG results from thermal analysis in Ar_(g) of pellet blends BOF-R1 and BOF-R2. The weight loss behavior of the two pellet blends is very similar until a temperature of 800°C is reached where pellet BOF-R1 achieves 11.5% more weight loss than pellet BOF-R2 due to carbon content in BF flue dust. Clearly, self-reduction is a key factor when recycling cold bonded agglomerates but is not always a necessary one, i.e. depending on whether agglomerates are used as scrap substitute or as dynamic coolant in the BOF. The purpose of these preliminary full-scale trials was to investigate the feasibility of using cold bonded agglomerates as dynamic coolant and thus a means to recycle in-plant by-products without causing disturbances to the BOF process and production. Therefore, pellet blend BOF-R2 was chosen for full-scale testing.

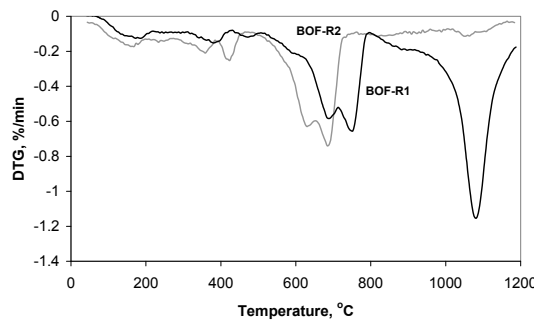


Figure 15. DTG results for pellet BOF-R1 and BOF-R2

Table 13 shows some results concerning steel chemistry during industrial tests, J6396 to J6485. The contents of carbon, phosphorus and sulphur in the steel product, from the pellet tests, are similar to

those results from reference tests without pellet charging. At pellet charging amounts of 2.5 tons, it is possible that carbon and sulphur content may increase more than 1σ above normal levels and have some effect on steel quality but this conclusion is premature without further testing over longer trial periods.

Table 13. Steel composition during BOF tests

Chg. #	Chg. wt. total (tons)	Chg. wt. BOF-R2 pellets (tons)	C %	P %	S %
J6396	104	Ref	0.059	-	-
J6398	116.6	Ref	0.053	0.01	0.014
J6431	105.1	0.5	0.051	0.01	-
J6433	112.9	1	0.063	0.01	0.007
J6434	111.9	1.5	0.053	-	-
J6435	108.9	1.5	0.064	0.01	0.008
J6482	110.3	2	0.058	-	-
J6483	111.1	2.5	0.100	0.01	0.007
J6484	114.9	2.5	0.054	0.01	0.019
J6485	109.7	2.5	0.091	0.01	0.013
Mean	-	-	0.065	0.007	0.007
Std	-	-	0.016	0.005	0.007

Figure 16 shows some slag composition results during two reference and two 2.5-ton pellet tests. From this figure it is apparent that BOF slag chemistry is relatively unaffected by cold bonded agglomerate charge at levels of up to roughly 2.2% of the total charge weight to the BOF. Slag volume was unfortunately not measured during the full-scale tests but given the large content of oxides in agglomerates a slight increase is expected.

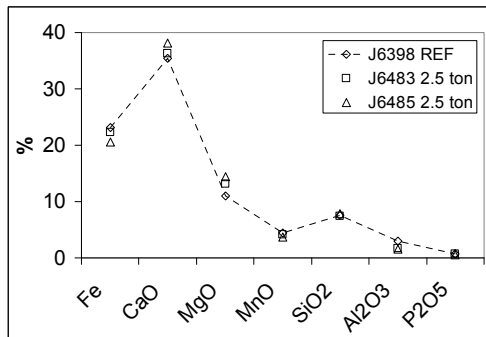


Figure 16. Slag composition during BOF tests

Figure 17 shows the results of the effect of charging CBPs on representative samples of BOF sludge generation. A slurry sample of equivalent volume was taken each minute of the blowing period and the amount of solids was recorded. The sludge generation for a BOF test with 2.5-ton pellets charge is similar to that from reference tests although a larger series of tests would be needed to make any conclusions with statistical merit. But from these results, one can presume that the slight decrease of sludge generation occurring during the early part of the blow when comparing 2.5 t pellet charge to the reference is due to a decrease in the scrap demand thereby decreasing the input of high vapor pressure elements, which vaporize early during the blowing period. Conversely, an increase in sludge generation during the latter part of the blow could be due to increased slag generation, from CBP addition, and thereby more slag particle ejection from the BOF.

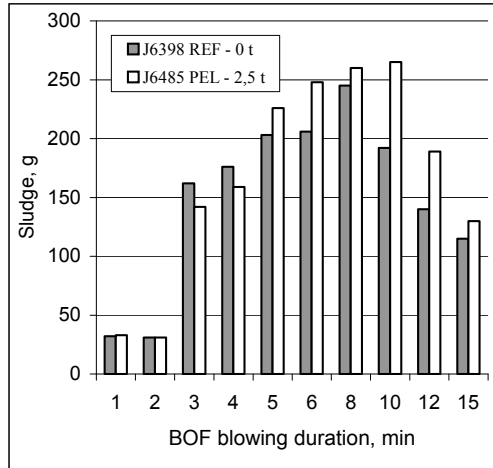


Figure 17. Sludge generation samples during BOF tests

In general during full-scale testing there were no adverse disturbances to the BOF process due to the addition of CBPs. A natural continuation to this work would be to initiate a longer trial with pellets charge in the BOF and to broaden the analysis base in order to calculate a heat and mass balance around the BOF during testing.

PILOT SCALE TEST IN THE EBF (Paper 2)

As mentioned in section 2.3.5, a pilot scale test campaign was completed with CBP charge (pellet blend B4) in the EBF. The pilot scale test was also complemented with lab-scale reduction tests and softening and melting tests. Table 14 shows the test parameters and results for isothermal reduction tests conducted on CBP samples at LKAB's metallurgical laboratory. CBPs have good isothermal tumbling strength (ITH) at low temperature, 500°C, with a value of 95.8% while at high temperature, 950°C, the ITH value is quite low at 31%.

Table 14. Isothermal reduction tests

Standard test	Gas comp. CO/CO ₂ /H ₂ /N ₂	Temp°C	Wt. (g)	Wt. Loss %	ITH.% +6.3/-0.5 mm
ISO 13930	20/20/2/58	500	500	9.49	95.8/2.9
ISO 4695	40/0/0/60	950	500	7.44	31.0/52.3
ISO 7992	40/0/2/58	1050	1200	23.08	NA

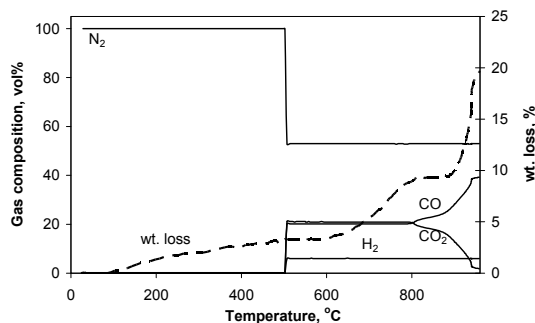


Figure 18. BF simulated reduction test

Figure 18 shows an example of the test gas composition and weight loss during a BF simulation reduction test on CBPs while Table 15 shows results from 3 separate tests ended at different temperatures. CBP samples suffer a considerable loss of binding strength between 700 and 900°C indicated by the loss in tumbler strength (wt% + 6.3mm) during this temperature interval, 63% to 29%.

Table 15. BF simulated reduction results

Duration (min.)	Temp. °C	Wt. (g)	Wt. Loss %	Wt.% +6.3/-0.5 mm
30	20-710	500	5.5	63.2/26.0
100	20-880	500	12.3	28.9/46.6
180	20-970	500	24.4	NA

Table 16 shows the softening and melting experiments run on mixture of CBPs and MPBO olivine pellets. The softening temperature, T(50), is defined as the temperature when the sample bed has shrunk to 50% of its original height. The melt-out temperature, T(Pmax), is defined as the temperature when the maximum pressure drop occurs over the sample bed. The cohesive zone temperature interval is defined as the difference between the temperature at which the bed stops shrinking, T(end), and the softening temperature. The cohesive zone temperature interval shows a decreasing trend when CBPs are mixed with the olivine pellets up to 10% CBP content and then an increase in the interval occurs between 10 and 20%. One reason for this behaviour might be that additions of CBPs above 10% of the mixture increase slag basicity in the mixture.

Table 16. Softening and melting properties
of different pellet samples, data in °C

$$CBP\% = \text{wt. CBP}/\text{wt.(CBP+MPBO)} \cdot 100$$

CBP %	0	5	10	20
T(50)	1356	1404	1427	1409
T(Pmax)	1487	1511	1477	1492
T(end)	1494	1511	1519	1528
Cohesive zone T(end)-T(50)	138	107	92	119

The effects from charging high amounts of CBPs on the BF process were evaluated during a pilot scale test in the EBF. The EBF is a very sensitive tool for detecting differences in properties of different ferrous burdens. The response time is much shorter in the EBF compared to a commercial blast furnace accentuating possible process problems that could arise during full-scale operation with CBPs. Table 17 shows the raw materials used during the different test and reference periods. Limestone and BOF slag additives were decreased when CBP charge was increased due to the high content of lime-containing oxides in CBPs.

Table 17. Raw materials used during EBF tests

Test periods 1,2,3	150 kg CBP/tHM	300 kg CBP/tHM	350 kg CBP/tHM	Ref.
Pellets	1290	1209	1193	1388
CBP	149	299	344	-
Limestone	15	-	-	47
Quartzite	20	16	29	17
BOF slag	30	-	-	45
Coke	402	390	389	402
PCI	120	122	114	131
O ₂ enrich.	6.09	5.98	5.87	4.31

Figure 19 gives a summary of the stability of various BF process parameters during the reference and testing periods. At levels of 150 kg CBPs/tHM, the parameters are stable and in some cases even more stable than when the furnace operates without CBPcharge. Operating the EBF at higher CBP charge rates causes a noticeable increase of instability for burden descent rate, gas utilization and permeability. The change in process conditions involved with a new burden composition, i.e. additional CBP burden content, will result in expected process variations which can be corrected with necessary adjustments. For instance, the increased thermal state in the furnace when operating with CBP charge could have caused variations in EBF parameters. However, the sum of variations to the process during test periods with high CBP charge rate was not fully explained after process adjustments were made.

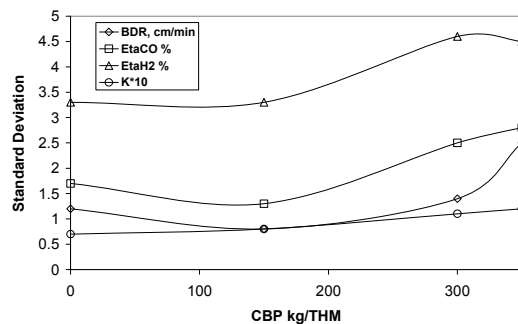


Figure 19. EBF process indicators: BDR (burden descent rate), EtaCO (CO utilization), EtaH2 (H₂ utilization), K (permeability resistance index)

The considerably high disintegration of CBPs in laboratory tests after isothermal reduction at 950°C in Table 15 indicates that disintegration of CBPs might occur during reduction in the EBF shaft. Figure 20 shows micrographs of one CBP sampled from the upper EBF shaft during a testing period with high CBP charge rate. The core of the pellet contains large pores and a reduced iron oxide matrix. While in the interface region between the pellet core and periphery, the microstructure shows signs of disintegration and highly dispersed particles with a periphery of dense microstructure. Furthermore, the disappearance of a predominant central gas flow during testing with 350 kg CBPs/tHM, as well as an increased EtaCO in the centre of the shaft could point to disintegration of CBPs leading to accumulation of fines in the centre of the furnace shaft. As a result of altered gas distribution, pellets of varied pre-reduction degree can reach the hearth. This might be a cause for increased variation of burden descent.

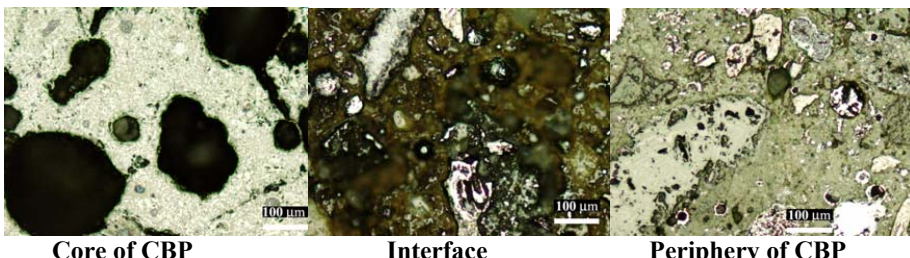


Figure 20. Optical micrographs of a CBP sample from the EBF shaft during testing with 300 kg CBP/tHM

Charging CBPs with the burden gave a decrease in fuel consumption when compared to the reference period. Operators at the EBF systematically reduced the coke and PCI rates to counter the excess thermal reserves in the furnace, see Figure 21. If the consumption of reducing agents during each test period is compared with the consumption during the reference period it is found that the consumption of reducing agents decrease with 11, 21 and 30 kg/tHM for test periods 1, 2 and 3 respectively. Addition of CBPs ($B_2 = 2.13$) to a certain degree with olivine pellets ($B_2 = 0.13$) will improve the slag formation. However, the slag volume increases significantly when the charging of CBPs is increased due to their high content of fluxes. One effect from increased slag volume might be decreased production efficiency.

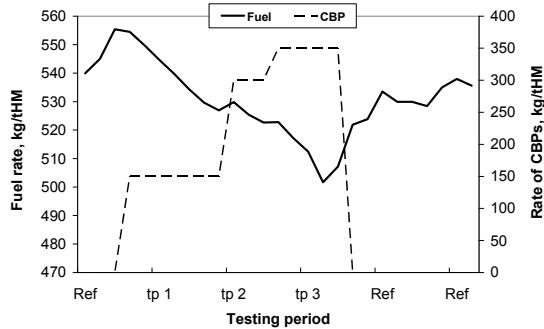


Figure 21. Fuel consumption during EBF testing

3.2 SELF-REDUCTION STUDIES (Papers 3, 4 & 5)

3.2.1 REACTIVITY OF CBP DURING HEAT TREATMENT IN INERT ATMOSPHERE (Paper 3)

The behavior of CBP blend B4, during heating in inert gas, was studied using thermodynamic calculations and TG/DTA/QMS experiments. Additionally, a series of separate TG experiments complemented with XRD and SEM analysis were carried out in order to ascertain the changes that occur in the sample when heated to and maintained at different temperatures.

Table 18. Proposed CBP reactions during heating in inert gas

Rxn #	Reaction Equation	Temp. range °C	Peak temp. °C	ΔH _{peak} (kJ/mol)	ΔG _{peak} (kJ/mol)
1	$Me(OH)_2 \rightarrow MeO + H_2O$ Me represents Ca, Mg...	200-450	420 _{Ca(OH)2}	101.74	-13.33
2	$H_2O + C \rightarrow CO + H_2$	450-540	500	135.46	-4.61
3	$3Fe_2O_3 + CO \rightarrow 2Fe_3O_4 + CO_2$	540-600	550	-29.59	-78.43
4	$Fe_3O_4 + CO \rightarrow 3FeO + CO_2$	600-680	640	17.67	-2.46
5	$FeO + CO \rightarrow Fe + CO_2$	600-680	660	-20.15	-2.31
6	$3CaCO_3 + Fe_3O_4 + 2Fe \rightarrow Ca_2Fe_2O_5 + 3FeO + CaO + 2CO + CO_2$	680-750	700	522.99	-15.45
7	$3FeO + 5CO \rightarrow Fe_3C + 4CO_2$	740-850	760	-207.76	-9.62
8	$Fe_3O_4 + CO \rightarrow 3FeO + CO_2$	800-850	820	16.32	-9.97
9	$Ca_2Fe_2O_5 + 2CO \rightarrow FeO + 2CaO + 2CO_2 + Fe$	850-900	880	25.11	-0.94
10	$FeO + Fe_3C \rightarrow 4Fe + CO$	900-1000	950	143.21	-32.87
11	$C + CO_2 \rightarrow 2CO$	1000-1080	1040	167.36	-58.96
12	$FeO + CO \rightarrow Fe + CO_2$	1080-1160	1100	-16.96	-3.76

The temperature isotherms were chosen based on the results from Figure 12 in section 3.2.2, i.e. the relevant temperatures at which there are distinct variations in the DTG curve coinciding with visible effects in the DTA curve. A summary of the proposed reaction history is given in Table 18, detailing the proposed reactions that can correspond with experimental results in Figure 22 showing the changes in DTG and DDTA vs. temperature.

The raw pellet sample contains mostly $CaCO_3$, Fe_3O_4 , Fe_2O_3 , FeO and Fe , with minor contents of various calcium silicates, carbon, hydrates and free moisture. During heat treatment, hydrates in the sample can react according to Rxn #1 (Figure 22, Table 18) in the temperature range of 200-450°C confirmed by the absence of hydrates in the XRD pattern at 500°C in Figure 23 and H_2O generation in gas analysis in Figure 12. Water vapor released during dehydroxylation can react with carbon in the pellet sample between 450 and 540°C resulting in carbon gasification according to Rxn #2. The CO gas generated from this reaction can react with Fe_2O_3 in Rxn #3 between 540-600°C resulting in a reduction to Fe_3O_4 confirmed by an exothermic peak in the DDTA curve, evidence of magnetite lamellae formation on hematite grains from SEM analysis in Figure 24, a disappearance of Fe_2O_3 in the XRD pattern below 600°C and CO_2 gas generation during this temperature interval. Iron reduction possibly continues to a small degree in Rxn #s 4 and 5 where Fe_3O_4 can reduce stepwise to FeO and Fe between 600-680°C indicated by consecutive endothermic and exothermic peaks in the DDTA curve and CO_2 generation during this temperature interval.

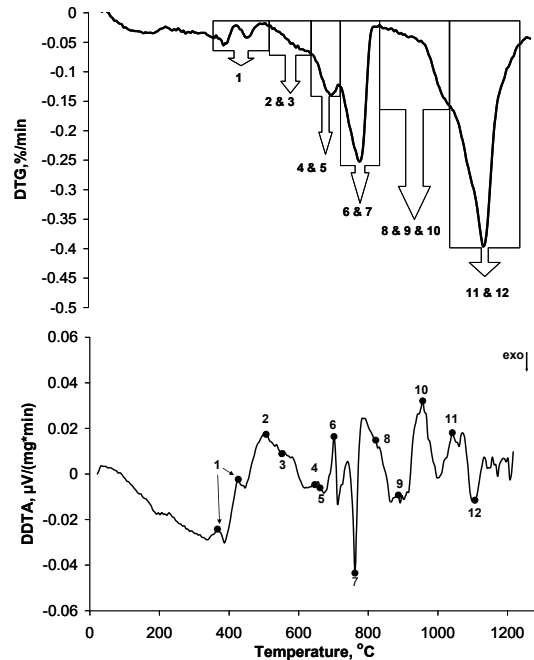


Figure 22. DTG/DDTA results for pellet B4 (Rxn # is coupled to Table 18)

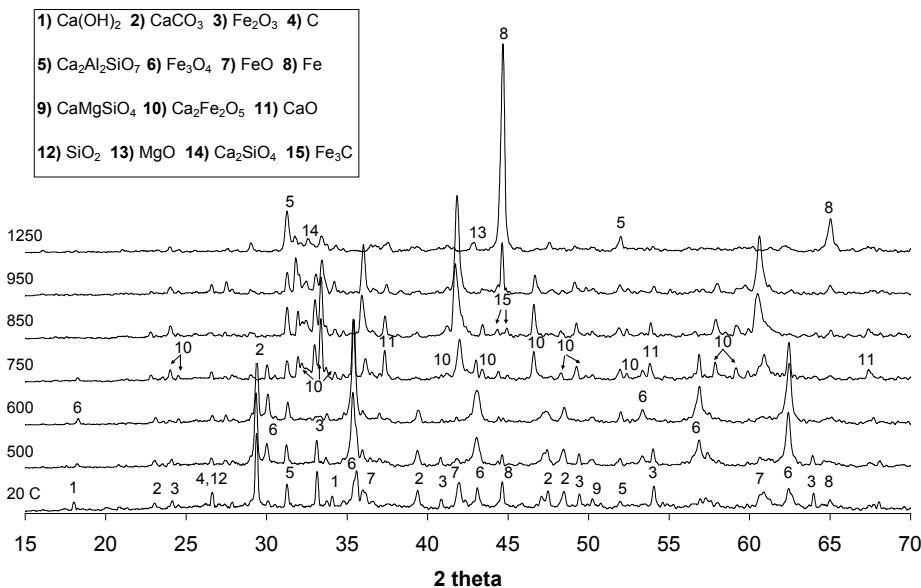


Figure 23. XRD patterns of pellet samples heated to different temperatures

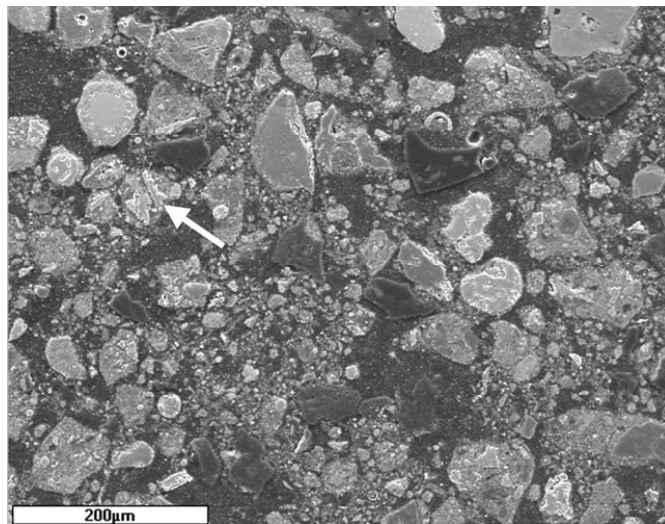


Figure 24. SEM micrograph of CBP heated to 600°C

From FACTSage® calculations, a complex reaction can occur during carbonate decomposition when reduced Fe is present at temperatures between 680 and 750°C, detailed in Rxn #6. Evidence of decreased peaks of Fe_3O_4 and CaCO_3 while peaks of FeO , CaO , and $\text{Ca}_2\text{Fe}_2\text{O}_5$ increase in the XRD pattern at 750°C, as well as increased generation of both CO and CO_2 gas in Figure 12, helps to support this assumption.

Furthermore, in Figure 25, there is evidence of calcium ferrite formation around an iron core. This is in agreement with equilibrium phases at 750°C and 69% CO_2 (marked as X) in Figure 26. Here, the phases that occur depend on the $\text{CaO}/\text{Fe}_2\text{O}_3$ ratio, which likely varies in the overall sample: at a ratio of 1/1; $\text{Ca}_2\text{Fe}_2\text{O}_5$, $\text{CaO}.\text{FeO}.\text{Fe}_2\text{O}_3$ and Fe_3O_4 exist and at a ratio of 1/2; FeO , $\text{CaO}.\text{FeO}.\text{Fe}_2\text{O}_3$ and Fe_3O_4 exist.^[64]

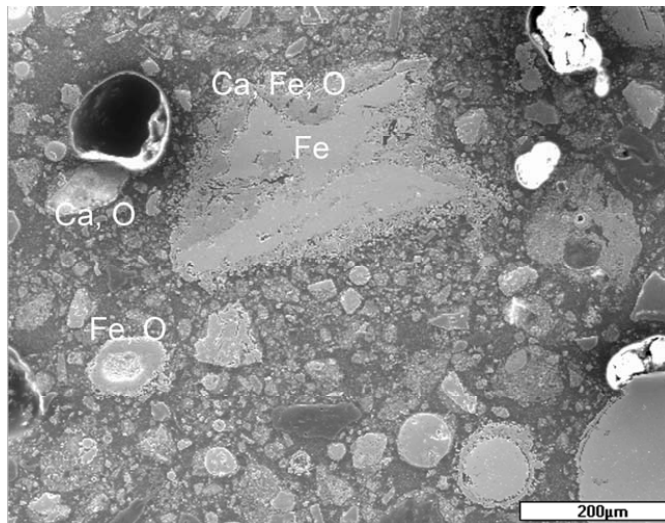


Figure 25. SEM micrograph of CBP heated to 750°C

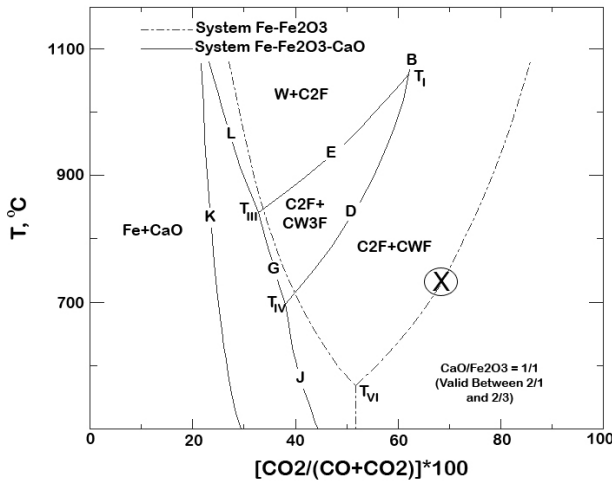


Figure 26. Fe- Fe_2O_3 -CaO system as a function of CO/CO_2 mixing ratio^[64].
 $\text{C} = \text{CaO}$, $\text{F} = \text{Fe}_2\text{O}_3$, $\text{W} = \text{FeO}$

Furthermore, peaks of Fe_3C appear in XRD at 750°C as well as 850°C coinciding with a large exothermic peak in the DDTA curve at 760°C. This supports a possible carbon deposition between 740 and 800°C shown in Rxn #7. Between 800 and 850°C, a minor iron oxide reduction can occur detailed in Rxn #8. Here the remnant Fe_3O_4 from Rxn #6 can reduce to FeO confirmed by the absence of Fe_3O_4 and the increase of FeO in the XRD pattern at 850°C and a small endothermic peak at 820°C on the DDTA curve. The product FeO from Rxn #8 can react again in Rxn #7 to form additional Fe_3C indicated by an increase in Fe_3C peaks in the XRD pattern at 850°C.

Above 850°C, reduction of $\text{Ca}_2\text{Fe}_2\text{O}_5$ possibly occurs between 850-900°C resulting in FeO , Fe and CaO according to Rxn #9. $\text{Ca}_2\text{Fe}_2\text{O}_5$ peaks in the XRD pattern at 950°C have decreased compared to those peaks at 850°C which is an indicator of this reaction as well as SEM analysis, Figure 27, that illustrates that particles containing Fe in the sample at 950°C show segregation from a disperse periphery to a core of dense iron formation.

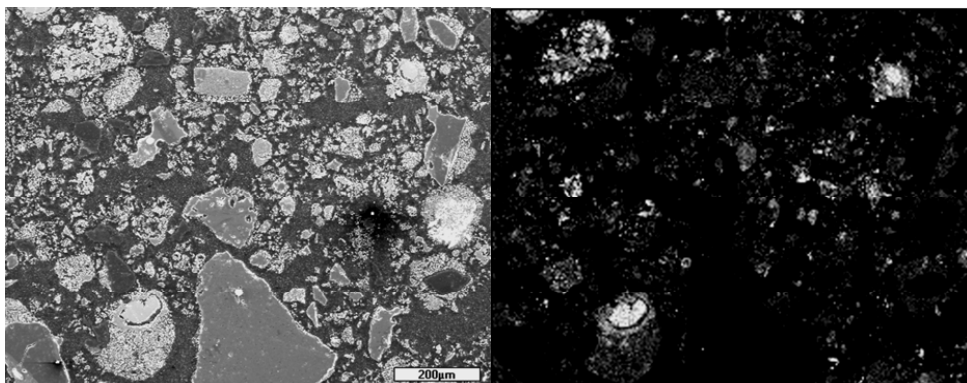


Figure 27. SEM micrograph (left) and Fe mapping (right) of CBP sample heated to 950°C

Next, in Rxn #10, Fe_3C could reduce some FeO in the sample producing metallic Fe and CO gas between 900-1000°C, which is confirmed by the disappearance of Fe_3C in the XRD pattern at 950°C and increased CO gas generation during this temperature range.

Above 950°C, carbon gasification can occur spontaneously by Rxn #11 confirmed by a sizeable increase in CO gas generation and an endothermic peak on the DDTA curve at 1040°C. Consequently, iron oxide reduction occurs by Rxn #12 beginning at 1080°C and nearly complete at 1200°C as seen in Figure 28 and XRD results from 1200°C.

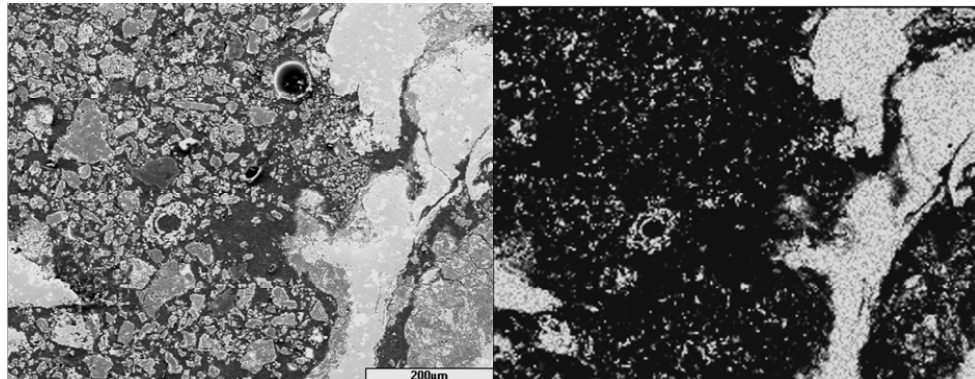


Figure 28. SEM micrograph (left) and Fe mapping (right) of CBP sample heated to 1200°C

3.2.2 LOW TEMPERATURE SELF-REDUCTION STUDY OF $\text{Ca}(\text{OH})_2\text{-C-Fe}_2\text{O}_3$ system (Papers 4 & 5)

The objective of these studies was to clarify the mechanisms of reaction in the $\text{Ca}(\text{OH})_2\text{-C}$, $\text{Ca}(\text{OH})_2\text{-Fe}_2\text{O}_3$ and $\text{Ca}(\text{OH})_2\text{-C-Fe}_2\text{O}_3$ systems at temperatures below 800°C in inert atmosphere and ambient pressure. These systems have proven critical to the understanding of low temperature self-reduction in CBPs. The chemical reactions of most importance to this study are listed below:



MECHANISTIC STUDY OF Ca(OH)₂ DEHYDRATION IN THE PRESENCE OF GRAPHITE OR HEMATITE (Paper 4)

As a pre-study to the ternary system, the binary systems of Ca(OH)₂-C and Ca(OH)₂-Fe₂O₃ have been investigated at low temperatures to shed light on the mechanisms of carbon gasification and calcium ferrite formation. Two types of tests were performed on reagent grade samples with compositions shown in Table 19. First, dynamic TG/DTA tests were conducted on samples heated from 20°C to 600°C at different heating rates in argon. Second, to investigate phase changes in the samples, different TG tests with larger sample sizes were conducted on selected samples.

Table 19. Mix compositions in wt%

Sample	Ca(OH) ₂	C	Fe ₂ O ₃
1	100	-	-
2	60.7	39.3	-
3	58.2	-	41.8

The TG results of samples 1-3 are given in Figure 29. Samples 1 and 3 have wt. losses that are comparable to but slightly less than the specific theoretical wt. loss of Ca(OH)₂ dehydration (dashed horizontal line in figures) for each sample composition. The reason for this is minor carbonate contamination of the reagent hydroxide (confirmed by XRD) which is practically unavoidable. Conversely, the wt. loss in sample 2 is more than that which can be attributed to hydroxide dehydration. This leads to a conclusion that in sample 2, dehydration isn't the only chemical reaction occurring between 300 and 600°C.

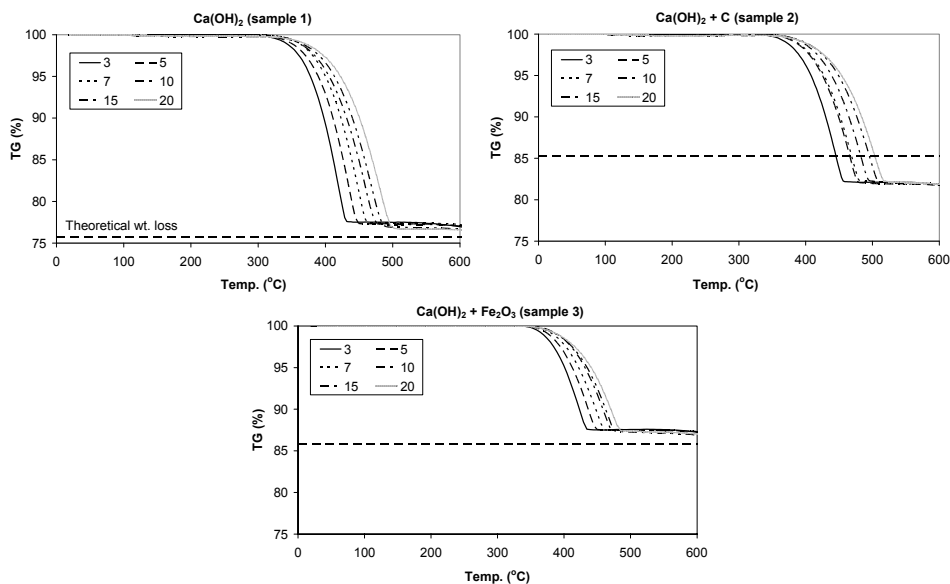


Figure 29. TG results of samples 1-3 at different heating rates ($\beta = 3, 5, 7, 10, 15, 20^{\circ}\text{C}/\text{min}$)

From XRD analysis the phases identified in sample 2 after heat treatment were, in order of decreasing intensity; CaO, C and CaCO₃. In sample 3 the identified phases were, in order of decreasing intensity; Fe₂O₃, CaO, CaCO₃ and Ca₂Fe₂O₅. Full width half magnitude (FWHM) measurements were used for qualitative crystallite parameter comparisons using the Scherrer equation.^[65]

$$L = \frac{K\lambda}{\beta \cos \theta_{hkl}} \quad (7)$$

where $K \approx 1$, $\lambda = 0.154$ nm for Cu $K\alpha$ radiation, β = FWHM, θ_{hkl} = the Bragg angle. Results are shown in Table 20.

Table 20. Comparison of calculated crystallite parameters based on FWHM results from XRD analysis. $\Delta(I/I_0)$ is the change in relative peak area intensities, ΔL_a and ΔL_c are the change in crystallite diameter and crystallite thickness consecutively, and ΔV is the change in crystallite volume. *(this value is the change in relative intensity of the (002) plane between two separate diffractograms, raw and 500°C, as only the (002) carbon peak could be evaluated)

Crystal plane	$^{\circ}2\theta$	FWHM smp 2		FWHM smp 3		$\Delta(I/I_0)$ %	Crystallite parameters (nm)		
		raw	500°C	raw	500°C		ΔL_a %	ΔL_c %	ΔV %
C (002)	26.47	0.305	0.316			8*	3	-3	1
CaO (200)	37.33		0.250		0.230	0	9		28
(222)	67.40		0.358		0.391	1	-8		-23
Fe ₂ O ₃ (012)	24.15			0.103	0.127	-1	-4	-19	-25
(113)	40.85			0.128	0.133	-9	-4	-19	-25

A comparison of the (002) graphite peak of sample 2 before and after heating shows an increase in FWHM and peak intensity after heat treatment to 500°C. An increase in FWHM commonly indicates a decrease in particle size and crystallinity but this would also correspond with a decrease in peak intensity, which is not the case here. Conversely, crystallite parameter calculations suggest that the average crystallite volume increases slightly or not at all. Using an interpretation of the mechanism suggested by Kercher and Nagle^[66], steam generated from Ca(OH)₂ decomposition could facilitate the conversion of disordered carbon content along the L_c dimension into ordered graphene along the L_a dimension resulting in micropore/microcrack formation in the graphite solid but resulting in little or no bulk crystallite volume change.

Measurements of the CaO peaks for samples 2 and 3 after heat treatment to 500°C show that the (200) peak exhibits less broadening while the (222) peak more broadening for sample 3 when compared to sample 2. The relative intensities of CaO peaks exhibit little or no change but changes in crystallite diameter point to an anisotropic grain growth of the (200) crystal plane in lieu of the (222) plane. Evidence of calcium ferrite peaks along with decreased crystallite size of Fe₂O₃ can lead to an assumption that a small amount of newly formed calcium ferrite dissolves in CaO preferentially parallel to the (200) plane. This can be possible in reference to Bergman^[67], that local equilibrium is established at the phase interfaces and the extent of solid solution is governed by the local oxygen potential.

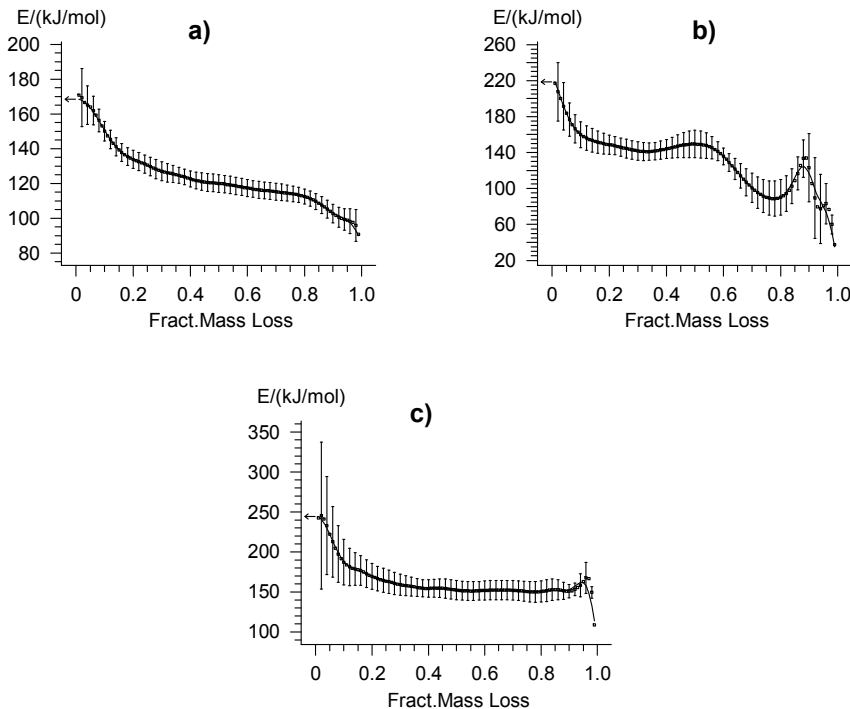


Figure 30. Estimation of E_a using Friedman analysis of **a)** sample 1 ($\text{Ca}(\text{OH})_2$) **b)** sample 2 ($\text{Ca}(\text{OH})_2+\text{C}$) **c)** sample 3 ($\text{Ca}(\text{OH})_2+\text{Fe}_2\text{O}_3$) from 6 experiments with each sample at $\beta = 3, 5, 7, 10, 15, 20^\circ\text{C}/\text{min}$.

Diagrams illustrating the model-free Friedman analysis of the TG results from samples 1-3 is given in Figure 30. Samples 1 and 3 exhibit roughly the same activation energy dependence, while sample 2 shows a divergence from this behavior at conversions of $0.5 < \alpha < 0.9$, where the activation energy sharply decreases and then increases again to a level of $\sim 120 \text{ kJ/mol}$. All three samples do show some dependence of the activation energy on conversion and this behavior is often a sign that the overall transformation contains multiple steps.^[55]

A comparison of master curves for the experimental results to theoretical kinetic models is shown in Figure 31. All samples show a trend between the F1 and F2 kinetic models at conversions of $\alpha \leq 0.5$. This behavior implies that the initial reaction mechanism occurring in all three samples is governed by $\text{Ca}(\text{OH})_2$ regardless of content. At higher degrees of conversion, sample 1 seems to follow a trend between the R2 and A2 curves. Sample 2 shows general agreement with the R2 curve at $0.5 < \alpha \leq 0.65$ and then jumps to a level between the A2 and A3 curves at greater conversion levels. Sample 3 shows a trend that follows the R2 curve at $\alpha > 0.5$ which is similar to that observed with sample 1 but with less affinity to the nucleation/growth models.

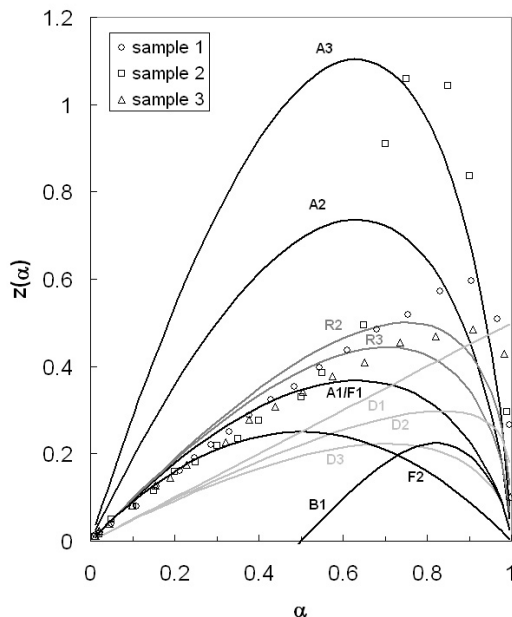


Figure 31. $Z(\alpha)$ master curves for theoretical kinetic models and experimental data

With knowledge gained from Friedman and master plot analysis, the decision was made to investigate a configuration of multiple reactions in the non-linear regression analysis. Results from the regression analysis of TG experiments for samples 1-3 are shown in Table 21.

The model for sample 1, $\text{Ca}(\text{OH})_2$ alone, can be interpreted as a mechanism beginning with slow product nuclei formation at $\alpha < 0.2$ that, at higher conversion ($\alpha < 0.7$), accelerates to form a dense reaction layer varying in thickness relative to the ease of H_2O escape.^[68] Evidence of this behavior was observed in SEM analysis of samples, see Figure 32. Here we see some crack formation on the surface of a dense reaction layer most likely due to gas pressure accumulation from inside the bulk reactant. The appearance of a dense surface reaction layer is prevalent at this point in the dehydration and the occurrence of crack formation seems to be dependent on individual particle size, i.e. larger particles show more crack formation.

Table 21. Selected results of regression kinetic analysis for samples 1-3

Model	order/dimension, <i>n</i>	Multivariate Non-Linear Regression results		
		<i>w</i> ^a	<i>E_a</i> (kJ/mol)	$\log A$ (s ⁻¹)
<i>Sample 1, Ca(OH)₂</i>				
1) Fn	1.44	0.17	174.23 ± 18.33	11.61 ± 1.62
2) Fn	0.45	0.50	123.52 ± 6.74	6.88 ± 0.56
3) R2	2		106.95 ± 21.01	5.26 ± 1.58
<i>Sample 2, Ca(OH)₂+C</i>				
1) F2	2	0.11	213.87 ± 41.77	14.51 ± 3.46
2) R2	2	0.67	142.67 ± 7.76	7.57 ± 0.72
3) A3	3		137.36 ± 10.97	7.37 ± 0.77
<i>Sample 3, Ca(OH)₂+Fe₂O₃</i>				
1) F2	2	0.17	260.43 ± 20.16	18.49 ± 1.60
2) R2	2		155.05 ± 1.53	8.69 ± 0.12

^a Parameter *w* is a weighting factor used in multiple reaction models

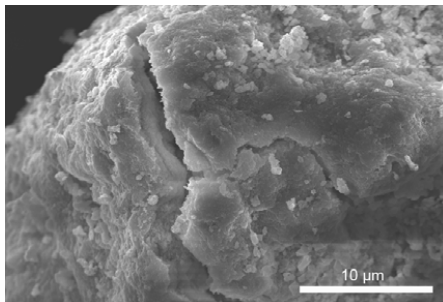


Figure 32. SEM micrograph of $\text{Ca}(\text{OH})_2$ sample after heat treatment to 380°C

The agreement with the R2 model at $\alpha > 0.7$ can be attributed to a reaction mechanism where advancement of the reaction interface is related to the layered crystal structure of $\text{Ca}(\text{OH})_2$, i.e. if product nucleation occurs at the more-reactive edge surfaces of a plate-like crystal then the reaction layer would progress inwards two-dimensionally.^[69] Although another possible explanation to this type of physico-geometric behavior was observed by Barret,^[70] i.e. the characteristics of the phase-boundary reaction depends on the shape of the crucible and the arrangement of powder used in experiments. Kinetic parameters arrived at here have precedence in the literature, where the predominant activation energies reported and the relevance of a kinetic model with multiple consecutive steps are in agreement with previously reported results.^{[55], [68], [71], [72]}

In comparison to sample 1, the n th order model in sample 2 only dominates in the first step of the transformation. With the addition of graphite in sample 2, water vapor can act as an intermediate at two separate reaction interfaces,^{[71], [73]} i.e. $\text{CaO}/\text{H}_2\text{O}_{(\text{g})}$ and $\text{H}_2\text{O}_{(\text{g})}/\text{C}$. This behavior can result in a more heterogeneous water vapor distribution in the sample after initial surface dehydration and nuclei formation thereby making the R2 model, in place of Fn, more appropriate as the next step in the transformation. Furthermore, the model for sample 2 includes a nucleation and growth step not present in the analysis of sample 1. If we consider the reversible carbon gasification/deposition Rxn (2) listed earlier, it is possible that the nucleation and subsequent ingestion or gasification of solid carbon at the $\text{H}_2\text{O}_{(\text{g})}/\text{C}$ interface is the mechanism implied by the A3 step. Again, evidence of this behavior was observed in Figure 33 where in the void between a particle of “ $\text{Ca}(\text{OH})_2/\text{CaO}$ ” and a graphite particle there is a formation of solid carbon having noticeable drop-like surface formations. These “drops” are quite possibly condensate carbon from gas phase.

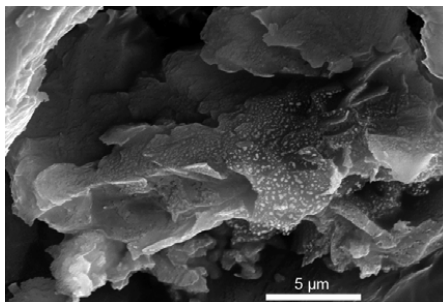


Figure 33. SEM micrograph of $\text{Ca}(\text{OH})_2 + \text{C}$ sample after heat treatment to 460°C

The mass loss behavior of sample 3 is quite similar to dehydration of pure $\text{Ca}(\text{OH})_2$ in sample 1. Although, like sample 2, the model which best fits sample 3 implies a more heterogeneous-type mechanism, i.e. adherence to the phase boundary model over a larger range of α . This can likely be

due to the formation of some intermediate amorphous $\text{CaO}\cdot\text{H}_2\text{O}\cdot\text{Fe}_2\text{O}_3$ phase at contact points of particle surfaces during the progression of the dehydration reaction interface. A consequence of this intermediate could be that subsequent calcium ferrite formation would be anion-modified and therefore more catalytically active^[74] and would more readily adsorb water molecules. Figure 34 shows a particle of crystalline CaO containing areas enriched with iron, circled in white, which could be the beginnings of calcium ferrite formation at the edges.

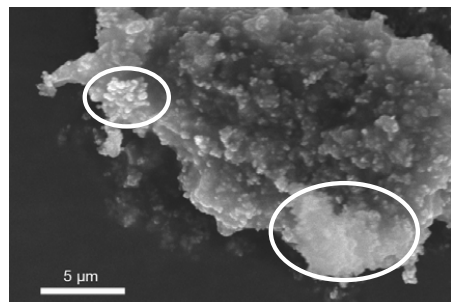


Figure 34. SEM micrograph of $\text{Ca}(\text{OH})_2 + \text{Fe}_2\text{O}_3$ sample after heat treatment to 600°C

OPTIMIZATION IN THE $\text{Ca}(\text{OH})_2\text{-C-Fe}_2\text{O}_3$ SYSTEM (Paper 5)

Two types of tests were performed on the samples. First, in order to find an optimal composition, dynamic TG/DTA tests were conducted on samples shown in Table 22 heated from 20°C to 800°C in helium. Second, to investigate the influence of heating rate and particle size on the optimal mix, thermokinetic TG/DTA tests were conducted on samples of mix 5 with two different particle sizes of hematite; one with an average particle size of ~ 300 nm (micro) and the other ~ 30 nm (nano).

Table 22. Mix compositions in wt%

Mix #	micro Fe_2O_3	$\text{Ca}(\text{OH})_2$	C
1	50	30	20
2	55	25	20
3	57.5	30	12.5
4	60	20	20
5	62.5	25	12.5
6	65	30	5
7	67.5	20	12.5
8	70	25	5
9	75	20	5

The TG/QMS curves for mix 5 are shown in Figure 35 as an example of the results acquired for all mixes. Weight loss and maximum gas intensity data in the temperature range $500\text{-}800^\circ\text{C}$ has been used to calculate apparent reduction degree, H_2O utilization degree (participation in carbon gasification) after dehydration of $\text{Ca}(\text{OH})_2$ content, and CO utilization degree in reduction reactions. Results are given in Table 23.

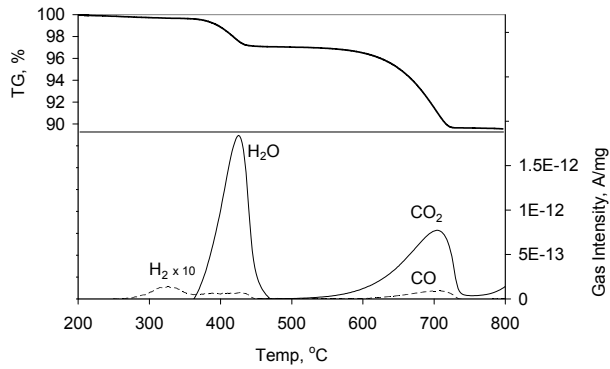


Figure 35. TG/QMS curves from mix 5

From Table 23, mix 1 and mix 5 are the only mixes which have better than average values for all responses. Preliminary analysis of the optimization experiments shows that Ca(OH)₂ content in mixes 1-9 has the best correlation with the responses given in Table 23. Furthermore, the relationship between C and Ca(OH)₂ contents for each mix has the best correlation with CO utilization, which is the most empirical of responses. With this in mind, a C:H₂O_(hydrate) molar ratio between 2 and 3 and a C:O_(iron oxide) molar ratio greater than 0.85, as in mix 1 and 5, seems optimal in the context of this study.

Table 23. Optimization responses

Mix #	Red. degree %	H ₂ O utilization %	CO utilization %
1	35.24	53.69	86.82
2	24.76	34.84	87.33
3	32.58	47.07	86.82
4	22.95	58.94	87.01
5	25.18	51.11	86.99
6	31.20	60.85	85.40
7	11.23	33.35	86.08
8	20.87	52.18	86.75
9	15.66	49.67	86.56
avg	24.41	49.08	86.64

XRD results from heat treated samples of mix 1 and mix 5 are quite similar except for the relative absence of remnant CaO and Fe₂O₃ in mix 5 when compared to mix 1 at 800°C. Consequently, it seems that the composition of mix 5 is more favorable for Fe₂O₃ reduction and formation of calcium ferrite than mix 1. Therefore, mix 5 was chosen as the composition to use in further studies because of its optimal combination of reduction and bonding, i.e. calcium ferrite formation, characteristics.

TG and DTA results for micro briquettes of mix 5 using micro and nano sized hematite are shown in Figure 36 as samples 1 (micro) and 2 (nano). TG results reveal obvious differences between the two samples. First, there is a difference in total weight loss between sample 1, ~10 wt%, and sample 2, ~8 wt%. Second, the fraction of total weight loss for the two separate TG steps (see Table 24) in each sample differs, i.e. sample 1 (step 1 ≈ 0.30, step 2 ≈ 0.70) and sample 2 (step 1 ≈ 0.75, step 2 ≈ 0.25). Furthermore, calculated H₂O utilization from step 1 of samples 1 and 2, 51% and 6% respectively, have a marked negative effect on the reduction degree from step 2 of sample 2, 7.5%, when compared to sample 1, 25%.

Table 24. Temp. interval definitions for each TG step in both samples 1 & 2

β (°C/min)	temperature intervals (°C)	
	step 1	step 2
2	320-430	450-680
10	340-470	500-740
32	370-510	540-800

DTA results support TG results where the heat flow in step 1 is roughly 2 times greater in sample 2 than that in sample 1, and during step 2 the heat flow is roughly 3.5 times greater in sample 1 than that in sample 2. Interestingly, a difference does occur between heating rates where both samples exhibit exothermic heat flow between 500 and 600°C when heated at 32°C/min but not observed at the lower heating rates. Reduction of Fe_2O_3 by CO in Rxn (5) is exothermic as well as carbon deposition by the reverse of Rxn's (2) or (4).

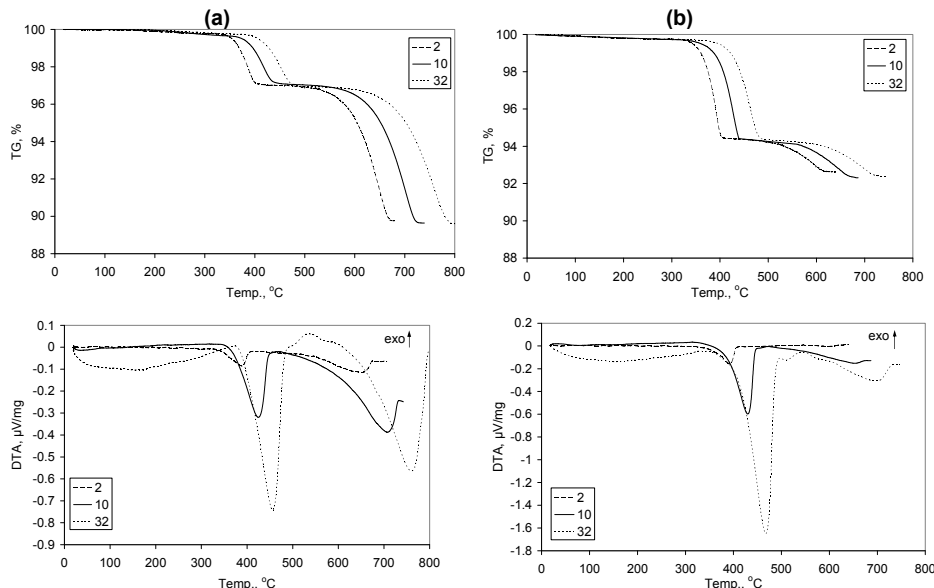


Figure 36. TG/DTA results from (a) sample 1 (w/ micro Fe_2O_3) and (b) sample 2 (w/ nano Fe_2O_3)

Diagrams illustrating the model-free Friedman analysis of the TG results from samples 1 & 2 are shown in Figure 37 and Figure 38.

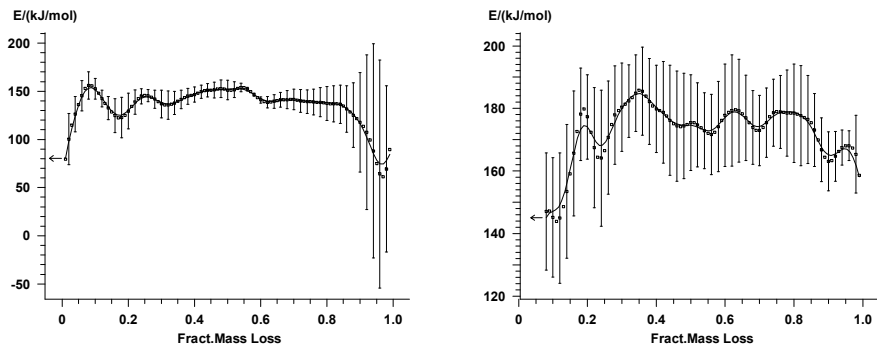


Figure 37 Friedman analysis of sample 1, left TG step 1, right TG step 2

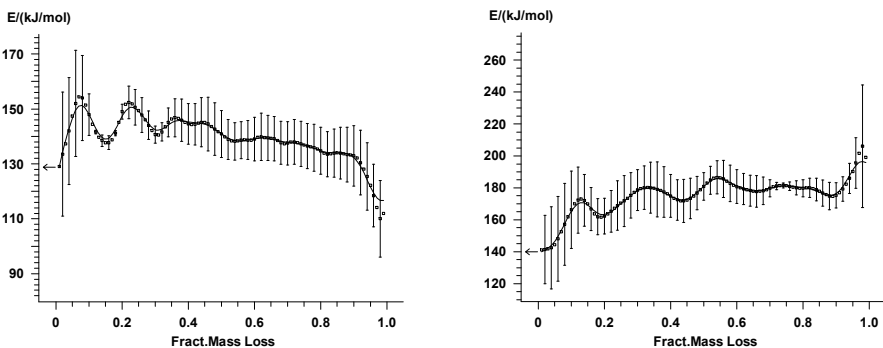


Figure 38. Friedman analysis of sample 2, left TG step 1, right TG step 2

In both samples, the activation energy dependence in TG step 1 is similar but at higher conversion than $\alpha = 0.5$ the activation energy seems to gradually increase with conversion for sample 1 while it gradually decreases in sample 2. Again in TG step 2, activation energy dependence is similar for both samples but at $\alpha > 0.8$ the activation energy for sample 1 decreases with conversion while that in sample 2 increases.

A comparison of master curves for the experimental results to theoretical kinetic models is shown in Figure 39 and Figure 40. The experimental results for step 1 in sample 1 seem to obey a trend between A1/F1 and A2/Fn ($n < 1$) kinetic models at conversions of $\alpha \leq 0.2$ with results from 2°C/min having a larger dimension/smaller order than results from 10 and 32°C/min. This behavior implies that the initial reaction mechanism is somewhat heating rate dependent. At higher degrees of conversion, $0.2 < \alpha \leq 0.8$, experimental results seem to follow a trend similar to that of the R2 kinetic model, and then follow the sharp negative slope of an An kinetic model near the end of conversion. Step 2, shows general agreement with the An/Fn curves at $\alpha \leq 0.3$ and then follows the R2 curve at greater conversion levels.

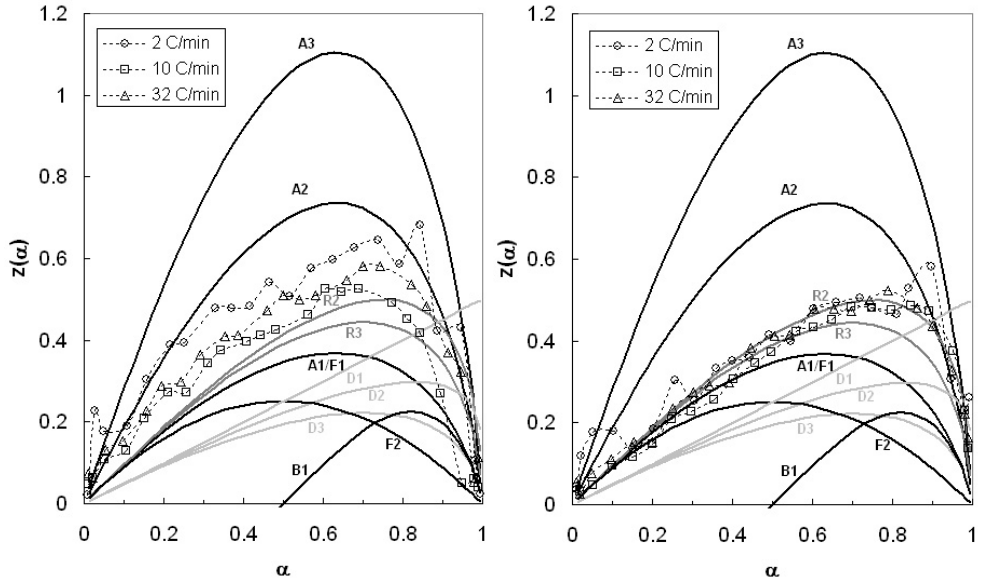


Figure 39. $Z(\alpha)$ diagrams for TG steps (1) and (2) in sample 1

Master curve results for step 1 in sample 2 also seem to obey a kinetic model between A1/F1 and A2/Fn throughout the entire conversion but at $0.6 \leq \alpha \leq 0.9$ results for 2°C/min deviate to a larger dimension/smaller order than do results from 10 and 32°C/min. Step 2 shows how experimental results are scattered but generally follow a trend comparable to An/Fn behavior at $\alpha \leq 0.4$ and then converge to a trend similar to R3 behavior at greater conversion levels. Although, results from 2 and 10°C/min do show some adherence to D1 behavior at $0.5 \leq \alpha \leq 0.8$.

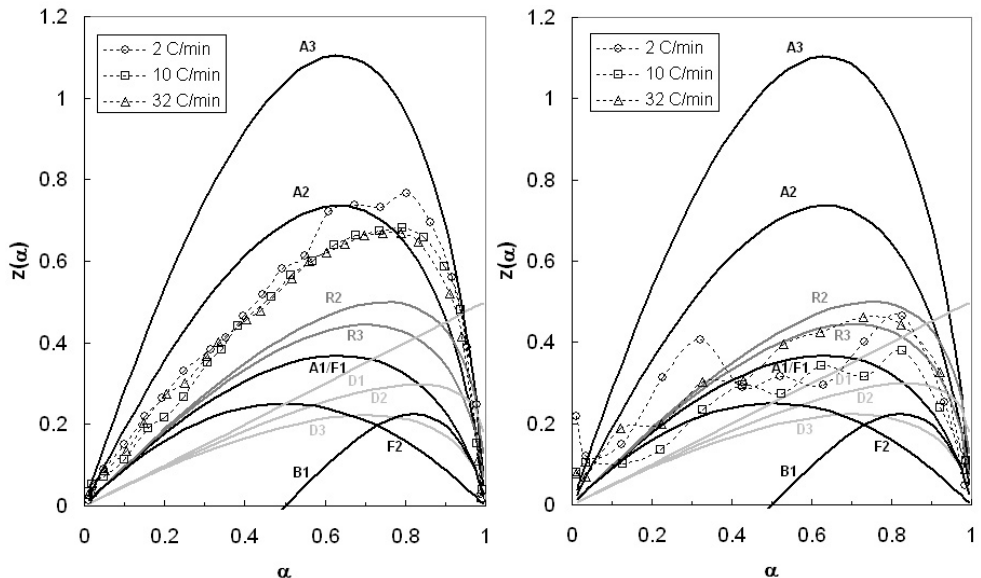


Figure 40. $Z(\alpha)$ diagrams for TG steps (1) and (2) in sample 2

With knowledge gained from Friedman and master plot analysis, the decision was made to investigate a configuration of multiple reactions in the non-linear regression analysis. Results from the regression analysis of TG experiments for samples 1 & 2 are shown in Table 25.

Table 25. Results of regression kinetic analysis for samples 1 & 2

Model	Multivariate Non-Linear Regression results				R^2
	order/dimension, n	w^a	E_a (kJ/mol)	$\log A$ (s^{-1})	
<i>Sample 1, micro hematite</i>					
TG step 1	1) Fn	0.75	0.19	179.41 ± 3.99	11.84 ± 0.38
	2) R2	2	0.74	148.63 ± 1.1	8.69 ± 0.08
	3) Fn	0.79		126.05 ± 14.35	6.68 ± 0.65
TG step 2	1) An	0.69	0.24	191.94 ± 5.51	8.36 ± 0.59
	2) R2	2		178.79 ± 2.44	6.83 ± 0.10
<i>Sample 2, nano hematite</i>					
TG step 1	1) Fn	0.54	0.37	153.83 ± 2.81	9.57 ± 0.29
	2) An	1.46	0.29	140.32 ± 10.52	8.70 ± 0.80
	3) An	2.12		139.97 ± 6.85	8.47 ± 0.47
TG step 2	1) Fn	1.32	0.32	152.98 ± 3.92	6.96 ± 0.23
	2) R3	3		188.42 ± 2.84	7.97 ± 0.17

^a Parameter w is a weighting factor used in multiple reaction models

In sample 1 the initial fractional-order (Fn) model in TG step 1 is similar to the earlier binary system evaluation with a mechanism beginning with CaO product nuclei formation. But here, the tightly packed micro briquette structure somewhat impedes nuclei formation by the reverse process of rehydration indicated by an order less than 1. The agreement with the R2 model at $0.2 < \alpha < 0.95$ is similar to the behavior in the $\text{Ca}(\text{OH})_2\text{-Fe}_2\text{O}_3$ binary system and can be due to the formation of some intermediate amorphous $\text{CaO}\text{-H}_2\text{O}\text{-Fe}_2\text{O}_3$ phase at contact points of particle surfaces during the progression of the dehydration reaction interface. In the final stage of TG step 1, Fn model behavior can be interpreted as the formation of $\text{CO}_{(g)}$ from graphite gasification. Here the activation energy is low knowing that activation energies for the steam-carbon reaction are usually of the magnitude 150 kJ/mol at atmospheric pressure but the magnitude of this transformation is highly dependent on the local steam partial pressure, temperature and CO/CO_2 ratio.^[75]

The initial model stage of TG step 2 is rationally tied to the end of TG step 1. Here, the An behavior ($\alpha < 0.25$) can be interpreted as the random growth of the $\text{CO}_{2(g)}/\text{Fe}_3\text{O}_4(s)$ interface where CO_2 is a product from hematite reduction by CO. Following the interface growth, the reduction of hematite apparently proceeds via phase boundary mechanism, R2. El-Geassy's work^[76] also concludes a mixed reaction mechanism such as this for the reduction of hematite. The apparent activation energy from the model, ~180 kJ/mol, lies in between energy values for gaseous reduction of iron oxide, 36-71 kJ/mol,^{[77]-[79]} and the intrinsic energy for the Boudouard reaction of approximately 400 kJ/mol.^[80] This behavior, i.e. the reaction between solid carbon and iron oxide occurring as the combination of carbon gasification and carbothermic reduction, is generally accepted in the literature.^[81]

In sample 2 the initial fractional-order (Fn) model in TG step 1 is similar to that in sample 1 but the order of reaction is lower. This is most likely due to the smaller particle size in sample 2 causing a decrease in total porosity and consequently making gas diffusion more difficult increasing the reversibility of the dehydration reaction. In contrast to the behavior in sample 1, sample 2 follows a An model behavior at $0.4 < \alpha$ rather than phase boundary behavior. In reference to TG results in Figure 36, it is evident that the maximum rate of weight loss in step 1 for sample 2 is faster than that in sample 1. An explanation can possibly be that instead of a slow advancement of the reaction interface seen in sample 1, crack development in sample 2 from excessive gas pressure results in more rapid and extensive dehydration with subsequent recrystallization of the CaO product. The final stage of TG step 1 in sample 2 follows A2 model behavior and can be interpreted as the growth of the $\text{CO}_{(g)}/\text{C}_{(s)}$ interface during graphite gasification. Here, the gasification reaction seems to be starved

due to low steam pressure, the small amounts of $\text{CO}_{(\text{g})}$ that are produced might likely remain adsorbed to solid graphite surfaces.^[82]

In TG step 2 the transition seems to follow Fn behavior ($\alpha < 0.35$) and can be interpreted as the direct reaction between a ionically-active $\text{C}_{(\text{s})}$ and $\text{Fe}_2\text{O}_3_{(\text{s})}$. Those surfaces which are in close contact with iron oxide can initiate direct reduction, which might be diffusion controlled at lower heating rates as seen by the apparent correlation to D1 behavior, master curve results in Figure 40(2), at 2 & 10°C/min. Following initial direct reduction, the reduction of hematite apparently proceeds via phase boundary mechanism, R3. The shrinking core model is more preferable in sample 2 than in sample 1. This is likely due to the much smaller hematite particle size in sample 2 as well as the larger apparent activation energy, ~190 kJ/mol, signifying more control applied by the Boudouard reaction, Rxn (4).

Results from SEM analysis support proposed reaction mechanisms discussed earlier. The left side of Figure 41 illustrates the morphology of sample 1 after heat treatment. Here, the CaO particles are intact and porous indicating that little structural change has occurred in the grain after dehydration. In sample 2, to the left, CaO grains are less porous and in some cases partial disintegration has occurred. Furthermore, crack formation, seen in Figure 41(right), occurs in sample 2 and was more prevalent at high heating rates. From EDS results, iron oxide particles in sample 1 have an average iron content lying between magnetite and wustite with a reduction degree that slightly increased with increasing heating rate. In contrast to sample 1, iron oxide reduction throughout the entire briquette was not seen in sample 2, but in specific areas with a high local concentration of graphite in contact with iron oxide. In these areas of intimate contact between graphite and iron oxide, reduction degree was in between wustite and reduced iron.

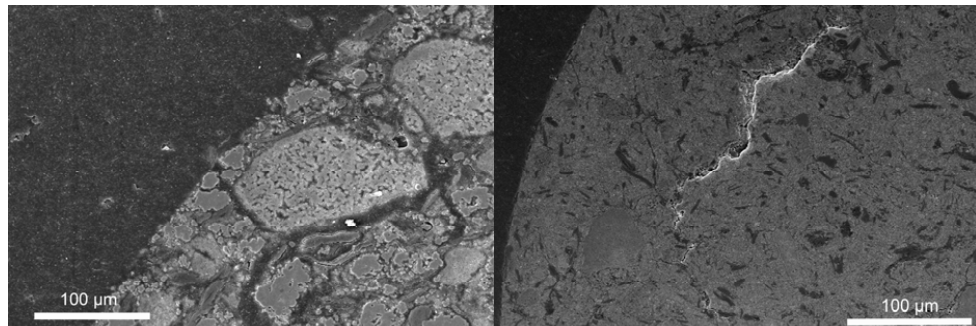


Figure 41. Comparison of the periphery of micro briquettes of sample 1 (left) and sample 2 (right) after heating to 800°C

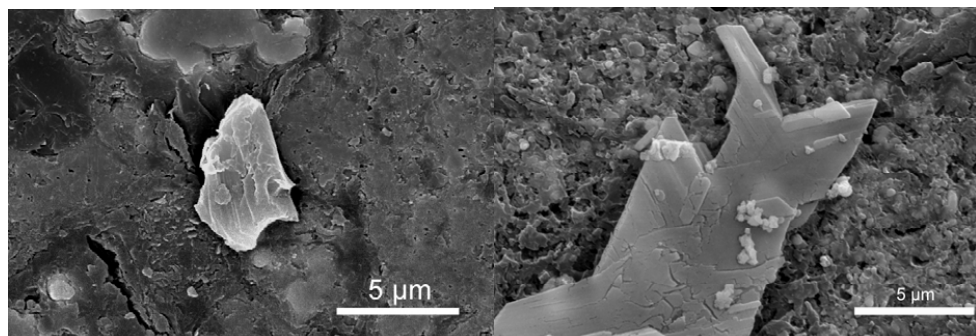


Figure 42. Comparison of the center of micro briquettes of sample 1 (left) and sample 2 (right) after heating to 800°C

Shown on the left side of Figure 42, a particle of calcium rich calcium ferrite located in the center of a micro briquette of sample 1 seemingly has started to crystallize and become more angular in shape. Where, on the right side of Figure 42, we observed a highly crystallized grain of $\text{Ca}_2\text{Fe}_2\text{O}_5$ in the center of a sample 2. The smaller particle size and consequently tighter particle packing in sample 2 compared to sample 1 possibly allows better thermal conductivity to the center of sample 2 resulting in more developed crystals of calcium ferrite.

COMPARISON OF CBP AND $\text{Ca}(\text{OH})_2$ -C- Fe_2O_3 SYSTEM

An attempt to compare the experimental behavior in CBP blend B4, from section 3.2.1, to the model for sample 1 (micro hematite) is shown in Figure 43. TG step 1, as described earlier, assumes the reactions, $\text{Ca}(\text{OH})_2$ dehydration and carbon gasification. The model has a good correlation with normalized DTG results of pellet B4 in the early stages of dehydration beginning at 340°C but seems to slightly underestimate the rate of dehydration at higher temperatures. Reasons for this could be that dehydration is more instantaneous in the loose powder of sample B4 with less obstruction for diffusion than the micro briquette the model is based on. Furthermore, it is possible that hydrates other than $\text{Ca}(\text{OH})_2$ add to the complexity of dehydration in this temperature range. The modelled apparent carbon gasification at the end of TG step 1 agrees with results from pellet B4 supporting the reaction scheme put forth in Table 18 where carbon gasification occurs in the temperature range 450-500°C.

In TG step 2 the model assumes iron reduction through carbon gasification. At temperatures between 500 and 600°C the model overestimates the reaction rate in the by-product pellet mix. This might be because the model is based on a system starting from hematite but the iron oxide composition in by-products is more reduced to begin with. Therefore, it's possible the prevailing reduction potential within the by-product sample is insufficient for further reduction via carbon gasification until temperatures reach ~600°C. At higher temperatures, the rate in B4 deviates from the model likely due to the calcination of carbonate content which is not accounted for in the simple model system. Then, CO_2 generated from calcination likely enters into further carbon gasification and subsequent iron oxide reduction above 700°C. Furthermore, the difference in rate can be attributed to the likelihood of diverse carbon particle structure in B4 originating from coal and coke particles in BF flue dust whereas the model is based on a more ordered graphite structure.

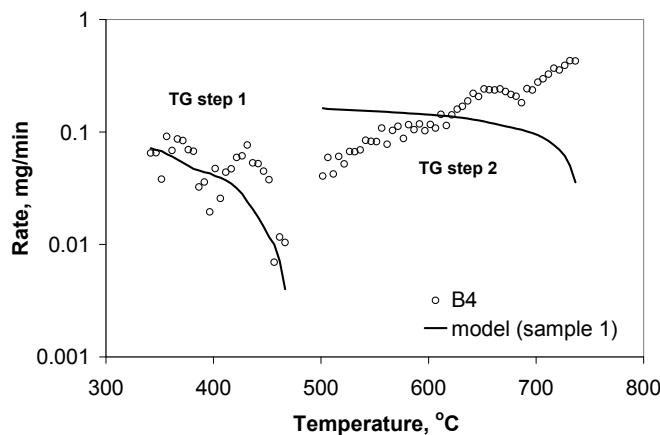


Figure 43. Rate comparison of experimental and modelled results from CBP blend B4

CHAPTER 4

CONCLUSIONS

The low and high temperature behavior of CBPs has been studied in lab scale experiments complimented with various material characterization techniques. Large scale testing of cold bonded by-product pellets in a commercial BOF and a pilot scale BF has also been completed. Lastly, the complex series of transformations occurring when CBPs are used as recycled iron charge in steelmaking processes was investigated on the basis of a simpler, model ternary system: $\text{Fe}_2\text{O}_3\text{-Ca(OH)}_2\text{-C}$.

The results show that it is possible to produce CBPs containing metallurgical by-products that meet high cold strength and capacity requirements. The cold strength of CBPs in this study is a factor of primarily, particle size distribution and hydration extent. Oily millscale sludge contains the largest fraction of oversized particles among raw materials in the pellet blend and therefore has the largest detrimental effect on cold strength and capacity. An optimal blend of BOF fine and coarse sludge in CBPs not only improves the particle size distribution in the pellet blend but also includes contents of CaO and/or Ca(OH)_2 improving bonding during hydration and curing and therefore has the largest beneficial effect on cold strength.

Self-reduction experiments based on TG/DTA/QMS testing of CBP samples show that hydrate and carbonate content in metallurgical by-products used in CBPs play a significant role in the reduction characteristics of contained iron oxides and the formation of bonding-type calcium ferrite phases. The formation of calcium ferrite phases begins below 600°C while the disintegration of said phases, according to literature, is believed to be caused by the reduction of hematite content in calcium ferrite to magnetite at temperatures greater than 800°C depending on the prevailing CO/ CO_2 ratio.

The complex series of transformations occurring when CBPs are recycled in iron and steelmaking processes have been investigated on the basis of the simpler $\text{Fe}_2\text{O}_3\text{-Ca(OH)}_2\text{-C}$ system heated from 20-800°C in inert atmosphere. The transformation starts with calcium hydroxide dehydration, whose first step, CaO nucleation, is partially impeded by the slow escape of H_2O imposed by the tight structure of the briquette depending on the hematite grain size. Dehydration proceeds by the inward 2D growth of the CaO grains when micro-sized grains of hematite are present. In briquettes with nano-sized hematite grains, large cracks develop, which is favored by high heating rates, and dehydration becomes rapid and more extensive. Evolved steam, depending on local partial pressure, in turn begins to gasify carbon grains, producing CO and H_2 . Then the reduction of hematite takes place by these gases, also via a 2D phase boundary mechanism, down to a reduction degree situated between magnetite and wustite. Parallel to the iron oxide reduction, a calcium ferrite phase appears, in the form of angular and calcium-rich particles. In the case of deficient carbon gasification by steam due to low partial pressures, nano-sized hematite is locally reduced at contact points with graphite particles resulting in a small amount of iron oxide grains reaching the reduction degree of wustite.

An optimal composition of the ternary mix, i.e. 62.5% Fe_2O_3 , 25% Ca(OH)_2 , 12.5% C , was determined, from TG tests and XRD analysis, as the most suitable for the concurrent optimization of both the reduction degree and formation of the bonding phase, calcium ferrite. In general, Ca(OH)_2 content in the system $\text{Fe}_2\text{O}_3\text{-Ca(OH)}_2\text{-C}$ has the best correlation with the reduction degree, H_2O utilization and CO utilization at low temperatures. With this in mind, a $\text{C:H}_2\text{O}_{(\text{hydrate})}$ molar ratio between 2 and 3 and a $\text{C:O}_{(\text{iron oxide})}$ molar ratio greater than 0.85, is optimal in the context of this

study. Furthermore, excess milling of by-products is discouraged due to the greatly adverse effects on reduction degree. The first step in the proposed kinetic model describing dehydration and carbon gasification in inert atmosphere has good correlation with behavior in CBPs during self-reduction testing. In contrast, the model fit to CBP behavior in the second step is unsatisfactory most likely due to variable oxidation state of iron oxides in raw CBP samples as well as carbonate content. These factors were not considered in the evaluated model system $\text{Fe}_2\text{O}_3\text{-Ca(OH)}_2\text{-C}$.

Full scale testing of cold bonded pellet charge in the BOF has proven to be feasible at levels up to 2.2% of total charge weight. At these levels, cold bonded pellet addition resulted in no adverse disturbances to steel and slag chemistry and to the BOF process in general. Charging CBPs at higher levels will most likely increase sulphur levels in the BOF if Portland cement is used as binder. Although changes in slag volume were not monitored during tests included in this work an increase is expected with CBP additions. But, increasing slag volume can be tempered by including carbon content in CBPs to ensure that all iron units report to the steel bath and not to the slag.

Pilot scale testing of CBPs in the EBF show that it is possible to charge quite high amounts of cold bonded agglomerates to a BF and the upper limit is dependent on chemical and/or metallurgical properties of the material. The metallurgical properties, i.e. the reduction and softening and melting behavior, of the cold bonded material become important when the charged amount is beyond 10% of the ferrous burden.

CHAPTER 5

FUTURE WORK

On bench scale, the present work concentrates primarily on the self-reduction characteristics of CBPs when heated in inert gaseous environment. Thus far, the reactions that have been proposed to occur during the heating of CBPs up to 800°C are based primarily on thermodynamic considerations coupled with results from TG/DTA/MS analysis and kinetic analysis of a simple ternary system.

It is more than likely that the mechanisms occurring in CBPs are far too complicated to completely fall within the small confines of this study. Factors such as the effect of other states of calcium and iron, i.e. CaCO₃, Fe₃O₄, FeO, Fe and other forms of carbon, such as coal and coke, need to be investigated to further understand the complex reaction occurring in CBPs between 600 and 800°C. Studies on the reactivity of reagent calcium ferrite phases would be prudent to investigate their stability at temperatures greater than 800°C and at different reduction potential.

Furthermore, it is important to investigate the kinetics of self-reduction on more CBP samples to develop a large data pool concerning the rates of by-product blends in varying temperature ranges to thereby compare simpler mineral system configurations for mechanism studies. More kinetic studies varying the type of binder and reductant in CBPs are of interest to help shed light on the mechanisms of high temperature disintegration attributed to CBPs. Finally, and most important for industrial consideration, studies of the reduction characteristics of CBPs when heated in reducing environments and when mixed with molten iron/steel are needed to better understand how these pellets can behave in the BF and the BOF. Hopefully, lab scale testing can be complimented with additional industrial scale testing to further increase the technological know-how concerning CBP use as feed material in metallurgical processes.

R e f e r e n c e s

- [1] A. Fleischanderl, J. Pesl and W. Gerbert: Aspect of Recycling of Steelworks By-Products Through the BOF, SEAISI Quarterly, April 1999, pp. 51-60.
- [2] R.L. Nyirenda: The Processing of Steelmaking Flue Dust: A Review, Conservation and Recycling, 1991, pp. 1003-1025.
- [3] J.M. McClelland, H. Tanaka, T. Sugiyama, T. Harada and H. Sugitatsu: FASTMET dust pellet reduction operation report on the first FASTMET waste recovery Plant, 2001 Ironmaking Conference Proceedings, pp. 629-640.
- [4] R.J. Fruehan, J.E. Astier and R. Steffen: Status of direct reduction and smelting in the year 2000, 4th ECIC, Paris 2000, ATS-PM, pp. 30-41.
- [5] J. Derycke and L. Bonte: Ironmaking perspectives for the early 21st century, 4th ECIC, Paris 2000, ATS-PM, pp. 693-702.
- [6] R. B. Smith et al.: The future for DR and SR: a European prospective, 4th ECIC, Paris 2000, ATS-PM, pp. 703-709.
- [7] E. Eichberger et al.: Modern hot metal production is given by COREX Technology, 4th ECIC, Paris 2000, ATS-PM, pp. 578-584.
- [8] J. Srb and Z. Ruzickova: Pelletization of fines, In Developments in Mineral Processing (advisory ed. D.W. Fuerstenau), Vol. 7, Elsevier Science Publishers B. V., Amsterdam, Netherlands, 1988.
- [9] M. Singh: Studies on the Cement-Bonded Briquettes of Iron and Steel Plant By-products as Burden Material for Blast Furnaces, Doctoral Thesis, Luleå University of Technology, 2002, pp. 23.
- [10] K.J.V. Svensson: Sätt vid kallhärdning av kuler, Swedish patent 226.608.
- [11] R. Linder and D. Thulin: Grangcold pelletizing of hematite iron ores, The Aus. IMM, Newcastle and district branch, Symposium on Pellets and Granules, Oct., 1974, pp. 193-206.
- [12] T. Inazumi, H. Furutaku, T. Kuwabara, K. Esaki, K. Nakayama, and S. Kohno: Recycling of LD converter sludge and iron-bearing fines using the NCP cold-bond pellet process, Conservation & recycling, Vol. 6, No. 4, 1983, pp. 167-179.
- [13] R. Takahasi, T. Akiyama and J. Yagi: Drying and reduction of cement-bonded pellets by using a moving bed reactor, Proc. 6th International Iron and Steel Congress, Vol. 1, ISIJ, Nagoya, 1990, pp. 108-115.
- [14] W. Pietsch: Agglomeration Processes – Phenomena, Technologies, Equipment, Wiley –VCH Verlag GmbH, Weinheim, 2002.
- [15] G. Berglund and L. E. Eriksson: Recycling of inplant fines at SSAB Tunnplat AB, Proceedings of MacMaster Symposium Iron and Steelmaking, Vol. 21, Pretreatment and Reclamation of Dusts, Sludges and Scales in Steel Plants, Hamilton, Canada, 1993, pp. 94-108.

- [16] F. Su, H.O. Lampinen and R. Robinson: Recycling of Sludge and Dust to the BOF Converter by Cold Bonded Pelletizing, ISIJ International, Vol. 44, No. 4, 2004, pp. 770-776.
- [17] S.R. Balajee, P.E. Callaway, L.M. Keilman and L.J. Lohman: Production and BOF recycling of waste oxide briquettes at Inland Steel, I&SM, August 1995, pp. 11-21.
- [18] F.M. Lea: The chemistry of cement and concrete. 3rd Edition, Edward Arnold (Publishers) Ltd., London, 1988, pp. 656-657.
- [19] D.R. Fosnacht: Recycling of ferrous steel plant fines, State-of-the-art. I&SM, April 1981, pp. 22-26.
- [20] D.R. Dinger and J.E. Funk: Particle Packing Part II – Review of Packing of Polydisperse Particle Systems, Interceram, 1992, 41 (2), p. 95-97, 41 (3), pp. 176-179.
- [21] P.G. Kihlstedt: Agglomeration of iron ore concentrates into cold-bound balls, Proc. 9th Int. Mineral Processing Cong., Prague, 1970, pp. 307-317.
- [22] F. Su: Optimering av restproduktblandningen för att uppnå maximal kapacitet och kvalitet vid tillverkning av kallbunden pellets, Proceedings of Minerateknik, Luleå, Sweden, Feb., 2001.
- [23] G. D'Alessio and W-K Lu: Cold Bond Agglomeration of Waste Oxides for Recycling, 55th Ironmaking Conf. Proc., Vol. 55, 1996, pp. 161-163.
- [24] M.C. Mantovani and Takano: The strength and high temperature behaviours of self-reducing pellets containing EAF dust, ISIJ Int., Vol 40, No. 3, 2000, pp. 224-230.
- [25] M.P. Landow, J.F. Torok, T.P. Barnett, J.F. Crum and J. Nelesen Jr.: An Overview of Steel Mill Waste Oxide Recycling by Cold Bonded Roll Briquetting, ICSTI, 1998, pp. 1237-1243.
- [26] F.W. Harrison et al.: Recycling Dusts and Sludges in the BOF, ISS 78th Steelmaking Conference, Nashville, TN, 1995, Iron and Steel Society Inc..
- [27] D.A. Dukelow et al.: Use of Waste Oxides in the Great Lakes BOP, ISS 78th Steelmaking Conference, Nashville, TN, 1995, Iron and Steel Society Inc..
- [28] R.J. Fruehan and C.L. Molloseau: Waste Oxide Recycling During Oxygen Steelmaking, I&SM, August, 2000, pp. 47-55.
- [29] H.W. Meyer et al.: Static and Dynamic Control of the Basic Oxygen Process, Journal of Metals, June 1964, pp. 501.
- [30] J.A Lopez C, R.V. Ballesteros B., J.M. Guipsot T., R. Ramirez: Development of B.F. flue dust briquette for recycling in BOF at AHMSA, ICSTI, 1998, pp. 1275-1279.
- [31] L. Nedár: Experimental and thermodynamic study of dust formation in BOF steelmaking, Licentiate Thesis, Luleå University of Technology, Trollhättan, 1997, pp. 9-10.
- [32] T. de Bruin and L. Sundqvist: Briquetting – one way of treating by-products at SSAB Tunaplåt in Luleå, ICSTI / Ironmaking Conf. Proc., 1998, pp. 1263-1273.

- [33] M. Kitamura, N. Konno, H. Shiota: The current situation of dust recycling of NSC's works, Proc. McMaster Symp. Iron and Steelmaking, Vol. 21, Hamilton, Canada, May 11-19, 1993, pp. 69-86.
- [34] K. Hattori, S. Ohba, M. Nose, A. Amano, S. Matsunaga: Development of cementless cold pellets, Proc. 6th Int. Symp. on Agglomeration, Nagoya, Japan, 1993, No. 15-17, pp. 215-219.
- [35] E.P. Quick: Blast furnace test with cement bonded pellets, Proc. of Symp. on Waste Oxide Recycling, McMaster Univ., Hamilton, Ontario, May 16-17, 1974, pp. 9/1-4.
- [36] M. P. Landow, M. Martinez, T. Barnett: The Recycling of Waste Oxides at Great Lakes Division, National Steel Corporation, Ironmaking Conference Proceedings, 1997, pp. 431-437.
- [37] R.T. Wargo, E.A. Bogdan, K.L. Myklebust, D.G. White: Evaluation of cold-bonded revert briquettes at the USS Gary No. 8 blast furnace, Ironmaking Conf. Proc., Washington D.C., 1991, Vol. 50, pp. 69-87.
- [38] L. Sundqvist, K.O. Jonsson, H.O. Lampinen, L.E. Eriksson: Recycling of in-plant fines as cold-bonded agglomerates, SSAB Tunnplat AB, technical report, 1999.
- [39] J. Szekely, J.W. Evans and H.Y. Sohn: Gas-solid reaction, New York, Academic Press, 1976, Chap. 4.
- [40] S. Prakash: Reduction and sintering of fluxed iron ore pellets-a comprehensive review, The Journal of The South African Institute of Mining and Metallurgy, January/February, 1996, pp. 3-16.
- [41] M.C. Mantovani and C. Takano: *ISIJ Int.*, Vol 40, No. 3, 2000, pp. 224-230.
- [42] H.Y. Sohn and E.M. Wadsworth: Rate Processes of Extractive Metallurgy, Plenum Press, New York, NY, 1979.
- [43] Y. Kashiwaya, M. Kanbe and K. Shii: *ISIJ Int.*, **41** (2001), pp. 818.
- [44] S. Mookherjee, H. S. Ray and A. Mukhrjee: Ironmaking and Steelmaking, 1986, 13, pp.229–235.
- [45] W.-K. Lu, C. Bryk and H. Gou: ‘Process Technology Proceedings’, Vol. 6 (Proc. 5th Int. Iron and Steel Congress, Book 3), Washington, DC, USA, April, 1986, 1065–1075; 1986, Warrendale, PA, ISS-AIME.
- [46] H. Gou, W.-K. Lu and C. Bryk: *ISIJ Int.*, 1992, 32, pp. 733–740.
- [47] K. Kumabe, H. Moritomi, R. Yoshiie, S.Kambara, K. Kuramoto, Y. Suzuki, H. Hatano, S.Y. Lin, and M.Harada: Gasification of Organic Waste with Subcritical Steam under the Presence of a Calcium-Based Carbon Dioxide Sorbent, *Ind. Eng. Chem. Res.* 2004, 43, pp. 6943-6947.
- [48] J. Wang and T. Takarada: Role of Calcium Hydroxide in Supercritical Water Gasification of Low-Rank Coal, *Energy & Fuels* 2001, 15, pp. 356-362.

- [49] T. Inui, T. Otowa, and F. Okazumi: Gasification of Active Carbon by Iron-Based Composite Catalysts for Obtaining Directly a Gas Optional H₂/CO Ratio, *Carbon*, Vol. 23, No.2, 1985, pp. 193-208.
- [50] S. Sato, S.Y. Lin, Y. Suzuki, and H. Hatano: Hydrogen production from heavy oil in the presence of calcium hydroxide, *Fuel* 82 (2003), pp. 561-567.
- [51] N.V.Y. Scarlett, M.I. Pownceby, I.C. Madsen and A.N. Christensen: Reaction Sequences in the Formation of Silico-Ferrites of Calcium and Aluminum in Iron Ore Sinter, *Met. And Mat. Tran. B*, Vol. 35B, October 2004, pp 929-936.
- [52] L.X. Yang and E. Matthews: Sintering Reactions of Magnetite Concentrates under Various Atmospheres, *ISIJ Int.*, Vol. 37, No. 11, 1997, pp. 1057-1065.
- [53] J. Orewczyk and S. Jasienksa: *J. Therm. Anal.*, 32 (1987), 1711.
- [54] H.P. Pimenta and V. Seshadri: Characterisation of structure of iron ore sinter and its behaviour during reduction at low temperatures, *Ironmaking and Steelmaking*, Vol. 29, No. 3, 2002, pp 169-174.
- [55] J. Opfermann: Kinetic Analysis Using Multivariate Non-Linear Regression, I. Basic concepts, *Journal of Thermal Analysis and Calorimetry*, Vol. 60 (2000), pp. 641-658.
- [56] A. Khawam and D.R. Flanagan: Solid-State Kinetics Models: Basics and Mathematical Fundamentals, *J. Phys. Chem. B*, Vol. 110, 2006, pp. 17315-17328.
- [57] A. Ortega: The Kinetics of Solid-State Reactions Toward Consensus, Part 2: Fitting Kinetics Data in Dynamic Conventional Thermal Analysis, *International Journal of Chemical Kinetics*, Vol. 34, 2002, pp. 193-208.
- [58] N. Koga, J. Sestak, and J. Malek: Distortion of the Arrhenius parameters by the inappropriate kinetic model function, *Thermochimica Acta*, Vol. 188, 1991, pp. 333.
- [59] J.M. Criado, A. Ortega, F. Gotor: Correlation between the shape of controlled-rate thermal analysis curves and the kinetics of solid-state reactions, *Thermochimica Acta*, Vol. 157, 1990, pp. 171-179.
- [60] G.I. Senum and R.T. Yang: Rational approximations of the integral of the Arrhenius function, *Journal of Thermal Analysis*, Vol. 11, 1977, pp. 445-447.
- [61] S.P.E. Forsmo and S-E Forsmo: PaRMAC – A New Method of Evaluating the Particle Size Distribution for Agglomeration, XXth IMPC, Aachen, Germany, September 21-26, 1997, pp. 347-353.
- [62] C.E. Grip et al.: The Development and Use of High Temperature Models for the Simulation of the Bosh in the Blast Furnace Part 1, *Scand. J. Metallurgy*, No. 5, 1976, pp. 229-236.
- [63] S.A. Mikhail and A.M. Turcotte: Thermal reduction of steel-making secondary materials, I. Basic-oxygen-furnace dust, *Thermochimica Acta* 311, 1998, pp. 113-119.
- [64] R.S. Roth, T. Negas and L.P. Cook: Phase Diagrams for Ceramists Vol. 4, The American Ceramic Society, INC., 1981.

- [65] P. Scherrer: *Nachrich. Gesellsch. Wissensch. Göttingen*, Vol. 2, 1918, pp. 98.
- [66] A.K. Kercher and D. C. Nagle.: Microstructural evolution during charcoal carbonization by X-ray diffraction analysis, *Carbon*, Vol. 41, 2003, pp. 15-27.
- [67] B. Bergman: Solid-State Reactions between CaO Powder and Fe₂O₃, *J. Am. Ceram. Soc.*, Vol. 69, No. 8, 1986, pp. 608-611.
- [68] Andrew K. Galwey and Genevieve M. Laverty; A kinetic and mechanistic study of the dehydroxylation of calcium hydroxide, *Thermochimica Acta*, 228 (1993), pp. 359-378.
- [69] N. Koga and H. Tanaka: A physico-geometric approach to the kinetics of solid-state reactions as exemplified by the thermal dehydration and decomposition of inorganic solids, *Thermochimic Acta*, Vol. 388, 2002, pp. 41-61.
- [70] P. Barret: International Proceedings of the 4th Symposium on the Reactivity of Solids, Amsterdam, 1960, pp. 178.
- [71] R.Sh. Mikhail, S. Brunauer, and L.E. Copeland: Kinetics of the Thermal Decomposition of Calcium Hydroxide, *Journal of Colloid and Interface Science*, 21 (1966), pp. 394-404.
- [72] D. Chen, X. Gao, and David Dollimore: The application of non-isothermal methods of kinetic analysis to the decomposition of calcium hydroxide, *Thermochimica Acta*, 215 (1993), pp. 65-82.
- [73] J. Gadsby, C.N. Hinshelwood, F.R.S., and K.W. Sykes: The kinetics of the reactions of the steam-carbon system, *Proceedings of the Royal Society of London. Series A, Mathematical and Physical Sciences*, Vol. 187, No. 1009 (Oct. 22, 1946), pp. 129-151.
- [74] A.P. Il'in, N.N. Smirnov, and A.A. Il'in: Mechanochemical Synthesis of Calcium and Copper Ferrite Catalysts for Medium-Temperature Carbon Monoxide Conversion, *Kinetics and Catalysis*, Vol. 47, No. 6, 2006, pp. 929-934.
- [75] M.D. Mann, R.Z. Knutson, J. Erjavec, J.P. Jacobsen: *Fuel*, 2004, vol. 83, pp. 1643-50.
- [76] A.H.A. El-Geassy: *Scandinavian Journal of Metallurgy*, 1998, vol. 27, pp. 205.
- [77] E.T. Turkdogan: 31st Ironmaking Conf. Proc., 1972, pp. 438-58.
- [78] E.T. Turkdogan and J.V. Vinters: *Metall. Trans.*, 1971, vol. 2, pp. 3175-88.
- [79] S.K. Dutta and A. Ghosh: *Iron Steel Inst. Jpn. Int.*, 1993, vol. 33, pp. 1168-73.
- [80] O.M. Fortini and R.J. Fruehan: *Metall. Mater. Trans. B*, 2005, vol. 36B, pp. 709-17.
- [81] R. Haque and H.S. Ray: *Metall. Mater. Trans. B*, 1995, vol. 26B, pp. 400-01.
- [82] E.T. Turkdogan and J.V. Vinters: *Carbon*, 1970, vol. 8, pp. 39-53.

I

Recycling of Sludge and Dust to the BOF Converter by Cold Bonded Pelletizing

Fenwei SU, Hans-Olof LAMPINEN and Ryan ROBINSON¹⁾

SSAB Tunnplåt AB, SE-971 88 Luleå, Sweden. E-mail: fenwei.su@ssab.com

1) Luleå University of Technology, 971 87 Luleå, Sweden.

(Received on September 29, 2003; accepted in final form on December 3, 2003)

With the aim to increase the recycling of fine sludge and dust disposed normally in landfill, cold bonded pelletizing of the sludge and dust using cement as binder was investigated in laboratory scale as well as in the pilot scale pelletizing plant. The influence of BF flue dust, BOF fine sludge and oily mill scale sludge on the cold strength, capacity and reduction degree of cold bond pellets was studied experimentally on the basis of a statistical procedure. With a coarser representative particle size, oily mill scale sludge has the greatest effect on the cold strength. BF flue dust has a negative effect for increasing both the cold strength and capacity for levels of over 25 % of the mixture. The BOF fine sludge has the positive effect on cold strength, while its interaction with BF flue dust has the negative effect on reduction degree.

The results of pelletizing tests in pilot scale show that the maximum cold strength (TTH 94 %) and capacity (13–15 t/h) of products is obtained at the conditions given by the optimal mixture design and cure time. The industrial tests on charging cold bonded pellets as burden material in the BOF converter were described. The charging weight of cold bonded pellets varied from 0.5 to 2.5 tons. The results of industrial tests indicated that the converter process was not subject to any adverse disturbances due to the addition of 2.5 tons of cold bonded pellets.

KEY WORDS: dust; sludge; recycling; cold bonded pellets; pilot scale tests; industrial tests.

1. Introduction

The recycling and utilisation of iron-bearing by-products such as dust, scale and sludge has long been promoted in iron and steel-making industry due to its several benefits: (i) to reduce the depletion of the earth's limited natural resources; (ii) to reduce pollution produced by discharging untreated waste; and (iii) to save energy indirectly. The recycling of dust and sludge generated in integrated steel plants currently can be realized by using one or two of five methods, which include sintering, cold bonded agglomeration, injection, direct reduction (DR) and smelting reduction (SR).^{1–5)} The choice of these methods, however, depends on several important factors such as the environmental requirements, energy policy, company's statutes, company's strategies in recycling, feasibility concerning economy and technology.⁶⁾

The ferrous burden in the blast furnace at SSAB Tunnplåt consists of 100% pellets due to the fact that the sinter plants were closed down in 1978 in Luleå for environmental reasons. As an alternative process, cold bond briquetting was proven to be a viable technique, attractive both economically and environmentally for recycling by-products.^{7,8)} The cold bond briquette plant at SSAB Tunnplåt in Luleå was started in 1993, and since then most of the iron-bearing by products have been recycled through the blast furnace by cold bonded briquetting. At present about 60 kg

of briquettes/thm, which means around five percent of the total burden material, are charged into BF.⁸⁾ This limit depends on several variables, such as the properties of by-products, the zinc content of materials, the strength of the cold bond briquette and the reduction conditions.

The studies reported in the literature and our investigations indicate that cold bonded pelletizing is considered to be the process most recommended for recycling fine dust and sludge from the comprehensive viewpoint of technical, economic and environmental aspects.^{9–12)} The objective of the work presented in this paper is to increase the recycling of fine sludge and dust disposed normally in landfill by developing cold bond pelletizing technology. In this paper, the development and application of the cold bonded pelletizing are reviewed briefly, the influence of by products, *i.e.*, BF flue dust, BOF fine sludge and oily mill scale sludge on the cold strength, capacity and reduction degree of cold bond pellets was studied on the basis of a statistical procedure. Additionally, pilot scale pelletizing tests with an optimum mixture design for the BOF converter are described and the results of industrial tests on charging cold bonded pellets as burden material in the BOF converter are presented.

2. Development of the Cold Bonded Pelletizing

2.1. History and Application of Cold Bonded Pelletizing

The idea of cold bonded pelletizing of fine iron ores originated in Sweden, where K. J. V. Svensson applied for a Swedish patent.¹⁰⁾ Cold bonded pelletizing has some specific features in contrast to the traditional pelletizing of iron ores. It consists of (i) material blending with binder (cement) at lower temperatures; (ii) balling of fines under normal atmospheric conditions and (iii) pellet self-hardening at room temperature or at 70–100°C with a relative moisture of 70%.

The first cold bonded pelletizing plant was put into operation at Grängesberg, Sweden in 1971 for the agglomeration of fine iron ores.¹³⁾ Since then, the cold bonded pelletizing method has aroused great interest in the world not only for treatment of iron ores but of other minerals as well. The cold bonded pelletizing related patents and know-how in the industry were developed further in some countries,¹⁴⁾ Japan in particular.^{15,16)} In the 1980's it became evident that cold bonded pelletization was an economically feasible method for agglomerating iron ore fines and in particular, recycling of dust and sludge.

2.2. Factors Effecting the Properties of Cold Bonded Pellets

The factors effecting the properties and capacity of the cold bonded pelletizing can usually be classified as three types: raw materials (by-products and binder); manufacturing techniques; and the requirements of metallurgical properties.^{9,16)} A summary of factors affecting cold bonded pelletizing is shown in Fig. 1.

According to current thinking, the vital metallurgical properties of the constituents of a BOF converter burden are those: i) Chemical composition of material such as Fe, C, S and P; ii) mechanical strength and porosity of pellets; iii) reducibility and thermoplastic properties. Thus, the above parameters should not be neglected when assessing the properties of cold bonded pellets.¹⁷⁾ Mechanical strength is an important property of cold bonded pellets, as the pellets must often be transported in the steel plant and must be resistant to compression and degradation caused by breakage on handling. The properties of cold bonded pel-

lets depend greatly on the chemical and mineralogical composition, and physical state, of the material as well as the production technologies. The by-products are considered to be very important and variable factors due to the change of chemical composition and particle size distribution.

2.3. Theoretical Considerations

In consideration of the importance of the cold strength of cold bonded pellets, the bulk of the work is being carried out on the basis of agglomeration theories to determine the binding mechanisms and the cohesive forces involved in the process. The binding mechanisms of agglomeration were first defined and classified by H. Rumpf and his co-workers.^{9,16)} A general formula describing the tensile strength of agglomerates, which are held together by binding mechanisms acting at the coordination points, is given as follows⁷⁾:

$$P = \varphi \frac{1-\varepsilon}{\varepsilon} \frac{1}{d} f(\delta)f(d) \quad \dots \dots \dots (1)$$

where P is the tensile strength of agglomerates, d is the particle size of material, δ is the wetting angle, φ is the coefficient of pores filled with water, and ε is the porosity. The porosity is calculated using the difference between the true density and apparent density:

$$\varepsilon = (1 - \rho_a/\rho_t) \times 100 \quad (\%) \quad \dots \dots \dots (2)$$

where ρ_a is the apparent density, and ρ_t is the true density.

According to the Eq. (1), the tensile strength of agglomerates rises with increasing surface tension and with decreasing porosity and grain size values. The equation shows that sufficient strength can be obtained in such cases by selecting a suitable binding mechanism featuring high adhesion or binding forces, using a powder with a small representative particle size, applying suitable curing techniques that produce permanent bonds with high strength, and incorporating temporary additives in the feed.

3. Experimental

3.1. Materials

The dust and sludge used for the experimental studies were taken from SSAB Tunplåt in Luleå and the cement was taken from LuleFrakt Brikett AB. All materials were sub-sampled respectively into 1–2 kg batches with a rotating splitter and stored in a cool, dry place. Table 1 shows the chemical analysis of the materials used for the experimental studies and the pilot scale production of cold bonded pellets charged into the BOF converter. As shown in Table 1 the sludge and dust are primarily composed of iron oxide (20–60%), and the remaining main components were CaO, MgO, SiO₂ and Al₂O₃. Except for BF flue dust and BOF coarse sludge, the chemical composition of all other materials are stable in metal oxide forms.

The results of particle size measurements show that the materials are coarser with ascending order as follows:

cement < BF flue dust < BOF fine sludge < BOF coarse sludge < oily mill scale sludge

The cement has a fineness of 97% passing 32 µm, which was determined by laser diffraction. The particle size of BF

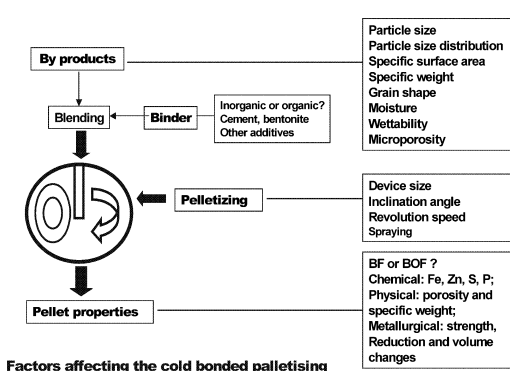


Fig. 1. A summary of factors affecting the cold bonded pelletizing.

Table 1. Chemical composition of the sludge and dust used for BOF pellets.

Composition (%)	BOF fine sludge	BOF coarse sludge	BF flue dust	Oily mill sludge
FeO	57.4	46.7	20.6	58.2
CaO	13.37	17.41	5.16	4.67
SiO ₂	0.91	1.38	4.98	6.47
MnO	0.93	0.67	0.62	0.84
P ₂ O ₅	0.13	0.14	0.07	0.13
Al ₂ O ₃	0.1	0.2	1.93	1.15
MgO	3.1	3.71	1.06	0.21
K ₂ O	0.04	0.04	0.06	0.18
TiO ₂	0.07	0.22	0.21	0.06
Cr ₂ O ₃	0.07	0.06	0.03	0
C	1.47	1.33	54.3	4.59
S	0.07	0.07	0.38	0.11
Zn	0.11	0.05	0.23	0.03

flue dust is about 80% passing 250 µm and the other materials have a wide range of particle size distributions.

3.2. Test Procedure

A 20-kg sample that consists of by-products and cement was mixed in a drum mixer for 4 min and then the blend was emptied into a container and was mixed further with 12.5–13.5% water for another 2 min. After mixing again and sitting for 20 min, the pellet mass was fed into the disc pelletizer that was run with a rotating speed of 18 rpm at an angle of 45°. The pellet mass was left to rotate in the pelletizer for 20 min. The newly rolled pellets were spread out onto the floor for 1 h and then stored for an additional 24 h before sieving. The pellets with a size fraction of 9–12.5 mm were used in the test evaluation.

3.3. Test Evaluation

The test evaluation criteria applied were the tumbler handling strength of cold bonded pellets (TTH), the abrasion handling strength (ATH), the capacity and the reduction degree of pellets with size fraction 9–12.5 mm. The tumbler handling strength of cold bonded pellets is the main quality index used in the iron and steel-making industry. The tumbler handling strength index (TTH) is an international standard method in metallurgical production and these tests were carried out at LKAB. The TTH apparatus is a 100 cm wide cylindrical drum that, loaded with 3 kg of pellets sample with size fraction 9–12.5 mm, is rotated at a standardized speed and time. The pellets and fines are captured after tumbling and then sieved to fractions of +6 mm and –0.5 mm. The wt% of the +6 mm fraction is recorded as the TTH value and the –0.5 mm fraction as the ATH value. A related statistical procedure was used to conduct reduction experiments in inert gas over a temperature range of 20–1 200°C.

3.4. Variables Examined and Design of Tests

The influence of BF flue dust, BOF fine sludge and oily mill scale sludge on the strength and capacity of cold bond pellets was studied experimentally. The amount of BOF sludge, BF flue dust and oily mill sludge were examined while other by-products and cement as well as pelletizing operation variables were kept constant. Experimental details of these groups of tests are presented in **Table 2**; each group was designed with a specific purpose.

By using the same reference recipe, the preliminary tests

Table 2. Experimental details of cold bound pellets in Lab.

Test No.	Conditions	Purpose	TTH %
TP1	10 min, ref, speed 18 rpm, angle 45°	Preliminary tests for judging pelletizing time intervals	60.0
TP2	15 min, ref, speed 18 rpm, angle 45°		78.8
TP3	20 min, ref, speed 18 rpm, angle 45°		88.8
TP4	20 min, ref, speed 18 rpm, angle 45°	Reproducibility	85.0
TP5	20 min, ref, speed 18 rpm, angle 45°		87.5
L1–L11	Table 3 Factorial design tests	Effect of by-products	

Table 3. Factorial design tests L1–L11 for BOF pellets.

Test No.	Level	Cap %	TTH %	ATH %
L1	A1B1C2	5,9	88,9	9,6
L2	A2B2C1	22,5	96,3	2,8
L3	ABC(cpt)	16,6	93,1	5,3
L4	A1B2C2	44,8	96,3	3,0
L5	ABC(cpt)	33,7	95,4	3,6
L6	A2B2C2	15,1	88,3	9,0
L7	A1B2C1	31,5	97,2	2,3
L8	ABC(cpt)	50,7	97,1	2,1
L9	A2B1C1	41,8	97,6	1,9
L10	A2B1C2	18,9	90,1	8,1
L11	A1B1C1	41,2	92,2	6,1

TP1, TP2 and TP3 were designed to judge the pelletizing time intervals by comparing the capacity of pellets with the size fraction 5–12 mm. Tests TP4 and TP5 were used to test the reproducibility of the results for a pelletizing time of 20 min.

Taking into account the amounts of sludge and dust normally sent to landfill and the burden requirements of the converter, full factorial experiments (L1–L11) were designed to examine the effect of by-products; BOF sludge, BF flue dust and oily mill scale sludge, on the cold strength and capacity of cold bonded pellets to be charged into the BOF converter.

4. Experimental Results and Discussion

4.1. Effect of Dust and Sludge on the Strength and Capacity of Cold Bonded Pellets

According to our previous studies based on full factorial design tests,¹¹⁾ the interaction between BF flue dust and BOF fine sludge was considered to have a negative effect on the cold strength and capacity of cold bonded pellets at 20°C. The separate effects of BOF fine sludge and BF flue dust on the cold strength and capacity, however, were less negative.

Table 3 shows result of factorial design tests, L1 to L11. The three factors are, A: BOF fine sludge with two levels, A1 (0 wt%) and A2 (20 wt%); B: BF flue dust with two levels, B1 (20 wt%) and B2 (30 wt%); and C: oily mill scale

sludge with two levels, C1 (0 wt%) and C2 (10 wt%). The level ABC (cpt) means the central point test for the three factors. The estimated effects of each factor for cold strength are shown in **Fig. 2**. The effect of a factor is defined as:

$$\text{effect} = (\text{mean response at high level}) - (\text{mean response at low level})$$

It is clear from **Fig. 2** that oily mill scale sludge has the greatest effect on the cold strength at 20°C. The interaction between oily mill scale sludge and BOF fine sludge is also significant for cold strength in comparison with the factors BF flue dust and the interaction between oily mill sludge and BF flue dust. These results agree with the theory of Eq. (1), indicating that with a coarser representative particle size, oily mill scale sludge is a dominant factor for decreasing the cold strength. Therefore, the pre-treatment of oily mill scale sludge by using rod grinding should be considered in the further tests for decreasing the effect of the coarser particle on the cold strength of cold bonded pellets. In general, an optimal recipe with sufficient cold strength and metallurgical requirements can be obtained in such

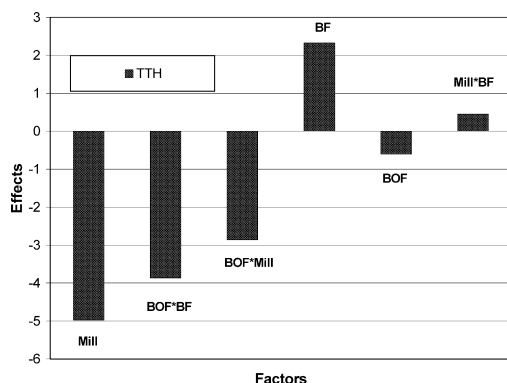


Fig. 2. Effects of factors BOF (BOF fine sludge), BF (BF flue dust) and Mil (Oily mill scale sludge) on the cold strength of cold bonded pellets.

cases by selecting a suitable percentage of binder and by products with a small representative particle size, and applying suitable curing techniques. Test L9 in Table 3 is considered an optimal recipe due to the high TTH and capacity values.

4.2. Effect of Dust and Sludge on the Reduction of Cold Bonded Pellets

TG/DTA/MS experiments were run, using a Netzsch STA 409C furnace and a Balzers QMG 422, on the cold-bonded pellet batches L1–L11 to evaluate the effects of composition on reduction characteristics. Micro pellets from the –5 mm fraction for batches L1–L11 were heated from 20 to 1200°C in an Argon gas environment. The heating rate was 10°C/min and a mass spectrometer was used to analyze the gas that evolved from the sample pellets. The weight loss from heating for each pellet batch is given in **Table 4**.

The reduction of these pellets, in inert gas, is nearly complete at 1200°C. A representative diagram of the information attained from these reduction experiments is given in **Fig. 3**. Reactions taking place during heating are similar for pellet batches L1–L11. Endothermic reactions occur at ~120, ~450, ~550, ~700, ~1050°C evolving H₂O/H₂ and CO/CO₂ gas mixtures. It is assumed that some initial evaporation/dehydration and ensuing reduction is occurring.

A comparison of the effect of different factors on the reduction degree of pellets is given in **Fig. 4**. The results from the statistical evaluation in **Fig. 4** show that the interaction between BOF fine sludge and BF flue dust (BOF*BF) has the largest negative effect on reduction degree and BOF fine sludge has the largest positive effect on reduction degree. One goal of the ongoing research is to find a blend of these factors that give an optimal relation between cold strength and reduction characteristics.

Table 4. The weight loss from heating for each pellet batch.

Test No.	L1	L2	L3	L4	L5	L6	L7	L8	L9	L10	L11
Wt. loss %	26,7	30,1	30,5	29,3	28,4	32,4	32,5	29,3	31,4	32,7	23,2

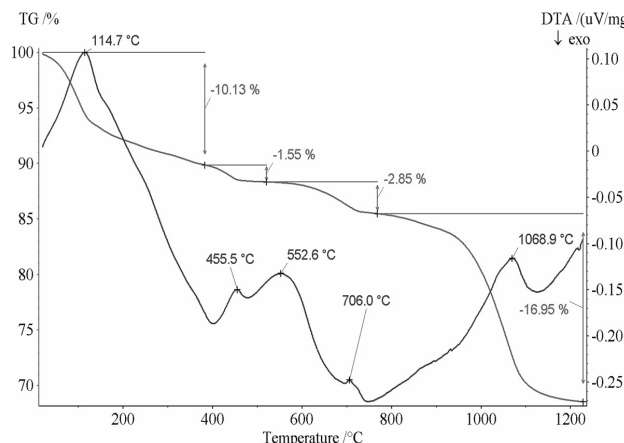


Fig. 3. TG/DTA diagram for pellet batch L9.

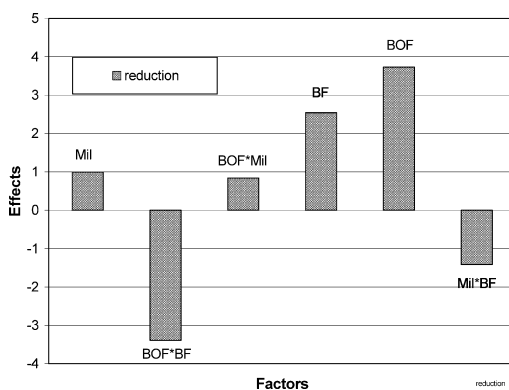


Fig. 4. Effects of factors BOF (BOF fine sludge), BF (BF flue dust) and Mil (Oily mill scale sludge) on the reduction of cold bonded pellets.

Table 5. TTH and capacity of BOF pellets in pilot scale tests in 2001 and 2002.

Date	2001 -R1	2001 -R2	2002 0514	2002 0515	2002 0516	2002 0517
Moisture, %	12,8	13,4	14	15	15,2	15
Capacity, t/h	13	13	12	13	15	13
TTH, %, after 1 day	94	94	96	95	95,5	95
TTH, %, after 3 days	94	94	95	95	96,5	95,6

5. Cold Bonded Pelletizing Tests in Pilot Scale

Pelletizing tests in pilot scale for BOF pellets were carried out at the LuleFrakt Brikett AB in 2001 and an amount of 74 tons of pellets were produced. The same pilot scale tests with an upgraded recipe (excluding BF dust) were carried out in 2002 and an amount of 300 tons of pellets were produced.¹⁸⁾

A test procedure was described in an earlier paper.¹⁷⁾ During the pilot scale tests, the pellet mass was fed by transport band to a disc pelletizer after material mixing, and then the produced pellets were sent to a rolled screen. The pellets with particle size greater than 10 mm were sent to a container by tractor. The pellets with particle size less than 10 mm were sent back to the disc pelletizer by transport band.

The recipe R1, based on lab test L9 and recipe R2, excluding BF flue dust, were used in the pilot scale pelletizing tests. **Table 5** shows some results of the pilot scale pelletizing test in 2001 and in 2002, which indicates that the cold strength (TTH values) for all tests were more than 94% after 24 h, while the capacity of pellets was about 12–15 t/h. **Table 6** shows the chemical analysis of cold bonded pellets in 2001 and in 2002, indicating that there is relatively little difference in chemical composition except sulphur content.

6. Industrial Tests on Charging Cold Bonded Pellets as Burden Material in the BOF Converter

The first group of industrial tests on charging cold bonded pellets as burden material in the BOF converter were carried out at the NO. 2 converter of SSAB Tunaplåt AB in

Table 6. Chemical analyses of pellets in pilot scale pelletizing tests for BOF converter in 2001 and in 2002.

Test Nr	Fe %	CaO %	SiO ₂ %	MnO %	P ₂ O ₅ %	Al ₂ O ₃ %	MgO %	Zn %	S %
2001-R1	41,3	17,5	5,52	0,73	0,11	1,47	3,45	0,10	0,12
2001-R2	49,2	19,1	4,44	0,73	0,12	0,98	3,57	0,07	0,06
2002	48,4	18,1	4,67	0,75	0,10	0,88	2,73	0,07	0,18

Table 7. The results of industrial tests on charging cold bonded pellets (0.5–2.5 t) as burden material in the BOF converter (114 t) in 2001.

Test Nr.	Charging Wight, t	Pellets Wight, t	C %	P %	S %
J6396	104	Ref	0,059	0	0
J6398	116,6	Ref	0,053	0,01	0,014
J6431	105,1	0,5	0,051	0,01	0
J6433	112,9	1,0	0,063	0,01	0,007
J6434	111,9	1,5	0,053	0	0
J6435	108,9	1,5	0,064	0,01	0,008
J6482	110,3	2,0	0,058	0	0
J6483	111,1	2,0	0,100	0,01	0,007
J6484	114,9	2,5	0,054	0,01	0,019
J6485	109,7	2,5	0,091	0,01	0,013

Table 8. Comparison of sulphur content in liquid metal, before and after the LD converter.

Test Nr.	Charging Weight, t	Pellet Weight, t	S-in %	S-out %	S-BOF %
J6396	116,6	Ref	0,02	0,01	0,014
J6433	112,9	1,0	0,05	0,00	0,007
J6435	108,9	1,5	0,03	0,00	0,008
J6483	111,1	2,5	0,01	0,00	0,007
J6484	114,9	2,5	0,02	0,01	0,019
J6485	109,7	2,5	0,03	0,01	0,013

2001. Two reference tests without cold bond pellets and eight tests with cold bond pellets were conducted. The desulphurized hot metal is poured into the converter after charging scrap, and then the cold bonded pellets are charged. The charging weight of cold bonded pellets varied from 0.5 to 2.5 tons. **Table 7** shows the results of industrial tests, No's J6396 to J6485, indicating that the contents of carbon, phosphorus and sulphur in the steel product, from the pellet tests, are close to the results from reference tests.

Table 8 shows the comparison of the sulphur content in liquid metal (S-in), before (S-out) and after the converter (S-BOF), indicating that the sulphur content in the steel product, for test J6484 with 2.5 ton cold bond pellets, changed slightly compared with reference test J6396 without pellets.

Figure 5 shows the sludge amount changes which take place during the blow duration from 1 to 15 min, indicating that the amount of BOF sludge produced is comparable to

the results from reference tests. In general, the converter process was not subject to any adverse disturbances due to the addition of cold bonded by-product pellets.

A second group of industrial tests on charging cold bonded pellets as burden material in the BOF converter

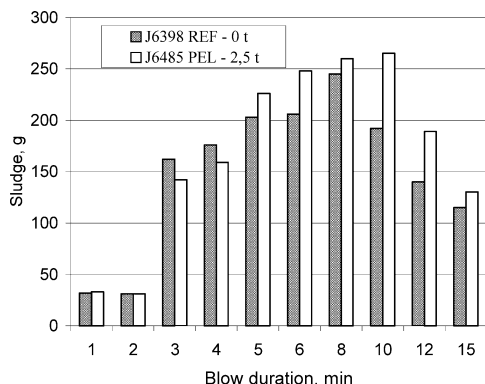


Fig. 5. The effect of charging cold bonded pellets on the amount of sludge generated in the BOF converter.

were carried out respectively at the No. 1 converter and No. 2 converter of SSAB Tunmplåt AB in 2002. The desulphurized hot metal is poured into the converter after charging pellets and scrap. The charging weight of cold bonded pellets was 2.0 tons. A total amount of about 300 tons of cold bonded pellets were used in the tests.

Table 9 shows some of the results of both the 1st and 2nd industrial tests regarding the effect of charging cold

Table 9. Some test results regarding effect of charging cold bonded pellets on the composition of the slag produced in the BOF converter in 2001 and 2002.

Samples	2001 J6398	2001 J6483	2001 J6485	2002 M6355	2002 M6233	2002 M6235
Pellets, t	0	2,5	2,5	0	2,0	2,0
Fe	23,2	22,3	20,6	18,62	15,04	15,19
CaO	35,5	36,3	38,1	45,57	43,41	45,16
MgO	11	13,2	14,5	10,75	12,87	10,6
MnO	4,42	4,21	3,65	3,88	3,7	3,3
SiO ₂	7,55	7,49	7,92	7,3	11,9	12,5
Al ₂ O ₃	3,03	1,75	1,61	0,74	1,46	0,97
P ₂ O ₅	0,66	0,67	0,58			
V ₂ O ₅				4,7	4,8	5,2

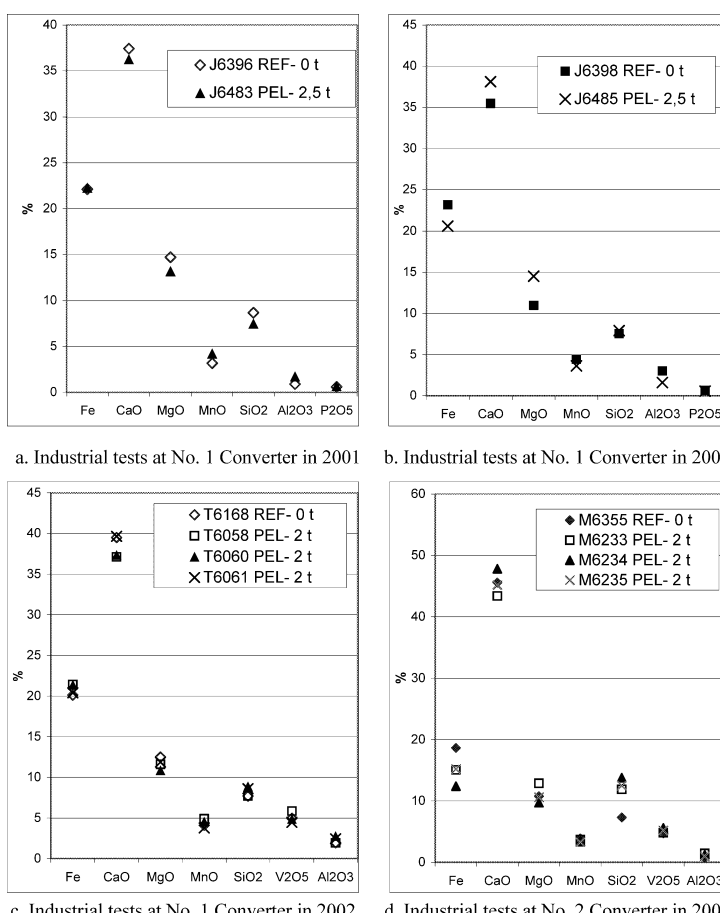


Fig. 6. The effect of charging cold bonded pellets on the composition of slag produced in the BOF converter.

bonded pellets on the composition of the slag produced in the BOF converter. Further information is given in detail in **Fig. 6**, which indicate that chemical composition of slag is stable with and without addition of cold bonded pellets for both the 1st and 2nd industrial tests.

In general, similar to the results in 2001, the results of the second group of industrial tests in 2002 indicated that the converter process was not subject to any adverse disturbances due to the addition of cold bonded by-product pellets, except for some minor boiling problems.

In fact, the boiling that occurs in the BOF converter depends on many factors such as the size of scrap material, the quality of hot metal, amount of pellets, and other operating conditions as well. Thus, it is obvious that there is a need to conduct tests on charging cold bonded pellets as burden material in the BOF converter under pre-chosen conditions.

7. Conclusions

The results from batch tests in lab show that with a coarser representative particle size, oily mill scale sludge has the greatest effect on the cold strength. The BOF fine sludge has the positive effect, while its interaction with BF flue dust has the negative effect on reduction degree. An optimal recipe with higher capacity and cold strength for cold bonded pellets was obtained under given conditions.

The pelletizing tests in pilot scale with an optimum pellet recipe for the BOF converter were carried out. The results show that the cold strength of cold bonded pellets is higher than 94% after a curing time of 24 h with a capacity of 13–15 t/h at given conditions. According to the results of industrial tests on charging cold bonded pellets as burden material in the BOF converter, there are no adverse disturbances to the converter process due to the addition of cold bonded by-product pellets.

Acknowledgements

The authors would like to express their thanks to Lena

Sundqvist-Öqvist and Dag Bergqvist, SSAB Tunnplåt AB, and Caisa Samuelsson and Bo Lindblom, Luleå University of Technology, for their suggestions and assistance in the course of the lab and industrial tests.

REFERENCES

- 1) J. M. McClelland, H. Tanaka, T. Sugiyama, T. Harada and H. Sugitatsu: Proc. of Iron Making Conf., ISS, Warrendale, PA, (2001), 629.
- 2) R. J. Fruehan, J. E. Astier and R. Steffen: Proc. of 4th ECIC, ATS-PM, Paris, (2000), 30.
- 3) J. Derycke and L. Bonte: Proc. of 4th ECIC, ATS-PM, Paris, (2000), 693.
- 4) R. B. Smith, R. Boom and M. G. Sexton: Proc. of 4th ECIC, ATS-PM, Paris, (2000), 703.
- 5) A. Eberle, D. Siuka, C. Böhm and W. Schiffer: *Steel World*, **7** (2002), 28.
- 6) G. Carlsson, G. Berglund, E. Nilsson and F. Su: Proc. of TMS Fall Extraction and Processing Division Meeting, Vol. 1, TMS, Warrendale, PA, (2002), 17.
- 7) G. Berglund and L. E. Eriksson: Proc. of MacMaster Symp., McMaster University, Hamilton, Canada, (1993).
- 8) L. Sundqvist, K.-O. Jonsson, H.-O. Lampinen, L.-E. Eriksson: Seminar Proc., Session 5, IISI, Brussels, (1999), 44.
- 9) J. Srb and Z. Ruzickova: Developments in Mineral Processing (advisory ed. D. W. Fuerstenau), Vol. 7, Elsevier Science Publishers B. V., Amsterdam, Netherlands, (1988), 275.
- 10) K. J. V. Svensson: Svenskt patent 226.608, (1966).
- 11) F. Su, H.-O. Lampinen, L. Sundqvist and L.-E. Eriksson: Proc. of Mineral Processing Conf., MinFo, Luleå, Sweden, (2001), 227.
- 12) R. Linder and D. Thulin: *Aufbereitungs-Technik*, **14** (1973), No. 12, 799.
- 13) T. Inazumi, H. Furutaku and T. Kuwabara: *Conserv. Recycling*, **6** (1983), No. 4, 167.
- 14) T. Akiyama, R. Takahashi and J. Yagi: *ISIJ Int.*, **29** (1989), 447.
- 15) R. Takahashi, M. Ishii, J. Yagi and A. M. Fudolig: Proc. of 6th Int. Symp. on Agglomeration, SPTJ, Kyoto, (1993), 220.
- 16) W. Pietsch: *Agglomeration Processes—Phenomena, Technologies, Equipment*, Wiley-VCH Verlag GmbH, Weinheim, (2002), 98.
- 17) F. Su, H.-O. Lampinen, R. Robinson and L.-E. Eriksson: Proc. of TMS Fall Extraction and Processing Division Meeting, Vol. 2, TMS, Warrendale, PA, (2002), 139.
- 18) H.-O. Lampinen and F. Su: Report of Industrial Tests on Charging Cold Bonded Pellets as Burden Material into BOF Converter, SSAB Tunnplåt AB, Luleå, (2002), 3.

II

Recycling of By-Product Pellets as Burden in the Blast Furnace Process: A Lab and Pilot Scale Investigation

Ryan Robinson* and Lena Sundqvist Ökvist**

*Luleå University of Technology, Luleå/ Sweden; ** SSAB Tunnplåt AB, Luleå/ Sweden

Cold bonded by-product briquettes have been recycled in the blast furnace at SSAB Tunnplåt in Luleå since 1993. Recently, much effort has been made to increase the recycling of by-products. One such project deals with the development of a cold bonded by-product pellet (CBP) agglomerated from very fine dusts. The pellets used in these tests are produced from a blend containing BF flue dust, filter dust, briquette fines and BOF coarse dust as well as cement binder.

The pellets were tested in the laboratory by reduction tests, softening and melting tests, thermo gravimetric analysis, differential thermo analysis, and mass spectrometry measurements. The test results indicate that the CBPs can disintegrate during reduction in the BF shaft, are self-reducing to a high extent and, as a supplement to the normal ferrous burden, they show quite good softening and melting properties. A pilot scale test in LKAB's experimental blast furnace was performed. CBPs were charged with rates of 150 kg/tHM, 299 kg/tHM and 344 kg/tHM respectively during test periods 1, 2 and 3. The blast furnace operation was very stable during test period 1 with 150 kg CBP/tHM, but the burden descent and gas distribution were disturbed during the periods with greater CBP burden content. The rate of reducing agents was significantly decreased and slag amount was increased when CBPs were charged.

Keywords: Cold bonded by-product pellet, compression strength, tumbler test, reduction, Experimental Blast Furnace, reducing agent, flux content.

Introduction

Since 1978, when the sinter plant was closed down, the blast furnaces at SSAB in Luleå have operated with 100% pellet burden. To recycle part of the by-products normally fed to the sinter plant, a cold bonded briquette is produced. Amounts of 40–85 kg/tHM of cold-bonded briquettes have been charged to the blast furnaces at SSAB Tunnplåt in Luleå since 1993 [1].

Today, the blend of by-products used for briquette production contains blast furnace flue dust, filter dust from environmental filters, briquette fines and a scrap mixture consisting of coarse particles of BOF sludge and fines of steel and desulphurisation scrap. The major part of these by-products contains very fine particles. This feature indicates that the by-products might be more suitable for pelletising instead of briquetting. The ratio of fine particles in the dust briquette increased significantly in August 2000 when SSAB Tunnplåt in Luleå inaugurated a new blast furnace that replaced the two smaller ones. The recovery of dry dust increased partly because of the greater production capacity of BF No.3 compared to the combined production capacity of both BF No.1 and No.2, but especially because of the new gas cleaning system with a cyclone and wet scrubber instead of a dust catcher and a wet scrubber. The new gas cleaning facilities have resulted in approximately 80% of dust recovered as dry flue dust compared to 60% in the old gas cleaning system. To be able to recycle the larger amount of in-plant fines the productivity of the briquetting plant had to be maximised. Increased ratio of fine particles in the briquetting blend also increases the demand of binder. Laboratory tests imply that the fine material might be more suitable for pelletising and also that the demand of cement can be lowered with this agglomeration method [2]. By producing CBPs the recycling of in-plant fines can possibly be increased.

In this study the CBP designed for BF use was tested in the laboratory as well as in pilot scale in the LKAB experimental BF (EBF). The high temperature properties of the CBPs and their effect on the softening and melting properties of the pellet bed have been investigated in laboratory reduction tests, thermal analysis and softening and melting tests. The effect from charging high amounts of CBPs on the BF process is evaluated in the pilot scale test in the LKAB EBF.

Characterization of the CBP - laboratory tests

Physical and chemical properties of CBPs

The pellets were produced at a pilot facility on the SSAB Tunnplåt site. Cold bonded pelletizing of the by-products, with cement as binder, was performed on an inclined pelletizing disc and reduced pellets were transferred from the disc to a roller screen by means of a conveyor belt. The undersize fraction was returned to the disc, while the oversize fraction was placed in storage for later use. When sieved, approximately 53% of CBPs lay in the fraction 9–12.5mm compared to 82% of olivine pellets (MPBO).

Cold strength experiments were carried out on the raw CBP samples. Compression strength tests (KTH) were done according to the ISO/DIS 4700 standard. A sample of 60 CBPs was tested. The average force measured for CBP was 55 daN compared to 215 daN for the standard olivine pellet, MPBO. Tumbler tests (TTH), which describe the disintegration tendencies of a sample, were conducted on CBP samples. The resulting pellets sample was then sieved and the weight fraction > 6 mm was recorded. The TTH values for two representative samples were: sample 1 = 99.1%, sample 2 = 98.4%. The by-product blend used in the CBP consists of BF flue dust, filter dust, briquette fines and BOF coarse dust as well as cement binder. Chemical composition

of the CBP is given in **table 1**. The pellet contains approximately 40% Fe and 12% C. This means that the content of slag forming oxides is much larger compared to that in the olivine pellets used. The single basicity B2 (CaO/SiO_2) of the CBP is 2.1 and is quite suitable to mix with olivine pellets with the B2 = 0.13.

Metallurgical properties of CBP

Isothermal reduction. Three different isothermal reduction tests were conducted on the CBP. A low temperature isothermal reduction test, LTB test ISO 13930, was run at 500 °C for 60 minutes with a gas flow of 20 Nl/min. Two high temperature isothermal reduction tests were also conducted on the CBP: ISO 4695 was run at 950 °C for 109 minutes with a gas flow of 50 Nl/min and ISO 7992 was run at 1050 °C for 65 minutes with a gas flow of 83 Nl/min. The results of these tests are given in **table 2**. The LTB value measured for CBPs was slightly higher than that for olivine pellets while the reduction strength value ITH was significantly lower.

Blast furnace simulated reduction. Blast furnace simulation tests were conducted on the CBP. A BF simulation experiment called TRTMAS that LKAB normally uses on olivine pellets was used to test CBP. The test is divided into three temperature zones where the gas composition, a mixture of CO, CO_2 , H_2 , and N_2 , and the applied force on the sample are varied from zone to zone in an effort to simulate blast furnace conditions. **Figure 1** shows an example of the test results for CBP. There is a stepwise weight loss occurring; a weight loss of ca 3.5% in 100% N_2 , ca 6.1% weight loss under mild reducing conditions and ca 10.3% weight loss under stronger reducing conditions. **Table 3** shows results from TRTMAS tests run for different durations of time. Weight loss is reported instead of reduction degree at this writing due to the difficulty of calculating reduction

Table 2. Isothermal reduction tests.

Standard test	Gas comp. $\text{CO}/\text{CO}_2/\text{H}_2/\text{N}_2$	Wt. (g)	Wt. Loss %	weight% +6.3/-0.5 mm
ISO 13930	20/0/2/58	500	9.49	95.8/2.9
ISO 4695	40/0/0/60	500	7.44	31.0/52.3
ISO 7992	40/0/2/58	1200	23.08	NA

degree without previous knowledge of phase and reduction characteristics of CBPs that contain appreciable amounts of hydrates, carbonates and carbon.

TG/DTA/MS. Self-reduction tests of by-product CBPs were run using a Netzch STA 409 instrument for simultaneous Thermo Gravimetric (TG), Differential Thermal Analysis (DTA), and Mass Spectrometric (MS) measurements. Pellet samples roughly 70 mg in mass contained in an alumina crucible were heated from room temperature to 1200°C, at a heating rate of 10°C/min in Ar atmosphere at a constant flow rate of 200ml/min. **Figure 2** shows the thermal analysis results from a sample of cold bonded by-product pellets agreeing well with previously published results [3]. Moisture was detected in the range of roughly 100-300°C with ca 2.8% weight loss and a broad endothermic peak. At temperatures between 330-460°C, chemically bonded water was released in two steps with ca 0.7% and 0.6% weight loss accompanied by small endothermic peaks, respectively. Shortly after, H_2 was detected indicating cracking of H_2O . Decomposition of carbonates occurred in the temperature range of 615-700°C with ca 4% wt. loss

Table 3. TRTMAS reduction tests.

Duration (min.)	Temp. °C	Wt. (g)	Wt. Loss %	ITH % +6.3/-0.5 mm
30	20-710	500	5.5	63.2/26.0
100	20-880	500	12.3	28.9/46.6
180	20-970	500	24.4	NA

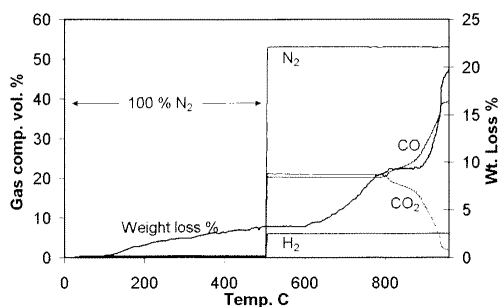


Figure 1. Blast furnace simulation test.

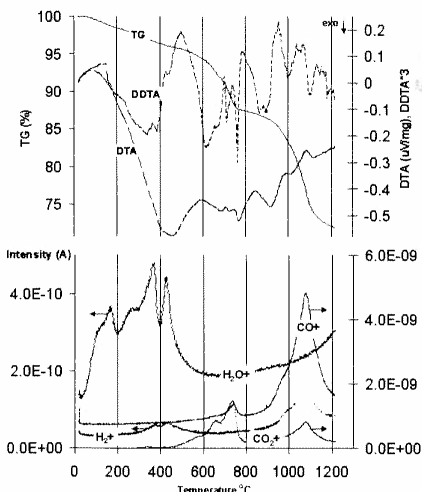


Figure 2. TG/ DTA/ MS test results.

coinciding with a small endothermic peak and CO_2 evolution. In the temperature range of 700–800°C, the CO_2 released from carbonate decomposition reacted further with carbon in the sample accompanied by an endothermic peak producing CO resulting in an additional ca 4% weight loss. Above 800°C, two almost indistinguishable transitions occurred with ca 16% total weight loss. The first transition occurred in a range approximately 900–1000°C where CO was produced by an endothermic reaction attributed to C directly reducing iron oxides within the sample. The second transition occurred when CO, produced from the previous transition, took part in reduction reactions in the temperature range of 1000–1100°C producing CO_2 which in turn reacted with C according to the Bouloard reaction signified by a large endothermic peak.

Softening and melting. Experiments for evaluating softening and melting properties were conducted on mixed samples of MPBO and CBP using blast furnace simulation test equipment at MEFOS. The pellets samples, pre-reduced to 30% reduction degree, were placed between coke layers inside a graphite crucible with applied load and heated in a reducing environment until the height of the sample had stopped shrinking. During the test several types of data were logged including: temperature, shrinkage of the sample bed and the pressure drop over the sample bed. **Figure 3** shows plots of data from two samples, a sample with exclusively MPBO olivine pellets and a sample with MPBO + 10% CBP. The softening temperature is defined as the temperature when the sample bed has shrunk to 50% of its original height. The melt out temperature is defined as the temperature when the maximum pressure drop occurs over the sample bed. The cohesive zone temperature interval is defined as the difference between the temperature at which the bed stops shrinking and the softening temperature. The tem-

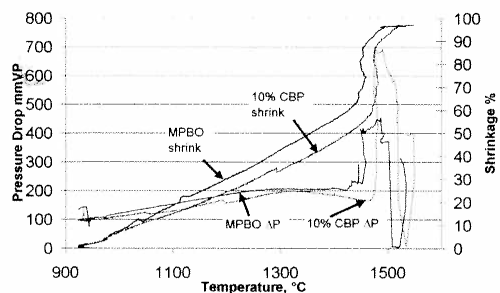


Figure 3. Results of pressure drop and shrinkage.

Table 4. Softening and melting properties of different pellet samples, data in °C; CBP% = wt. CBP/wt. (CBP + MPBO · 100)

CBP %	0	5	10	20
T(50)	1356	1404	1427	1409
T(Pmax)	1487	1511	1477	1492
T(end)	1494	1511	1519	1528
Cohesive zone T(end)-T(50)	138	107	92	119

perature interval of cohesive zone was decreased when CBP were added to the olivine pellets up to 10% addition, as seen in table 4. An addition of 20% CBP increases the width of the cohesive zone marginally.

Test in the LKAB Experimental Blast Furnace (EBF)

Technical description of the EBF and its injection system

A simplified layout of the EBF is shown in **figure 4**. It has a working volume of 8.2 m³ and a hearth diameter of 1.2 m. There are three tuyeres placed at 120-degree intervals. The blast is normally pre-heated to 1200°C in a new type of pebble heater.

The EBF is equipped with a bell-type top. A moveable ar-

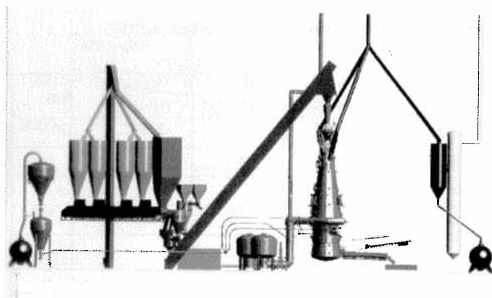


Figure 4. Illustration of the BF and its peripheral equipment.

mour is used for the burden distribution control. Two mechanical stock rods monitor the burden descent and control the charging of the furnace. The EBF is equipped with a lock-hopper coal-injection system. A cylindrical fluidising chamber is fitted below the injection vessel. That chamber fluidises the coal and supplies the pipes with coal for transport to the blast furnace. There is one transport line for each tuyere. For the auxiliary injection a separate vessel is connected to the fluidisation chamber, with a volumetric screw feeder. The added injectant is mixed together with the coal powder in the fluidisation chamber.

The furnace has one tap hole, which is opened with a drill and closed with a mud gun. The hot metal and slag are tapped into a ladle without separation. Probes for temperature measurements, gas analysis and solid sampling over the blast furnace diameter are installed at three different levels. To facilitate dissection and repair, the hearth is detachable and can be separated from the furnace.

Operating the EBF

The blast furnace is operated in campaigns of 4 to 10 weeks at a productivity ranging from 3.2 to 3.8 t/m³day. The normal tap-to-tap time is 60 minutes and the normal tapping duration 5-15 minutes. Process data are logged continuously and stored in a database where reports and trend charts are generated as well as process calculations are carried out. The EBF is a very sensitive tool for detecting differences in properties of different ferrous burdens. The response time is much shorter for the EBF compared to a commercial furnace.

Raw materials

Excluding the trial CBPs for which the tests are conducted, the raw materials used are olivine pellets (MPBO) from LKAB in Malmberget; coke produced at the coking plant at SSAB Tunnplåt AB in Luleå; pulverised coal from the coal injection plant at BF No. 3 as injectant; and limestone, BOF slag and quartzite as additives, **table 5**.

The coke was crushed and sieved into a fraction of 15-30 mm, i.e. standard coke for the EBF. The top-charged slag-forming materials were limestone, quartzite and BOF slag. The size fraction of slag formers was 9-15 mm and 80% of

the particles of the pulverised coal were smaller than 100 µm.

Results from the test in the Experimental Blast Furnace

Process. In general the blast furnace process was relatively stable with some minor disturbances during the entire test. As can be seen in **table 6**, the permeability resistance index (K) increased when CBPs were charged. The gas utilisation ratios Eta-CO and Eta-H₂ and K became increasingly unstable during periods 2 and 3. The burden descent rate was stable during test period 1 with 150 kg CBP/tHM. During test periods 2 and 3, with 300 kg CBP/tHM and 350 kg CBP/tHM respectively, the burden descent rate variations increased. Moisture was added to the blast to overcome this problem. A short stop to change a valve in the dust collection system was made during test period 2. Due to a high heat level in the furnace there were problems with material movements at start up after the stop.

Table 6. Average and standard deviation of gas utilisation, burden descent rate (BDR) and permeability resistance index (K).

	Test p1		Test p2		Test p3		Ref.	
	\bar{x}	σ	\bar{x}	σ	\bar{x}	σ	\bar{x}	σ
BDR, cm/min	6.4	0.8	6.3	1.4	5.9	2.5	5.5	1.2
Eta-CO	46.6	1.3	44.6	2.5	46.1	2.8	46.8	1.7
Eta-H ₂	54.2	3.3	49.6	4.6	49.1	4.5	54.7	3.3
K*10	10.4	0.8	10.9	1.1	10.7	1.2	8.5	0.7

Consumption of reducing agents. As can be seen from **table 5**, the consumption of reducing agents, based on mass balance calculations, was lower, 522 kg/tHM, during test period 1 than during the reference period, 533 kg/tHM. When charging of CBP was further increased during test periods 2 and 3, the consumption of reducing agent decreased to 512 kg/tHM and 503 kg/tHM, respectively. The heat level of the blast furnace was significantly increased when the charging amounts of CBP increased. Therefore, to adjust the heat level, the coke rate was decreased in several steps.

Hot metal and slag. **Table 7** shows the average composition of hot metal and slag for each period of the test. As can be seen in **figure 5**, the C content was quite stable and was increased when the CBPs were charged. The C content was approximately 4.6% for test periods 2 and 3 with 300 kg CBP/tHM and 350 kg CBP/tHM. At the same time the Si content was decreased from 1.75% to 1.20% and the hot metal temperature from 1487°C to 1459 °C. The CBP had a high content of S compared to MPBO, consequently increasing the S content of the ferrous burden in the successive test periods, **table 1**. However, the higher sulphur content during reference and test period 3, when compared with test periods 1 and 2, can be explained by a lower basicity of the slag (**table 7**) and a lower heat level in the BF.

Table 5. Raw materials used during the test, kg/tHM.

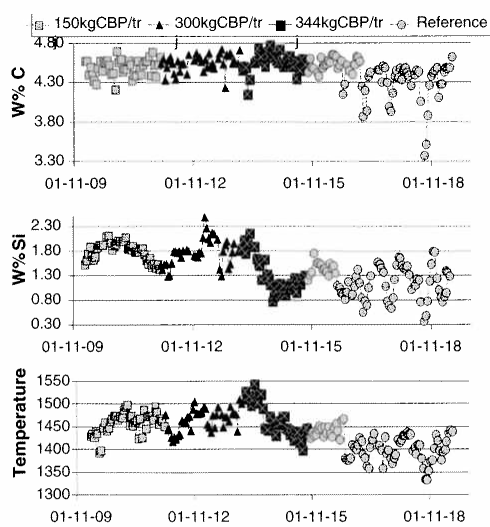
Test periods 1,2,3	150 kg CBP/tHM	300 kg CBP/tHM	350 kg CBP/tHM	Ref.
Pellets	1290	1209	1193	1388
CBP	149	299	344	
Limestone	15			47
Quartzite	20	16	29	17
BOF slag	30			45
Coke	402	390	389	402
PCI	120	122	114	131
O ₂ enrich.	6.09	5.98	5.87	4.31

Table 7. Chemical composition of hot metal and slag.

$$B2 = \frac{(\text{wt.\%CaO})}{(\text{wt.\%SiO}_2)}$$

$$BR = \frac{(\text{wt.\%CaO} + 0.69 * \text{wt.\%MgO})}{(0.93 * \text{wt.\%SiO}_2 + 0.18 * \text{wt.\%Al}_2\text{O}_3)}$$

	Test p1	Test p2	Test p3	Ref.
Hot metal				
Temp. °C	1463	1487	1459	1420
%C	4.50	4.62	4.58	4.44
%Si	1.80	1.75	1.20	1.18
%S	0.04	0.04	0.07	0.07
Slag				
%CaO	32.64	32.30	31.70	31.93
%SiO ₂	34.58	34.34	38.00	35.48
%MgO	18.40	18.18	15.45	17.18
%Al ₂ O ₃	13.92	14.29	12.66	12.93
B2	0.95	0.94	0.84	0.91
BR	1.31	1.30	1.13	1.24
Slag vol. kg/tHM	160	169	205	153
S distribution (kg in slag)/(kg in HM)	7.0	8.1	4.1	3.4
K ₂ O yield % in slag	36.2	39.4	95.9	73.9

**Figure 5.** Temperature and contents of C and Si in hot metal.

Gas distribution and temperature profile

During the reference period and test periods 1 and 2, the temperature measurements in the top of the EBF indicated a central gas flow. During test period 3 the temperature profile in the top was almost flat.

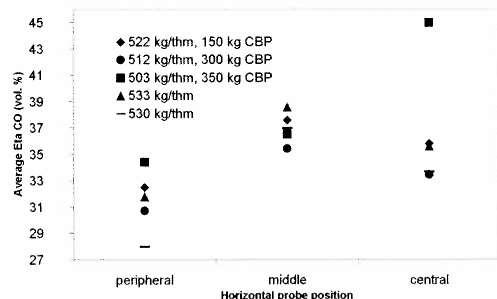
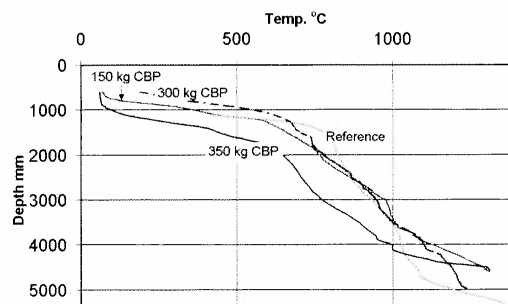
The EBF is equipped with gas and material sampling probes, two probes at different shaft levels and a slanted probe for sampling in the cohesive zone. Gas composition readings from upper shaft probe #3 were used to calculate the average CO utilisation quotient at three different positions along the horizontal profile of the furnace shaft. **Figure 6** highlights the results showing a localised increase of CO utilisation in the central position of the shaft during test period 3, 350 kg CBP/tHM and 503 kg fuel/tHM.

Temperature probes were fed from the top of the EBF shaft at different times in order to record the vertical temperature profile in the furnace with different burden compositions. **Figure 7** gives a summary of the vertical temperature probe results. During test period 3, 350 kg CBP/tHM, a noticeable decrease in the heating rate of the burden occurred. A high moisture content of the CBPs during this test period might have had some effect. The high moisture content did result in dust recovery as sludge instead of dry dust.

Discussion

Effects on BF process

Altered levels of Eta-CO, Eta-H₂, K and increased variations of these parameters and the burden descent rate are some of the effects on the BF process. An increased supply

**Figure 6.** Eta-CO values in upper shaft.**Figure 7.** Vertical temperature profiles for different burden compositions.

of reducing agents in the form of C content of the CBP and a decreased demand of reducing agents in the form of Fe_{met} content in the CBP are some reasons for decreased Eta-CO and Eta- H_2 , and increased K. The change in process conditions involved with a new burden composition, i.e. additional CBP burden content, resulted in expected process variations which could be corrected with necessary adjustments. However, the sum of variations to the process was not fully explained after adjustments were made. The considerably high disintegration of CBPs in laboratory tests after isothermal reduction at 950°C indicates that disintegration of CBPs might occur during reduction in the EBF shaft. Samples taken with burden probes during the pilot scale test contained CBPs that were strong and well reduced, but it is still possible that fines were generated in the shaft. The disappearance of a predominant central gas flow during test period 3, 350 kg CBP/tHM, as well as an increased Eta-CO in the centre of the shaft could point to disintegration of CBPs leading to accumulation of fines in the centre of the furnace shaft. Also, the high moisture content of CBPs could result in re-circulation of water in the BF top having an additional effect on the temperature distribution and Eta-CO if H_2O participates in the water-gas shift reaction. As a result of altered gas distribution, pellets of varied pre-reduction degree can reach the hearth. This might cause variations of burden descent. Another reason for un-uniform burden movement might be slag formation problems discussed later.

Effect on fuel consumption

Charging CBPs with the burden allowed for a decrease in fuel consumption when compared to the reference period without CBPs. Operators at the EBF systematically reduced the coke and PCI rates to counter the excess thermal reserves in the furnace, **figure 8**. If the consumption of reducing agents during each test period is compared with the consumption during the reference period, it is found that the consumption of reducing agents decrease with 11, 21 and 30 kg/tHM for test periods 1, 2 and 3 respectively. The estimated decreased consumption of reducing agents, based on the content of C and Fe_{met} in charged CBP, corresponds to 27, 55 and 63 kg/tHM, respectively, when 149, 299 and 344 kg CBPs are charged per ton hot metal. The decreased

consumption of reducing agents is less during the test in the EBF because of increased heat level of hot metal and increased slag rate during the three test periods. The decreased amount of limestone additives will decrease the consumption of reducing agents. These changes, according to the literature [4], will result in increased coke consumption for test periods 1-3 of 33, 35 and 13 kg/tHM respectively. If this is taken into consideration, the consumption of reducing agents decreased more than expected during the pilot-scale test. This indicates an efficient use of C contained in the CBP.

When studying the DTA results from experiments run on CBPs, we see that reactions between CO/ CO_2 and solid carbon account for the majority of the weight loss in an inert gas atmosphere above 700°C. If the assumption is made that the major product from reactions occurring above 700°C is CO, a simple calculation shows that C consumption in the CBP accounts for ~7.6% weight loss. Thereby giving roughly a 63% utilisation of reducing agent in the CBP under inert conditions.

Effect on slag formation

Addition of CBP ($B_2 = 2.13$) to a certain amount with olivine pellets ($B_2 = 0.13$) will improve the slag formation. However, as is shown in table 5, the slag amount increases significantly when the charging of CBPs is increased due to a high content of fluxes in the CBPs. The basicity B_2 and Bells ratio of the primary slag will increase during the test periods. To adjust the slag basicity, limestone, BOF slag and quartzite are added during reference and test period 1 and only quartzite during test period 2 and 3. Because of a high SiO_2 content (92.4%) of quartzite the amount added is quite low. The small amount added in combination with uneven distribution will result in local variations of basicity in the burden.

In BF No. 3 at SSAB Tunaplåt, in Luleå, the Si content of hot metal is approximately 0.30 %, considerably lower than in the EBF. From a chemical composition point of view, it is possible to charge approximately 340 kg/tHM of cold bonded agglomerate without addition of any fluxes, but the slag volume will increase with 35-40 kg/tHM. One effect from increased slag volume might be decreased production efficiency.

The softening and melting tests indicate that the softening and melting properties are improved up to an addition of 10% CBP. One reason to this might be that the basicity gradually increases with increased addition of CBPs.

Conclusions

The test shows that it is possible to charge quite high amounts of cold bonded agglomerates to a BF and the upper limit is dependent on chemical and/or metallurgical properties of the material. The BF behaviour of the cold bonded agglomerate has a significant effect on the BF process. The metallurgical properties of the cold bonded material become important when the charged amount is beyond 10% of the ferrous burden.

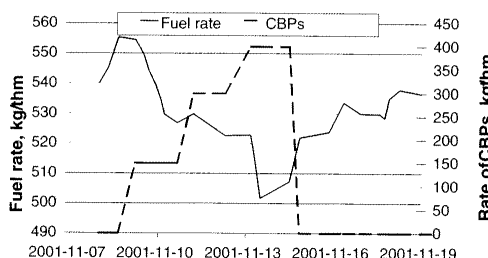


Figure 8. Fuel consumption during pilot test.

Acknowledgements

We wish to thank LKAB for giving us the possibility to carry out the test campaign in the EBF. The encouragement from colleagues, the work done by the personnel participating in the test campaign and the analyses performed by laboratory staff at SSAB, LKAB and MiMeR are also very much appreciated. Financial support from VINNOVA is also gratefully acknowledged.

(A2003088; presented in Düsseldorf on 17 June 2003)

Contact: Ryan Robinson
Luleå Technical University
Dept. of Chemical and Metallurg. Eng.
Division of Process Metallurgy
97187 Luleå / Sweden

References

- [1] T. de Bruin, L. Sundqvist: Briquetting- One Way of Treating By-Products at SSAB Tunplåt in Luleå , 2nd International Congress on the Science and Technology on Ironmaking and 57th Ironmaking Conference Proceedings, Toronto Canada, 1998.
- [2] L. Sundqvist, K-O. Jonsson, H-O. Lampinen, L-E. Eriksson: Recycling of in-plant fines as cold bonded agglomerates. Committee on Raw Materials- Seminar Proceedings, p 44-60, Brussels, Belgium, 1999.
- [3] S.A. Mikhail, A.M. Turcotte: Thermochimica Acta, 311 (1998), 113/9.
- [4] A.K. Biswas: Principles of Blast Furnace Ironmaking, Cotta Publishing House, 1981.

III



Available online at www.sciencedirect.com



Thermochimica Acta 432 (2005) 112–123

thermochimica
acta

www.elsevier.com/locate/tca

High temperature properties of by-product cold bonded pellets containing blast furnace flue dust

Ryan Robinson*

Luleå University of Technology, SE-97187 Luleå, Sweden

Received 23 November 2004; received in revised form 21 March 2005; accepted 7 April 2005

Abstract

In this investigation, the fundamental reactions occurring during the heat treatment of cold bonded pellets (CBP) comprised of iron and steelmaking by-products have been studied. Blast furnace (BF) flue dust, which contains fractions of coal and coke particles, has been included in the CBP blend as a source of solid reductant. Thermal analysis was performed on CBP samples in inert atmosphere at a heating rate of 10 °C/min in order to observe their high temperature properties, specifically, the mechanisms of self-reduction within CBPs. Both endothermic and exothermic reactions were observed during heating. The gases generated during thermal analysis were analyzed using a quadrupole mass spectrometer (QMS). Furthermore, CBP samples heated to several different temperatures and quenched in argon were analyzed using X-ray diffraction (XRD) and scanning electron microscopy (SEM). Results from this investigation demonstrate that the decomposition of hydrates and carbonates in CBP samples contribute, as gaseous intermediates, to an earlier reduction of contained iron oxides. The gaseous intermediates are responsible for an initial gasification of carbon contained in blast furnace flue dust leading to low temperature iron oxide reduction. The step-wise reduction of iron oxides in CBPs at the given conditions begins at ~500 °C and is nearly completed at 1200 °C. This work can help to provide a fundamental understanding of the reduction characteristics of iron and steelmaking by-product agglomerates.

© 2005 Elsevier B.V. All rights reserved.

Keywords: Cold bonded pellets (CBP); Iron oxide reduction; By-products; Thermal analysis

1. Introduction

In the global steel industry, more than 400 kg of solid by-product is generated per ton of steel produced. Most of this by-product (70–80%) is in the form of slag, which after much research, is now used largely in the cement industry and for road and civil construction. The remaining solid by-products can be classified as dusts, sludge and oily/non-oily mill scale. Traditionally, the majority of generated dust, sludge and scale are recycled back to the BF by means of the sintering process. In Sweden, all sinter plants have been closed due to environmental regulation thereby halting the consumption of these solid by-products as recycle in blast furnaces. Barring a sintering process, the fraction of solid by-products classified as fine particles (60% of dusts and sludge) is very difficult

to recycle without extensive pre-treatment and until recently has been by in large deposited in landfills. These by-products are problematic to recycle not only because of their small particle size but also for their high content of impurities of which the saleable content is not high enough to make further processing economical [1,2]. In recent years, as costs for depositing solid by-products from the steel industry in landfills have increased due to lack of space and increasing environmental restrictions, the recycling of these solid by-products, not only to avoid depositing costs but also to recover valuable iron metal fractions, has become a near necessity. Hence, recycling of various by-products as cold bonded agglomerates in the BF has become a regular practice in Sweden [3].

The optimization of reduction properties of cold bonded agglomerates, containing by-product oxides from the steel industry, is essential for the beneficial recovery and use of the agglomerated iron and carbon units during recycling. While there have been earlier studies of the high temperature be-

* Tel.: +46 920 49 13 09; fax: +46 920 49 11 99.
E-mail address: ryan.robinson@ltu.se.

havior of metallurgical by-product agglomerates containing a supplementary carbon source [4,5] and iron ore mixed with a supplementary carbon source [6], few studies have thoroughly investigated the high temperature properties of cold bonded by-product agglomerate mixes utilizing the carbon content in BF flue dust as a carbon source in self-reducing by-product pellets.

The objective of the present work is to describe the thermal behavior of cold bonded pellets containing BF flue dust, various other metallurgical by-products and Portland cement. Pellet samples have been tested using thermal analysis coupled with QMS gas analysis at temperatures ranging from 20 to 1250 °C in argon gas. Thermal analysis results are complemented with phase and morphological investigations.

2. Materials and methods

2.1. Cold bonded by-product pellets (CBPs)

Samples of prefabricated CBPs having a composition similar to that of cold bonded briquettes currently recycled in the BF at SSAB Tunplåt AB in Luleå, Sweden were investigated. The pellets were produced on a lab scale basis using the following procedure: 20 kg sample that consists of by-products and cement was mixed in a drum mixer for 4 min, then the blend was emptied into a container and mixed with water (12.5–13.5 wt.%) for another 2 min. After mixing again and left standing for 20 min, the pellet mass was fed into the disc pelletizer run at a rotating speed of 18 rpm and an angle of 45°. The pellet mass was left to rotate in the pelletizer for 20 min. The green pellets were spread out onto the floor and left to cure for 1 h. Afterwards, the pellets were stored in a container for an additional 24 h before sieving. Pellets in the size fraction of 9–12.5 mm were used in this study.

The CBP blend contains basic oxygen furnace (BOF) fine and coarse sludge, BF flue dust, diverse filter dusts and cold bonded briquette fines. Contents of scrap fines, present in cold bonded briquettes currently recycled at SSAB Tunplåt AB, were excluded from the CBP blend due to their incompatible particle size. The chemical composition of the raw materials

Table 1
Chemical composition of raw materials for cold bonded pellets (wt.%)

	BOF fine	BOF coarse	Filter dust	BF-1 flue	BF-2 flue	Portland cement	Briquette fines
Fe _{tot}	53.70	74.40	65.80	30.80	35.60	2.40	39.3
CaO	13.90	9.62	0.56	6.54	6.52	62.00	16.60
SiO ₂	1.04	1.97	1.65	4.12	4.39	20.00	6.44
MnO	0.97	0.94	0.26	0.74	0.59	—	0.97
P ₂ O ₅	0.07	0.14	0.05	0.04	0.05	—	0.11
Al ₂ O ₃	0.10	0.15	0.39	1.54	1.55	4.40	1.96
MgO	3.35	3.19	1.16	1.34	1.72	3.05	3.27
K ₂ O	0.05	0.04	0.31	0.03	0.04	1.40	0.10
TiO ₂	0.09	0.31	0.23	0.20	0.29	—	0.49
Cr ₂ O ₃	0.06	0.08	0.19	0.03	0.05	—	0.11
C	1.64	1.01	0.55	35.3	30.6	—	11.7

Table 2
Pellet composition and particle size of materials

Material	Wt.%	–100 µm fraction (%)
BOF coarse sludge	35	34.3
BOF fine sludge	20	39.3
BF flue dust	20	57.9
Briquette fines	10	12.9
Portland cement	10	100.0
Filter dust	5	100.0
Total	100	47.7

in CBPs is given in Table 1 as well as the pellet composition and particle size in Table 2.

2.2. Thermal analysis

A Netzsch STA 409 instrument equipped with simultaneous thermogravimetric (TG), differential thermal analysis (DTA) coupled with a QMS was used to study the high temperature properties of CBPs. The sensitivity of this STA instrument is ±1 µg. A schematic diagram of the thermal analysis instrument is given in Fig. 1. An initial sample was prepared by crushing and grinding 50 g of CBPs to a size of –75 µm and was thoroughly mixed in order to homogenize the material for subsequent thermal analysis experiments.

Two types of tests were performed on the CBP sample. First, to determine the temperature intervals of interest, dynamic TG/DTA/QMS tests were conducted on sub-samples weighing ~70 mg. Two alumina crucibles, one containing alumina powder as a reference and the other a CBP sample, were heated from 20 to 1200 °C at a heating rate of 10 °C/min in argon with a constant flow rate of 200 ml/min.

Second, to investigate phase and morphology structure at various temperatures, additional TG tests were conducted on sub-samples weighing between 2 and 2.5 g. A larger alumina crucible with CBP sample was used for TG experiments, exclusive of DTA and QMS analysis, with a heating program comprised of a controlled dynamic heating to various temperatures and then an isothermal heating for 1 h. The temperature versus time layout for the experiments is given in Fig. 2. The dynamic heating rates ranged from 5 to 10 °C/min and ar-

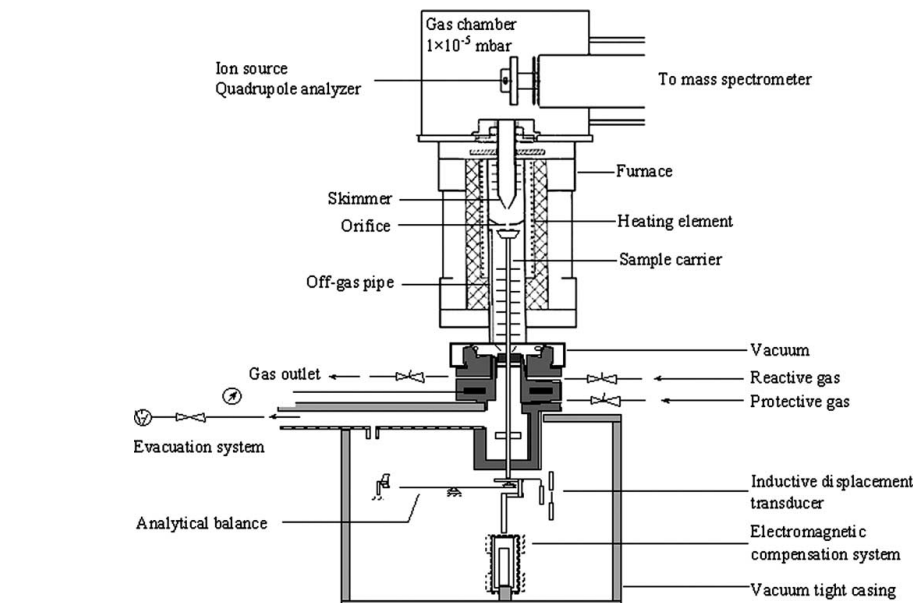


Fig. 1. Thermal analysis instrument.

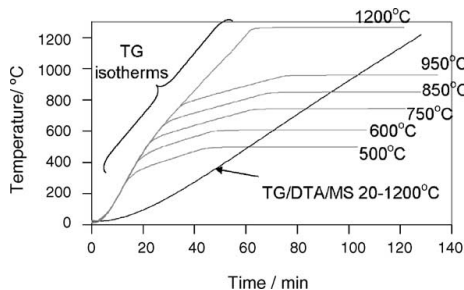


Fig. 2. Temperature vs. time for the thermal analysis experiments.

gon gas was used as in the first experiments. The precision, defined as 2σ , of TG data for all tests was ± 1.95 wt.%.

2.3. Reduction degree

Due to the relative small sample sizes used in this investigation, chemical analysis of the samples after thermal

treatment was not feasible. Therefore, an attempt to calculate reduction degree was done using results from chemical analysis, TG/DTA analysis and gas analysis (intensities I_{CO} and I_{CO_2} given in Table 3) in Eqs. (1)–(3). Reduction degree has been defined as follows:

$$RD (\%) = \left[\frac{\Delta m_{O,red}}{m_{O,initial}} \right] \times 100 \quad (1)$$

where $RD (\%)$ is the reduction degree, $\Delta m_{O,red}$ is the change in mass due to oxygen removal from iron oxide, $m_{O,initial}$ is the initial mass of oxygen bound to iron,

$$m_{O,initial} = 100 - m_{Fe_{tot}} - m_{oxides} - m_{CO_2,carbonates} - m_{H_2O} \quad (2)$$

where $m_{Fe_{tot}}$ is the initial wt.% of total Fe from chemical analysis, m_{oxides} is the initial wt.% of oxides other than iron oxide from chemical analysis, $m_{CO_2,carbonates}$ is the initial wt.% of CO_2 from TG data in the temperature transition 680–760 °C, m_{H_2O} is the initial wt.% of H_2O from TG data in the temper-

Table 3

Maximum CO and CO_2 gas intensities (I) for a CBP sample at different temperature intervals

Temperature range	I_{CO}	I_{CO_2}	$I_{CO}/(I_{CO} + I_{CO_2})$	$I_{CO_2}/(I_{CO} + I_{CO_2})$
500–600 °C	1.89E – 10	3.99E – 10	0.32	0.68
600–750 °C	6.43E – 10	1.46E – 09	0.31	0.69
750–850 °C	5.94E – 10	1.10E – 09	0.35	0.65
850–950 °C	1.16E – 09	2.78E – 10	0.81	0.19
950–1200 °C	4.10E – 09	8.09E – 10	0.84	0.16
S.E.	–	–	0.01	0.01

ature transition 40–480 °C,

$$\Delta m_{O,\text{red}} = \Delta m_{\text{total},\text{red}}$$

$$\times \left[\frac{M_O I_{CO}}{M_{CO}(I_{CO} + I_{CO_2})} + \frac{M_{O_2} I_{CO_2}}{M_{CO_2}(I_{CO} + I_{CO_2})} \right] \quad (3)$$

where $\Delta m_{\text{total},\text{red}}$ is the wt.% total change in mass from TG data in the temperature transitions 480–680 and 760–1200 °C, M_x is the molecular weight of “x”, I_y is the maximum intensity of gas “y” from QMS data in the temperature transitions.

Some assumptions were made to facilitate the calculation of reduction degree: H₂O vaporization and dehydroxylation are the lone causes for weight loss during the temperature transition 40–480 °C, CO₂ generation from the decomposition of carbonates is the lone cause for weight loss during the temperature transition 680–760 °C, CO/CO₂ generation from exclusively iron oxide reduction, and solid carbon gasification leading to iron oxide reduction, is the lone cause for weight loss during the temperature transitions 480–680 and 760–1200 °C.

2.4. Phases and morphology

CBP samples from TG experiments heated to temperatures ranging from 20 to 1250 °C were studied using XRD and SEM. A Siemens D5000 X-ray powder diffractometer using Ni filtered Cu K α radiation at 40 kV and 50 mA was used for phase analysis of samples. The morphology of different samples was investigated using a Philips XL 30 SEM equipped with energy dispersive spectra (EDS) analysis for chemical mapping.

3. Results and discussion

3.1. TG/DTA/QMS and reduction degree

Fig. 3 shows the TG/DTA/QMS results of heating a CBP sample from 20 to 1200 °C at 10 °C/min in 200 ml Ar/min. Refer to this figure for QMS results when comparing with later figures. The results show agreement with previous work [6,7]. Free moisture is detected from gas analysis in the temperature range of 100–200 °C with ca. 1.6%wt. loss and a broad endothermic peak in the DTA curve. At temperatures between 300 and 460 °C, chemically bonded water is released with ca. 2.5%wt. loss accompanied by small endothermic peaks and H₂O generation. Presumably, a decomposition of hydrates has occurred as seen in Fig. 4 illustrating the derivative thermogravimetry (DTG) and derivative differential thermal analysis (DDTA) curves.

Between 450 and 600 °C, CO₂ > CO evolution is observed with ca. 1.7%wt. loss. On closer examination shown in Fig. 5, an endothermic peak occurs in the DDTA curve at 500 °C indicating possible carbon gasification at this temperature.

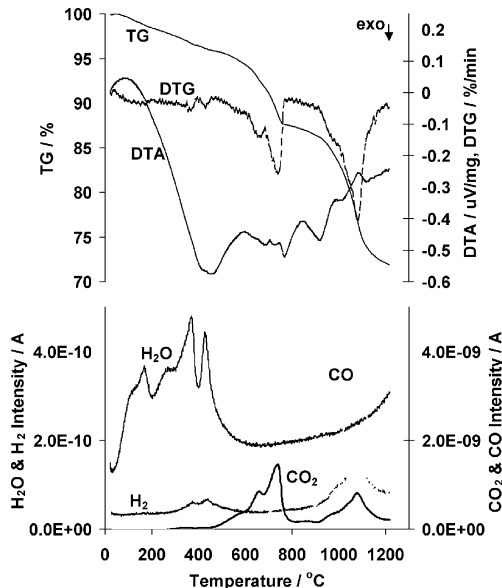


Fig. 3. TG/DTA/QMS results of CBP sample.

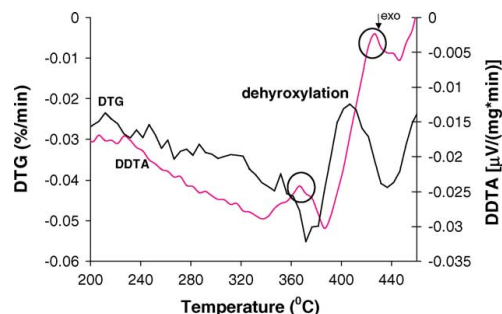


Fig. 4. DTG/DDTA between 200 and 400 °C.

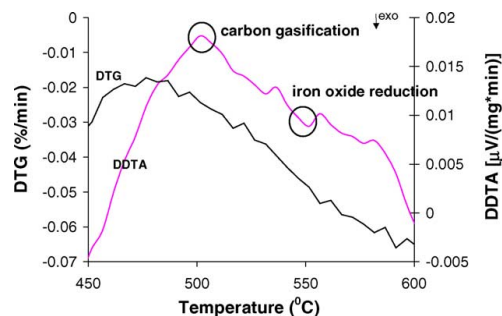


Fig. 5. DTG/DDTA between 450 and 600 °C.

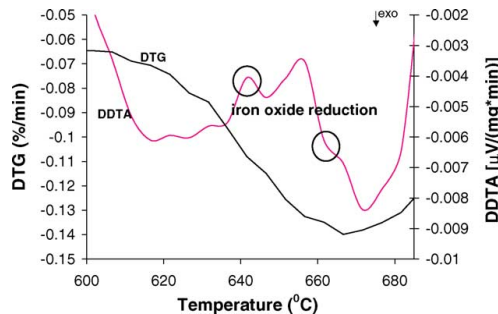


Fig. 6. DTG/DDTA between 600 and 685 °C.

Then an exothermic peak occurs at 550 °C indicating possible iron oxide reduction in this temperature interval.

Next, a new transition occurs in the temperature range of 600–685 °C with ca. 2.3%wt. loss coinciding with an endothermic peak and an exothermic peak, and $\text{CO}_2 \gg \text{CO}$ gas evolution. Fig. 6 shows a closer view of this temperature interval highlighting possible iron oxide reduction occurring first as an endothermic reaction at approximately 640 °C and then as a small exothermic reaction at 660 °C.

In the temperature range of 685–800 °C, a transition occurs with two reactions supported by a pair of peaks, endothermic and exothermic, and $\text{CO}_2 > \text{CO}$ evolution with 4%wt. loss. The first reaction is possibly a decomposition of carbonates occurring at approximately 700 °C and the second reaction a carbon deposition at 760 °C as shown in Fig. 7.

Above 800 °C, a large transition occurs with ca. 16% total wt. loss in Fig. 3. In the range of roughly 800–900 °C, a small amount of iron oxide reduction can occur coinciding with an endothermic peak at 820 °C and $\text{CO} > \text{CO}_2$ generation in Fig. 8. Then, some sort of decomposition seems to occur with an endothermic peak at 880 °C and $\text{CO} > \text{CO}_2$ generation. In the temperature range of 900–1000 °C, further iron oxide reduction can occur corresponding with a large endothermic peak at 950 °C and $\text{CO} \gg \text{CO}_2$ generation.

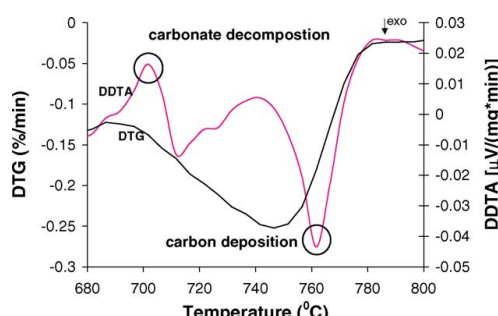


Fig. 7. DTG/DDTA between 680 and 800 °C.

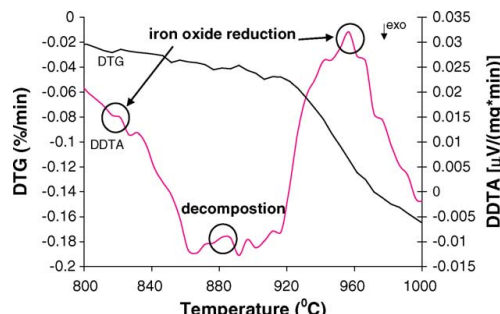


Fig. 8. DTG/DDTA between 800 and 1000 °C.

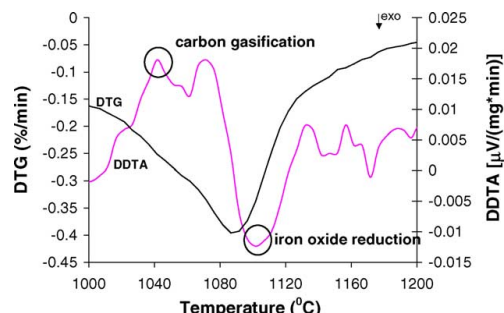


Fig. 9. DTG/DDTA between 1000 and 1200 °C.

Between 1000 and 1200 °C, an endothermic peak occurs at roughly 1040 °C and a subsequent exothermic peak occurs at 1100 °C with $\text{CO} \gg \text{CO}_2$ generation. These reactions are proposed in Fig. 9 as carbon gasification and iron oxide reduction.

Fig. 10 shows the calculated reduction degree (RD) at different temperatures during thermal analysis of CBP samples. Iron oxide reduction seems to start in a relatively low temperature range, between 500 and 600 °C. A possible explanation is that some carbon gasification, catalyzed by H_2O from dehydroxylation of hydrates, has occurred resulting in

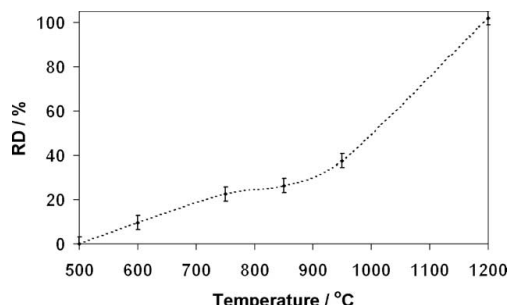


Fig. 10. Calculated reduction degree of CBP sample heated in Ar from 20 to 1200 °C.

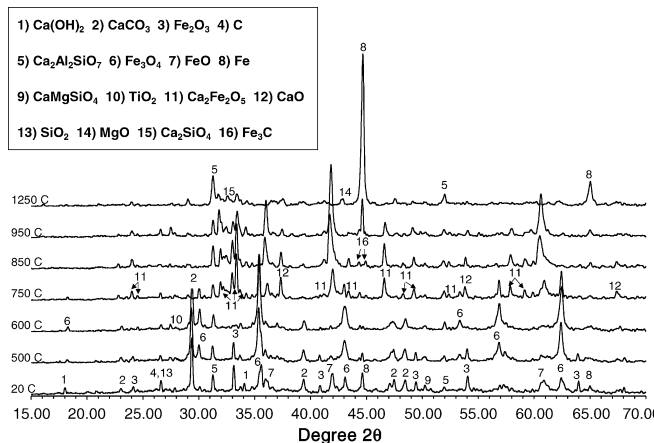


Fig. 11. XRD analysis of CBP samples heated at different temperatures.

local CO generation leading to reduction of Fe_2O_3 to Fe_3O_4 ($\text{RD}=9.57\%$). In the next transition, 600–750 °C, Fe_3O_4 can partly reduce to FeO and then to Fe ($\text{RD}=22.45\%$) coupled with local carbon gasification. During the transition from 750 to 850 °C ($\text{RD}=26.29\%$), reduction of iron oxide is limited possibly due to carbon deposition during this temperature interval. Between 850 and 950 °C, reduction of FeO ($\text{RD}=37.52\%$) could occur with CO_2 generation leading to substantial carbon gasification and a calculated complete reduction of iron oxide ($\text{RD}=101.95\%$) in the range of 950–1250 °C.

3.2. TG and XRD analysis

CBP samples were loaded into an alumina crucible and heated to various temperatures and then held at these temperatures for 1 h in order to attempt an approach to equilibrium conditions, see Fig. 2. After the 1 h isotherm, furnace effect was stopped and the samples were left to cool in Ar gas until room temperature was reached. Samples heated above 1000 °C were submitted to a controlled cooling at –20 °C/min until 800 °C when furnace effect was completely stopped.

At room temperature, the raw sample contains mostly CaCO_3 , Fe_3O_4 , Fe_2O_3 , FeO and Fe , with minor phases of various calcium silicate hydrates, carbon and $\text{Ca}(\text{OH})_2$, see Fig. 11. At 500 °C (3.92% total wt. loss), the hydrates in the sample have disappeared. The main reaction occurring below 500 °C is:

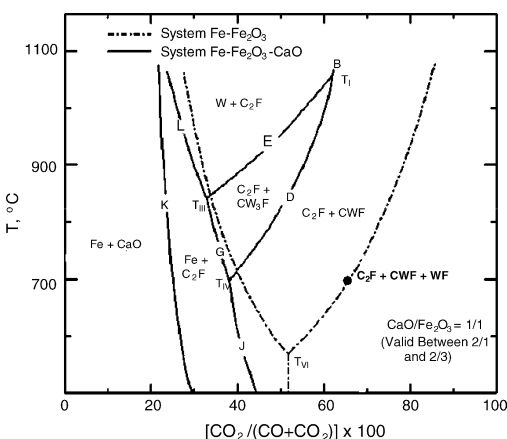


with Me representing Ca or Mg. At 600 °C (5.87% total wt. loss), peaks of Fe_2O_3 have disappeared supporting a reduction to Fe_3O_4 below this temperature. The reduction is proposed to occur through gaseous intermediates, with CO as the

reducing gas, based on noticeable CO_2 generation between 500 and 600 °C in Fig. 3, possibly by the following reactions:



At 750 °C (10.83% total wt. loss), peaks of Fe_3O_4 and CaCO_3 have decreased while peaks of FeO , CaO and $\text{Ca}_2\text{Fe}_2\text{O}_5$ have increased thereby supporting the occurrence of complex carbonate decomposition at 700 °C shown in Fig. 7. The phases detected in XRD also agree with some of the reported phases in Fig. 12 at 700 °C and 65% CO_2/CO mixing ratio. This complex decomposition is most likely comprised of multiple elementary reactions of which the number and order of reactions has not been considered at this time, but a proposed

Fig. 12. Fe– Fe_2O_3 –CaO system as a function of CO_2/CO mixing ratio; C=CaO, F= Fe_2O_3 , W= FeO .

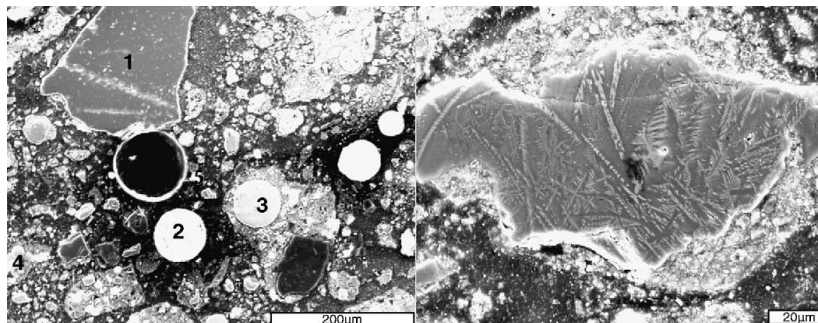
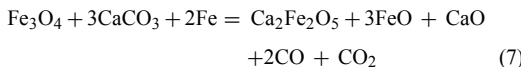
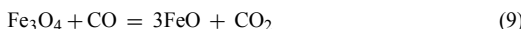


Fig. 13. SEM images of the raw CBPs.

overall reaction is given in Eq. (7). Small peaks of Fe_3C appear at 750 °C as well supporting possible carbon deposition starting at roughly 740 °C. The possible reactions occurring below 750 °C are:



At 850 °C (11.70% total wt. loss), the Fe_3O_4 peaks disappear while peaks of FeO and Fe_3C increase. Possibly, the Fe_3O_4 remaining after $\text{Ca}_2\text{Fe}_2\text{O}_5$ formation reduces to FeO , 820 °C in Fig. 8, according to the following reaction:



The resulting FeO in turn facilitates further Fe_3C formation via Eq. (8) between 740 and 800 °C.

At 950 °C (14.95% total wt. loss), peaks of CaO , $\text{Ca}_2\text{Fe}_2\text{O}_5$ and Fe_3C have decreased while peaks of FeO and Fe have increased. A partial decomposition of $\text{Ca}_2\text{Fe}_2\text{O}_5$ below 950, 880 °C in Fig. 8, would result in an increase of FeO and Fe in the sample. Furthermore, Fe_3C could reduce some FeO in the sample producing metallic Fe , 950 °C in Fig. 8.



At 1250 °C (25.87% total wt. loss), the sample contains predominately metallic Fe , Gehlenite ($\text{Ca}_2\text{Al}_2\text{SiO}_7$) and Periclase (MgO) with some other minor calcium silicate phases. A large generation of CO in Fig. 3 between 950 and 1200 °C coupled with the peaks in the DDTA curve in Fig. 9 signifies extensive carbon gasification, Eq. (12), in this temperature interval leading to nearly complete reduction of iron oxide in Eq. (13).

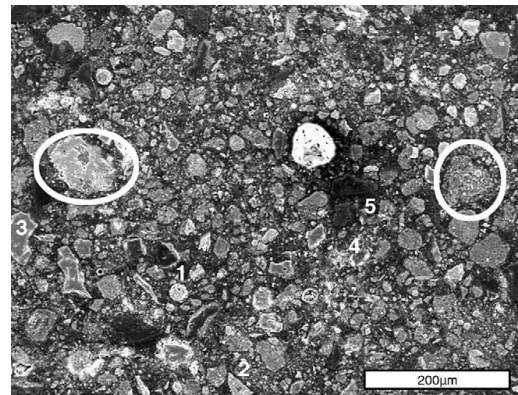


Fig. 14. SEM image of CBP sample heated to 500 °C.

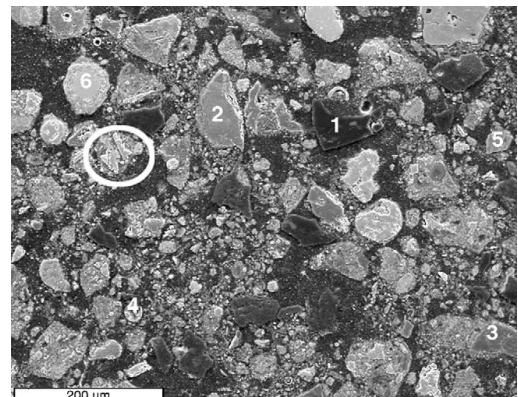


Fig. 15. SEM image of CBP sample heated to 600 °C.

3.3. SEM analysis

Samples from the TG experiments were cast in epoxy resin and polished before observation with SEM. The chemical

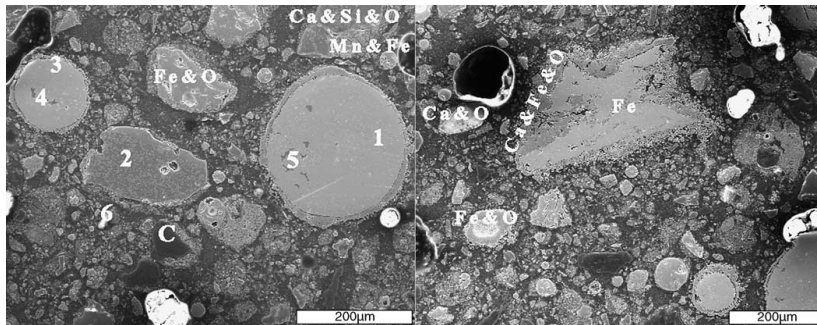


Fig. 16. SEM images of a CBP sample heated to 750 °C.

composition at spots designated by numbers in Figs. 13–16 was investigated using EDS. For a summary of EDS results refer to Table 4. In Fig. 13, the morphological aspect of a raw CBP sample is shown. The micrograph to the left shows an array of discreet particles with various sizes partially enveloped in larger areas of calcium ferrous silicate phases containing some macropores. A typical coke particle is seen below and to the right of spot 3. A separate image of a single particle appears to the right in Fig. 13. This particle has some dendritic structure indicating previous smelting of the metallic phases. The dendrites contain elements Fe>Si and the surrounding areas contain Si>Al>Ca>Fe.

Fig. 14 shows the microstructure of a CBP sample after heating to 500 °C. Here, it is evident that much of the hydrate phase present in the raw material has thermally decomposed. Compared to Fig. 13, particle sizes are much smaller and structural deterioration is observed in some particles (circled in white).

Fig. 15 shows morphological aspects of a CBP sample heated to 600 °C. Evidence of some hematite reduction is present in the form of magnetite lamellae (circled in white) as well as some local oxidation of metallic iron with a dense iron core, spot 6 and a porous iron oxide shell. A general increase in porosity in the sample at 600 °C compared to

Table 4
Summary of EDS image and spot analysis

SEM image	Major elements	Minor elements	Possible phases
Raw CBP (Fig. 13)	Ca, Fe, Si	O, Mg, Al	
Spot 1	Si	O	SiO ₂
Spot 2	Si, Mg, O	Ca, Fe	Ca _x (Fe,Mg) _y SiO _z
Spot 3	Fe	O	Fe _x O _y
Spot 4	Ca	Fe, O, Si	Ca _x Fe _y SiO _z
Spot 5	Ca	Fe	Ca _x Fe _y
500 °C CBP (Fig. 14)	Fe, Ca	O, Si, Mg, Al	
Spot 1	Fe	O	Fe _x O _y
Spot 2	Fe, Ca	O, Si, Mg, Al	Ca _x (Mg,Fe,Al) _y SiO _z
Spot 3	Ca, Si, Mg	O, Al	Ca _x (Mg,Al) _y SiO _z
Spot 4	Ca, Si	O, Mg, Al, K, Fe	Ca _x (Mg,K,Al,Fe) _y SiO _z
Spot 5	Al, Mg	O	Mg _x Al _y O _z
600 °C CBP (Fig. 15)	Ca, Fe	Si, O, Mg, Al	
Spot 1	C	K, Fe, Ca	(Ca,Fe,K) _x C _y
Spot 2	Ca, Mg, Fe	Si, Mn, O, Ti	Ca _x (Mg,Fe,Mn,Ti) _y SiO _z
Spot 3	Si	K, Al, O	K _x Al _y SiO _z
Spot 4	Fe	O, Si	Fe _x SiO _y
Spot 5	Ti, Ca	Fe, Si, Al, O, K	Ca _x (Fe,Al,Ti,K) _y SiO _z
Spot 6	Fe	—	Fe
750 °C CBP (Fig. 16), left side	Ca, Fe, Si	O, Al, Mg	
Spot 1	Fe	—	Fe
Spot 2	Ca, Si	Ti, Mn, Fe, O	Ca _x (Fe,Mn,Ti) _y SiO _z
Spot 3	Fe	—	Fe
Spot 4	Si, Ca	Mn, K, O, Fe, Ti	Ca _x (K,Fe,Mn,Ti) _y SiO _z
Spot 5	Ca, Si	Fe, Ti, Mn, Mg, O	Ca _x (Mg,Fe,Mn,Ti) _y SiO _z
Spot 6	Ca, O	»Fe, Si	CaO
750 °C CBP (Fig. 16), right side, particle shell	Fe, Ca	O	Ca _x Fe _y O _z

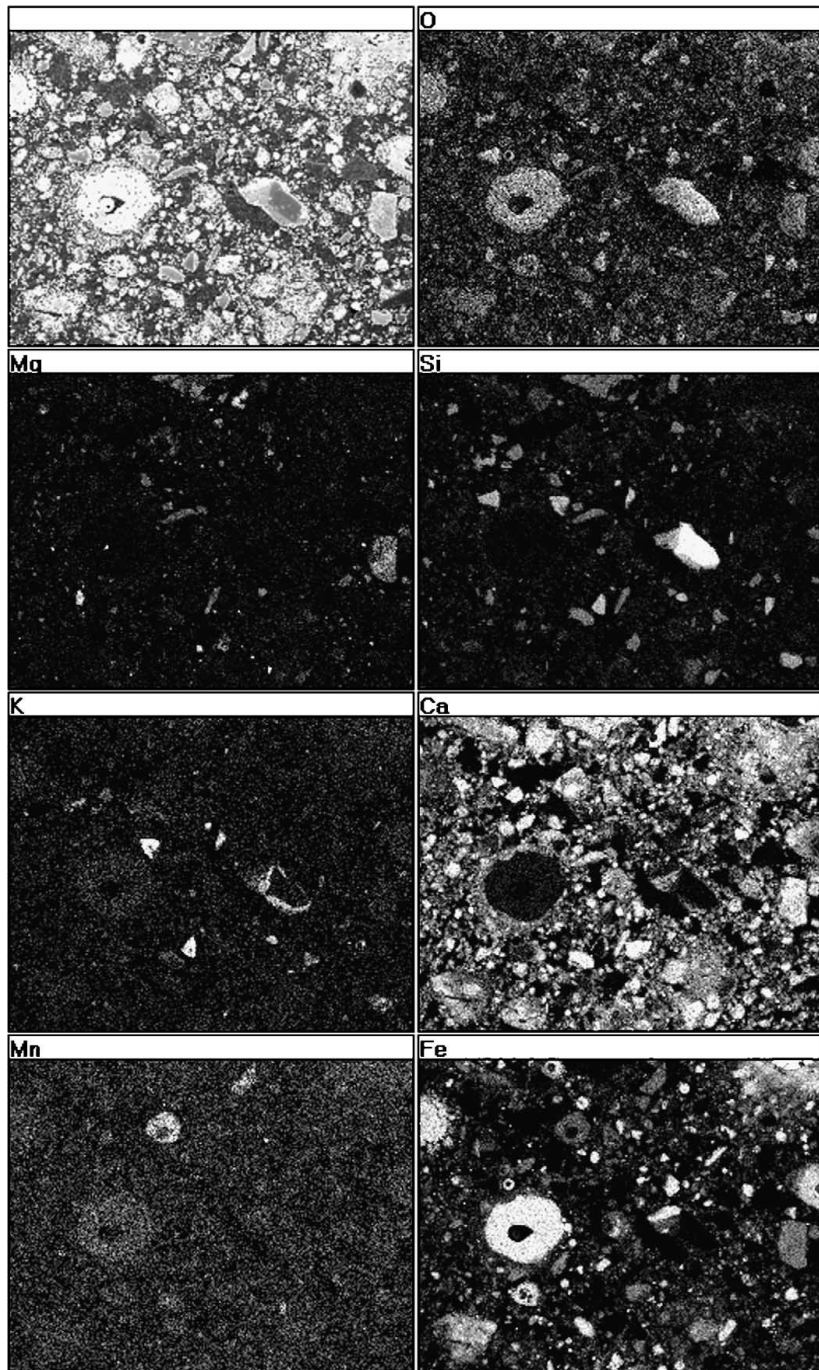


Fig. 17. SEM EDS mapping image from CBP sample heated to 850 °C.

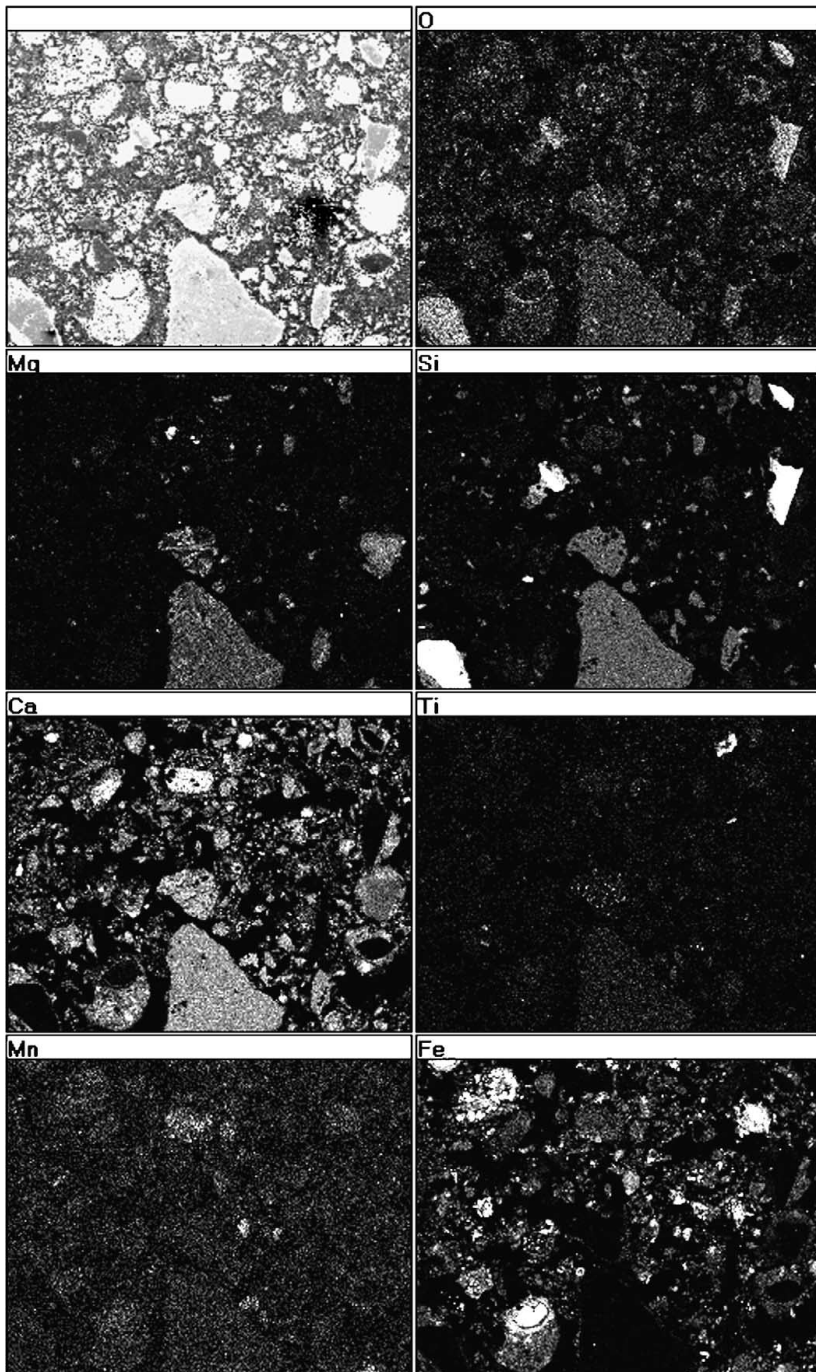


Fig. 18. SEM EDS mapping image from CBP sample heated to 950 °C.

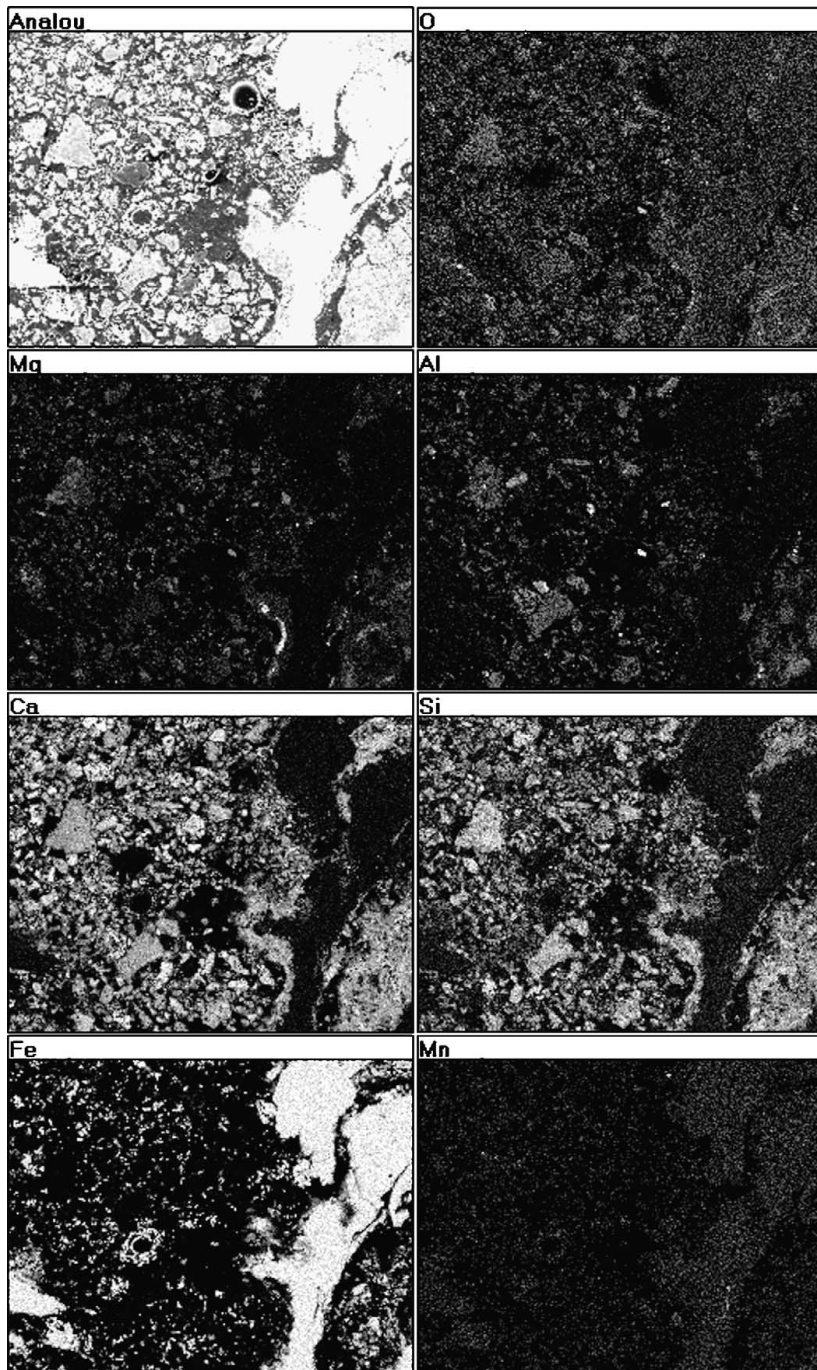


Fig. 19. SEM EDS mapping image from CBP sample heated to 1200 °C.

500 °C indicates possible local gas evolution around some individual particles.

Fig. 16 contains two micrographs from a sample heated to 750 °C. The images show that significant change has occurred in the sample between 600 and 750 °C. In the left image, a calcium ferrous oxide phase has accumulated as a shell around large metallic iron particles, spots 1 and 3, with inclusions, spots 4 and 5. Smaller particles of iron oxide, coke and slag (spot 2) lie in the vicinity of the larger metallic iron particles and even some traces of CaO shown in spot 6. The image to the right supports the proposed complex carbonate decomposition in Eq. (7).

Fig. 17 shows EDS mapping of a sample after heat treatment to 850 °C. The micrograph in the upper left corner of the figure shows the analog image of the entire sample while the remaining micrographs show the dispersion of various elements in the sample. Elements Fe, Ca and O dominate the image with minor amounts of Si, Mg, Al, K and Mn. The majority of Fe content overlaps with Ca content in the sample except for smaller metallic Fe particles and some larger porous iron oxide particles. Si, K and Al content overlap with each other while Mg overlaps with Ca and Mn with Fe.

Fig. 18 shows the EDS mapping results from a sample heated to 950 °C. Areas containing Fe in the sample show large amounts of disintegration except for small amounts of dense metallic iron formation. This could possibly be explained by large $\text{Ca}_2\text{Fe}_2\text{O}_5$ particle's dissolution to smaller CaO , FeO and Fe_{met} particles in Eq. (10) coinciding with extensive gas evolution in Eqs. (11) and (12). Silicon oxide content is large in certain particles, possibly as a remnant from carbon gasification of coke and coal particles. Calcium dominates the sample combining with other elements forming a slag matrix.

At 1200 °C, the morphology of the CBP sample is dominated by metallic iron formation surrounded by calcium silicate slag with minor inclusions of Al, Mg, Mn and V. **Fig. 19** illustrates these SEM results.

4. Conclusions

These conclusions can be drawn from the current work:

- With the given conditions, heat treatment of the CBP sample from 20 to 1200 °C at 10 °C/min in 200 ml Ar/min, 100% calculated reduction degree of contained iron oxides is possible.
- Hydrates and carbonates in the CBP sample play a significant role in the reduction characteristics of iron oxides.
- Fe_2O_3 is reduced to Fe_3O_4 between 500 and 600 °C.
- Carbonate decomposition occurs as part of a complex series of reactions initiating at ~700 °C under given conditions forming $\text{Ca}_2\text{Fe}_2\text{O}_5$ among other products.
- Fe_3O_4 is reduced to FeO and between 640 and 850 °C.
- FeO is reduced to Fe between 850 and 1200 °C.

Acknowledgements

I wish to thank my colleagues at the Division of Process Metallurgy, especially Dr. Nourredine Menad, for suggestions and assistance during the course of this work and financial support from VINNOVA is also gratefully acknowledged.

References

- [1] A. Fleischanderl, et al., Aspect of recycling of steelworks by-products through the BOF, *SEAISI Q.* 28 (April (2)) (1999) 51–60.
- [2] R.L. Nyirenda, The processing of steelmaking flux dust: a review, in: Proceedings of the First International Conference—Minerals Engineering '91, Singapore, 1991, pp. 1003–1025.
- [3] T. de Bruin, L. Sundqvist, Briquetting—one way of treating by-products at SSAB Tunplåt in Luleå, in: ICSTI/Ironmaking Conf. Proc., Toronto, Canada, 1998, pp. 1263–1273.
- [4] M.C. Mantovani, C. Takano, The strength and high temperature behaviours of self-reducing pellets containing EAF dust, *ISIJ Int.* 40 (3) (2000) 224–230.
- [5] J.A.C. Lopez, et al., Development of B.F. Flue Dust Briquette for Recycling in BOF at AHMSA, ICSTI, Toronto, Canada, 1998, pp. 1275–1279.
- [6] G.-s. Liu, et al., Thermal investigations of direct iron ore reduction with coal, *Thermochim. Acta* 410 (2004) 133–140.
- [7] R.T. Wargo, et al., Evaluation of cold-bonded revert briquettes at the USS Gary No. 8 blast furnace, in: Ironmaking Conf. Proc., vol. 50, Washington, DC, 1991, pp. 69–87.

IV

A MECHANISTIC STUDY OF $\text{Ca}(\text{OH})_2$ DEHYDRATION IN THE PRESENCE OF GRAPHITE OR HEMATITE IN RELEVANCE TO REACTIONS IN AGGLOMERATES OF IRON AND STEELMAKING BY-PRODUCTS

R. Robinson¹, F. Patisson², N. Menad³ and B. Björkman¹

¹*Luleå University of Technology, SE-97187 Luleå, Sweden*

²*LSG2M, Nancy-Université, Parc de Saurupt, CS 14234, F-54042 Nancy Cedex, France*

³*Bureau de Recherche Géologique et minière, C. Guillemin, PB. 360009, 45060 Orléans cedex 2-France*

Abstract

The optimization of reduction properties of cold bonded agglomerates, containing iron and steelmaking by-product oxides, is essential during recycling of said agglomerates. Metal hydrate content in cold bonded by-product agglomerates can play a significant role in the low temperature self-reduction of cold bonded agglomerates; specifically the decomposition of hydrated lime can promote the low temperature direct reduction of iron oxides by solid carbon through gaseous intermediates. In this study we have attempted to explain the complex reactions that occur during the dehydration of $\text{Ca}(\text{OH})_2$, in the presence of solid carbon alternatively Fe_2O_3 , in order to clarify their role as eventual precursors to the reduction and high temperature strength characteristics in feedstock agglomerates of iron and steelmaking by-products. Simultaneous thermo-gravimetric (TG) and differential thermal analysis (DTA) was performed on reagent grade sample mixes of $\text{Ca}(\text{OH})_2/\text{C}$ and $\text{Ca}(\text{OH})_2/\text{Fe}_2\text{O}_3$ using several different heating rates from 3-20°C/min in a temperature range of 20-600°C in inert (Ar) atmosphere. Furthermore, selected samples were investigated using X-ray diffraction (XRD) analysis and electron microscope (SEM) analysis. Comparative analysis of the results reveals details of the different reaction processes involved in each system. Under the current experimental conditions; $\text{Ca}(\text{OH})_2$ follows a reaction mechanism described by consecutive nth-order and 2-dimensional phase boundary reaction models, the system $\text{Ca}(\text{OH})_2+\text{C}$ follows a reaction mechanism described by consecutive second-order, 2-dimensional phase boundary, and nucleation-growth reaction models, and the system $\text{Ca}(\text{OH})_2+\text{Fe}_2\text{O}_3$ follows a reaction mechanism described by consecutive second-order and 2-dimensional phase boundary reaction models.

1. Introduction

Traditionally, the majority of generated residual dust, sludge and scale from integrated iron and steelmaking are recycled back to the blast furnace (BF) by means of the sintering process. In Sweden, sinter plants have been closed due to environmental regulation thereby halting the conventional consumption of these solid by-products as recycle in the BF. Barring a sintering process, the fraction of solid by-products classified as fine particles (60% of dusts and sludge) is very difficult to recycle without extensive pre-treatment. These by-products are problematic to recycle not only because of their small particle size but also for their high content of impurities of which the saleable content is not high enough to make further processing economical [1], [2]. In recent years as costs for land filling solid by-products from the steel industry have increased, the recycling of these solid by-products, not only to avoid depositing costs but also to recover

valuable iron metal fractions, has become a near necessity. Hence, recycling of various by-products as cold bonded agglomerates in the BF has become a regular practice in Sweden and recycling in the BOF has gained acceptance in other plants around the world [3]-[7].

The optimization of reduction and strength properties of cold bonded agglomerates, containing by-products from the steel industry, is essential in order to ensure adequate properties of recycled agglomerates prior to softening and melting in the BF process. By-product dusts and sludge from iron and steelmaking furnaces contain considerable amounts of iron oxides, hydrated lime and carbon [8], [9]. Previous studies by the authors [9], [10], have shown that by-product material as well as reagent mixes simulating by-product chemistry, when heat treated under inert conditions, show evidence of carbon gasification via thermal decomposition of calcium hydroxide resulting in subsequent reduction of iron oxide through gaseous intermediates, see Figure 1.

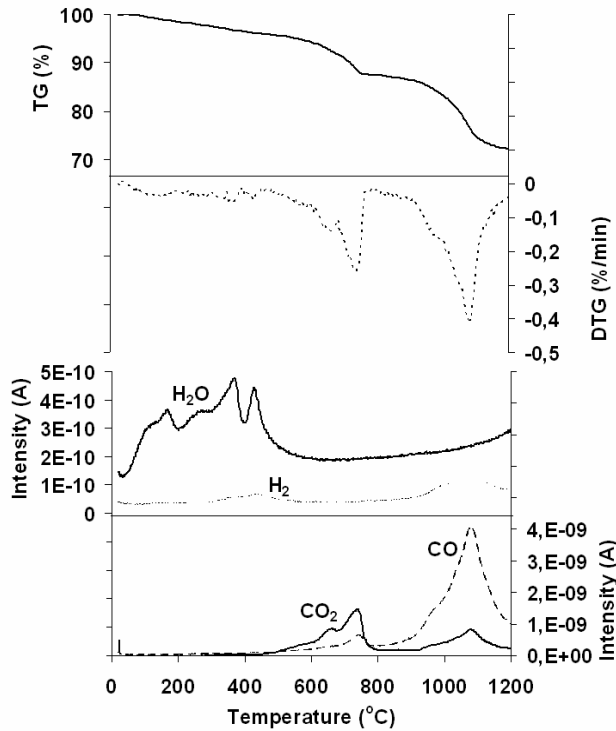


Figure 1. TG/DTA/QMS results of cold bonded pellet sample in argon [9].

Additionally, Mantovani and Takano have reported that the reduction of self-reducing pellets containing a mixture of EAF dust and coal can be described by the following reactions: (1) direct reduction (solid/solid) between iron oxides and carbon; and (2) gas/solid reactions. As the speed of solid/solid reaction is much slower than the gas/solid reaction, the global process occurs via gaseous intermediates such as $\text{CO}_{(g)}$, $\text{CO}_{2(g)}$, $\text{H}_{2(g)}$ and $\text{H}_2\text{O}_{(g)}$ [11].

Various studies have been found in the literature concerning gasification of carbonaceous material in the presence of different metal-based sorbents/catalysts, mostly at elevated pressure ~20 MPa [12]-[14]. Results from S. Sato et al. have shown that water contained in Ca(OH)_2

molecules is sufficient to produce $H_{2(g)}$ from reaction with carbon content in samples of a vacuum residue of Arabian light crude oil at temperatures above 600°C and pressures 4-5 MPa [15].

Therefore, the objective of the present work is to study the mechanisms of reaction in the $Ca(OH)_2-C$ and $Ca(OH)_2-Fe_2O_3$ systems at temperatures below 600°C and ambient pressure. The chemical reactions of most importance to this study are listed below:



2. Experimental

2.1 Materials

The raw materials used in this study are all laboratory grade reagents. Calcium hydroxide, 99.8% pure powder, was supplied from Riedel-deHaen; Hematite, 99.8% (metals basis) pure and -325 mesh powder, was supplied from Alfa Aesar; Graphite, 99% pure and -300 mesh, was supplied from Alfa Aesar. The particle size distributions of the reagents used are given in Figure 2. The reagent mixtures used during experimental work are shown in Table 1.

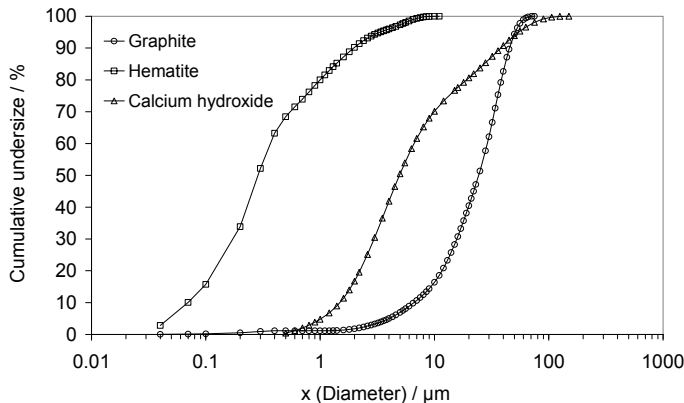


Figure 2. Particle size distribution of reagent graphite and hematite

Table 1 Mix compositions in wt%

Sample	$Ca(OH)_2$	C	Fe_2O_3
1	100	-	-
2	60.7	39.3	-
3	58.2	-	41.8

2.2 Methods

A Netzsch STA 409 instrument equipped with simultaneous thermo-gravimetric (TG) and differential thermal analysis (DTA) was used to study the properties of samples 1-3. The sensitivity of the TG balance is $\pm 5 \mu\text{g}$.

Two types of tests were performed on the samples. First, dynamic TG/DTA tests were conducted on samples weighing between 50-60 mg heated from 20°C to 600°C at different heating rates ranging from 3-20°C/min in argon with a constant flow rate of 100 ml/min. Cylindrical α -Al₂O₃ crucibles with a diameter of 6 mm and a capacity of 300 μl were used in these tests. The TG results were later evaluated with a kinetics software package and some selected samples were analyzed using a Philips XL 30 scanning electron microscope.

Second, to investigate phase changes in the samples, different TG tests were conducted on select samples. These samples were heated from room temperature at 10°C/min in argon to various temperatures, then the furnace was turned off and the samples left to cool naturally in flowing argon. Cylindrical α -Al₂O₃ crucibles with a diameter of 17 mm and a capacity of 3.4 ml were used in these tests. Samples were later analyzed using a Siemens D5000 X-ray powder diffractometer using Ni filtered Cu K α radiation at 40 kV and 50 mA.

2.3 Kinetic Analysis

TG results from experiments have been analyzed using the Netzsch Thermokinetic software package [16]. In the kinetic analysis, experimental TG results have been expressed as reaction extent α ,

$$\alpha = (W_i - W) / (W_i - W_f) \quad (6)$$

where W is the weight or wt.% of the sample at a given time, and W_i and W_f are the initial and final values for the transformation.

A multi-curve method has been applied to the non-isothermal measurements of each sample, specifically the Friedman iso-conversion method. Friedman analysis is based on the Arrhenius equation in a form shown here in Eq. (7):

$$\ln(d\alpha/dt) = \ln(A/f(\alpha)) - E/RT \quad (7)$$

The software provides values for the activation energy, E , and the logarithm of the pre-exponential factor, $\log A$. This analysis has been used as a precursor to linear and non-linear regression parts of the kinetic analysis software in order to estimate the magnitude of activation energy in correlation to conversion degree and temperature. In the multiple linear regression section, a series of experimental data was fit to a variety of different kinetic models for a one-step process. Based on results from Friedman analysis and multiple linear regression, multivariate non-linear regression was used to fit TG data to multi-step consecutive processes with the goal of outlining reaction mechanisms of the systems; Ca(OH)₂, Ca(OH)₂-C and Ca(OH)₂-Fe₂O₃ within the temperature range of 300-600°C. The kinetic models appearing in this study are summarized in Table 2.

Table 2 Kinetic models used in the rate equation, $d\alpha/dt = -A \exp(-E_a/RT) f(\alpha)$

Code	$g(\alpha)$	$f(\alpha)$	Kinetic model type
Fn	$(1/(1-\alpha)^{n-1})-1$	$(1-\alpha)^n$	n^{th} -order
R2	$1-(1-\alpha)^{1/2}$	$2(1-\alpha)^{1/2}$	Two-dimensional phase boundary
R3	$1-(1-\alpha)^{1/3}$	$3(1-\alpha)^{2/3}$	Three-dimensional phase boundary
B1	$\ln(\alpha/(1-\alpha))$	$(1-\alpha)\alpha$	Prout-Tompkins autocatalysis
An	$(-\ln(1-\alpha))^{1/n}$	$n(1-\alpha)[-ln(1-\alpha)]^{(n-1)/n}$	Avrami-Erofeev n -dimensional nucleation/growth
D1	α^2	$1/2\alpha$	1D-diffusion
D2	$\alpha+(1-\alpha)\ln(1-\alpha)$	$-1/\ln(1-\alpha)$	2D-diffusion
D3	$[1-(1-\alpha)^{1/3}]^2$	$[3(1-\alpha)^{2/3}]/[2[1-(1-\alpha)^{1/3}]]$	3D-diffusion

3. Results and Discussion

3.1 TG/DTA results

The TG results of samples 1-3 are given in Figure 3. Samples 1 and 3 have wt. losses that are comparable to but slightly less than the specific theoretical wt. loss of Ca(OH)_2 dehydration (dashed horizontal line in figures) for each sample composition. The reason for this is minor carbonate contamination of the reagent hydroxide (confirmed by XRD) which is practically unavoidable. Conversely, the wt. loss in sample 2 is more than that which can be attributed to hydroxide dehydration. This leads to a conclusion that in sample 2, dehydration isn't the only chemical reaction occurring between 300 and 600°C.

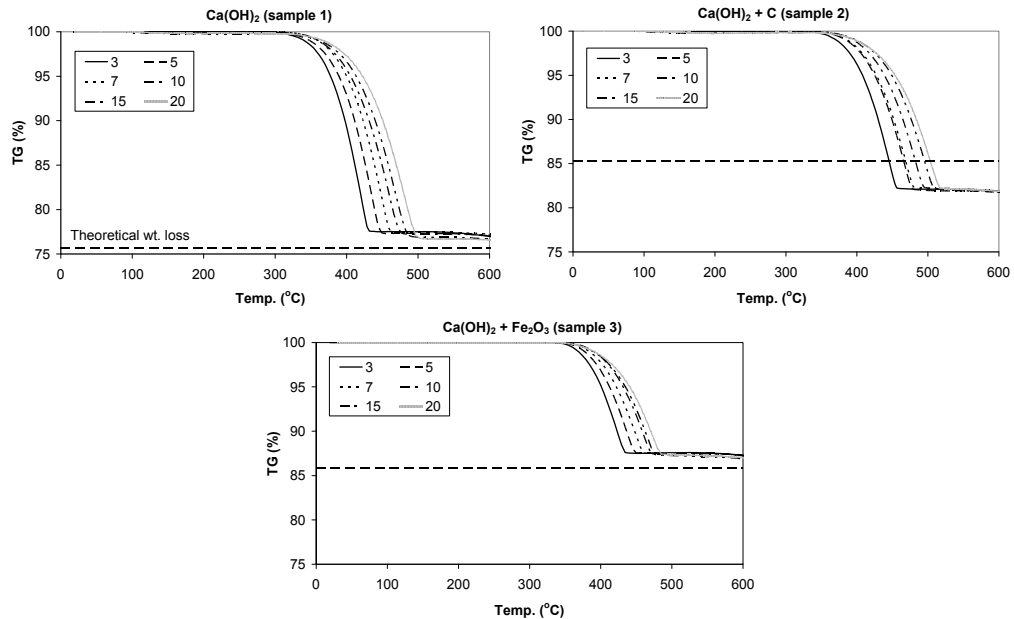


Figure 3 TG results of samples 1-3 at different heating rates ($\beta = 3, 5, 7, 10, 15, 20$ °C/min)

Table 3 shows the peak wt. loss temperature for all samples at the different heating rates used in this study. When using sample 1 as a reference, the peak temperatures for samples 2 & 3 are similar in some aspects but differ in others. On one hand, the weight loss in samples 2 & 3 seems to be less heating-rate dependent than sample 1 because the temperature interval

between the minimum and maximum peak temperatures is less than that for sample 1. On the other hand, both samples 2 & 3 reach maximum rates of weight loss at higher temperatures than sample 1 for heating rates lower than 7°C/min, whilst at higher heating rates of 15 and 20°C/min, sample 3 has peak temperatures that are less than those for sample 1.

A comparison of DTA results for all samples heated at 10°C/min (median representative of all heating rates) is given in Figure 4. Calculation of the peak areas reveals that the peak area of sample 2 is roughly 20% larger and that of sample 3 roughly 20% smaller than the peak area of sample 1. Considering that the content of Ca(OH)₂ is more or less the same for both samples 2 & 3 the difference in heat flow is substantial.

Table 3 Peak temperature °C for weight loss of samples 1-3

sample	Heating rate °C/min					
	3	5	7	10	15	20
1	419.6	438.9	451.1	461.4	471.5	480.9
2	446.2	470.9	471.2	483.9	496.1	499.3
3	424.4	439.7	450.6	464.7	466.1	475.3

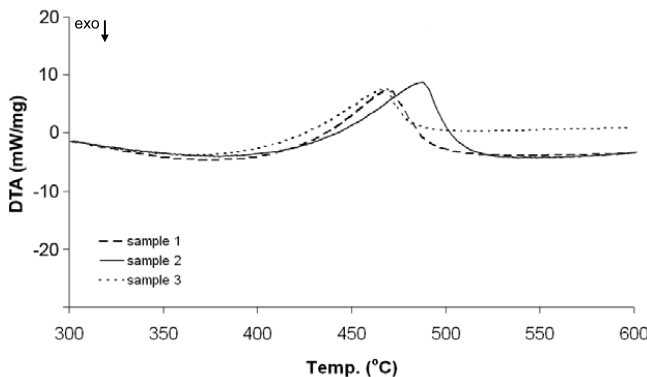


Figure 4 DTA results of samples 1-3 at 10°C/min

3.2 XRD results of raw samples and heat treated samples (10°C/min)

Larger amounts, ~2 grams, of samples 2 and 3 were heated at 10°C/min from room temperature to 500°C under the same conditions as earlier tests in order to investigate the phase and crystal structure changes which occur. Results for sample 2 are given in Figure 5 and for sample 3 in Figure 6. As expected, the phases identified in sample 2 after heat treatment were, in order of decreasing intensity; CaO, C and CaCO₃. In sample 3 the identified phases were, in order of decreasing intensity; Fe₂O₃, CaO, CaCO₃ and Ca₂Fe₂O₅. Full width half magnitude (FWHM) measurements were used for qualitative crystallite parameter comparisons using the Scherrer equation [17]:

$$L = \frac{K\lambda}{\beta \cos \theta_{hkl}} \quad (8)$$

where $K \approx 1$, $\lambda = 0.154$ nm for Cu $K\alpha$ radiation, $\beta = \text{FWHM}$, θ_{hkl} = the Bragg angle. Results are shown in Table 4.

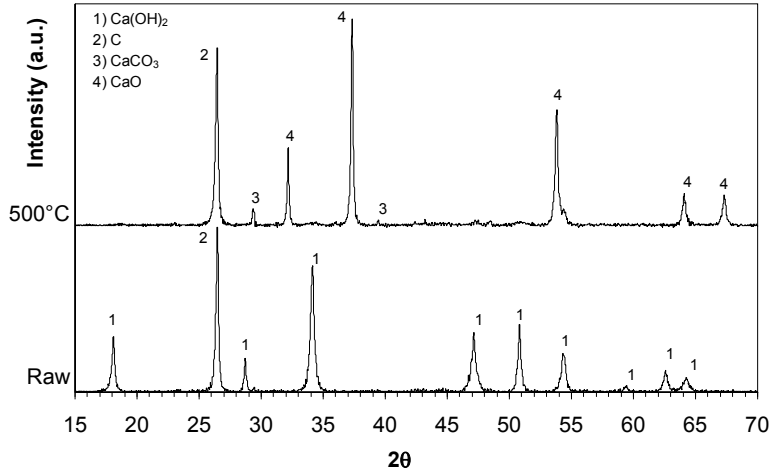


Figure 5 XRD analysis of sample 2 ($\text{Ca}(\text{OH})_2+\text{C}$) before and after heat treatment

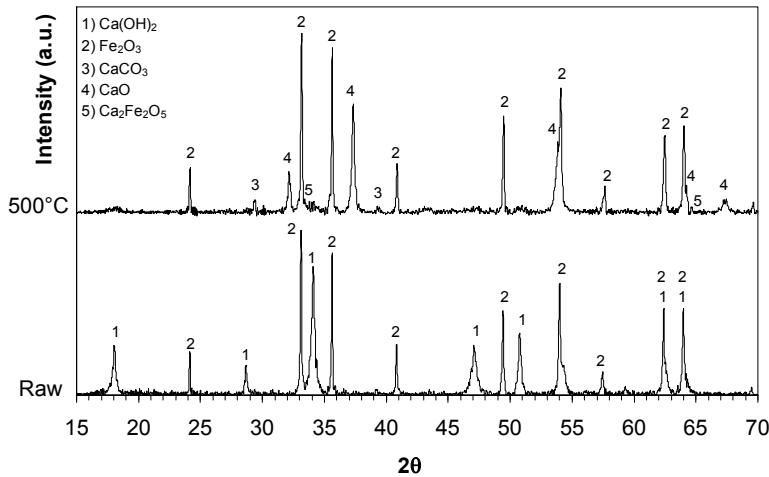


Figure 6 XRD analysis of sample 3 ($\text{Ca}(\text{OH})_2+\text{Fe}_2\text{O}_3$) before and after heat treatment

A comparison of the (002) graphite peak of sample 2 before and after heating shows an increase in FWHM and peak intensity after heat treatment to 500°C. An increase in FWHM commonly indicates a decrease in particle size and crystallinity but this would also correspond with a decrease in peak intensity, which is not the case here. Conversely, crystallite parameter calculations suggest that the average crystallite volume increases slightly or not at all. Using an interpretation of the mechanism suggested by Kercher and Nagle [18], steam generated from Ca(OH)₂ decomposition could facilitate the conversion of disordered carbon content along the L_c dimension into ordered graphene along the L_a dimension resulting in micropore/microcrack formation in the graphite solid but resulting in little or no bulk crystallite volume change.

Measurements of the CaO peaks for samples 2 and 3 after heat treatment to 500°C show that the (200) peak exhibits less broadening while the (222) peak more broadening for sample 3 when compared to sample 2. The relative intensities of CaO peaks exhibit little or no change but changes in crystallite diameter point to an anisotropic grain growth of the (200) crystal plane in lieu of the (222) plane. Evidence of calcium ferrite formation in Figure 6 along with decreased crystallite size of Fe₂O₃ can lead to an assumption that a small amount of newly formed calcium ferrite dissolves in CaO preferentially parallel to the (200) plane. This can be possible in reference to Bergman [19], that local equilibrium is established at the phase interfaces and the extent of solid solution is governed by the local oxygen potential.

Table 4 Comparison of calculated crystallite parameters based on FWHM results from XRD analysis. $\Delta(I/I_0)$ is the change in relative peak area intensities, ΔL_a and ΔL_c are the change in crystallite diameter and crystallite thickness consecutively, and ΔV is the change in crystallite volume. *(this value is the change in relative intensity of the (002) plane between two separate diffractograms, raw and 500°C, as only the (002) carbon peak could be evaluated)

Crystal plane	$^{\circ}2\theta$	FWHM smp 2 ($^{\circ}2\theta$)		FWHM smp 3 ($^{\circ}2\theta$)		Crystallite parameters (nm)			
		raw	500°C	raw	500°C	$\Delta(I/I_0)$ %	ΔL_a %	ΔL_c %	ΔV %
C (002)	26.47	0.305	0.316			8*	3	-3	1
CaO (200)	37.33		0.250		0.230	0	9		28
(222)	67.40		0.358		0.391	1	-8		-23
Fe ₂ O ₃ (012)	24.15			0.103	0.127	-1	-4	-19	-25
(113)	40.85			0.128	0.133	-9	-4	-19	-25

3.3 Kinetic results of Ca(OH)₂, Ca(OH)₂/C and Ca(OH)₂/Fe₂O₃ samples

3.3.1 Friedman Analysis and Master Plots

A diagram illustrating the model-free Friedman analysis of the TG results from samples 1-3 is given in Figure 7. From Figure 7a, we see for sample 1 that the activation energy is initially in the range of 170-140 kJ/mol at low fractional mass loss, $\alpha < 0.2$. As the mass loss increases the activation energy decreases and levels off to a range of 120-100 kJ/mol.

In sample 2, Figure 7b, it is again observed that the activation energy is initially large, 200-160 kJ/mol, at low fractional mass loss, $\alpha \leq 0.1$. Then, as mass loss increases the activation energy decreases and temporarily levels off to a range of 160-140 kJ/mol. Afterwards, at $\alpha > 0.5$, the activation energy sharply decreases and then increases again to a level of ~120 kJ/mol.

Sample 3, Figure 7c, begins with an activation energy that is initially large, 250-180 kJ/mol and then levels off to ~160 kJ/mol as mass loss increases. This behavior is quite similar to that which we observed in sample 1 with exception that the activation energy in sample 3 is noticeably less α dependent at $\alpha > 0.2$. However, all the samples do show some dependence of the activation energy on conversion and this behavior is often a sign that the overall transformation contains multiple steps [16].

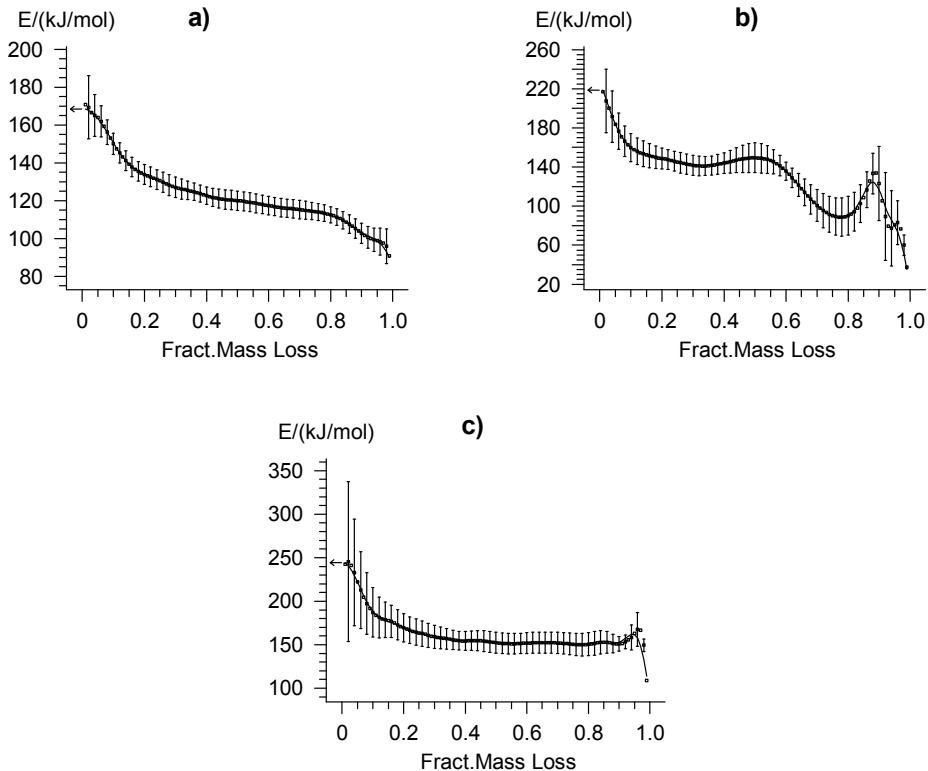


Figure 7 Estimation of E_a using Friedman analysis of **a)** sample 1 ($\text{Ca}(\text{OH})_2$) **b)** sample 2 ($\text{Ca}(\text{OH})_2+\text{C}$) **c)** sample 3 ($\text{Ca}(\text{OH})_2+\text{Fe}_2\text{O}_3$) including 6 experiments each at $\beta = 3, 5, 7, 10, 15, 20^\circ\text{C}/\text{min}$.

In order to more closely evaluate the possible kinetic models that best describe the transformations occurring in samples 1-3, a “master plot” can be constructed to compare theoretical curves with the current experimental curves. This method allows the user to discern the predominant kinetic model or family of models that best match the experimental results using a relationship that is generally independent of the measured kinetic parameters. The specific master plot used here is based on the following function [20][21][22]:

$$Z(\alpha) = \frac{d\alpha/dt}{\beta} \mu(x)T \quad (9)$$

If we substitute the derivative and integral form of the Arrhenius rate equation into Eq. (9),

$$\frac{d\alpha}{dt} = Af(\alpha)\exp(-E/RT) \quad (10)$$

$$g(\alpha) = \frac{AE}{R\beta} \exp(-x) \frac{\mu(x)}{x} \quad (11)$$

where $x = E/RT$, $\beta = dT/dt$ and the fourth-degree rational approximation of the temperature integral taken from Senum and Yang [23]:

$$\mu(x) = \frac{x^3 + 18x^2 + 88x + 96}{x^4 + 20x^3 + 120x^2 + 240x + 120} \quad (12)$$

we arrive at the expression,

$$Z(\alpha) = f(\alpha)g(\alpha) \quad (13)$$

As seen in Figure 8, the theoretical values of $Z(\alpha)$ for the most common kinetic models have been plotted against α using Eq. (13) and expressions for $f(\alpha)$ and $g(\alpha)$ from Table 2. Experimental values of $Z(\alpha)$ have been plotted for samples 1-3 at 10°C/min using Eq. (9) and Eq. (12).

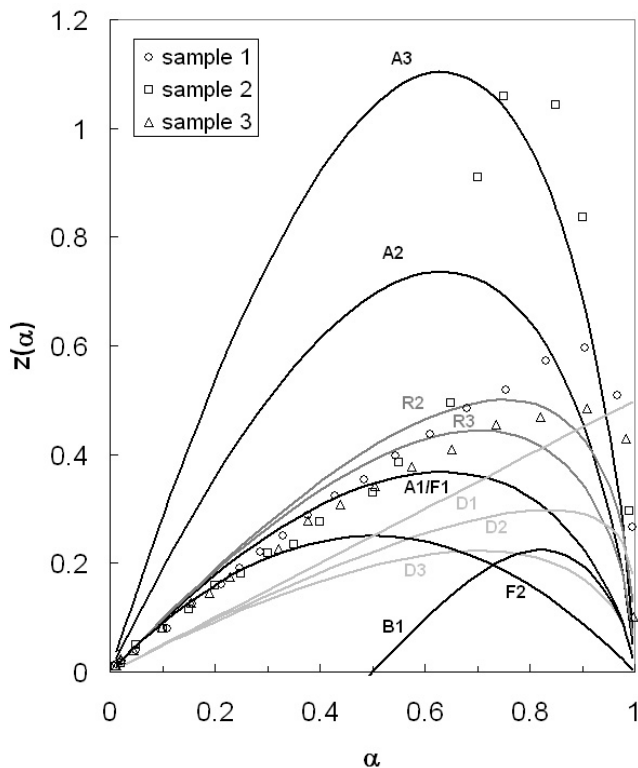


Figure 8 $Z(\alpha)$ master curves for theoretical kinetic models and experimental data

The experimental results in Figure 8 show a fit between the F1 and F2 kinetic models at conversions of $\alpha \leq 0.5$ for samples 1-3. This behavior implies that the initial reaction mechanism occurring in all three samples is governed by Ca(OH)_2 regardless of content. At higher degrees of conversion, sample 1 seems to lie between the R2 and A2 curves, if shifted to the right, suggesting that the dehydration of the Ca(OH)_2 sample in this study is a multi-step process. Sample 2 shows general agreement with the R2 curve at $0.5 < \alpha \leq 0.65$ and then jumps to a

level between the A2 and A3 curves at greater conversion levels. In sample 2, it seems the graphite content brings an additional step to the overall transformation likely due to a reaction between dehydration products and solid graphite. Sample 3 shows a trend that follows the R2 curve at $\alpha > 0.5$ which is similar to that observed with sample 1 but with less affinity to the nucleation/growth models.

3.3.2 Linear and Non-linear Regression Analysis

Sample 1

Results from the regression analysis of TG experiments involving sample 1 are shown in Table 5. First, multi-curve linear regression analysis was conducted in order to evaluate which single-step kinetic models best fit the experimental data. As seen in Table 5, the kinetic models with good fit show very similar correlation coefficients with slightly weaker fit for the An model over the whole of the transformation. These results comprised a likely list of models to test in further analysis of multi-step processes. From the linear regression analysis and with knowledge gained from Friedman and master plot analysis, the decision was made to investigate a configuration of multiple consecutive reactions in the non-linear regression analysis.

The best fit was given for a three step model starting with an n th-order (Fn) step of order $n = 1.44$, E_a between 156-193 kJ/mol, and $\log A$ between 11-14 s⁻¹ until $\alpha = 0.17$. Second, another n th-order step of order $n = 0.45$, E_a between 116-131 kJ/mol, and $\log A$ between 6-8 s⁻¹ until $\alpha = 0.67$. Lastly a two-dimensional phase boundary (R2) step follows with an E_a between 86-128 kJ/mol and $\log A$ between 5-7 s⁻¹.

Table 5 Selected results of regression kinetic analysis for sample 1

Model	order/dimension, <i>n</i>	Linear Regression results			<i>R</i> ²
		<i>E</i> _a (kJ/mol)	$\log A$ (s ⁻¹)		
Fn	0.61	127.36 ± 1.67	6.92 ± 0.13	0.9987	
R3	3	129.23 ± 1.58	6.60 ± 0.12	0.9986	
R2	2	124.37 ± 1.50	6.37 ± 0.12	0.9985	
An	1.11	131.82 ± 2.99	7.36 ± 0.23	0.9974	
Multivariate Non-Linear Regression results					
Model	order/dimension, <i>n</i>	<i>w</i> ^a	<i>E</i> _a (kJ/mol)	$\log A$ (s ⁻¹)	<i>R</i> ²
1) Fn	1.44	0.17	174.23 ± 18.33	11.61 ± 1.62	
2) Fn	0.45	0.50	123.52 ± 6.74	6.88 ± 0.56	0.99938
3) R2	2		106.95 ± 21.01	5.26 ± 1.58	
1) Fn	0.73	0.48	143.46 ± 3.85	8.62 ± 0.35	
2) An	2.18		117.55 ± 4.21	6.23 ± 0.31	0.99936
1) Fn	1.60	0.09	199.85 ± 27.42	14.09 ± 2.37	
2) R2	2		124.43 ± 1.89	6.37 ± 0.13	0.99931

^a Parameter *w* is a weighting factor used in multiple reaction models

The two Fn steps can be interpreted as a mechanism beginning with slow product nuclei formation at $\alpha < 0.2$ that, at higher conversion ($\alpha < 0.7$), accelerates to form a dense reaction layer varying in thickness relative to the ease of H₂O escape [24]. The agreement with the R2 model at $\alpha > 0.7$ can be attributed to a reaction mechanism where advancement of the reaction interface is related to the layered crystal structure of Ca(OH)₂, i.e. if product nucleation occurs at the more-reactive edge surfaces of a plate-like crystal then the reaction layer would progress inwards two-dimensionally [25]. Although another possible explanation to this type of physico-

geometric behavior was observed by Barret [26], i.e. the characteristics of the phase-boundary reaction depends on the shape of the crucible and the arrangement of powder used in experiments. Furthermore, the kinetic parameters arrived at here have precedence in the literature, where the predominant activation energies reported and the relevance of a kinetic model with multiple consecutive steps are in agreement with previously reported results by other authors [16], [24], [27], [28].

Sample 2

Table 6 summarizes the regression kinetic analysis for TG experiments with sample 2. Compared with sample 1, the linear regression analysis for sample 2 shows a good, but slightly less correlated, fit with familiar kinetic models. In contrast, sample 2 gives apparent activation energies that are ~ 15 kJ/mol greater than that in sample 1. Furthermore, the best fit model for a one-step process is the R3 model compared to an n th order reaction model in sample 1. In light of results from Friedman and master curve analysis, configurations of two and then three consecutive reactions were tested in the non-linear regression analysis.

The best fit given here is for three consecutive reactions beginning with an 2nd order (F2) reaction with E_a between 172-256 kJ/mol and $\log A$ between $11\text{-}18 \text{ s}^{-1}$ until $\alpha = 0.11$. Afterwards a 2-dimensional phase boundary (R2) reaction follows with E_a between 134-149 kJ/mol and $\log A$ between $7\text{-}9 \text{ s}^{-1}$ until $\alpha = 0.78$. Finally, a three dimensional nucleation/growth (A3) reaction commences with E_a between 126-181 kJ/mol and $\log A$ between $7\text{-}9 \text{ s}^{-1}$. In comparison to sample 1, the n th order model in sample 2 only dominates in the first step of the transformation. With the addition of graphite in sample 2, water vapor can act as an intermediate at two separate reaction interfaces [27], [29], i.e. $\text{CaO}/\text{H}_2\text{O}_{(g)}$ and $\text{H}_2\text{O}_{(g)}/\text{C}$. This behavior can result in a more heterogenous water vapor distribution in the sample after initial surface dehydration and nuclei formation thereby making the R2 model more appropriate as the next step in the transformation. Furthermore, the model for sample 2 includes a nucleation and growth step not present in the analysis of sample 1. If we consider the reversible carbon gasification/deposition reaction (2) listed earlier in the introduction, it is possible that the nucleation and subsequent ingestion or gasification of solid carbon at the $\text{H}_2\text{O}_{(g)}/\text{C}$ interface is the mechanism implied by the A3 step.

Table 6 Selected results of regression kinetic analysis for sample 2

Model	order/dimension, n	Linear Regression results		
		E_a (kJ/mol)	$\log A$ (s^{-1})	R^2
R3	3	144.63 ± 3.20	7.40 ± 0.24	0.99828
Fn	0.71	142.88 ± 3.53	8.00 ± 0.27	0.99826
R2	2	139.61 ± 2.24	7.17 ± 0.17	0.99802
An	1.06	151.19 ± 4.93	8.45 ± 0.36	0.99762
Multivariate Non-linear Regression results				
Model	order/dimension, n	w	E_a (kJ/mol)	$\log A$ (s^{-1})
1) F2	2	0.11	213.87 ± 41.77	14.51 ± 3.46
2) R2	2	0.67	142.67 ± 7.76	7.57 ± 0.72
3) A3	3		137.36 ± 10.97	7.37 ± 0.77
1) Fn	1.83	0.14	205.43 ± 43.19	13.72 ± 3.56
2) R2	2		142.05 ± 6.03	7.36 ± 0.43
1) Fn	0.76	0.42	162.56 ± 10.28	9.76 ± 0.91
2) An	1.86		141.41 ± 7.53	7.66 ± 0.54

Sample 3

Table 7 shows regression results from TG tests of sample 3. Similar to samples 1&2, the same familiar kinetic models give the best fit in linear regression analysis of sample 3 although with the lowest R^2 of all three samples. As with sample 2, one-step models in sample 3 show increased average apparent activation energies, ~30 kJ/mol larger, when compared to sample 1. Friedman and master curve analysis point to multi-step behavior in sample 3. Therefore, in non linear regression analysis a configuration of multiple consecutive reactions was investigated.

The result of the best-fit model starts as a 2nd order step with E_a between 240-281 kJ/mol and $\log A$ between 16-20 s⁻¹ until $\alpha = 0.17$ and then a two dimensional phase boundary (R2) step commences with E_a between 153-157 kJ/mol and $\log A$ 8-9 between s⁻¹. The mass loss behavior of sample 3 is quite similar to dehydration of pure Ca(OH)₂ in sample 1, as seen by the similar peak weight loss temperatures at lower heating rates in Table 3. Although, like sample 2, the model which best fits sample 3 implies a more heterogenous-type mechanism, i.e. adherence to the phase boundary model over a larger range of α . This can likely be due to the formation of some intermediate amorphous CaO•H₂O•Fe₂O₃ phase at contact points of particle surfaces during the progression of the dehydration reaction interface. A consequence of this intermediate could be that subsequent calcium ferrite formation would be anion-modified therefore more catalytically active [30] and would more readily adsorb water molecules.

Table 7 Selected results of regression kinetic analysis for sample 3

Model	order/dimension, n	Linear regression results		
		E_a (kJ/mol)	$\log A$ (s ⁻¹)	R^2
Fn	0.80	161.92 ± 4.66	9.59 ± 0.36	0.99736
An	1.00	170.38 ± 6.23	10.29 ± 0.47	0.99717
R3	3	156.59 ± 4.16	8.68 ± 0.32	0.99707
R2	2	150.69 ± 4.05	8.37 ± 0.31	0.99615
Non-linear regression results				
Model	order/dimension, n	w	E_a (kJ/mol)	$\log A$ (s ⁻¹)
1) F2	2	0.17	260.43 ± 20.16	18.49 ± 1.60
2) R2	2		155.05 ± 1.53	8.69 ± 0.12
1) Fn	0.93	0.39	193.21 ± 16.55	12.61 ± 1.41
2) An	1.73		154.44 ± 11.28	9.00 ± 0.82

3.4 SEM results of raw samples and heat treated samples (10°C/min)

Figure 9 shows micrographs of samples from tests with sample 1, Ca(OH)₂, interrupted at temperatures corresponding to the fractional mass loss at the beginning or end of reaction steps defined earlier in the kinetic results. Particle "a" in Figure 9 is a representative particle of polycrystalline reagent Ca(OH)₂ at room temperature.

Particle "b" illustrates the progress of reaction to 380°C and $\alpha < 0.2$. Here we see some crack formation on the surface of a dense reaction layer most likely due to gas pressure accumulation from inside the bulk reactant. The appearance of a dense surface reaction layer is prevalent at this point in the dehydration and the occurrence of crack formation seems to be dependent on individual particle size, i.e. larger particles show more crack formation. Particle "c" shows an example of the plate-like crystal CaO product observed after heat treatment to 600°C.

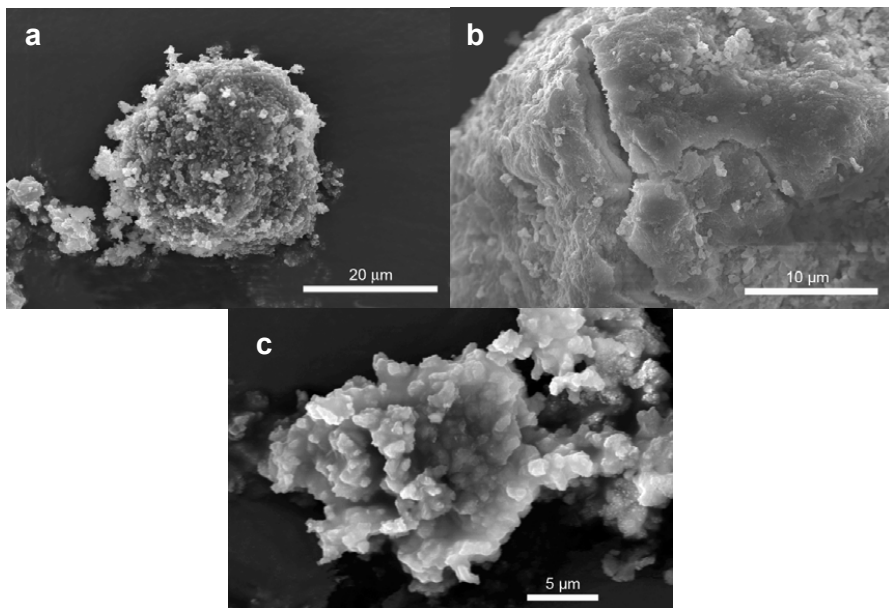


Figure 9 SEM micrographs of $\text{Ca}(\text{OH})_2$ samples; a) raw, b) 380°C , c) 600°C

Figure 11 shows micrographs of reagent graphite and heat treated samples of sample 2 $\text{Ca}(\text{OH})_2 + \text{C}$. Micrograph “a” shows a general view of the reagent graphite used in the current study demonstrating that graphite particles are to a majority plate-like in shape with some spherical particles present.

Particle “b” from heat treatment of sample 2 at 420°C ($\alpha < 0.15$) shows how a graphite particle seemingly has started to wrap itself around a partially reacted $\text{Ca}(\text{OH})_2/\text{CaO}$ grain. This phenomenon appears regularly in particles observed from sample 2 after heat treatment. An explanation for this can be interpreted from the XRD results where we observed that after heat treatment the calculated graphite crystallite length/width grew in lieu of the stacking height perhaps facilitated by the dehydration of $\text{Ca}(\text{OH})_2$ particles. A gasification and subsequent deposition of graphite crystallites would most likely occur at the edges of graphite particles tangent to the $\text{Ca}(\text{OH})_2/\text{CaO}$ particle surface, thereby causing the plate-like graphite to “wrap” itself around the $\text{Ca}(\text{OH})_2/\text{CaO}$ particles. An illustration of the mechanism is shown in Figure 10.

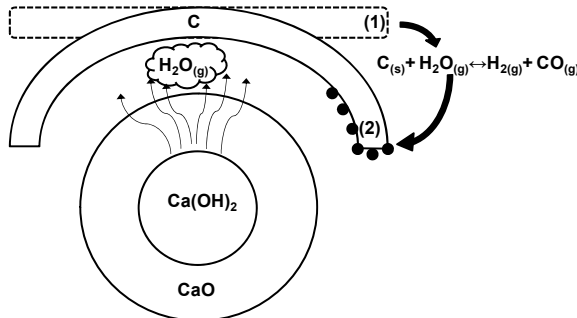


Figure 10 Illustration of graphite gasification/deposition

At a larger fractional mass loss ($\alpha > 0.5$ and 460°C) we observed morphology illustrated by particle "c". In the space between a particle of " $\text{Ca(OH)}_2/\text{CaO}$ " and a graphite particle there is a formation of solid carbon having noticeable drop-like surface formations. These "drops" are quite possibly condensate carbon from gas phase. Particle "d" shows the formation of polycrystalline plate-like particles of CaO enveloped by a partially reacted graphite particle.

Figure 12 shows micrographs of samples of reagent hematite and $\text{Ca(OH)}_2 + \text{Fe}_2\text{O}_3$. Particle "a" is an example of the polycrystalline reagent hematite used in this study. Particle "b" shows areas of Fe_2O_3 to the upper right and areas of partially dehydrated Ca(OH)_2 to the lower left with a small area of intermediate phase in between the two at the left. This intermediate phase could be the amorphous phase referenced earlier in the kinetic analysis. Particle "c" shows a particle of crystalline CaO containing areas enriched with iron, circled in white, which could be the beginnings of calcium ferrite formation at the edges.

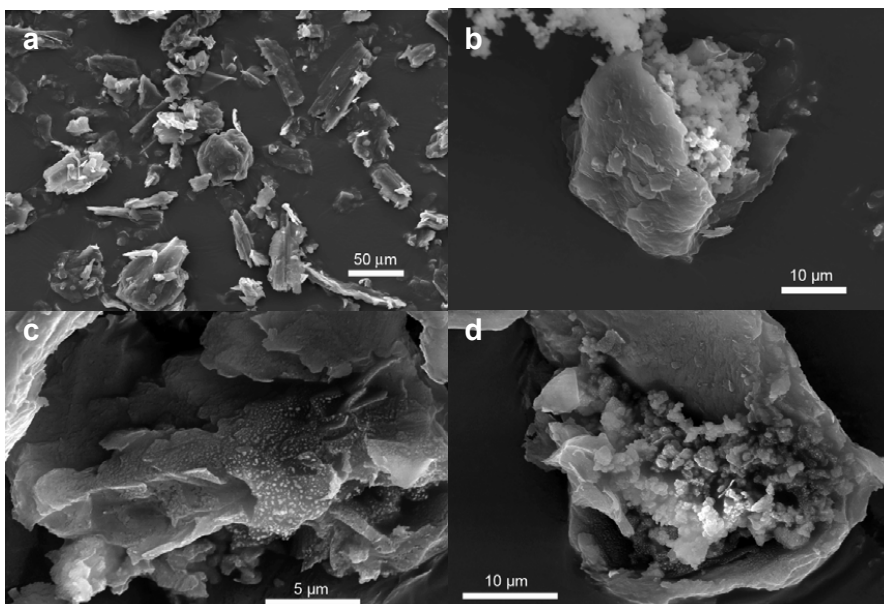


Figure 11 SEM micrographs of $\text{Ca(OH)}_2 + \text{C}$ samples; a) raw graphite, b) 420°C , c) 460°C , d) 600°C

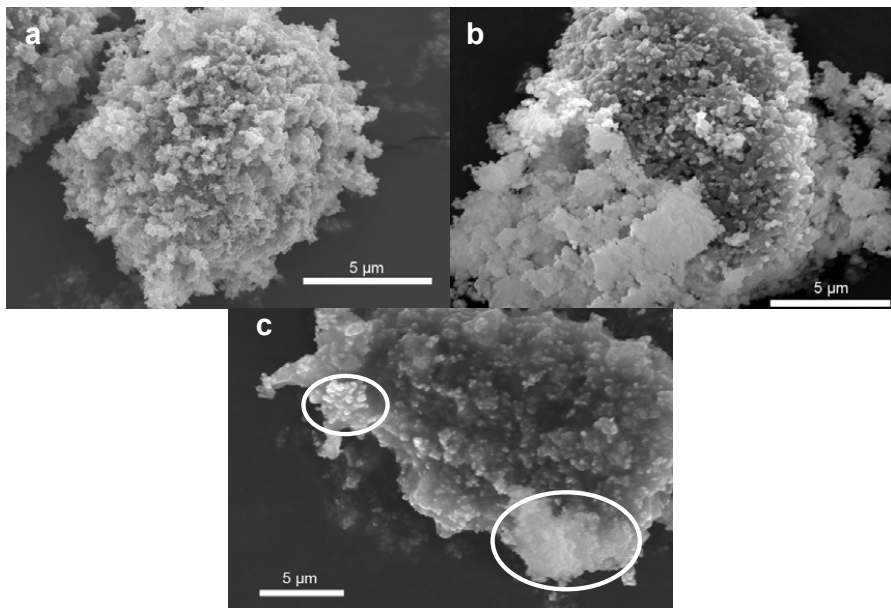


Figure 12 SEM micrographs of $\text{Ca}(\text{OH})_2 + \text{Fe}_2\text{O}_3$ samples; a) raw hematite, b) 420°C , c) 600°C .

4. Conclusions

The dehydration of the reagent $\text{Ca}(\text{OH})_2$ under the experimental conditions in this study occurs in two main steps. First, a probable n th order mechanism function occurs divided into two parts, a slow product nuclei formation and then an accelerated dense reaction layer formation varying in thickness relative to the ease of H_2O escape. Second, a probable two-dimensional phase boundary mechanisms function where CaO grain growth begins at the more-reactive edge surfaces of a plate-like crystal and predominately progresses inwards two-dimensionally.

The dehydration of $\text{Ca}(\text{OH})_2$ in the presence of C is superimposed by several reactions involving C. The overall transformation occurs in three main steps. First, an initial 2nd order function describing slow nuclei formation dominates. Second, a two-dimensional phase boundary function is believed to control the CaO grain growth over a larger conversion interval, than $\text{Ca}(\text{OH})_2$ alone, because water vapor acts as an intermediate at two separate reaction interfaces causing a more heterogeneous water vapor distribution in the sample after initial surface dehydration and nuclei formation. Third, a three-dimensional nucleation and growth function dominates and can be described as the nucleation and subsequent ingestion or gasification of solid carbon at the $\text{H}_2\text{O}_{(g)}/\text{C}$ interface.

The dehydration of $\text{Ca}(\text{OH})_2$ in the presence of Fe_2O_3 is very similar to $\text{Ca}(\text{OH})_2$ alone. Again, the dehydration occurs in two main steps. First, a 2nd order function which describes nuclei formation and second, a two-dimensional phase boundary function over a larger range of conversion when compared to $\text{Ca}(\text{OH})_2$ alone. This behavior is likely due to the formation of some intermediate amorphous $\text{CaO}\cdot\text{H}_2\text{O}\cdot\text{Fe}_2\text{O}_3$ phase at contact points of particle surfaces during the progression of the dehydration reaction interface that later results in minor calcium ferrite formation.

5. References

- [1] A. Fleischanderl, J. Pesl, and W. Gerbert: Aspect of Recycling of Steelworks By-Products Through the BOF, SEAlSI Quarterly, v 28, n 2, April 1999, p. 51-60.
- [2] R. L. Nyirenda: The Processing of Steelmaking Flue Dust: A Review, Proc. of the First Int. Conf. of Minerals Engineering '91, Singapore, 1991, p. 1003-1025.
- [3] T. de Bruin and L. Sundqvist: Briquetting: One way of treating by-products at SSAB Tunnpåt in Luleå, ICSTI / Ironmaking Conf. Proc., Toronto, Canada, 1998, p. 1263-1273.
- [4] S.R. Balajee, P.E. Callaway Jr., and L.M. Keilman: Production and BOF recycling of waste oxide briquettes at Inland Steel, I&SM, August 1995, p. 11-21.
- [5] M.P. Landow, J.F. Torok, T.P. Barnett, J.F. Crum, and J. Nelesen, Jr.: An Overview of Steel Mill Waste Oxide Recycling by Cold Bonded Roll Briquetting, ICSTI, 1998, p. 1237-1243.
- [6] F.W. Harrison, G. A. Dunlop, T. J. Bonham, and R. D. Borthwick: Recycling of Dusts and Sludges in the BOF, Steelmaking Conference Proceedings. Vol. 78, Nashville, TN, USA, 2-5 April, 1995, p. 47-50.
- [7] J.A. Lopez C., R.V. Ballesteros B., J.M. Guipsot T., and R. Ramirez: Development of BF flue dust briquette for recycling in BOF at AHMSA, ICSTI, 1998, p. 1275-1279.
- [8] J.S. Ahn, C.M. Chon, H.S. Moon, and K.W. Kim: Arsenic removal using steel manufacturing byproducts as permeable reactive materials in mine tailing containment systems, Water Research, Vol 37, Issue 10, May 2003, p. 2478-2488.
- [9] R. Robinson: High temperature properties of by-product cold bonded pellets containing blast furnace flue dust, *Thermochimica acta* 432 (2005), p. 112-123.
- [10] R. Robinson, Nourreddine Menad and Bo Björkman: Low Temperature Behavior of the $\text{Ca}(\text{OH})_2\text{-C}$ System and its Significance on the Self-Reduction of Cold Bonded By-Product Agglomerates: The Fourth International Congress on the Science and Technology of Ironmaking : Proceedings, ICSTI 06. The Iron and Steel Institute of Japan, 2006, p. 311-314.
- [11] M.C. Mantovani and C. Takano: The Strength and the High Temperature Behaviors of Self-reducing Pellets Containing EAF Dust, *ISIJ Int.*, Vol 40, No. 3, 2000, p. 224-230.
- [12] K. Kumabe, H. Moritomi, R. Yoshiie, S. Kambara, K. Kuramoto, Y. Suzuki, H. Hatano, S.Y. Lin, and M. Harada: Gasification of Organic Waste with Subcritical Steam under the Presence of a Calcium-Based Carbon Dioxide Sorbent, *Ind. Eng. Chem. Res.* 2004, 43, p. 6943-6947.
- [13] J. Wang and T. Takarada: Role of Calcium Hydroxide in Supercritical Water Gasification of Low-Rank Coal, *Energy & Fuels* 2001, 15, p. 356-362.
- [14] T. Inui, T. Otowa, and F. Okazumi: Gasification of Active Carbon by Iron-Based Composite Catalysts for Obtaining Directly a Gas Optional H_2/CO Ratio, *Carbon*, Vol. 23, No.2, 1985, p. 193-208.
- [15] S. Sato, S.Y. Lin, Y. Suzuki, and H. Hatano: Hydrogen production from heavy oil in the presence of calcium hydroxide, *Fuel* 82 (2003), p. 561-567.
- [16] J. Opfermann: Kinetic Analysis Using Multivariate Non-Linear Regression, I. Basic concepts, *Journal of Thermal Analysis and Calorimetry*, Vol. 60 (2000), p. 641-658.
- [17] P. Scherrer: *Nachrich. Gesellsch. Wissensch. Göttingen*, Vol. 2, 1918, p. 98.
- [18] A.K. Kercher and D. C. Nagle.: Microstructural evolution during charcoal carbonization by X-ray diffraction analysis, *Carbon*, Vol. 41, 2003, p. 15-27.
- [19] B. Bergman: Solid-State Reactions between CaO Powder and Fe_2O_3 , *J. Am. Ceram. Soc.*, Vol. 69, No. 8, 1986, p. 608-611.
- [20] A. Ortega: The Kinetics of Solid-State Reactions Toward Consensus, Part 2: Fitting Kinetics Data in Dynamic Conventional Thermal Analysis, *International Journal of Chemical Kinetics*, Vol. 34, 2002, p. 193-208.

- [21] N. Koga, J. Sestak, and J. Malek: Distortion of the Arrhenius parameters by the inappropriate kinetic model function, *Thermochimica Acta*, Vol. 188, 1991, p. 333.
- [22] J.M. Criado, A. Ortega, F. Gotor: Correlation between the shape of controlled-rate thermal analysis curves and the kinetics of solid-state reactions, *Thermochimica Acta*, Vol. 157, 1990, p. 171-179.
- [23] G.I. Senum and R.T. Yang: Rational approximations of the integral of the Arrhenius function, *Journal of Thermal Analysis*, Vol. 11, 1977, p. 445-447.
- [24] Andrew K. Galwey and Genevieve M. Laverty: A kinetic and mechanistic study of the dehydroxylation of calcium hydroxide, *Thermochimica Acta*, 228 (1993), p. 359-378.
- [25] N. Koga and H. Tanaka: A physico-geometric approach to the kinetics of solid-state reactions as exemplified by the thermal dehydration and decomposition of inorganic solids, *Thermochimic Acta*, Vol. 388, 2002, p. 41-61.
- [26] P. Barret: International Proceedings of the 4th Symposium on the Reactivity of Solids, Amsterdam, 1960, p. 178.
- [27] R.Sh. Mikhail, S. Brunauer, and L.E. Copeland: Kinetics of the Thermal Decomposition of Calcium Hydroxide, *Journal of Colloid and Interface Science*, 21 (1966), p. 394-404.
- [28] D. Chen, X. Gao, and David Dollimore: The application of non-isothermal methods of kinetic analysis to the decomposition of calcium hydroxide, *Thermochimica Acta*, 215 (1993), p. 65-82.
- [29] J. Gadsby, C.N. Hinshelwood, F.R.S., and K.W. Sykes: The kinetics of the reactions of the steam-carbon system, *Proceedings of the Royal Society of London. Series A, Mathematical and Physical Sciences*, Vol. 187, No. 1009 (Oct. 22, 1946), p. 129-151.
- [30] A.P. Il'in, N.N. Smirnov, and A.A. Il'in: Mechanochemical Synthesis of Calcium and Copper Ferrite Catalysts for Medium-Temperature Carbon Monoxide Conversion, *Kinetics and Catalysis*, Vol. 47, No. 6, 2006, p. 929-934.

V

OPTIMIZATION IN THE Ca(OH)₂-C-Fe₂O₃ SYSTEM WITH REGARD TO INTERNAL RECYCLING IN INTEGRATED STEELMAKING: PRACTICAL AND KINETIC STUDIES

R. Robinson¹, F. Patisson² and B. Björkman¹

¹Luleå University of Technology, SE-97187 Luleå, Sweden

²LSG2M, Nancy-Université, Parc de Saurupt, CS 14234, F-54042 Nancy Cedex, France

Abstract

By-products from integrated iron and steel production are currently not utilized optimally in light of their suitability as recycle. A large content of the fine particulate by-products from iron and steelmaking consist of iron oxides, calcium based minerals and carbon in various forms. The understanding and optimization of the mineral systems in these fines can therefore increase reduction efficiency and decrease dependency on ever increasing raw material costs. In this study we have attempted to explain the complex reactions that occur during the dehydration of Ca(OH)₂, in the presence of solid carbon and Fe₂O₃, in order to clarify their role as eventual precursors to the reduction and high temperature strength characteristics in feedstock agglomerates of iron and steelmaking by-products. Initially, thermal analysis testing was used to determine an optimum mix of Ca(OH)₂, C, and Fe₂O₃ from a reduction and strength standpoint. A factorial design was used to arrive at the different mix compositions. From these results, more detailed simultaneous thermogravimetric (TG) and differential thermal analysis (DTA) testing was performed on the chosen optimal mix of Ca(OH)₂, C, and Fe₂O₃ to test the influence of heating rate and particle size on the transformations occurring below 800°C in inert atmosphere. Furthermore, selected samples were investigated using X-ray diffraction (XRD) analysis and electron microscope (SEM) analysis. Comparative analysis of the results reveals details of the different reaction processes involved in each system.

1. Introduction

Worldwide, iron and steelmaking facilities generate between 30-40 million tons of by-product dusts that are feasible for recycling [1]. The recycling and utilization of by-product agglomerates containing these dusts has shown to result in several industrial benefits, mostly in the decrease of natural resource dependence, reduction of landfill and indirectly as energy savings [2]. These by-product dusts contain considerable amounts of iron oxides, hydrated lime and carbon [3], [4]; a chemistry that is suitable for preparation of self-reducing/self-fluxing agglomerates. The inherent chemistry and proximity of reactants in self-reducing by-product agglomerates also gives a technical advantage as the rate of reaction is high resulting in a process with high productivity [5]. Therefore, a good understanding of the self-reduction characteristics is essential for the further development of cold bonded agglomerates containing by-products for use as recycle in the steelmaking industry. In recent decades many researchers have studied the reduction behavior of composites containing various assemblages of iron oxide and carbon. Mantovani and Takano have reported that the reduction of self-reducing pellets containing a mixture of EAF dust and coal can be described by the following reactions: (1) direct reduction

(solid/solid) between iron oxides and carbon; and (2) gas/solid reactions. As the speed of solid/solid reaction is much slower than the gas/solid reaction, the global process occurs via gaseous intermediates such as $\text{CO}_{(g)}$, $\text{CO}_{2(g)}$, $\text{H}_{2(g)}$ and $\text{H}_2\text{O}_{(g)}$ [6]. Likewise, Kashiwaya et al. showed that the basic reaction mechanism of a composite pellet containing hematite and graphite starts at ~923 K as a reaction caused by the direct contact between iron oxide and carbon and then, after subsequent separation of the iron oxide/carbon interface, the reaction continues as a coupling phenomenon between reduction and carbon gasification [7]. Reduction can start at even lower temperatures in the event of gas generation in the solid due to decomposition and/or volatilization. Mookherjee et al. observed that the volatile matter in non-coking coal contributed to the reduction of iron ore at temperatures over 773 K [8]. Furthermore, Lu et al. showed that volatile matter in coal contributed to the reduction of iron oxide and was effectively consumed in the process and direct contact of iron ore fines and coal fines increased the reduction rate in the *prereduction* stage of an LB furnace [9], [10].

Various studies have been found in the literature concerning gasification of carbonaceous material in the presence of different metal-based sorbents/catalysts, mostly at elevated pressure ~20 MPa [11]-[13]. Results from S. Sato et al. have shown that water contained in $\text{Ca}(\text{OH})_2$ molecules is sufficient to produce $\text{H}_{2(g)}$ from reaction with carbon content in samples of a vacuum residue of Arabian light crude oil at temperatures above 600°C and pressures 4-5 MPa [14].

Some critical reactions that are relevant for conditions occurring in cold bonded pellet samples during heat treatment in inert gas have been found in the literature. These reactions are defined as metal dehydration, the steam-carbon reaction and/or water-gas shift reaction, the Boudouard reaction and subsequent reduction of iron oxide through its reaction with gaseous reductants generated from former reactions [15]. From previously published results [16], Figure 1 demonstrates that during the decomposition of hydrated lime in the presence of graphite other gaseous products, in relatively smaller amounts, are generated besides H_2O .

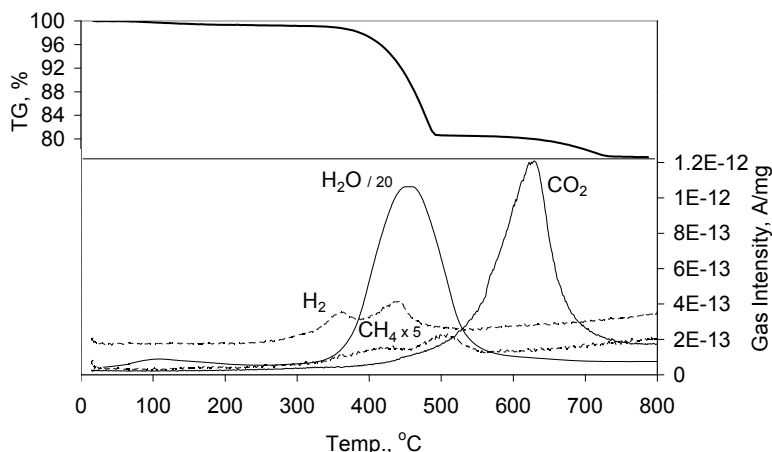


Figure 1 TG and gas analysis of $\text{Ca}(\text{OH})_2:\text{C}$ (mol 1:4) sample at 10°C/min in Ar [16]

Therefore, the objective of the present work is to study the mechanisms of reaction in the $\text{Ca}(\text{OH})_2\text{-C-Fe}_2\text{O}_3$ system at temperatures below 800°C and at ambient pressure. The reactions of most importance to this study are listed below:



2. Experimental

2.1 Materials

The raw materials used in this study are all laboratory grade reagents. Calcium hydroxide, 99.8% pure powder, was supplied from Riedel-deHaen; standard Hematite, 99.8%(metals basis) pure and -325 mesh powder, was supplied from Alfa Aesar; Graphite, 99% pure and -300 mesh, was supplied from Alfa Aesar. Micro briquettes were prepared from the reagent powder mixtures in a hand press, 1.5N/mm², resulting in cylinders having average dimensions of 3mm ϕ x 3mm H and sample weights of 15.7 ± 2.3 mg. The particle size distributions of the standard sized reagents are given in Figure 2. The reagent mixture compositions, shown in Table 2, used during initial optimization experimental work are based on relative compositions between the three reagents in previously studied cold bonded agglomerates [4].

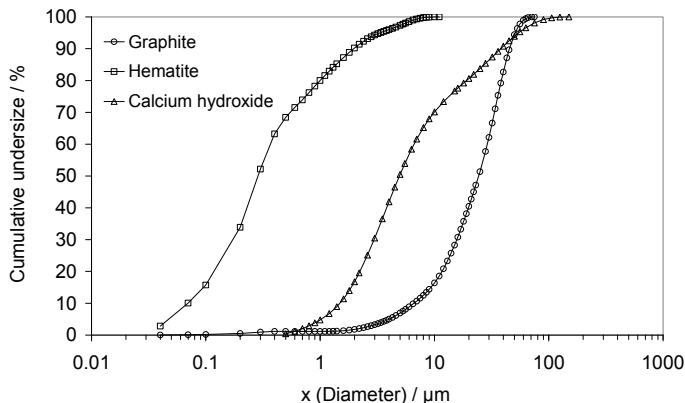


Figure 2. Particle size distribution of the reagents

Table 1 Mix compositions in wt%

Mix #	standard		
	Fe ₂ O ₃	Ca(OH) ₂	C
1	50	30	20
2	55	25	20
3	57.5	30	12.5
4	60	20	20
5	62.5	25	12.5
6	65	30	5
7	67.5	20	12.5
8	70	25	5
9	75	20	5

For reasons explained later in this study, mix 5 in Table 1 was chosen as the optimal mix composition to investigate further. In order to study the influence of particle size on the transformations occurring in the Ca(OH)₂-C-Fe₂O₃ system the particle size of Fe₂O₃ was changed between sample 1 and sample 2 as shown in Table 2; the standard-sized Hematite as described earlier and a nano-sized Hematite, 99.999% pure powder with an average size of 30 nm, supplied from Aldrich. Again, micro briquettes were prepared using the same method mentioned earlier resulting in an average sample size of 18 ± 1 mg.

Table 2 Mix 5 sample compositions in wt%

Sample	Ca(OH) ₂	C	standard	nano
			Fe ₂ O ₃	Fe ₂ O ₃
1	25	12.5	62.5	
2	25	12.5		62.5

2.2 Methods

A Setaram Setsys Evolution instrument equipped with simultaneous thermo-gravimetric (TG), differential thermal (DTA), and quadrapole mass spectrometric (QMS) analysis was used in thermal analysis studies. The sensitivity of the TG balance is ± 0.3 µg.

Two types of tests were performed on the samples. First, in order to find an optimal composition, dynamic TG/DTA tests were conducted on samples shown in Table 1 heated from 20°C to 800°C at 10°C/min in helium with a constant flow rate of 60 ml/min. Cylindrical α-Al₂O₃ crucibles with a diameter of 4 mm and a capacity of 100 µl were used in these tests. Selected samples were later analyzed using a Siemens D5000 X-ray powder diffractometer using Ni filtered Cu Kα radiation at 40 kV and 50 mA.

Second, to investigate the influence of heating rate and particle size on the optimal mix, TG/DTA tests were conducted on samples shown in Table 2 heated at three different heating rates 2, 10 and 32°C/min with other conditions held constant. Selected samples were later analyzed using a Philips XL 30 scanning electron microscope. These TG results were evaluated with a kinetics software package.

2.3 Kinetic Analysis

TG results from experiments have been analyzed using the Netzsch Thermokinetic software package [17]. In the kinetic analysis, experimental TG results have been expressed as reaction extent α ,

$$\alpha = (W_i - W) / (W_i - W_f) \quad (7)$$

where W is the weight or wt.% of the sample at a given time, and W_i and W_f are the initial and final values for the transformation.

A multi-curve method has been applied to the non-isothermal measurements of each sample, specifically the Friedman iso-conversion method. Friedman analysis is based on the Arrhenius equation in a form shown here in Eq. (8):

$$\ln(d\alpha/dt) = \ln(A/f(\alpha)) - E/RT \quad (8)$$

The software provides values for the activation energy, E , and the logarithm of the pre-exponential factor, $\log A$. This analysis has been used as a precursor to linear and non-linear regression parts of the kinetic analysis software in order to estimate the magnitude of activation energy in correlation to conversion degree and temperature. In the multiple linear regression section, a series of experimental data was fit to a variety of different kinetic models for a one-step process. Based on results from Friedman analysis and multiple linear regression, multivariate non-linear regression was used to fit TG data to multi-step consecutive processes with the goal of outlining reaction mechanisms of the system $\text{Ca}(\text{OH})_2\text{-C-Fe}_2\text{O}_3$ within the temperature range of 300-800°C. The kinetic models appearing in this study are summarized in Table 3.

Table 3 Kinetic models used in the rate equation, $d\alpha/dt = -A\exp(-E_a/RT)f(\alpha)$

Code	$g(\alpha)$	$f(\alpha)$	Kinetic model type
Fn	$(1/(1-\alpha)^{n-1})-1$	$(1-\alpha)^n$	n^{th} -order
R2	$1-(1-\alpha)^{1/2}$	$2(1-\alpha)^{1/2}$	Two-dimensional phase boundary
R3	$1-(1-\alpha)^{1/3}$	$3(1-\alpha)^{2/3}$	Three-dimensional phase boundary
B1	$\ln(\alpha/(1-\alpha))$	$(1-\alpha)\alpha$	Prout-Tompkins autocatalysis
An	$(-\ln(1-\alpha))^{1/n}$	$n(1-\alpha)[-\ln(1-\alpha)]^{(n-1)/n}$	Avrami-Erofeev n -dimensional nucleation/growth
D1	α^2	$1/2\alpha$	1D-diffusion
D2	$\alpha+(1-\alpha)\ln(1-\alpha)$	$-1/\ln(1-\alpha)$	2D-diffusion
D3	$[1-(1-\alpha)^{1/3}]^2$	$[3(1-\alpha)^{2/3}]/[2[1-(1-\alpha)^{1/3}]]$	3D-diffusion

3. Results and Discussion

3.1 Mix Optimization

The TG/QMS curves for mix 5 are shown in Figure 3 as an example of the results acquired for all mixes. Weight loss and maximum gas intensity data in the temperature range 500-800°C has been used to calculate apparent reduction degree, H_2O utilization degree (participation in carbon gasification) after dehydration of $\text{Ca}(\text{OH})_2$ content, and CO utilization degree in reduction reactions. Results are given in Table 4.

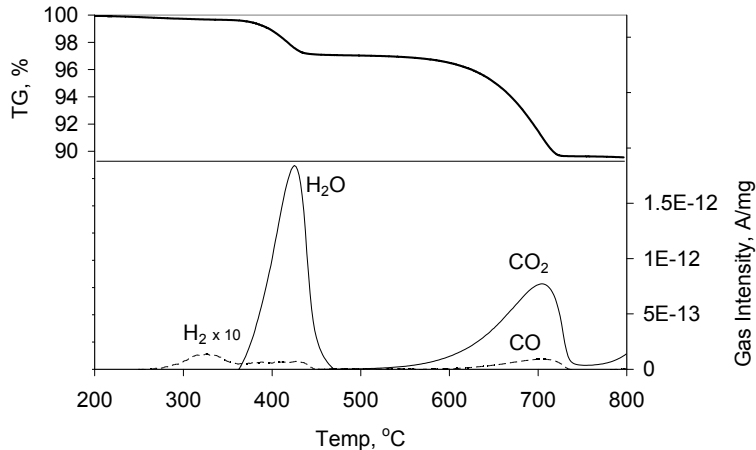


Figure 3 TG/QMS curves from mix 5

Apparent reduction degree was calculated using the following relationships,

$$\Delta m_{O,red} = \Delta m_{total,red} \left[\frac{M_O I_{CO}}{M_{CO}(I_{CO} + I_{CO_2})} + \frac{M_{O_2} I_{CO_2}}{M_{CO_2}(I_{CO} + I_{CO_2})} \right] \quad (9)$$

$$RD\% = \left[\frac{\Delta m_{O,red}}{m_{O,initial}} \right] * 100 \quad (10)$$

where $\Delta m_{total,red}$ is the total weight loss in the temperature range 500-800°C, M_x is the molecular weight of "x", I_y is the maximum intensity of gas "y" from QMS data in the given temperature range and $m_{O,initial}$ is the initial mass of oxygen bound to iron.

Apparent H₂O utilization degree was defined as,

$$\eta_{H_2O} = 100 \times \left(1 - \frac{\Delta m_{dehyd, exp.}}{\Delta m_{dehyd, theor.}} \right) \quad (11)$$

where $\Delta m_{dehyd, exp.}$ is the weight loss due to H₂O below 500°C and $\Delta m_{dehyd, theor.}$ is the calculated theoretical weight loss due to dehydration of Ca(OH)₂ content in every mix.

Apparent CO utilization degree was defined as,

$$\eta_{CO} = 100 \times \left(1 - \frac{I_{CO}}{I_{CO} + I_{CO_2}} \right) \quad (12)$$

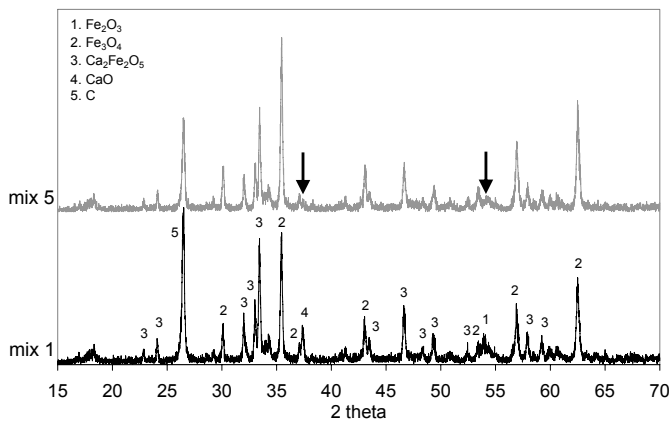
where I_{CO} and I_{CO_2} are the maximum gas intensities from QMS data in the temperature range 500-800°C.

Table 4 Calculated optimization responses

Mix #	Red. degree %	H ₂ O utilization %	CO utilization %
1	35.24	53.69	86.82
2	24.76	34.84	87.33
3	32.58	47.07	86.82
4	22.95	58.94	87.01
5	25.18	51.11	86.99
6	31.20	60.85	85.40
7	11.23	33.35	86.08
8	20.87	52.18	86.75
9	15.66	49.67	86.56
avg	24.41	49.08	86.64

From Table 4, mix 1 and mix 5 are the only mixes which have better than average values for all responses. Preliminary analysis of the optimization experiments shows that Ca(OH)₂ content in mixes 1-9 has the best correlation with the responses given in Table 4. Furthermore, the relationship between C and Ca(OH)₂ contents for each mix has the best correlation with η_{CO} , which is the most empirical of responses. With this in mind, a C:H₂O_(hydrate) molar ratio between 2 and 3 and a C:O_(iron oxide) molar ratio greater than 0.85, as in mix 1 and 5, seems optimal in the context of this study.

XRD results from heat treated samples of mix 1 and mix 5 are shown in Figure 4. The results are quite similar except for the relative absence of remnant CaO and Fe₂O₃ in mix 5 when compared to mix 1 (see arrows in Figure 4). Consequently, it seems that the composition of mix 5 is more favorable for Fe₂O₃ reduction and formation of Ca₂Fe₂O₅ than mix 1. Therefore, mix 5 was chosen as an optimal composition to use in further studies because of its optimal combination of reduction and bonding phase (Ca₂Fe₂O₅) formation characteristics.

**Figure 4** XRD patterns for mix 1 and 5 after heat treatment to 800°C in Ar

3.2 TG/DTA results from samples 1 & 2

From the mix optimization results above, further testing has been conducted on micro briquettes of the optimal mix 5 to investigate the kinetic effect of heating rate and hematite grain size. Three heating rates have been used; 2, 10, and 32°C/min. As mentioned earlier,

the two different average grain sizes of reagent hematite that have been used are ~300 nm (standard) and ~30 nm (nano). TG and DTA results are shown for sample 1 and 2 in Figure 5 and Figure 6.

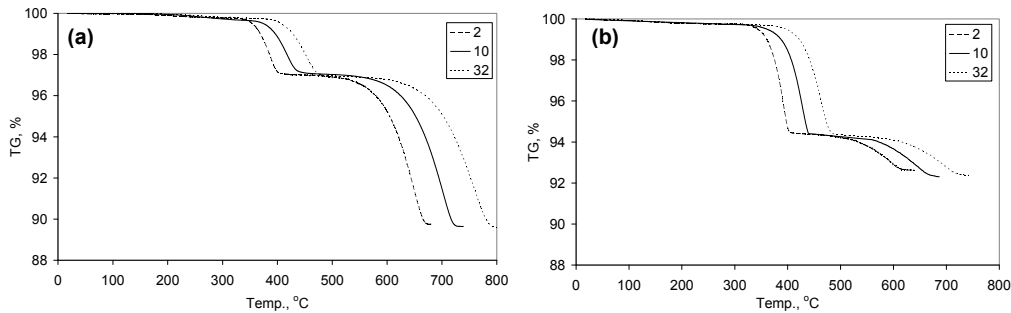


Figure 5 TG results from (a) sample 1 (w/ standard Fe_2O_3) and (b) sample 2 (w/ nano Fe_2O_3) at different heating rates

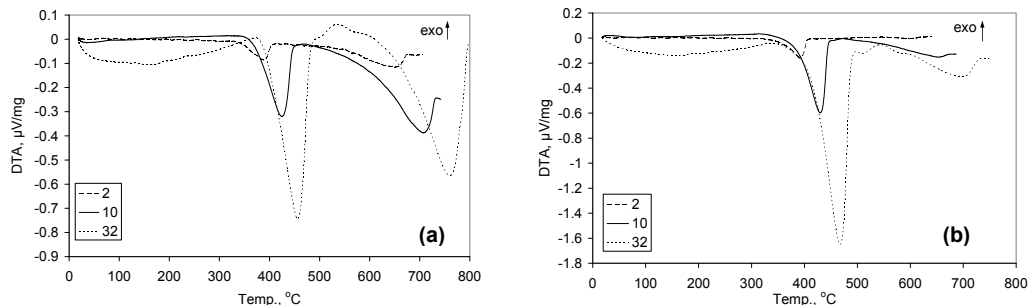


Figure 6 DTA results from (a) sample 1 (w/ standard Fe_2O_3) and (b) sample 2 (w/ nano Fe_2O_3) at different heating rates

TG results reveal obvious differences between the two samples. First, there is a difference in total weight loss between sample 1, ~10 wt%, and sample 2, ~8 wt%. Second, the fraction of total weight loss for the two separate TG steps (see Table 5) in each sample differs, i.e. sample 1 (step 1 ≈ 0.30 , step 2 ≈ 0.70) and sample 2 (step 1 ≈ 0.75 , step 2 ≈ 0.25). Furthermore, Table 6 shows a clear difference in the calculated H_2O utilization of samples 1 and 2 having a marked negative effect on the reduction degree of sample 2.

Table 5 Temp. interval definitions for each TG step in both samples 1 & 2

β (°C/min)	temperature intervals (°C)	
	step 1	step 2
2	320-430	450-680
10	340-470	500-740
32	370-510	540-800

Table 6 Average calculated responses for sample 1 & 2

Sample	Red. degree %	H_2O utilization %	CO utilization %
1	25.18	51.11	86.99
2	7.52	6.00	73.53

DTA results compliment TG results where the heat flow in step 1 is roughly 2 times greater in sample 2 than that in sample 1, and during step 2 the heat flow is roughly 3.5 times greater in sample 1 than that in sample 2. Interestingly, a difference does occur between heating rates where both samples exhibit exothermic heat flow between 500 and 600°C when heated at 32°C/min but not observed at the lower heating rates. Reduction of Fe_2O_3 by CO in Rxn (5) is exothermic as well as carbon deposition by the reverse of Rxn's (2) & (4).

3.3 SEM results of raw samples and heat treated samples 1 & 2

A comparison of the micro briquette samples at room temperature is seen in Figure 7. The difference in particle packing is obvious when comparing sample 1 with standard-sized hematite to sample 2 with nano-sized hematite.

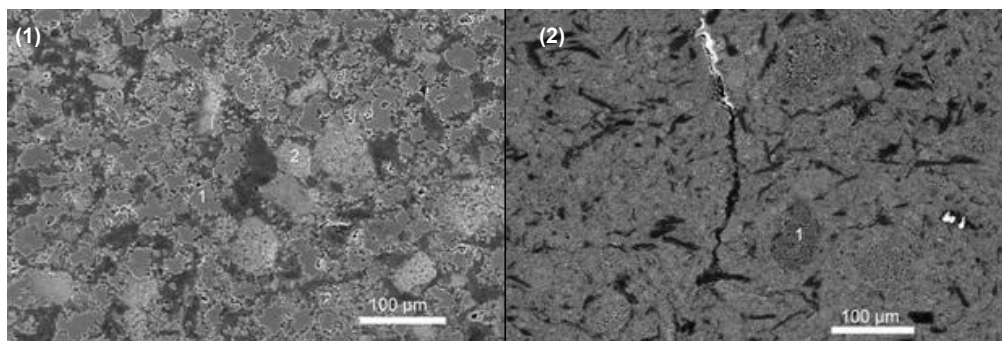


Figure 7 SEM of the raw micro briquette samples (1) and (2)

Figure 8 shows cross sections of micro briquettes of sample 1 heated to 800°C. Micrograph (a) shows the outer edge of a sample heated at 2°C/min. In this sample CaO particles are intact and porous indicating that little structural change has occurred in the grain after dehydration. From EDS results we observed that iron oxide particles have an average iron content lying between magnetite and wustite. Figure 8(b) shows a large iron oxide particle or sintered grouping of many particles after heating at 10°C/min. Here we observed a reduction gradient where points 1 & 3 have iron content close to magnetite and 2 & 4 hematite. In micrograph (c) a particle of calcium rich calcium ferrite seemingly has started to crystallize and become more angular in shape. The reduction degree of iron oxide in sample 1 did increase slightly with an increase in heating rate.

Figure 9(a) shows an example of crack formation in a micro briquette of sample 2 heated at 10°C/min. This behavior was occurred at all heating rates tested but was more prevalent at 10 and 32°C/min. In micrograph (b) we observed a higher degree of reduction in iron oxide grains 2 (semi reduced FeO) & 3 (FeO) than in sample 1. This behavior was not seen throughout the entire micro briquette but in specific areas with a high local concentration of graphite in contact with iron oxide. Grain 1 shows an example of calcium ferrite with a gradient between Ca and Fe content. In Figure 9(c) we observed a highly crystallized grain of $\text{Ca}_2\text{Fe}_2\text{O}_5$ in the middle of a sample heated at 32°C/min.

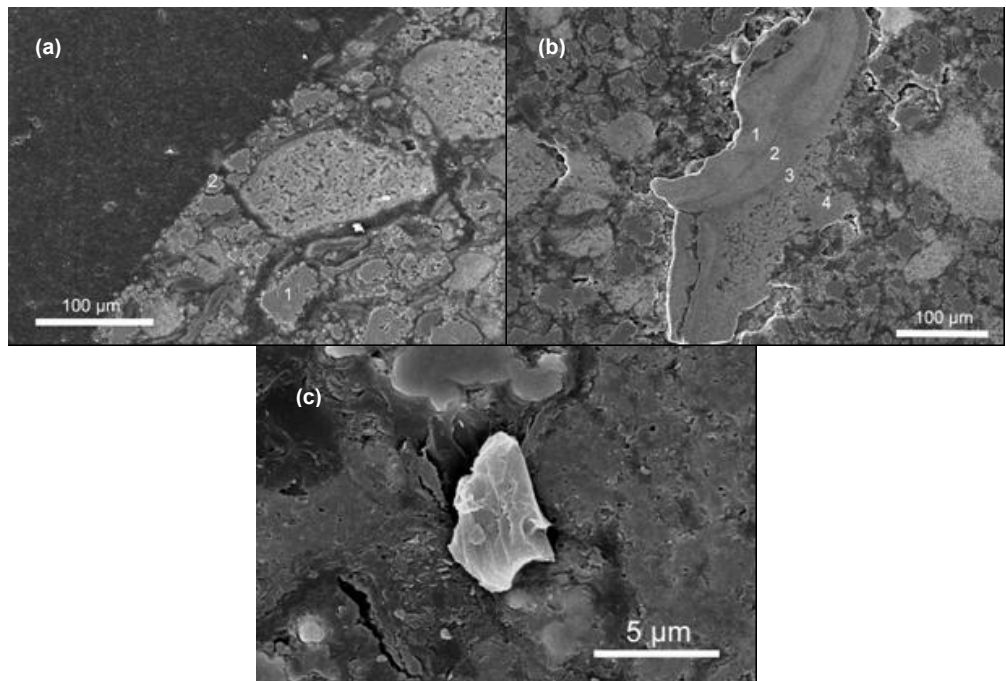


Figure 8 SEM cross sections of heat treated sample 1 at (a) 2°C/min (b) 10°C/min (c) 32°C/min

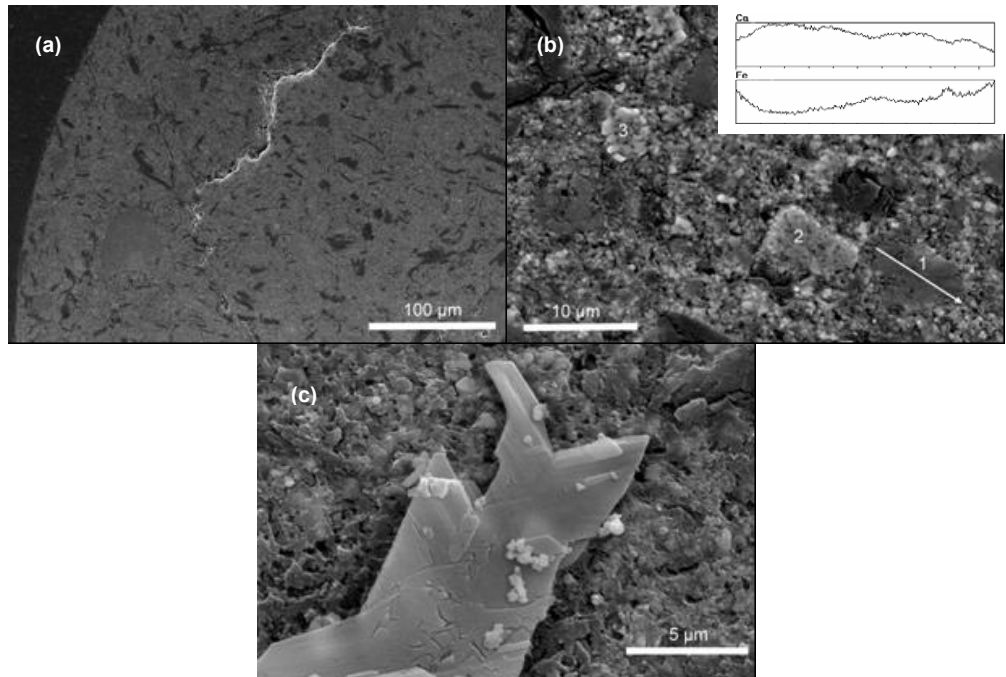


Figure 9 SEM cross sections of heat treated sample 2 at (a) 2°C/min (b) 10°C/min (c) 32°C/min

3.4 Kinetic results from samples 1 & 2

3.4.1 Friedman Analysis and Master Plots

Diagrams illustrating the model-free Friedman analysis of the TG results from samples 1 & 2 are shown in Figure 10 and Figure 11. The TG results have been treated as two step transformations in both samples for ease of evaluation. From Figure 10(1), we see for sample 1 that the activation energy in transition step 1 jumps from an initial value of 80 to 170 kJ/mol at fractional mass loss $\alpha < 0.1$. In the range $0.1 < \alpha < 0.6$, the activation energy fluctuates between 120-150 kJ/mol eventually settling to a value of 150 kJ/mol. Above $\alpha = 0.6$, the activation energy adjusts to a lower level of 140 kJ/mol and gradually decreases near the end of transition. In transition step 2, Figure 10(2), energy levels start understandably where step 1 finished. At $\alpha \leq 0.35$, the activation energy initially increases sharply and then more gradual to a level of 190 kJ/mol. As mass loss increases in this transition, the activation energy decreases and fluctuates between 170 and 180 kJ/mol.

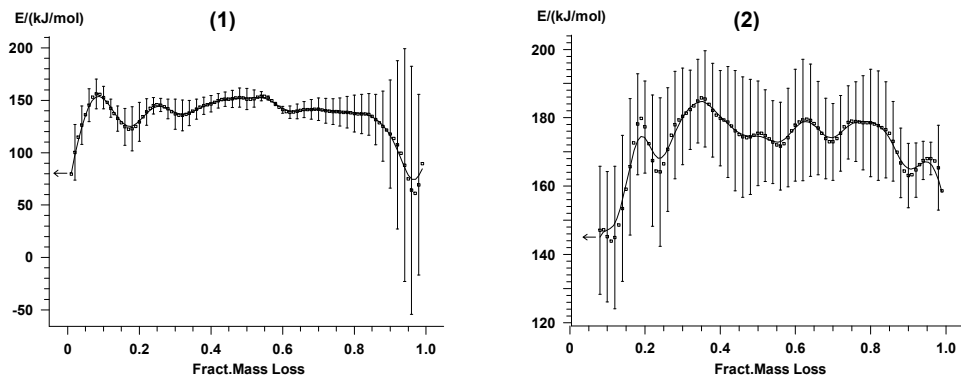


Figure 10 Friedman analysis of sample 1, (1) TG step 1 (2) TG step 2

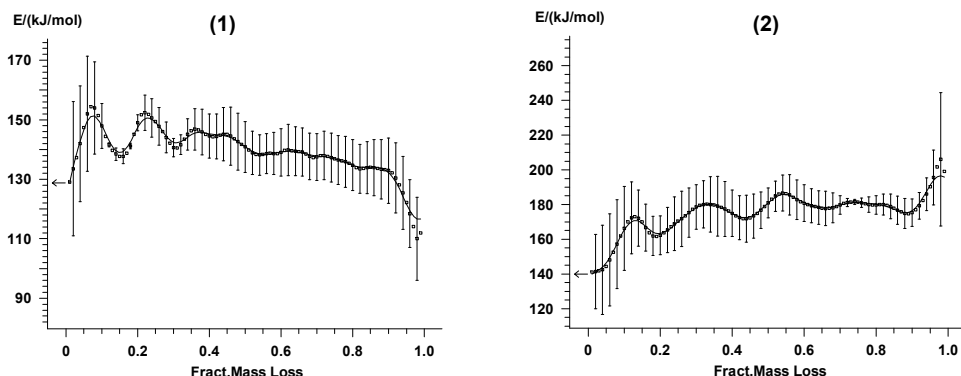


Figure 11 Friedman analysis of sample 2, (1) TG step 1 (2) TG step 2

In sample 2, Figure 11, energy levels in transition step 1 are very similar to that in sample 1 apart from a noticeably smaller decrease in activation energy at the end of the transition, $\alpha > 0.9$. During transition step 2, Figure 11(2), the activation energy increases sharply at $\alpha \leq$

0.15, similar to the behavior in sample 1, but at higher conversion the activation energy seems to gradually increase with conversion which differs from the behavior in sample 1. Nevertheless, both samples do show some dependence of the activation energy on conversion and this behavior is often a sign that each transition contains multiple steps [17].

In order to more closely evaluate the possible kinetic models that best describe the transformations occurring in samples 1 & 2, a “master plot” can be constructed to compare theoretical curves with the current experimental curves. This method allows the user to discern the predominant kinetic model or family of models that best match the experimental results using a relationship that is generally independent of the measured kinetic parameters. The specific master plot used here is based on the following function [18][19][20]:

$$Z(\alpha) = \frac{d\alpha/dt}{\beta} \mu(x)T \quad (13)$$

If we substitute the derivative and integral form of the Arrhenius rate equation into Eq. (13),

$$\frac{d\alpha}{dt} = Af(\alpha)\exp(-E/RT) \quad (14)$$

$$g(\alpha) = \frac{AE}{R\beta} \exp(-x) \frac{\mu(x)}{x} \quad (15)$$

where $x = E/RT$, $\beta = dT/dt$ and the fourth-degree rational approximation of the temperature integral taken from Senum and Yang [21]:

$$\mu(x) = \frac{x^3 + 18x^2 + 88x + 96}{x^4 + 20x^3 + 120x^2 + 240x + 120} \quad (16)$$

we arrive at the expression,

$$Z(\alpha) = f(\alpha)g(\alpha) \quad (17)$$

As seen in Figure 12 and Figure 14, the theoretical values of $Z(\alpha)$ for the most common kinetic models have been plotted against α using Eq. (17) and expressions for $f(\alpha)$ and $g(\alpha)$ from Table 3. Experimental values of $Z(\alpha)$ have been plotted for samples 1 & 2 using Eq. (13) and Eq. (16).

The experimental results for step 1 in sample 1 (Figure 12) seem to obey either an n th-order or nucleation/growth type kinetic model between A1/F1 and A2/Fn at conversions of $\alpha \leq 0.2$ with results from 2°C/min having a larger dimension/smaller order than results from 10 and 32°C/min. This behavior implies that the initial reaction mechanism is somewhat heating rate dependent. At higher degrees of conversion, $0.2 < \alpha \leq 0.8$, experimental results seem to follow a trend similar to that of the R2 kinetic model, and then follow the sharp negative slope of an An kinetic model near the end of conversion. Step 2, Figure 13,

shows general agreement with the An/Fn curves at $\alpha \leq 0.3$ and then follows the R2 curve at greater conversion levels.

Master curve results for step 1 in sample 2 (Figure 14) also seem to obey either an n th-order or nucleation/growth type kinetic model between A1/F1 and A2/Fn throughout the entire conversion but at $0.6 \leq \alpha \leq 0.9$ results for 2°C/min deviate to a larger dimension/smaller order than do results from 10 and 32°C/min. Step 2, Figure 15, shows how experimental results are quite sporadic but generally follow a trend comparable to An/Fn behavior at $\alpha \leq 0.4$ and then converge to a trend similar to R3 behavior at greater conversion levels. Although, results from 10 and 32°C/min do show some adherence to D1 behavior at $0.5 \leq \alpha \leq 0.8$.

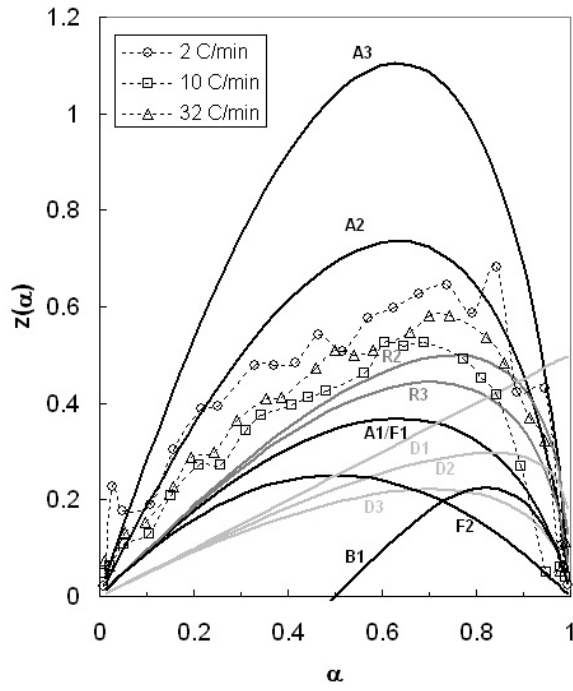


Figure 12 $Z(\alpha)$ diagram for TG step (1) in sample 1

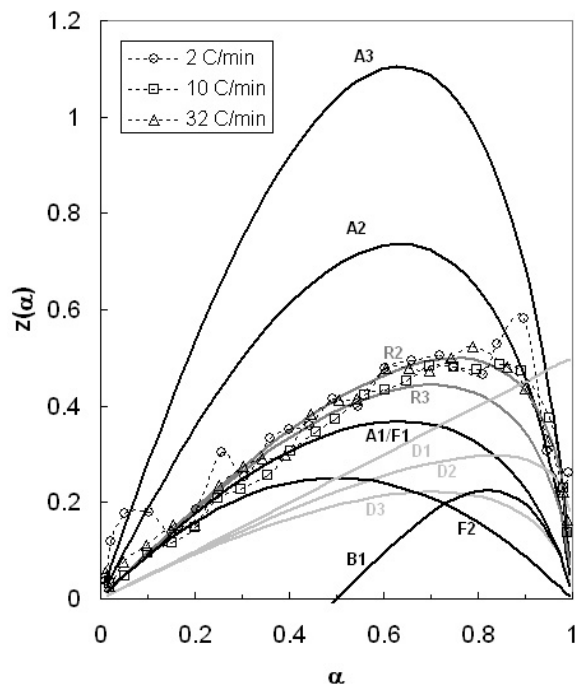


Figure 13 $Z(\alpha)$ diagram for TG step (2) in sample 1

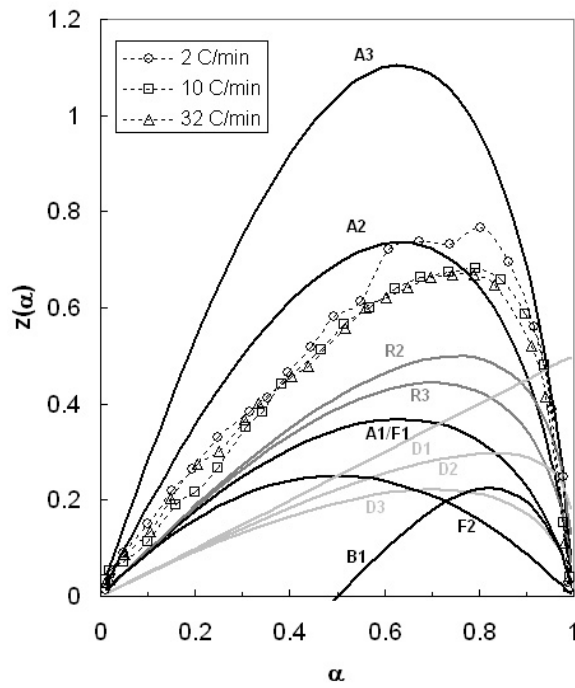


Figure 14 $Z(\alpha)$ master curve for TG step (1) in sample 2

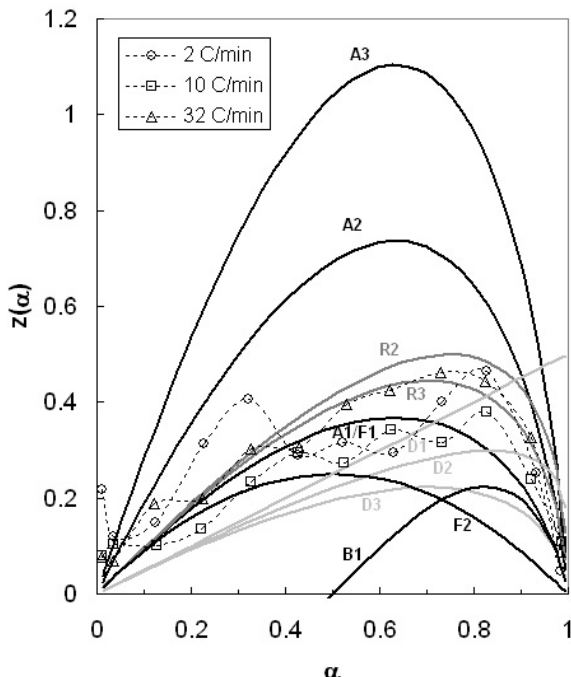


Figure 15 $Z(\alpha)$ master curve for TG step (2) in sample 2

3.4.2 Non-linear Regression Analysis

Sample 1

Results from the regression analysis of TG experiments involving sample 1 are shown in Table 7. With knowledge gained from Friedman and master plot analysis, the decision was made to investigate a configuration of multiple reactions in the non-linear regression analysis.

In TG step 1, the best fit was given for a three step model starting with an n th-order (F_n) step of order $n = 0.75$, E_a between 173-181 kJ/mol, and $\log A$ between 11-12 s^{-1} until $\alpha = 0.19$. Second, a two-dimensional phase boundary (R2) step with E_a between 116-131 kJ/mol and $\log A$ between 8-9 s^{-1} until $\alpha = 0.93$. Lastly, another F_n step of order $n = 0.79$ commences with E_a between 111-141 kJ/mol and $\log A$ between 6-8 s^{-1} .

Continuing with TG step 2, the best fit was given for a two step model starting with an A_n reaction of dimension $n = 0.69$, E_a between 186-198 kJ/mol, and $\log A$ between 7-9 s^{-1} until $\alpha = 0.24$. Second, a R2 reaction commences with E_a between 176-182 kJ/mol and $\log A$ between 6-7 s^{-1} .

Table 7 Results of regression kinetic analysis for sample 1

Model	Multivariate Non-Linear Regression results				
	order/dimension, <i>n</i>	<i>w</i> ^a	<i>E_a</i> (kJ/mol)	log <i>A</i> (s ⁻¹)	<i>R</i> ²
TG step 1	1) Fn	0.75	0.19	179.41 ± 3.99	11.84 ± 0.38
	2) R2	2	0.74	148.63 ± 1.1	8.69 ± 0.08
	3) Fn	0.79		126.05 ± 14.35	6.68 ± 0.65
TG step 2	1) An	0.69	0.24	191.94 ± 5.51	8.36 ± 0.59
	2) R2	2		178.79 ± 2.44	6.83 ± 0.10

^a Parameter *w* is a weighting factor used in multiple reaction models

The initial fractional-order (Fn) model in TG step 1 can be interpreted as a mechanism beginning with CaO product nuclei formation that is somewhat impeded by the reverse process of rehydration indicated by an order less than 1. Normally, CaO nuclei formation would be followed by the formation of a dense reaction layer [22], but because of the tightly packed multi-component structure in the micro briquettes (see Figure 7(1)) gas diffusion is hindered thereby increasing the residence time of product H₂O gas allowing rehydration to occur. The agreement with the R2 model at $0.2 < \alpha < 0.95$ can possibly be attributed to a reaction mechanism where advancement of the reaction interface is related to the layered crystal structure of Ca(OH)₂, i.e. if product nucleation occurs at the more-reactive edge surfaces of a plate-like crystal then the reaction layer would progress inwards two-dimensionally [23]. Although, another possible explanation to this type of physico-geometric behavior was observed by Barret [24], where the characteristics of the phase-boundary reaction were shown to depend on the shape of the crucible, i.e. a cylindrical crucible results in R2 behavior. The activation energy for the R2 model is slightly higher than the energy for dehydration of Ca(OH)₂ found in literature, ~120 kJ/mol. This can be due to overlap with subsequent Fn model behavior during the formation of CO_(g) from graphite gasification. Activation energies for the steam-carbon reaction are of the magnitude 150 kJ/mol at atmospheric pressure but are highly dependent on the local steam partial pressure, temperature and CO/CO₂ ratio [26].

The initial model stage of TG step 2 is rationally tied to the end of TG step 1. Here, the An behavior ($\alpha < 0.25$) can be interpreted as the random growth of the CO_{2(g)}/Fe₃O_{4(s)} interface where CO₂ is a product from hematite reduction. Following the interface growth, the reduction of hematite apparently proceeds via phase boundary mechanism, R2. El-Geassy's work also concludes a mixed reaction mechanism such as this for the reduction of hematite [25]. The apparent activation energy from the model is ~180 kJ/mol lies in between energy values for gaseous reduction of iron oxide, 36-71 kJ/mol [27][28][29], and the intrinsic energy for the Boudouard reaction of approximately 400 kJ/mol [30]. This behavior, i.e. the reaction between solid carbon and iron oxide occurring as the combination of carbon gasification and carbothermic reduction, is generally accepted in the literature [31].

Sample 2

Results from the regression analysis of TG experiments involving sample 2 are shown in Table 8. Again, considering earlier Friedman and master plot analysis, the decision was made to investigate a configuration of multiple reactions in the non-linear regression analysis.

In TG step 1, the best fit was given for a three step model starting with a Fn reaction of order *n* = 0.54, *E_a* between 151-157 kJ/mol, and log *A* between 9-10 s⁻¹ until $\alpha = 0.37$. Next,

an An reaction of dimension $n = 1.46$, E_a between 129-151 kJ/mol, and $\log A$ between 8-10 s^{-1} until $\alpha = 0.66$. Lastly, an A1 reaction commences with E_a between 133-147 kJ/mol and $\log A$ between 8-9 s^{-1} .

Continuing with TG step 2, the best fit was given for a two step model starting with a Fn reaction of order $n = 1.32$, E_a between 149-157 kJ/mol, and $\log A$ between 6-8 s^{-1} until $\alpha = 0.32$. Second, a R3 reaction commences with E_a between 185-192 kJ/mol and $\log A$ between 7-9 s^{-1} .

Table 8 Results of regression kinetic analysis for sample 2

Model	Multivariate Non-Linear Regression results				
	order/dimension, n	w^a	E_a (kJ/mol)	$\log A$ (s^{-1})	R^2
TG step 1	1) Fn	0.54	0.37	153.83 ± 2.81	9.57 ± 0.29
	2) An	1.46	0.29	140.32 ± 10.52	8.70 ± 0.80
	3) An	2.12		139.97 ± 6.85	8.47 ± 0.47
TG step 2	1) Fn	1.32	0.32	152.98 ± 3.92	6.96 ± 0.23
	2) R3	3		188.42 ± 2.84	7.97 ± 0.17

^a Parameter w is a weighting factor used in multiple reaction models

In sample 2 the initial fractional-order (Fn) model in TG step 1 is similar to that in sample 1 but the order of reaction is lower. This is most likely due to the smaller hematite grain size in sample 2 causing a decrease in total porosity (see Figure 7(2)) and consequently making gas diffusion more difficult increasing the reversibility of the dehydration reaction. In contrast to the behavior in sample 1, sample 2 follows “An” model behavior at $0.4 < \alpha$ rather than phase boundary behavior. In reference to Figure 5, it is evident that the maximum rate of weight loss in step 1 for sample 2 is faster than that in sample 1. An explanation can be that instead of a slow advancement of the reaction interface seen in sample 1, crack development occurs in sample 2 due to excessive gas pressure resulting in more rapid and extensive dehydration. At the same time, the n exponent is ~ 1.5 , signifying that nucleation is instantaneous and growth occurs preferably in one direction more than the other [32]. The final stage of TG step 1 in sample 2 follows A2 model behavior and can be interpreted as the growth of the $\text{CO}_{(g)}/\text{C}_{(s)}$ interface during graphite gasification. The gasification reaction can be starved due to low steam pressure, so the small amounts of $\text{CO}_{(g)}$ that are produced will more likely remain adsorbed to solid graphite surfaces [33] rather than participate in reduction reactions.

In TG step 2 the transition seems to follow Fn behavior ($\alpha < 0.35$) and can be interpreted as the direct reaction between a ionically-active $\text{C}_{(s)}$ and $\text{Fe}_2\text{O}_{3(s)}$. Those surfaces which are in close contact with iron oxide can initiate direct reduction. Following initial direct reduction, the reduction of hematite apparently proceeds via phase boundary mechanism, R3. The shrinking core model is more preferable in sample 2 than in sample 1. This is likely due to the much smaller hematite particle size in sample 2 as well as the larger apparent activation energy, ~ 190 kJ/mol, signifying more control applied by the Boudouard reaction, Rxn 4.

4. Conclusions

The complex series of transformations occurring when iron and steelmaking by-product agglomerates are used as recycled iron charge in steelmaking processes was investigated on the basis of a simpler, model system: $\text{Fe}_2\text{O}_3\text{-Ca(OH)}_2\text{-C}$ in inert atmosphere. First, the composition of the ternary mix, i.e. 62.5% Fe_2O_3 , 25% Ca(OH)_2 , 12.5% C, was determined,

from TG tests and XRD analysis, as the most suitable for the concurrent optimization of both the reduction degree and, through calcium ferrite formation, the agglomerate strength.

Next, the kinetics of two samples of this optimum mix, with two different grain sizes of hematite, was investigated. The overall transformation below 800°C involves a series of reactions, including calcium hydroxide dehydration, carbon gasification, iron oxide reduction, and calcium ferrite formation.

With micro-sized hematite grain briquettes, the transformation starts with calcium hydroxide dehydration, whose first step, CaO nucleation, is somewhat impeded by the slow escape of H₂O imposed by the tight structure of the briquette. Dehydration proceeds by the inward 2D growth of the CaO grains. Evolved steam in turn begins gasifying carbon grains, producing CO and H₂. Then the reduction of hematite takes place by these gases, also via a 2D phase boundary mechanism, down to a reduction degree situated between magnetite and wustite. Parallel to the iron oxide reduction, a calcium ferrite phase appears, in the form of angular and calcium-rich particles.

In the case of briquettes containing nano-sized hematite, the course of the transformation is slightly different. Nucleation of CaO starts more slowly due to lower total porosity of the briquette, but soon after, the development of cracks, which is favored by high heating rates, makes dehydration more rapid and more extensive. Carbon gasification by steam is penalized by lower water pressures after crack formation. Locally, where hematite grains are in close contact with carbon particles, an almost direct reduction can occur, with some iron oxide grains being reduced down to wustite.

In general, when considering by-product compositions with large contents of iron oxide, calcium oxides and carbon a few comments can be made. Hydrated lime or other hydrate content in the system Fe₂O₃/metal hydrate/C has the best correlation with the reduction degree, H₂O utilization and CO utilization at low temperatures. With this in mind, a C:H₂O_(hydrate) molar ratio between 2 and 3 and a C:O_(iron oxide) molar ratio greater than 0.85, is optimal in the context of this study. Furthermore, excess milling of by-products before agglomeration is discouraged due to the greatly adverse effects on reduction degree.

5. Acknowledgments

The authors would like to express their gratitude to Mr. Bernard Rouat for all help in laboratory and the Foundation of King Carl XVI Gustaf's 50th Birthday Fund for financial support during the completion of this work.

6. References

- [1] C. Takano, R.C. Nascimento, G.F.B.L. Silva, D.M. dos Santos, M.B. Mourao: EPD Congress 2001, TMS, 183-193.
- [2] H.W. Gudenu, D. Senk, S. Wang, K. De Melo Martins, C. Stephany: ISIJ International, Vol. 45 (2005), No. 4, 603-608.
- [3] J.S. Ahn, C.M. Chon, H.S. Moon, and K.W. Kim: Water Research, Vol 37, Issue 10, May 2003, 2478-2488.
- [4] R. Robinson: Thermochimica acta 432 (2005), 112-123.

- [5] C. Takano, M.B. Mourao: Mineral Processing & Extractive Metall. Rev., 24, 2003, 233-252.
- [6] M.C. Mantovani and C. Takano: *ISIJ Int.*, Vol 40, No. 3, 2000, p. 224-230.
- [7] Y. Kashiwaya, M. Kanbe and K. Shii: *ISIJ Int.*, **41** (2001), 818.
- [8] S. Mookherjee, H. S. Ray and A. Mukhrjee: Ironmaking and Steelmaking, 1986, 13, 229-235.
- [9] W.-K. Lu, C. Bryk and H. Gou: 'Process Technology Proceedings', Vol. 6 (Proc. 5th Int. Iron and Steel Congress, Book 3), Washington, DC, USA, April, 1986, 1065-1075; 1986, Warrendale, PA, ISS-AIME.
- [10]H. Gou, W.-K. Lu and C. Bryk: *ISIJ Int.*, 1992, 32, 733-740.
- [11]K. Kumabe, H. Moritomi, R. Yoshiie, S.Kambara, K. Kuramoto, Y. Suzuki, H. Hatano, S.Y. Lin, and M.Harada: Gasification of Organic Waste with Subcritical Steam under the Presence of a Calcium-Based Carbon Dioxide Sorbent, *Ind. Eng. Chem. Res.* 2004, 43, p. 6943-6947.
- [12]J. Wang and T. Takarada: Role of Calcium Hydroxide in Supercritical Water Gasification of Low-Rank Coal, *Energy & Fuels* 2001, 15, p. 356-362.
- [13]T. Inui, T. Otowa, and F. Okazumi: Gasification of Active Carbon by Iron-Based Composite Catalysts for Obtaining Directly a Gas Optional H₂/CO Ratio, *Carbon*, Vol. 23, No.2, 1985, p. 193-208.
- [14]S. Sato, S.Y. Lin, Y. Suzuki, and H. Hatano: Hydrogen production from heavy oil in the presence of calcium hydroxide, *Fuel* 82 (2003), p. 561-567.
- [15]H.Y. Sohn and E.M. Wadsworth: Rate Processes of Extractive Metallurgy, Plenum Press, New York, NY, 1979.
- [16]R. Robinson, N. Menad and B. Björkman: The Fourth International Congress on the Science and Technology of Ironmaking : Proceedings, ICSTI 06. The Iron and Steel Institute of Japan, 2006, 311-314.
- [17]J. Opfermann: *Journal of Thermal Analysis and Calorimetry*, Vol. 60 (2000), p. 641-658.
- [18]A. Ortega: *International Journal of Chemical Kinetics*, Vol. 34, 2002, p. 193-208.
- [19]N. Koga, J. Sestak, and J. Malek: *Thermochimica Acta*, Vol. 188, 1991, p. 333.
- [20]J.M. Criado, A. Ortega, F. Gotor: *Thermochimica Acta*, Vol. 157, 1990, p. 171-179.
- [21]G.I. Senum and R.T. Yang: *Journal of Thermal Analysis*, Vol. 11, 1977, p. 445-447.
- [22]Andrew K. Galwey and Genevieve M. Laverty: *Thermochimica Acta*, 228 (1993), p. 359-378.
- [23]N. Koga and H. Tanaka: *Thermochimic Acta*, Vol. 388, 2002, p. 41-61.
- [24]P. Barret: *International Proceedings of the 4th Symposium on the Reactivity of Solids*, Amsterdam, 1960, p. 178.
- [25]A.H.A. El-Geassy: *Scandinavian Journal of Metallurgy*, 1998, vol. 27, p. 205.
- [26]M.D. Mann, R.Z. Knutson, J. Erjavec, J.P. Jacobsen: *Fuel*, 2004, vol. 83, pp. 1643-50.
- [27]E.T. Turkdogan: 31st Ironmaking Conf. Proc., 1972, pp. 438-58.
- [28]E.T. Turkdogan and J.V. Vinters: *Metall. Trans.*, 1971, vol. 2, pp. 3175-88.
- [29]S.K. Dutta and A. Ghosh: *Iron Steel Inst. Jpn. Int.*, 1993, vol. 33, pp. 1168-73.
- [30]O.M. Fortini and R.J. Fruehan: *Metall. Mater. Trans. B*, 2005, vol. 36B, pp. 709-17.
- [31]R. Haque and H.S. Ray: *Metall. Mater. Trans. B*, 1995, vol. 26B, pp. 400-01.
- [32]J. Malek: *Thermochimica Acta*, 1995, vol. 267, pp. 61-73.
- [33]E.T. Turkdogan and J.V. Vinters: *Carbon*, 1970, vol. 8, pp. 39-53.

